KAUNAS UNIVERSITY OF TECHNOLOGY

YATINKUMAR PATEL

RESEARCH AND DEVELOPMENT OF FUNCTIONAL NANOPOROUS ALUMINUM OXIDE MEMBRANES FOR MICRO/NANO FILTRATION DEVICES IN BIOENGINEERING

Doctoral dissertation
Technological Science, Mechanical Engineering (T 009)

Kaunas, 2022

KAUNO TECHNOLOGIJOS UNIVERSITETAS

YATINKUMAR PATEL

FUNKCINIŲ NANOPORINIŲ ALIUMINIO OKSIDO MEMBRANŲ, SKIRTŲ MIKRO/NANO FILTRAVIMO ĮRENGINIAMS BIOINŽINERIJOJE, TYRIMAS IR KŪRIMAS

Daktaro disertacija
Technologijos mokslai, mechanikos inžinerija (T 009)

Kaunas, 2022

Disertacija rengta 2018–2022 metais Kauno technologijos universiteto Mechanikos inžinerijos ir dizaino fakultete, Mechanikos inžinerijos katedroje. Mokslinius tyrimus rėmė Lietuvos mokslo taryba.

Doktorantūros teisė Kauno technologijos universitetui suteikta kartu su Vytauto Didžiojo universitetu.

Mokslinis vadovas:
Prof. habil. dr. Arvydas PALEVIČIUS (Kauno technologijos universitetas, technologijos mokslai, mechanikos inžinerija, T 009).

Redagavo: anglų kalbos redaktorius dr. Armandas Rumšas (leidykla „Technologija"), lietuvių kalbos redaktorė Violeta Meiliūnaitė (leidykla „Technologija")

Mechanikos inžinerijos mokslo krypties disertacijos gynimo taryba:
prof. habil. dr. Vytautas OSTAŠEVIČIUS (Kauno technologijos universitetas, technologijos mokslai, mechanikos inžinerija, T 009) – pirmininkas;
prof. dr. Regita BENDIKIENĖ (Kauno technologijos universitetas, technologijos mokslai, mechanikos inžinerija, T 009);
prof. dr. Vytenis JANKAUSKAS, (Vytauto Didžiojo universitetas, technologijos mokslai, mechanikos inžinerija T 009);
prof. dr. Sergei KRUCHININ (Bogoliubovo teorinės fizikos institutas, Ukraina, gamtos mokslai, fizika, N 002);
doc., dr. Kęstutis PILKAUSKAS (Kauno technologijos universitetas, technologijos mokslai, mechanikos inžinerija, T 009).

Disertacija bus ginama viešame mechanikos inžinerijos mokslo krypties disertacijos gynimo tarybos posėdyje 2022 m. gruodžio 14 d. 14 val. Kauno technologijos universiteto Studentų miestelio bibliotekoje, salėje M7.

Adresas: Studentų g. 48–M7, Kaunas, LT-51367, Lietuva.
Tel. (+370) 608 28 527; el. paštas doktorantura@ktu.lt

Disertacija išsiųsta 2022 m. lapkričio 14 d.
Su disertacija galima susipažinti internetinėje svetainėje http://ktu.edu, Kauno technologijos universiteto (K. Donelaičio g. 20, LT-44239, Kaunas) ir Vytauto Didžiojo universiteto (K. Donelaičio g. 52, LT-44244, Kaunas) bibliotekose.

Table of Contents

List of Tables

List of Figures

10

12

14

Abbreviations

3D – Three-dimensional
AAO – Anodic aluminum oxide
AC – Alternate current
AL_2O_3 – Aluminum oxide
Ag – Silver
Au – Gold
BSED – Back scattered electron detector
CH_4 -– Methane
CMC – Crystal violet
CO_2 -– Carbon dioxide
CVD – Chemical vapor deposition
DC – Direct current
DNA – Deoxyribonucleic acid
D_c – Interpore distance/ distance between pores
D_p – Pore diameter
E-beam – Electron beam
EP – Electrophoresis
HA – Hard anodization
kHz – Kilohertz
MA – Mild anodization
MD700 – Perfluoropolyether (PFPE)-urethane dimethacrylate
MEMS -– Micro-electromechanical systems
MHz – Megahertz
Mid-IR – Mid infrared spectroscopy
N_2 -– Nitrogen
NAO61 – Norland Optical Adhesive 61
NIL – Nanoimprint lithography
NIR – Near infrared spectroscopy
Ni – Nickel
PAA – Polyacrylic acid
PC – Polycarbonate
PCL – polycaprolactone
PCR – Polymerase chain reaction
PDMS – Polydimethylsiloxane
PE – polyethylene
PEFDA – Peltophorum dasyrhachis
PEG – Poly(ethylene glycol)
PET – Polyethylene terephthalate
PLA – Polylactic acid
PMMA – Polymethylmethacrylate
PS – Polystyrene

PSA – Pressure Sensitive Adhesive
PTFE – Polytetrafluoroethylene
PVDF – Polyvinylidene fluoride
PZT –– Piezoelectric material (Piezoceramic PZT-5H)
SAW –– Surface acoustic waves
SDS – Sodium dodecylsulfate
SE – Scattered electron
SED – Scattered electron detector
SEM – Scanning electron microscopy
Si – Silicon
SiO_2 – Silicon dioxide
TPE – Thermoplastic elastomers
TiO_2 – Titanium dioxide
UV – Ultraviolet
ZnO – Zinc oxide
ZrO_2 – Zirconium dioxide

Introduction

With the development of nanotechnology in the twenty-first century, numerous solutions for creating materials with extraordinary qualities have been developed. These compounds can be used in conventional systems to improve their efficiency, or else they can be used to interact with microorganisms to achieve a breakthrough in healthcare. These unique features are the result of the regular arrangement of nanoscale dimensions. Other technical factors can be used to adjust the arrangement and dimensions of these elements. The development of nano systems needs more profound understanding of the relevant materials and chemical engineering so that to reduce the size of the conventional systems as well as to increase the efficiency and accuracy of the system. Reducing the use of conventional parts, such as a liquid pump, to nano systems also poses a considerable technical challenge. The nano systems technology offers the potential to significantly reduce the size of large laboratory equipment, which would result in several highly beneficial characteristics: compactness, reduced reagent consumption, faster reactions, and more precise analytical parameters. Thus, the benefits of these technologies are not limited to the capacity of microorganisms of undergoing damage or distortions. Such particle control is advantageous in a variety of fields, and it is of importance not only for researchers, but also for professionals working in other fields.

With the need for a more efficient and environmentally friendly liquid filtration process, attention has been paid to such advanced materials as nanofiber membranes for filtration equipment. Separation and filtration of bio particles is an important issue in the identification and analysis of industries, specifically, biochemical and biomedical industries, for the development of new devices which would be able to help upgrade the process, but would also focus on the development of an efficient and effective method. In the past, many technologies were used to purify liquids, such as distillation, chemical disinfectant treatment, or sand filtration. Meanwhile, micro/nano membrane filtration is a relatively new method with certain advantages, such as buoyancy, low energy consumption, chemical-free liquid cleaning, or low operating temperatures.

The recent developments in the field of microfluidic device fabrication for the application of filtration and separation at the micro/nano level can be improved by using the membrane based micro filtration technique. Membranes are semi-permeable media which allow only certain particles and compounds to penetrate, while preventing others from passing through. The membrane filtration system can be improved by using nanofiber media. Nanofibers are denoted by high porosity and well-bonded pore structures as well as good permeability, thereby making them ideal for cleaning liquids. This fiber can also be used to filter high viscosity liquids, such as oil. If fiber is used as a tool to study materials, then the nonlinear properties of materials can be studied very accurately in a variety of studies. Recently, the nanoporous anodic aluminum oxide membrane (AAO) has gained significant

attention of researchers for a variety of applications in the field of the micro-electromechanical system (MEMS). Especially, the design of new generation microfluidic devices based on the nanoporous membrane requires excellent characteristics for efficient work in the biological environment. The nanoporous aluminum oxide membrane provides high mechanical strength, offers a low cost as well a relative ease of fabrication, along with the ease of control the geometry by changing the process parameters.

Acoustic wave propagation in the nanostructured membrane expands the application possibilities of nanoporous membranes in terms of controling the flow in the channel and the particles passing through nanotubes. Acoustics in the micro-hydraulic research is a new field aiming to investigate, explain, and exploit the effects of acoustic waves in hydraulic devices. Surface acoustic waves (SAW) are employed for modulation by using the piezoelectric material (PZT) actuator. This goal has been widely pursued since the accurate manipulation of micro/nano particles became possible in micro hydraulic devices. Acoustic flow is the uniform motion of a fluid caused by the acoustic pulse flow absorbed by the fluid. This effect is used to control the acoustic flow in order to amplify or suppress the acoustic flow. This effect is most commonly applied in such areas as particle control and concentration. Many techniques have been developed to be used for the separation and filtration of micro particles based on the membrane. Also, clogging is one of the most common problems of filtration through the nanoporous membrane, but it can be overcome by employing surface acoustics which helps to avoid clogging nanopores and reduces the friction between microparticles and the wall of nanotubes thus providing an efficient filtration process by using the acoustic radiation force which helps to align the micro/nano particles inside nanotubes and, by using sound pressure, particles can move in the lower acoustic pressure region and be centered in the laminar fluidic flow thus reducing the friction between the wall of the tube. Therefore, the filtration of a biological cell results in a lower risk of damaging cells.

In many manipulation systems, the dimensions of the fluid channels are generally similar to the acoustic wavelength. There are two different mechanisms for controlling liquid particles. The first one is based on the force of acoustic radiation which allows particles to move relative to the body of the surrounding fluid. In the second method, the acoustic flow can be used to pull the particles together with the acoustic fluid flow. In this way, individual particles or large quantities of them can be controlled in the non-contact manner. The non-contact method indicates that the objects being manipulated are not otherwise affected or deformed, which is very important for micro/nano cells and for the biomedical science in general.

Therefore, there is obvious need for an efficient and low-cost membrane-based technology using surface acoustics for micro/nano particle separation/filtration. As the research of aluminum nanomembranes is at an early stage, it is fundamentally important to develop methods so that to expand their capabilities and deepen knowledge on this topic in order to better understand the ongoing process(es). The research and development of the nanoporous aluminum

oxide membrane for the purpose of filtration/separation is covered in this work, including the fabrication process, characterization, evaluation of the properties as well as the surface acoustics wave modulation on the surface of the nanoporous AAO membrane using the PZT actuator. Additionally, the application of the nanoporous AAO membrane for gas separation is bound to be presented.

Research Aim and Tasks:

The **aim** of the research is to develop functional micro nano elements based on the nanoporous aluminum oxide membrane that would be used in biomedical micro hydraulic system(s). In order to achieve this aim, the following **tasks** have been carried out:

1. To carry out an overview of research literature on micro hydraulics in micro fluidics, membrane-based microfluidics, and nanoporous anodic aluminum oxide application in biomedical sciences.
2. Design and development of an experimental setup for the fabrication of a nanoporous membrane with a uniform porous structure by using two-step electrochemical anodization and a cooling system based on the Peltier element.
3. To analyze the geometrical structure, the chemical composition, and the hydrophobic properties of the fabricated nanoporous aluminum oxide membrane.
4. To investigate the mechanical characteristics and to research the resonance frequencies of the fabricated nanoporous aluminum oxide membrane and their application in a physical prototype for micro/nano filtration in micro/nano hydraulic systems.
5. To design a numerical model of the physical prototype for the investigation of acoustic pressure distribution in a nano tube and to use the bulk acoustic phenomenon in the design of the micro/nano hydraulic system devoted for nano-filtration could be of use in biomedicine for the fabrication of a nanoporous aluminum oxide membrane. Also, to conduct experimental analysis of the applicability of the fabricated nanoporous AAO membrane for gas separation.

Research Methods and Equipment

The fabrication of the nanoporous AAO membrane was achieved by using the designed experimental setup and the two-step electrochemical anodization method.

Scanning electron microscopy (SEM HITACHI S-3400N) was utilized to investigate the chemical composition and the geometrical structure of the fabricated nanoporous AAO membrane, including the pore diameter, the interpore distance, and membrane thickness. The measurement of the hydrophobic properties of the fabricated AAO membrane was done by using the designed experimental setup, and the obtained images were analyzed by using the image processing software *ImageJ*.

The mechanical properties of the fabricated nanoporous alumina were analyzed by using micro indentation (*CSM instruments*, Micro combi tester) with the Olive and Pharr method using a diamond indenter tip.

The theories of vibration and acoustic wave were applied by using a piezoelectric actuator to functionalize the nanoporous membrane for the acoustic wave distribution analysis. Resonance frequencies were determined by using commercially available software *COMSOL Multiphysics 5.4*. For the validation of the computational results, experiments were performed by using nondestructive testing methods by employing a 3D scanning vibrometer (POLYTECH) and holographic interferometry (PRISM system) in order to analyze the various geometrical forms and to investigate the resonance frequency of the system.

For gas transmission and separation, a gas permeation experiment was performed for with three different gases: CO_2, N_2, and CH_4.

The research work was carried out at the Faculty of Mechanical Engineering and Design, the Institute of Mechatronics, the Institute of Materials Science, Kaunas University of Technology. Also, the analysis of the membrane was conducted at Lithuanian Energy Institute, Kaunas and Agriculture Academy, Vytautas Magnus University, Kaunas.

Scientific Novelty

1. The experimental setup was designed based on the Peltier element cooling system for the effective electrochemical anodization process so that to fabricate the desired quality of the nanoporous aluminum oxide membrane for microfluidic application.
2. An efficient and low-cost experimental research method and a stand have been developed to assess the hydrophobic quality of the nanoporous aluminum oxide membrane and other surfaces in micro/nano engineering.
3. Numerical modeling of the distribution of acoustics waves has been developed for surface acoustic wave modulation on the surface of the nanoporous membrane for the desired application of the fabricated membrane for nano filtration using a piezoelectric actuator.
4. Numerical modeling has been developed for acoustic pressure distribution inside the nanotube, and the time required for particles to align in the center of the nanotube to reduce friction between the particles and the wall of the tube during nanofiltration for biomedical MEMS has been determined.

Practical Value

1. By using the experimental study on the fabrication method, low-cost nanoporous membranes with predetermined parameters for the desired geometrical structure of nanopores and nanotubes can be fabricated. It also helps to control the geometry during the fabrication process.

2. Experimental research of analyzing the hydrophobic properties of the membrane allows understanding the surface behavior of the membrane with different fluids and structural properties.
3. Numerical modeling of the bulk acoustic wave module was used to develop a filtration model using the fabricated nanoporous aluminum oxide membrane. Their application in various experiments is possible by changing the model parameters while using the same principle of acoustic actuation.
4. Numerical modeling of acoustic pressure distribution allows understanding the phenomenon of pressure distribution inside a nanotube under bulk acoustics and can be used for the development of a microhydraulic filtration device using PZT actuation.

Statements Presented for Defense

1. The introduction of a cooling system based on the Peltier element allows controlling or maintaining the temperature during the electrochemical anodization process, and this directly affects the quality of the nanoporous structure of the membrane, which affects the applicability for the filtration/separation of micro/nano bioparticles.
2. The methodology used for the characterization and acoustic wave formation for experimental investigation allows evaluating the functionality and usability of the functional micro/nano element for micro hydraulic or micro fluidic systems in biomedicine.
3. The elevation in the driving frequency leads to the deformation of the membrane in various forms, and it allows manipulating the nanotubes formed in a nanoporous membrane so that to eliminate clogging; it also increases the efficient filtration in microhydraulics for biomedicine.

Publication and Approbation of Research Work

The research results presented in the dissertation have been presented in seven publications. Two of them are publications cited in the *Web of Science* database journals with a citation index Q1 and Q4, three of them are publications referenced in the *Web of Science* database without a citation index, and two publications were delivered in conference proceedings. The results of the research have been presented at nine international conferences: *Materials Today*: proceedings: Third international conference on aspects of materials science and engineering (ICAMSE 2021, India), *Materials Today*: proceedings: Second international conference on aspects of materials science and engineering (ICAMSE 2022, India), *IEEE XVI* international conference on the perspective technologies and methods in MEMS design (MEMSTECH, Ukraine, 2020), *SPIE: Frontiers in Ultrafast Optics*: biomedical, scientific, and industrial applications (USA, 2020), The *NATO Seminar on Advanced Nanomaterials for Detection of CBRN* (Ukraine, 2019), the 65th

international conference for students of physics and natural sciences (Open readings 2022, Lithuania), the *2nd international research workshop in biomechanical microsystems* (IRWBM 2021, Lithuania), the *63rd international conference for students of physics and natural sciences* (Open readings 2020, Lithuania), and the *international research workshop in biomechanical microsystems* (IRWBM 2019, Lithuania).

Scope and Structure of the Dissertation

This doctoral dissertation consists of an introduction, 5 main chapters, conclusions, bibliography, summary of the dissertation, a list of the author's publications and the author's CV. The volume of the dissertation is 189 pages. The main part of the dissertation, covering 127 pages, contains 91 figures and 34 tables; it uses 174 references.

The first chapter deals with the literature review section. It covers micro hydraulic systems in microfluidics, micro/nano porous membrane based microfluidic systems, the methods of the integration of membranes in microfluidic systems, the controlling methods of micro particles in microfluidic systems, the types of micro/nano porous membranes and materials. The chapter also covers the nanoporous aluminum oxide membrane fabrication process and parameters, as well as the application of the AAO membrane in biomedicine for filtration and separation. At the end of the chapter, the aim and tasks of the dissertation are formulated.

The second chapter deals with the design of a cooling system based on the Peltier element aiming to develop the experimental setup so that to maintain the desired temperature of the electrolyte solution during the electrochemical anodization process for the fabrication of a nanoporous AAO membrane with various process parameters. The theoretical and experimental analysis of the designed cooling system was performed in order to determine the temperature of electrolytes during the anodization process. The fabrication of a nanoporous AAO membrane was performed at various process parameters by using the developed experimental setup.

The third chapter describes the analysis of the geometrical structure of pores, as well as the chemical composition and the hydrophobic properties (by using the developed methodology and the devised stand) of the fabricated nanoporous AAO membrane obtained by using various process parameters for the applicability of the AAO membrane for the filtration and separation of micro/nano particles in microhydraulic devices for biomedicinal purposes.

The fourth chapter covers the mechanical properties (the hardness and elastic modulus) of the fabricated nanoporous AAO membrane by using the micro indentation test. The effect of different pore sizes, porosity, and thickness on the hardness and elastic modulus of the AAO membrane was discussed. The functionality of the fabricated nanoporous AAO membrane for filtration was

evaluated by using a piezoelectric actuator while considering bulk acoustic waves. The theoretical and experimental study of the formation of acoustic waves was performed for the functionality of the fabricated AAO membrane for micro/nano filtration in biomedicine.

The fifth chapter presents the theoretical investigation of the flow characteristic in a nanotube, the acoustic pressure distribution and the particle motion inside a nanotube while taking into consideration the bulk acoustic waves. The applicability of the fabricated nanoporous membrane was investigated experimentally by using acoustic waves for fluid permeation. Also, the applicability of the fabricated nanoporous AAO membrane for gas separation with the objective of removing toxic gases was evaluated experimentally.

The conclusions of the dissertation summarize the results of the conducted theoretical and experimental research.

I.   Literature Review

This chapter is devoted to the microhydraulic development in microfluidics systems. It consists of literature overview on membrane-based microfluidic devices, the methods of membrane integration in microfluidic devices, and it also discusses the method of particle manipulation in microfluidics. The types of micro/nano porous membranes used for the development of biomedical devices, as well as the membrane fabrication methods are discussed. Lastly, discussion about the micro/nano porous aluminum oxide membrane fabrication process, the process parameters, the methods of fabrication, and its application in the biomedical science is presented.

The demand for and the advancement of technology in engineering fields requires novel materials with superior properties with multicycle usage. Currently, in biomedical applications, micro hydraulic systems are more popular; they have been rapidly changing by improving the physical dimensions of the devices at the micro and nano level. MEMS research has led to the creation of novel micro actuation techniques. The primary motivation for MEMS research is the weight, size, and the power consumption reduction. Electromagnetic, electrostatic, thermomechanical, piezoelectric, and shape memory alloy actuators are being used today. Electro-hydrostatic actuation is a unique technique that makes advantage of the pressure fluctuations caused by temperature changes in confined fluid. Microhydraulics is a subsystem of MEMS and microfluidic systems that work in conjunction with other electronic devices.

1.1 Micro/nano Hydraulic Systems

The micro/nano hydraulic science and the related technologies involve the flow of a fluid in a system with at least one nanoscale dimension from 1 nm to 100 nm, and micro hydraulics covers the range from 100 nm to 100 μm [1]. With such dimensions, the Reynolds number is small, and the flow is usually laminar, but the flow rate itself is often high, which results in unique microhydraulic mixing devices. According to the *International Union of Pure and Applied Chemistry* (IUPAC), the size of the pores of nano hydraulic devices falls into three categories: micropores, mesopores, and micropores with the pore sizes in the system of less than 2 nm, 2 nm to 50 nm, and greater than 50 nm, respectively [2]. These pores can be used to obtain complex structures, such as gel matrices, ion tracks, engraved membranes, and many others. Such structures have been investigated and used in the fields of separation, filtration, and catalysis. These technologies are widely used in both science and industry.

Micro/nano hydraulic systems are mostly used in microfluidics for the flow control and control of micro/nano particles or the presence of cells in flowing fluids through nanochannels and nanotubes in microfluidic systems. Mixing, pumping, and valve systems are distinguished for flow control. By virtue of being designed for particle control, microhydraulic systems are used for separation, focusing, and

positioning. The commonly used microhydraulic systems in microfluidics are shown in Fig. 1.1.
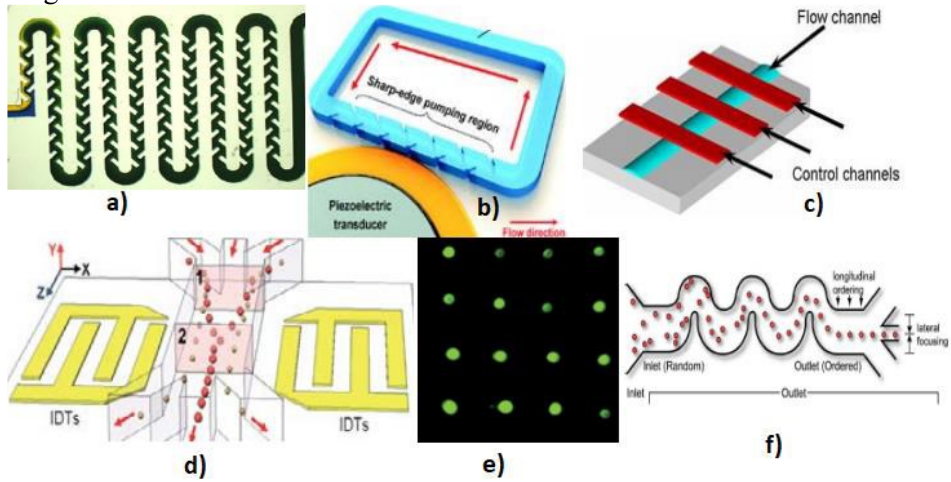
Fig. 1. 1 Microhydraulic systems in microfluidics: mixing (a), suction (b), valves (c), separation of particles (d), positioning (e), and focusing (f) [3]

For these systems of microhydraulic equipment for fluid and particle control, two methods are most commonly used: geometric and acoustic. The geometric control method uses the structure of the device and moving elements which can direct the particles in one way or another. Due to the acoustic pressure, fluid flows can be controlled. In this method, the liquid is exposed to high frequency oscillations generated by a particular source of oscillation. Often, the two methods are combined to obtain specific fluid management capabilities [4].

There are three main types of systems designed to control the movement of fluids in micro hydraulic systems. Some systems use differential pressure devices (hydrostatic or pressure generators), while other systems allow the flow rate to be set directly because a specific amount of fluid is injected. There are liquid pumps and electroosmotic pumps that can be used to create the flow of a liquid.

The flow generated by hydrostatic pressure makes it easier to control the flows in the microhydraulic system. Hydrostatic pressure is the pressure of a standing fluid at a selected depth point. Pressure difference can also be obtained by varying the height of the liquid-atmosphere interface in different tanks. This pressure occurs at the air-liquid interface and depends on the nature of the liquid, the atmosphere, the tank capacity, and the shape of the tank. Due to the gradually changing amount of the liquid in the tank, the pressure of the liquid also changes gradually, which becomes a negative feature for the stability of the system. The main disadvantage of this system is the limited control of the applied pressure in the microchannels [5].

As an alternative to the hydrostatic pressure, the pressure generated by the pump can be used. These pumps usually consist of a pressure source, a diaphragm,

and a manometer to monitor the pressure. The reliability and stability of this system depends on the reliability of the components and their compatibility. Thus, the pumps can react very quickly and increase or decrease the flow in the system. The pumps can also be paired with flow sensors to provide flow rate control rather than pressure control. Pressure can also be controlled by using solenoid valves that are controlled electronically. The advantage of this technology is the fast response that can be obtained by using microvalves. The main disadvantage of two-valve electronic pressure generators is the generation of fluctuating pressure [6].

An unconventional solution for liquid administration is the infusion pumps. These systems were primarily developed and used for 'perfusion' systems in the medical field. The improvement of this system was subsequently adapted for microhydraulic systems. The main advantage of this system is the ability to control the flow through microchannels regardless of the fluid resistance. The fundamental drawback of infusion pumps is the development of pulsed flows at low flow rates, and it requires a longer period of time to steady the flow. In order to address these issues, researchers have developed an infusion pump stabilizer that consists of a kit designed to mitigate and/or equalize flow rate fluctuations. Another unconventional solution for creating pressure in a liquid is 'electric' pumps. These pumps do not have flow fluctuation problems because their operation is based on the electricity-powered pumping of a liquid through nanoporous materials. The only drawback of this concept is that the system requires the use of a low electrical conductivity fluid [7].

All of the hydrostatic pumps listed above are designed to control micro-hydraulic systems. These systems require very small amounts of liquid (up to a femtoliter in some cases). These small amounts of liquid are denoted by different properties from the liquids used in everyday life, which is an incentive for new scientific experimentation and innovation. The main and most difficult task is to integrate all the necessary components (valves, ducts, pressure/flow sensors, etc.) into a micro-sized system and to make it work as a macro-system. The basis of the microsystem network of microchannels connected to the cut-out holes in the macrosystem. Through these holes, fluid is injected into the micro-hydraulic system. Automation and high-throughput systems are developed by directing, mixing, or manipulating the liquid entering the microchannel. In order to obtain the desired properties, the design of the microchannel network must be precisely prepared, and, in order to precisely manage the liquids inside the microchannels, special systems are required [8].

1.1.1 Elements of Micro/nano Hydraulic Systems

Hydraulic devices used on the micro and nanoscale change the control capabilities of small amounts of fluids. This allows the development of systems that can be used to analyze particle separation and chemical properties. The structure of such devices is uncomplicated. Microhydraulic systems use the same elements as conventional systems: valves, pumps, mixers, actuators, filters, etc. [9].

Microhydraulic pumps that carry small amounts of fluid are widely used in research. Microhydraulic pumps can be combined with other elements on chips with the objective to create portable analysis systems. Due to the efficient and accurate flow control in microhydraulic equipment, many types of pumps have been investigated, such as: electric, magnetic, acoustic, and mechanical energy-based pumps. These elements need to be applied depending on the type of a microhydraulic system [10].

Microvalves are widely used in microhydraulics and can be active or passive in systems. Active microvalves can be of various constructions: pneumatic, magnetic, electrostatic, or piezoelectric. A passive microvalve is used as a non-return valve to allow fluid to flow in one direction through the channel. Microvalves are divided into mechanical and non-mechanical. More energy is needed to control mechanical valves. What concerns non-mechanical valves, they use a diaphragm made of smart materials that change their physical or chemical properties [11].

Mixers are used in micro/nano hydraulic systems. They are divided into two types: active, i.e., the ones which use external energy, and passive, i.e., the ones which use diffusion and chaotic mixing. In practice, passive mixers are more widely used. They increase the efficiency of the microchannel network. Micromixers are used to mix different materials and to speed up the reaction time [12].

Another component of the microhydraulic system is the filter. The entire system consists of microfilters, supply channels, and leakage components. These systems, with the installed analysis equipment, allow rapid analysis with a minimum number of samples. Microfilters can be used, for example, to purify biological samples, separate DNA, and/or perform liquid chromatography. The main criteria for choosing this method are the repeatability, cost-effectiveness, and the reliability of the results. An alumina nanomembrane is used to filter particularly fine particles. This membrane can filter objects with a diameter of 10 nm [13].

1.1.2 Advantages and Disadvantages of Micro/nano Hydraulic Systems

There are several advantages of micro/nano hydraulic devices over the traditional hydraulic system. The main advantages and disadvantages of micro/nano hydraulic system are presented in Table 1.1.

Table 1. 1. Advantages and disadvantages of micro/nano hydraulic system

Advantages	Disadvantages
• Cost-effectiveness by using small quantity of biological analytes • Increase of the precision due to high control on the experimental conditions • Compactness of the instrument • Shortening of the time of experiments by allowing multiple analytes processing at the same time	• Time-consuming process for patterning micro/nano geometry • Sometimes, it needs a special process for preparing micro/nano channels • Complexity of patterning the device for such materials as paper

• Flexibility in the application of the devices due to the small design setup, which allows easy transportation	

In today's world, microsystems are being widely used in biological analysis. Microhydraulic devices exhibit the physical and chemical properties of liquids and gases on the microscale.

Microhydraulic systems allow smaller samples, chemicals, and reagents to be analyzed and used, and thus to reduce the testing costs [14]. Due to the compact size of the system, the duration of the experiment is often shortened, and more operations can be performed simultaneously. When working on the microscale, excellent data accuracy and significant parameter management can be expected, thereby allowing the automation of the process while maintaining the performance levels. Microhydraulic systems are denoted by a variety of features: faster reaction times, increased analytical accuracy, and improved temperature control. Microhydraulic channels can be upgraded to allow the user to integrate automation into the system and perform multistage reactions. Microsystems can perform such functions as the detection of toxins up to the DNA (deoxyribonucleic acid) sequence analysis or the development of inkjet printers. In today's world, microsystems are being widely used in biological analysis [15].

1.2 Membrane Based Micro/nano Hydraulic Systems in Microfluidics

There are many different structures, such as nanomembranes or nanotubes that are used to design systems for micro/nano hydraulic devices. The main advantage of these nanomembranes is that the membrane can be used as a matrix to create other nanostructures. In these membranes, the individual pores are neatly arranged over a relatively large area. The production of these membranes does not require expensive lithographic processes. The nanomembrane can be used in the manufacturing of electronic devices, ultrasonic recording media, and nano catalysts [16]. Recently, nanomembranes have been widely used for nanomagnets which are an economically competitive alternative to the SmCo (Segment samarium cobalt) and ferrite magnets currently in use. Nanomagnets have a strong magnetic field compared to the magnetic field of the conventional magnets. This feature makes it possible to reduce the size of magnets, which makes it possible to modify the design of the currently available systems and make them even more compact [17].

Microfluidics is a broad term used in research to refer to the exact manipulation of fluid dynamics on the micron scale. In the field of analytical chemistry, microfluidics-based research applications are currently one of the most widely explored and forward-looking frontiers of progress due to such qualities as miniaturization, integration, automation, mobility, minimal reagent consumption,

28

and real-time detection [18]. In a liquid or a gas, a membrane acts as a selective permeable barrier allowing only certain substances to pass through. Concentration gradients, pressure variations, heat changes, and electricity can all be used to drive molecules across a membrane barrier selectively. The membrane-based separation technology is relatively cheap, denoted by the ease of use, more adaptive, and more ecofriendly than the traditional alternative [19]. Due to the membrane's adaptability, it can be employed efficiently for adsorption or other catalytic applications. A combination of the membrane technology and microfluidic systems can alleviate some of the problems associated with microfluidic chips [20-22].

Bibliometric analysis has been used to summarize data on the membrane and microfluidic binding throughout the past two decades. The *Web of Science* was searched in the course of the current research for microfluidics and membranes, and the bibliometric results are displayed in Fig. 1.2. Statistical analyses indicate that the number of publications in this field has increased significantly during the last two decades. Prior to 2012, there were fewer articles per year, which demonstrates that researchers recognized the critical nature of the membrane performance in microfluidic systems early on. Membrane research has accelerated since then, particularly after 2015.
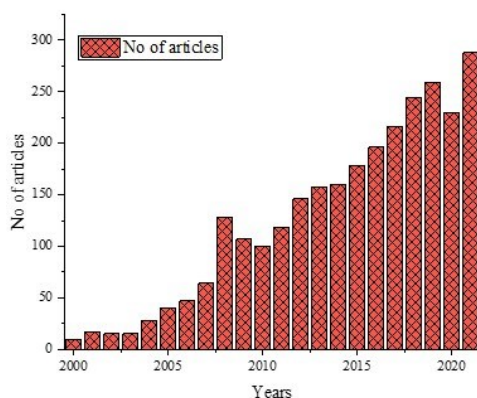
Fig.1. 2 Results of the number of published papers dealing with microfluidic-based membrane over the last two decades in the *Web of Science* database

Interfacial phenomena and microfluidic dynamics are important in the micro/nanofluidic area, as they allow evolving lab-on-a-chip technology to be used in such domains as biology, medicine, and chemistry. The interface has potentially a slight impact on microfluidic devices powered by electro-osmosis, electro-hydrodynamics, magneto-hydrodynamics, centrifugation, and pressure gradient microchannels. Capillary action enables microfluidics and fluid manipulation. Electrical wetting, dielectric electrophoresis, acoustophoresis, and thermal capillary action are all techniques for controlling fluid-fluid or fluid-solid interactions in microdevices with thin membranes, droplets, and bubbles. Broad shallow slit microchannel flows that can be reduced to two-dimensional flows, totally formed

stereotyped tube flows, and Stokes flows with a low Reynolds number are examples of the typical microchannel flows [23].

In microfluidics, the membrane is typically utilized as a particle separation barrier allowing only selected particles to flow out through the membrane from one side to the other when an external force is applied. Typically, there are two main membrane forms: *porous* and *dense*. In most of the microfluidics applications, porous structural membranes are employed. In a porous membrane, the transportation mechanism works on the basis of the porous structure of the membrane, thus it is not based on the material inherently. The process control mostly depends on the membrane's morphology which (rather than the inner structure) plays an important role.

The combination of microfluidics and the membrane is employed in many research areas and applications [24]. The most promising application of the porous membrane is for filtration and separation; in this case, the applied external force helps to separate the solution, micro particles, and gases in microfluidic devices. The employment of such a membrane in a microfluidic system can ensure precisely fabricated filtration based on size, or deformability.

1.2.1 Methods of the Integration of Micro/nano membrane in Microfluidic Systems

The microfluidics technology has contributed to the advancement of several fields of biology and biomedicine by allowing for the creation of sophisticated devices. Over the last decade, the development of new components and processes for injecting drugs, blending, manipulating, and storing fluids, filtration, and separation in microchannels has been observed, and the significant increase in the number of microfluidic systems in biomedical and chemistry applications is also notable. Microfluidic systems are used in a variety of biomedical applications for the diagnosis, detection, and separation of biological components. The integration of nanoporous membranes in microfluidic chips and devices has broadened the device applicability in biomedicine sciences.

Over the last decade, membrane-based microfluidic systems have been evolved, and many emerging novel methods for the fabrication and integration of membranes in microfluidics have been introduced; they are presented in Table 1.2. Methods for the integration of membranes in microfluidics can broadly be divided into two main categories, including the membrane being coupled to the chip directly, and the parallel preparation of the membrane and the chip.

Table 1. 2. Methods of integration of micro/nano membranes in a chip [24**]**

Integration method	Approach(es)	Advantage (s)	Disadvantage(s)
Membrane coupled to the chip directly	Membrane bonding and clamping (Commercial membrane) Deposing of metal membrane Membranes are used to separate capillaries	Variety of materials and form of the membrane Flexible designing is possible	Issue with air tightness
Parallel preparation of membrane and chip	Membrane preparation in chip Porous oxide membrane preparation Growth of zeolite crystal Polymeric membrane preparation Porous silicon membrane preparation	Excellent vacuum More dimensions control	Operating cost is high More complicated operations
	Membranes in chips were prepared in-situ. Monomer photopolymerization Porous polymers polymerization	High level air tightness Accurate control over the position and the membrane state	More complicated operations Repeatability is low Influencing factors are strong
	Use of sheet membrane properties Other polymeric chips PDMS chips	Operation is simple Application is more flexible	Comparatively poorer performance than commercial membranes

The membrane can be coupled directly to the microfluidic system or the device by using a clamp or glue for the purpose of studying the membrane. It can be either fabricated in laboratories or purchased from the commercially available platforms. As early as in 1999, an investigation was carried out by preparing sandwich type microfluidic systems (Fig. 1.3) while using two different micro dialysis membranes in between three polycarbonate chips; as a result, the in-line macromolecule removal and the desalination of biological samples was done in a timely and efficient manner [25].
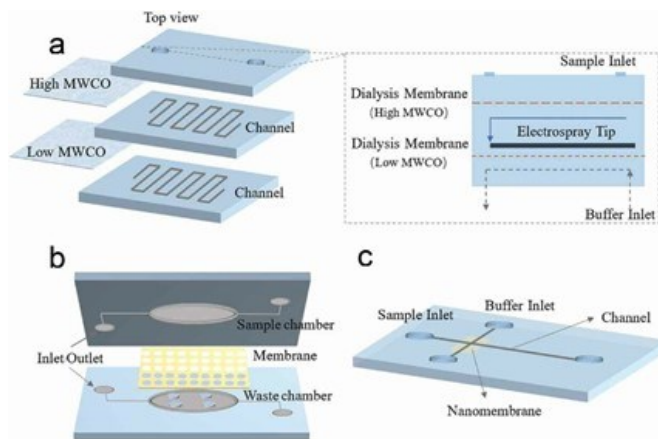
Fig. 1. 3 Direct couple membrane integration: Step of clamping (a), PET porous membrane clamped between two PDMS channels for cell culture (b), fabrication of a high precision microfiltration device for the rapid separation of CTCs from blood by using PDMS membrane [25]

In Fig. 1.3a, the sample is injected through the input, then passed through the high sieve membrane, and then it travels through the micro channel to the second stage of micro dialysis. Schuster *et al*. developed a new catalytic membrane to solve the phase contact problem for gas/liquid/solid incorporation with a hydrophobic membrane which allows achieving some improvement in gas separation and conversion [26]. By using a membrane-based microfluidic technology, Srigunapalan *et al*. demonstrated the isolation of lung cancer cells from a sample of blood (Fig. 1.3b). Samples of blood are drawn from the intake and then processed by the microfluidic device which uses a sacrificial transfer membrane to separate the cells from the unwanted debris. In Fig. 1.3c, a membrane with nanopores is sandwiched between two plates containing embedded microchannels. In this type of microsystem, the material between two fluidic layers is controlled by voltage, which is achieved because of isolation function of the membrane [27].

Another method of the integration of a membrane in microfluidic systems is the parallel preparation of a membrane and a chip. In this method, the membrane fabrication is done during the chip fabrication. This type of membranes is different from the conventional membrane fabrication as it uses etching, ion tracing, or the growth of a zeolite crystal in a nanochannel to create a porous structure. This is possible to achieve through nanotechnology which provides a custom structure and the properties of a porous membrane. Other manufacturing techniques in current use include membrane deposition for the fabrication of a microscopic sieve. Aluminum oxide, silicon, zeolite, and titanium oxide are also used to prepare a porous membrane [28-30].

The introduction of a polycarbonate membrane filter with a trajectory carved into it into the reservoir of a polycarpellary electrophoresis microchip enables for the

selective screening of insoluble particles [31]. An adequate membrane pore structure can reduce the flux loss, thus making it possible to simultaneously develop a microfluidic system with a single pore filter so that to achieve the appropriate separation. Porous membranes can be made in a variety of techniques, as shown in Fig. 1.4a [32].
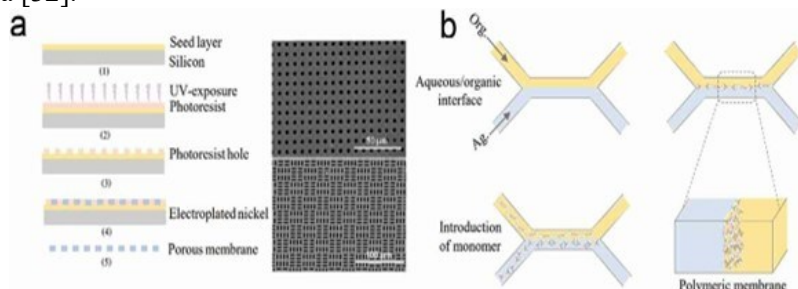
Fig. 1. 4 Scheme of membrane fabrication in chip for copore filter (a), top and cross-sectional views of in-channel membranes fabricated by using the polymerization technique (b) [32-33]

Pham *al et*. demonstrated that, when applying a simple coupling agent, it is possible to bind the Nafion polymer sheet directly to the PDMS substrate [33]. Another type of a liquid membrane that can be synthesized on the chip is artificial lipid bilayers. When a lipid solution is brought into contact with a buffer, as shown in Fig. 1.4b, the membrane takes on the structure of the living organism's cell wall. The various approaches for manufacturing widespread microfluidic chip-integrated membranes are briefly described in Table 1.3.

Table 1. 3. Types of integration and the application of membranes in microfluidics

Type of integration	Material of membrane	Pore diameter / Thickness	Material of Chip	Application	References
Clamping	Polyvinylidene fluoride (PVDF)	0.1 mm	PDMS	Testing and isolation	[34]
	Polypropylene	0.3 μm / 75 μm	Polyester	SO_2 detection	[35]
	PTFE	5 mm	PMMA	Air bubble removal	[36]
	Polycarbonate	0.4 mm	PDMS	Permeability of drugs	[37]
	Cellulose esters	Various MWCO	PC	Separation and removal	[38]
		100-500 MWCO	PDMS	Concentration	[39]
Parallel preparation	Zeolite	0.1 ~ 100 μm	Silicon wafer	Separation	[40]

	Polymer		PDMS	Various microfluidic operations	[41]
	PC	Different pores	Dimethyl siloxane	Filtering	[42]
	Silicon nitride	Micron pores	Glass	Cell culturing	[43]
Adhesive	Polyester		Silicon wafers	Cell culture	[44]
	NAO61		PMMA	Modification of channel	[45]
	PVDF	0.45 µm / 110 µm	PMMA	Microfluidic pump	[46]
	PC	1-200 µm	PMMA, PC	Separation	[47]
	PC	0.4 to 1 µm / 25 µm	PC, PSA tape	Electroosmotic flow	[48]
	Porous polymer monoliths	0.1 ~ 4 µm	PMMA	Extracellular vesicle isolation	[49]
Laser welding	Polyimide	220 MWCO	APET	Nano filtration	[50]
Solvent binding and embedding	Aluminum Oxide Al$_2$O$_3$	Pore: 100 nm, 65 µm thick	PC	Nucleic acid analysis	[51]
TPE based bonding	PC	0.8-10 µm	TPE bonding	Particle separation	[52]
Pore forming after chip bonding	Polyimide	0.05–2 µm	Pore formation after chip bonding	Filtration	[53]
In-situ growth	PAA	Nano channel	PDMS	Enrichment	[54]
In-situ photopolymerization	Styrene sulfonate	Nano channel	Silicon wafers	Concentration	[55]

In the review of the microfluidic system and its application, it is clear that the area of application is widespread in the field of biomedical sciences, chemistry, and analytical science. However, the integration of membranes in microfluidic chips or systems increases the area of application for the filtration and separation of micro/nano particles, biological compounds, cell cultures, cell growth, particle separation, bioparticle manipulation, and drug delivery systems.

1.2.2 Methods of Particle Manipulation in Micro/nano Microfluidic Systems

Particle manipulation is often required in a vast array of applications, such as the biomedical field, clinical diagnostics, drug administration, and self-cleaning surfaces. Rapid advancements in micro- and nanoengineering have stimulated the creation of a vast array of particle manipulation technologies, including well-established microfluidic techniques. For fundamental research and applications, such as biomedical and biochemical research, precise manipulation of nanoparticles (both synthetic and biological, such as cells) is essential [56]. Microfluidics, in which fluids are manipulated inside the microchannels, is a most prominent technology for biomedical and biochemical devices surpassing the traditional technologies regarding such aspects as low consumption of the reagents, low costs, high flux with precision, flexible and temporal fluid flow control, real time observation, and microengineering; these qualities offer the full-scale integration of the diverse functions on offer [57-59].

The most important methods of particle manipulation in microfluidic devices include hydrodynamic methods, the acoustic method, the electric method, optical tweezers, and the magnetic method. The schematic presentation (Fig. 1.5) of different categories of manipulation in microfluidic devices includes the hydrodynamic flow base (Fig. 1.5a), the microenvironment gradient base (Fig. 1.5b) (temperature, gas, and salt concentration), microfluidic manipulation, non-contact type manipulation (Fig. 1.5c) (magnetic, acoustic and optical beam), and the contact type electric field (Fig. 1.5d) (DC electric field, AC electric field, and ion concentration polarization).

Hydrodynamic particle manipulation (Fig. 1.5a) approaches extensively utilize complex microchannel networks to manipulate particles, primarily by balancing opposing transverse forces exerted on particles passing through a microfluidic channel. A particle's lateral equilibrium positions are determined by the particle's attributes (size and deformability), the channel's dimensions, the mass density and viscosity of the fluid, and the flow of the fluid [60-61]. A high flux rate and a faster manipulation of the particle is possible when using this method. The only problem is that only a limited range of flow rates is possible, and the dependence on the structure of the channel and the number of particles in the water is also prominent. It may also be a factor in cell viability if detergents are mixed with water at high speeds. There are also problems with clogging in some microfluidic devices denoted by complicated channel geometries and many different types of outlet closures.

The acoustic method of particle manipulation (Fig. 1.5c) enables the treatment of particles without the use of physical contact. The acoustic particle manipulation method works on standing acoustic waves which are generated by a transducer by applying electrical input. Standing waves are created by the interference of waves that are bounced back and forth by the reflection and match layers, which results in pressure distribution in the fluid. In response to the influence of acoustic radiation

forces acting on a particle, particles are gravitated to a cluster at either the pressure nodes or at the antinodes of the acoustic wave, depending on the situation.
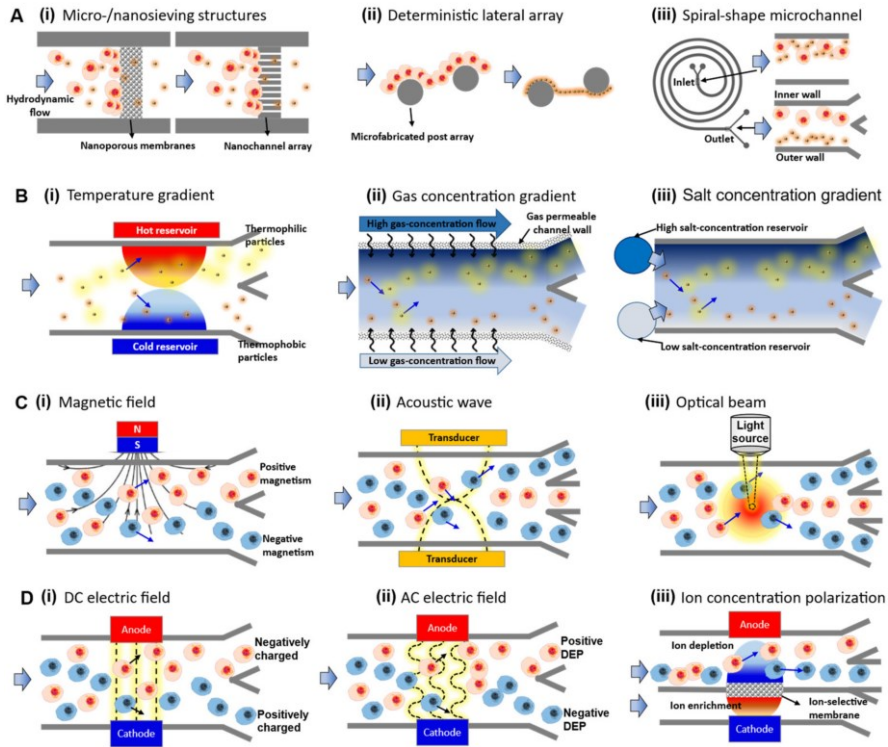
Fig. 1. 5 Schematic representation of the method of manipulation in a microfluidics device: hydrodynamic flow base (a), microenvironment gradient (b), microfluidic manipulation non-contact type (c), and microfluidic manipulation contact type electric force (d) [56-66]

According to the fundamental theory on particle manipulation using acoustic tweezers [61-62], acoustic particle manipulation has its own set of constraints. Acoustic systems, for example, are difficult and time-consuming to design and build, and, as a result, they are expensive to buy and install. Real device configurations can only be optimized for a narrow range of the particle volume fraction, shapes, and mass flow; hence, this technique can only be used with suspended particles.

Electrical fields can be used to control the movement of particles within a microfluidic device in a variety of ways including electrophoresis, electro-osmosis, and dielectrophoretic. When an electric field is generated, a charged surface moves in proportion to a stationary liquid, and this process is known as electrophoresis (EP). Charged particles can be transported, sorted, or trapped inside a liquid via this effect. A liquid's conductivity must be very low for electrical screening to operate,

which means that the liquid must have lowest concentration of ions present. Otherwise, charged particles will be concentrated around ions and nullify their charge to some extent. EP may only be used to particles and fluids with certain restrictions [61-62].

Ashkin *et al*. invented optical tweezers (1986). They employ a highly concentrated laser light to precisely catch and control tiny particles or living cells. When a laser beam with a Gaussian intensity profile contacts a particle or a cell, it imparts some of its momentum on it. This causes it to exert a net force on that particle or cell that pulls it toward its center, trapping it there; therefore, it follows the beam's path [64].

Magnetic approaches manipulate particles by generating a magnetic field with a permanent magnet or electromagnets. An electromagnetic or electromagnetically tagged particle/cell is drawn to the stronger magnetic field in a non-uniform magnetic field. Not only the gradient of the magnetic field, but also the particle/size cells and magnetic characteristics have an effect on the magnetic force. Continuous particle separation based on the particle size is a popular application because particles with the maximum magnetic volume are subjected to the strongest magnetic forces, and, as a result, they end up at an outlet closest to the magnet [65-66].

Microscale items, such as cells, platelets, and bacteria, are the primary targets of the acoustofluidic separation technology which has made quite a few advancements in the separation of nanoparticles. The acoustic-fluidic separation technology has been recognized as having great potential because of its advantages for label-free, biocompatible, and contact-free separation. The adaptability of the acoustofluidic separation technology has been demonstrated in a variety of biological and biomedical researches and experimental applications due to the efforts of engineers, scientists, and specialists. There is still a long way to go before analytical techniques can be transformed into healthcare tools and technologies. Also, devices based on acoustofluidics reduce the risk of clogging and provide a better throughput, as well as efficient operations in biomedicine for the filtration and separation purposes.

There are many alternative ways to manipulate particles in a liquid. Each method is denoted by its own advantages and disadvantages. The optimal control choice depends on the following parameters: the flow rate, the required accuracy, the particle concentration, the particle properties, and the budget. The classic methods of particle manipulation are centrifugation and mechanical filtration. Acoustic hydraulic research is a field that has only been newly explored; it aims to investigate, explain, and exploit the effects of acoustic waves on a fluid. There are two different methods allowing particles in a liquid to be manipulated: the acoustic force that scatters the particles to the edges of the space, or the acoustic force that creates the flow which allows the particles to be pulled along with the liquid. The handling and management of particles by this method is called acoustophoresis [67]. In this way, single particles, or large quantities of them, are possible to control in a

non-contact manner, thereby creating an acoustic flow. Acoustic flow is the motion of a fluid calculated in terms of duration through spatial fluctuations [68]. Acoustic hydraulics are typically excited particles fluctuating in high (MHz) or low (kHz) frequency modes. Piezoelectric transducers, which excite a structure-creating acoustic field inside a liquid, are commonly used for this purpose [69].

Piezoelectric materials can transform electrical energy into mechanical deformation. These transducers operating at ultrasonic frequencies can create a levitation effect that will be used in the study of this work. Because of its high piezoelectric constant, relative permeability, and electromechanical coefficient, lead zirconate titanate, more commonly known as PZT, is an excellent choice for the construction of an ultrasonic transducer. This device can achieve high operating frequencies, which is necessary to obtain high-intensity focusing and the ability to focus particles on nanometer-sequence alumina channels [70].

Acoustic pressure is denoted by both positive and negative properties. One of the biggest advantages is that particles are manipulated in a non-contact manner because particles (biological cells) are very tenuous. In Lithuania, acoustophoresis and particle manipulation research is also ongoing. Golinka successfully defended his dissertation [71] at Kaunas University of Technology in 2018. In the dissertation, ultrasonic methods for the separation of microparticles in a liquid while utilizing traditional piezoceramics were investigated and developed. The high thermal intensity of optical forceps, a high electric field, and strong magnetic fields are often dangerous to living cells or organisms [72]. Since the force fields of an acoustic fluid can be formed according to the available device design (with a complex design), it is possible to reach all areas of the design, and it is also possible to change the field of force by changing the amplitude of excitation, the range of frequency, and the phase of transducers [73]. By using optical tweezers, thousands of particles can be controlled concurrently. Another benefit of acoustic fluid devices is their low production and operation expenses. The acoustic, electric, optical, and magnetic fields would not conflict with one another [74]. As a fluid's acoustic force is independent of magnetic, electrical, or optical particles, acoustic hydraulic manipulation is a viable alternative in situations when alternative methods are unsuitable. The use of acoustic pressure to manipulate particles in a cavity can be generated by the piezoelectric excitation method. It helps micro/nano particles to concentrate in the center of nanotubes, and also helps to reduce the friction between particles and the wall of the nano tube. The use of this method reduces the risk of damaging the bioparticle in biomedical science devices for filtration and separation.

1.3 Types of Nanoporous Membrane Used in Biomedical Science Microfluidics

Micro/nano porous membrane materials have demonstrated practical and potential functionality in numerous scientific and medical uses, including filtration and isolation, cell separation and sorting, microarrays, tissue reconstruction *in vitro*, high-throughput manipulation and analysis, and real-time sensing. There is an increasing demand in miniaturization devices and materials in the production of

38

biomedical devices, water purification devices, food industries, and medical applications. Micro/nano membranes, in particular, comprise identical through pores with a homogeneous shape and size on the micro/nano scale. They have demonstrated significant potential applications in biomedical fields, such as biomanipulation and bioanalysis [75-76]. The micro/nano porous membrane has already been used in life sciences to separate colloidal particles; it offers potential in terms of biomolecules-based protein and nucleic acid-based filtration properties for nanofiltration, ultrafiltration and dialysis applications [77-78]. The properties and application of the micro/nano porous membrane are primarily determined by the size of the pores, the porosity, the area, the thickness of the membrane, and the material [79]. Because of their simplicity, cylindrical holes are assumed in the most widely accepted theories. This essentially means that pores in membranes are shaped to resemble parallel cylindrical capillaries in their actual function. The potential application of micro/nano porous membranes accelerated the development of the method(s) of fabrication and application. The overview of recent advancements in micro/nano porous membrane technologies in biomedical engineering is shown in Fig. 1.6. It shows the fabrication methods for the micro/nano porous membrane (the inner ring), as well as the biomedical application of the micro/nano porous membrane (the outer ring).
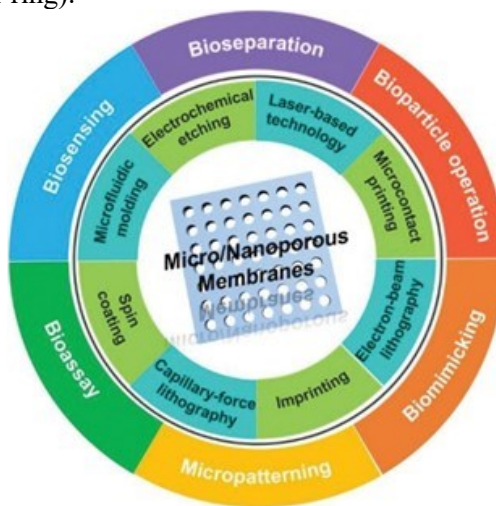
Fig. 1. 6 Summary of the current advancements in the production and application of micro/nano porous membranes

Nanoporous micro/nano membranes are classified based on their material type including organic and inorganic material type micro/nano membranes. Further, it is possible to sub-categorize them based on the material of the membrane, the types of pores, and the fabrication method of the micro/nano membrane.

1.3.1 Type of Material of Micro/nano Porous Membranes

The recent advances in biomaterials have upgraded the materials used in porous membranes. Through-hole membrane materials are classified as inorganic, organic, or composite (the hybrid membrane) [80-83].

Organic material type micro/nanoporous membranes are manufactured from a variety of materials because they can be made of a combination of two materials. Organic membranes are mostly fabricated from polymeric materials including polycarbonate (PC), polyethylene (PE), polymethyl methacrylate (PMMA), polysulfone, perylene, polydimethylsiloxane (PDMS), polyethylene terephthalate (PET), polyurethane acrylate (PUA), and MD700 [84]. The main advantages of the organic material-based micro/nano porous membrane are the relatively low cost of fabrication and its bio-compatibility.

Inorganic micro/nano porous membranes are mostly composed form various inorganic materials including metals, composites, alloys, and semiconductors. Metal micro/nano membranes are fabricated from metal oxides, specifically, made from aluminum oxide (Al_2O_3), titanium dioxide (TiO_2), zinc oxide (ZnO), gold (Au), etc. Micro/nano porous membranes with ordered pores, including porous alumina and silica, have recently received a lot of attention regarding their biological applications [84-85]. Nanoporous alumina is a very well know metal oxide membrane material which has been known for more than four decades due to its well-ordered porous structure with a wide range of pore diameters.

The hybrid type micro/nano porous membrane was introduced to demonstrate the high stability of the membrane. However, it is made up from a combination of more than one organic or inorganic materials (addition of ceramics to a polymer); it is more complex to synthesize and can have a variety of properties for this type of porous membranes [86].

1.3.2 Type of Pores and Porous Structure of Micro/nano Porous Membranes

Micro/nano porous membranes are frequently studied in terms of the pore diameter, the pore size distribution, the pore morphology, and their orientation. Typically, the pore size is classified based on the *International Union of Pure and Applied Chemistry* (IUPAC). Porous structures having a pore diameter of ≤ 2 nm are considered as *microporous* structures, the pore diameter between 2–50 nm is considered to be a *mesoporous* structure, whereas the ≥ 50 nm pore diameter structure is known as the *macroporous* structural pore structure. According to *Cigane* [87], all porous structures having a pore diameter of less than 100 nm are regarded as nanoporous structure. The shape of a porous structure of the micro/nano porous membrane (Fig. 1.7) can be of the cylindrical, channel (a), regular (b), tortuous, or complementary (c), and irregular shape (d).
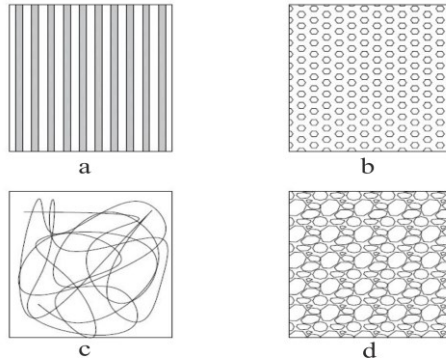
Fig. 1. 7 Nanopore shape in the micro/nano porous membrane [87]

The nanoporous structure, the pore size, the porosity, and the pore distribution exert influence on the suitability, applicability, and selectivity of the micro/nano porous membrane in a biomedical microfluidic system. To be effective in biomedical devices, nanoporous interfaces require several key membrane features to be present, as shown in Fig. 1.8. Firstly, precise control of the molecule transport can be achieved through specific pore sizes and narrow pore size distributions in the fabricated membrane. Secondly, a lower flow resistance is required in many applications to allow high flux (identified by a porous structure and a relatively thin membrane) [88-89].
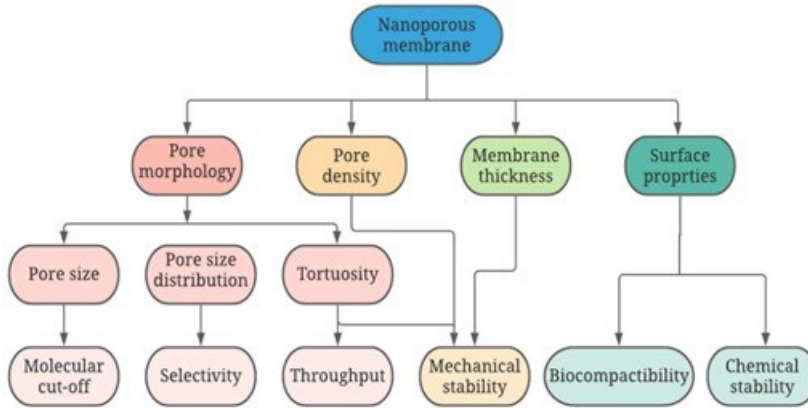
Fig. 1. 8 Schematic representation of the critical membrane properties determining the performance

Long-term use requires acceptable mechanical strength in terms of the transmembrane pressure, as well as a suitable temperature and chemical stability in a variety of biological environments. Furthermore, the mechanical strength of a nanoporous membrane is determined by its porous structure, pore diameter, and thickness. Finally, in order to avoid an immune reaction and functional degradation when used *in vivo*, devices must be biocompatible and resistant to biofouling.

1.3.3 Type of Fabrication Methods for Micro/nano Porous Membranes

The fabrication of micro/nano porous membranes is possible by electrochemical anodization (anodic etching), laser lithography (micromachining), 3D printing, layer-by-layer deposition, sol-gel, and other options.

Lithography (Fig. 1.9a) is the most convenient fabrication method to develop a micro/nano porous membrane from polymeric materials with an ordered porous cylindrical array to overcome problems related to the poor pore size distribution, mechanical properties, and biocompatibility of the membrane associated with the polymeric micro/nano porous membrane. There are two forms of lithography: masked and maskless. In the mask base method, a patterned mask is used to transfer a pattern on the base material, whereas, in the maskless lithography method, a pattern is fabricated by using serial writing (i.e., a mask is not used for patterning on the base material) [90-91]. The mask-based method includes photolithography and nanoimprint lithography; it may produce a porous structure of 2–3 µm and 6–40 nm, whereas the maskless lithography method involves the use of electron beam lithography (e-beam) and provides a porous structure of ≤ 5 nm. Fig. 1.9a illustrates the fundamental steps of photolithography, nanoimprinting lithography, and e-beam lithography.
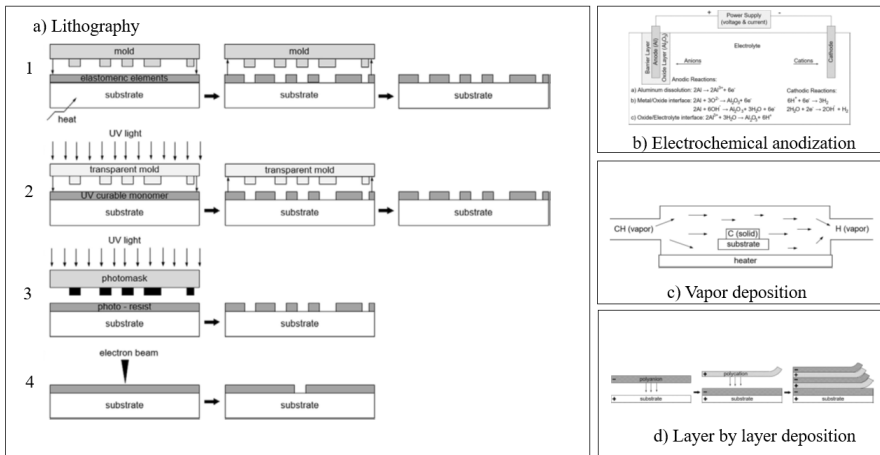
Fig. 1. 9 Methods of fabrication of the micro/nano porous membrane: lithography (a), electrochemical anodization (b), vapor deposition (c), and layer-by-layer deposition (d) [87]

Previous research has identified two types of electrochemical anodization (Fig. 1.9b): steady state and non-steady state. The steady state involves mild and hard anodization, of which, mild anodization fabricates the non-uniform porous oxide layer. Meanwhile, the hard anodization method provides a faster growth of the anodized alumina layer with an ordered porous structure; due to the fast-going process, it releases more heat during the anodization and requires precise control over the temperature during the anodization process [92]. What regards the non-steady state fabrication method of anodic alumina, it consists of pulse and periodic

42

anodization, of which, the periodic anodization method provides better control of the internal structure of pores and various pore diameters inside the fabricated nanotubes, whereas the employed apparatus enables a variety of application areas. However, the alumina layer thickness and other porous geometry can be controlled electrochemically by altering several process parameters, such as the anodization time and technique, and the applied voltage, electrolyte solution and temperature.

By using non-hot embossing imprinting lithography (Fig. 1.9a 1), the formation of micro/nano structures is done on heated polymeric materials by applying the load perpendicularly to the heated monomers. This nanoimprinting method requires less time for completing the entire process [93-94]. In nano UV imprinting (Fig. 1.9a 2), the desirable micro/nano structure is formed by using ultraviolet (UV) light exposed to a UV curable monomer which is in contact with a transparent mold. The replacement of a mold is required after using it for fifty cycles, and it can be performed on high viscosity polymers due to the size of the pattern and its density. This is one of the limitations of the method [95]. In photolithography (Fig. 1.9a 3), the UV light travels through a photomask and has an influence on a particular area of the photo-resistant surface; this aspect is more extensively discussed below. The inorganic photoresist is a substance that is delicate to ultraviolet light. Photolithography offers several advantages, including great efficiency, the ability to employ any common structure and size, and the ease with which the shape and size of the substrate may be monitored. The e-beam lithography process is done by using the spot of the electron beam (Fig. 1.9a 4) which moves over the surface of the electron-sensitive surface and fabricates the desire surface patterns [96]. In addition, the carbon nanomembrane and a variety of composite nanomembranes can be manufactured by using the lithography approach.

Micromachining is one of the methods of nanoimprinting, but this method has received great attention recently because of its use in terms of fabricating a nano structure on various metals, alloys, semiconductors, and polymeric materials. The micromachining method uses a laser beam to fabricate a micro/nano pattern on the surface by moving the laser beam on a defined path over the surface including metals (Au, Ag, Ni), semiconductor materials including Silicon (Si), and polymeric materials. Additionally, this method of fabrication is more popular because it produces membranes with high precision and relatively limited dimensions [97].

Chemical vapor deposition (CVD) is a process for fabricating micro/nano membranes (Fig. 1.9c). A chemical interaction in the vapor phase causes the deposition of a solid heating surface, which is referred to as CVD. At high temperatures, the precursor decomposes. Next, the gaseous atoms adhere to the substrate and form deposits. A continuous layer is developed throughout the surface chemical process [98]. By using CVD, a variety of nanoporous materials can be fabricated, including oxides (iron, titanium), semiconductors (molybdenum disulfide), and metal alloys (platinum cobalt).

 The layer-by-layer deposition approach (Fig. 1.9d) comprises the layer-by-layer deposition of different charged molecules on the substrate's surface. We can

43

consider the following scenario: a substrate having 1 nm thickness is submersed in a dilute solution of cationic electrolyte for adsorption, followed by further washing and drying of the wafer. A fresh layer is created on top of the previously formed layer by placing the polished coated substrate in a dilute dispersion of polyanions. The washing and drying of the wafer is repeated several times to form a multi-layer nanoporous membrane with a thickness of up to 500 nm [99]. By using the layer-by-layer formation, various metals (gold, graphene), polymeric materials (polyamide, poly(sodium sulfone), poly(alkylamine hydrochloride) can be used for layer-by-layer fabrication.

Sol-gel is a wet chemical forming method for the fabrication of a nanoporous membrane which consists of four main steps. The process begins with the preparation of a homogeneous solution by using a salt or a metal, followed by an increase of the concentration of the prepared homogeneous solution, then, the formation of a gel by condensing the solution, and, lastly, drying the condensed gel. This method provides a membrane having excellent mechanical, electrical, optical, magnetic, and thermal characteristics [100].

3-dimension printing (3D printing) is commonly known as the additive manufacturing method. It is used to fabricate diverse and complex geometrical shapes from a variety of materials including PLC, PLA, PEG, zirconia, tricalcium phosphate, hydroxyapatite, etc. [101-102]. There are several materials in use due to the low fabrication cost, biocompatibility, mechanical properties, and the simplicity of the process. Ceramics and hybrid materials can be used for 3D printing to improve the mechanical strength, bioactivity, and the ease of processing, but these materials still have limitations.

However, there are various methods to fabricate a micro/nano porous membrane using organic, inorganic, and hybrid membranes except for the methods explained above. Those methods include phase separation, track etching, the vapor phase separation method, electrospinning, micro molding, drop coating, and manual punching. A classification of micro/nano porous membranes is presented in Table 1.4.

Table 1. 4. Types of micro/nano porous membranes and their application

Porous membrane type	Inorganic membrane	Organic membrane	Composite (Hybrid)
References	[90-92]	[93-96]	[97-102]
Durability	Acceptable	Excellent	Fair/good
Chemical stability	Very good	Good / very good	Good
Fabrication material	Anodic Al_2O_3, SiO_2, ZrO_2, TiO_2, Si, and semiconductors	Polymeric materials PC, PE, PET, PS, PDMS, PCL, PMMA, PUA, PEGDA, MD700, polysulfone	Ceramics/polymer, oxide + polymer, carbon + metal oxide coated, nafion + TiO_2

44

Method of fabrication	Electrochemical anodization, sol-gel, micromachining, powder sintering, lithography, nano imprinting	Ion-track etching, lithography, phase separation, spin coating, hot embossing, ion beam lithography, micro molding, imprinting, laser, microcontact printing	CVD, atomic layer deposition, Sol-gel, layer-by -later, grafting technique, block copolymerization
Pore size	1 nm – 10 µm	0.7 nm – 800 µm	≥ 10 nm
Pore distribution	Narrow / wide	Narrow / medium	Medium tortuous
Comments	Good chemical and physical stability, ordered porous structure, better performance, biocompatible, low toxicity, low cost of fabrication, high pore density	Low fabrication cost, excellent biocompatibility, transparency, precise molding, low toxicity, good thermal, chemical, mechanical stability, high flux, biodegradability, chemical inertness	Superior biocompatibility, narrower porous structure, additional functionality, chemical and mechanical stability.
Application	Micro/nano filtration, drug delivery, cell culturing, biosensing, particle shorting, chromatography, nano patterning, ultrafiltration, separation	Microfiltration, bioassay, micropatterning, separation, drug delivery, organ chip, tissue engineering, water purification, cell operation, filtration	Microfiltration, ultrafiltration

As shown in Table 1.4, organic, inorganic, and composite material-based micro/nano porous membranes are available across a wide range in terms of the pore diameter, the porous structure, the characteristics of the membranes, and the method of fabrication. However, the application of a specific membrane type depends on the characteristic of the membrane, but it is also possible to adjust the characteristic of the micro/nano porous membrane by using the proper fabrication method and materials.

1.4 Nanoporous Aluminum Oxide Membrane

Anodic aluminum oxide (AAO) membranes are among the most studied nanoporous materials that can be etched with electrochemical agents. Porous alumina membranes prepared by conventional anodic methods typically have a hexagonal porous structure with a short range spacing. The parameters selected for the anodization procedures can influence the pore geometry and morphology.

Recent years have seen significant advancements in the fabrication of AAO membranes with highly organized nanochannel arrays. Through a self-organized

process, the typical anodizing of aluminum could result in an ordered nanochannel array with a limited range of pore widths. The degree to which the hole array self-organizes is dependent on the anode voltage and the acid used in manufacturing. To achieve large-scale production of ordered porous anodic alumina, the pretexture technique, which includes first establishing a shallow ordered pattern on the surface of an aluminum wafer before anodizing it to form the ordered channel structures, is the most effective approach. By using the pretexture process, a defect-free nanoporous structure can be developed by using a two-step anodization method with the pore diameter and interpore distance of 70–200 nm and 100 nm, respectively [103].

As discussed in the previous section about anodized micro/nano porous membranes, it is possible to fabricate them by using different process parameters including the electrolyte solution, the type of anodization, the temperature, and the voltage. The effect of anodization using different parameters-based characterizations is presented in Table 1.5.

Table 1. 5. Effect of the process parameter (electrolyte type, temperature, and method) on nanoporous AAO characterization

Electrolyte Type	Method of anodization	Anodization temperature	Applied voltage	Diameter of pore, (nm)	Distance between pores, (nm)	References
Oxalic acid	HA	1	100-150	49-59	200-300	[104]
		-	130	40	≥ 400	[103]
		0-5	140-200	~100	-	[105]
	Two step anodization	17	40	50	100	[106]
		5-7	20-50	~70	-	[107]
		17	40	52	100	[108]
		3	40	24	105	[108]
	Pulse anodization	15-25	-7 to 30	30-60	-	[109]
	Cyclic anodization	0-1	20-50	Branched pores	-	[110]
Sulphuric acid	Two step anodization	1	15-25	18-26	49-65	[111]
		-8 to 10	15-25	5.7 – 15.3	2.7 – 37	[112]
		0.85	25	33	63	[108]
	HA	1	27-80	15-30	70-145	[113]
	Pulse anodization	1	23-35	16-35	-	[114]
Phosphoric acid	Two step anodization	0	100-160	85-140	-	[115]
		12	195	254	490	[108]
		-5 - 0	100-160	≥ 100	250-490	[116]
		0	160-195	140-190	405	[117]

| | Step anodization | 25 | 160-20 | 160-30 | 580-87 | [118] |
| | Cyclic anodization | -1 | 20-300 | 300-1200 | - | [119] |

The characterization of the nanoporous aluminum oxide membrane refers to the pore diameter, the interpore distance, the thickness, and the porosity. All these characteristics are strongly dependent on the process parameters during the fabrication of the micro/nano porous aluminum oxide membrane. Fig. 1.10 shows the schematic of the nanoporous array of the AAO membrane.
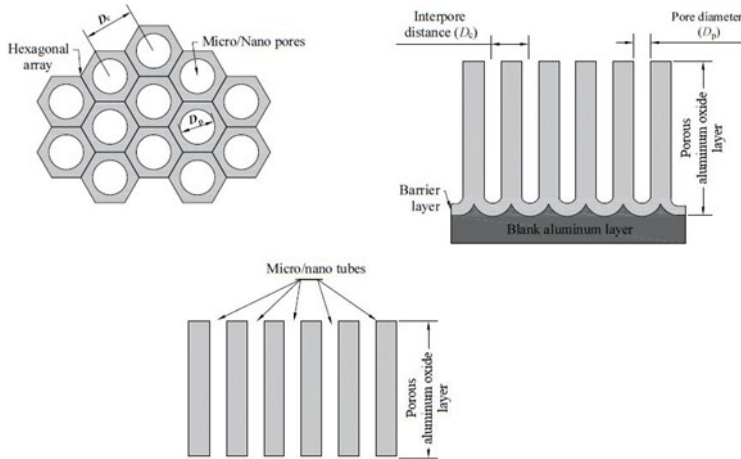
Fig. 1. 10 Hexagonal array, 2D view of the nanoporous structure and formation of nanotubes in AAO porous membrane

The hexagonal cell (honeycomb) structure contains the pore with tubes tangent to the formed surface of the micro/nano porous AAO membrane. The diameter of the pore (D_p) (Fig. 1.10) depends on the fabrication process parameters as presented in Table 1.5. Mostly, the diameter of the pore depends on the applied voltage, whereas the anodization voltage increments result in the pore diameter increments, and a low voltage produces pores with a smaller diameter. Moreover, the concentration of the electrolyte also affects the pore size and the oxidation process; if the concentration of the electrolyte is high, it produces a small pore diameter with a faster growth rate. This is supported by the fact that the Pilling Bedworth (PB) ratio increases with the pore formation; it can be calculated as follows:

$$PB = \frac{produced\ oxide\ layer}{consumed\ metal} \tag{1.1}$$

The distance between the centers of two neighboring pores is defined as the interpore distance (D_c). The distance between pores also depends on the applied voltage during the anodization process:

$$D_c = \delta V \tag{1.2}$$

47

Here, δ is the proportional constant applier voltage with a value of 2.5 nm/V

The following formula expresses the relationship between the pore diameter and the interpore distance:

$$D_c = D_p + 2W_t \tag{1.3}$$

Here, D_p is the diameter of the pore, and W_t is the thickness of the wall. The interpore distance is claimed to be independent of temperature when it comes to temperature in terms of the interpore distance [120-121].

The porosity of the micro/nano porous AAO can be customized by customizing the fabrication process affecting the pore diameter and the distance between pores. The porosity of the membrane is obtained as follows:

$$Porosity = \frac{\pi}{2\sqrt{3}} \times \frac{D_p}{D_c} \tag{1.4}$$

The pore density of a membrane is calculated by using Formula 1.5. It is related to the diameter of the pore and the number of the pores fabricated during the anodization process.

$$No\ of\ pores = \frac{A}{\pi/4} \times (D_p)^2 \tag{1.5}$$

Here, A denotes the area of the pore, and D_p is the diameter of the pore. The pore density is possible to control by controlling the pore diameter during the anodization process.

1.5 Nanoporous Aluminum Oxide Membrane Application in Biomedicine

Smart implanted drug delivery systems, bioartificial tissues, and other micro medical devices are actively developing natural filtering nanoporous systems. Nanotechnology advancements have made it possible to accurately regulate the properties of pores in nanoporous materials such as morphological, physical, and chemical, and thus make them usable for a wide range of applications. AAO membranes are among the most popular extensively explored porous materials utilizing electrochemical etching. Porous alumina membranes prepared by the conventional anodic methods typically have a hexagonally porous structure with a small distance order.

Nanoporous AAO membranes are already widely adopted for use in filtration systems for controlling diffusion. According to *Kipke* [122], SDS (sodium dodecylsulfate) encapsulated crystal violet molecules diffuse through pores with a diameter of 20 to 200 nm, which results in the release of crystal violet molecules from their SDS-encapsulated host. Using SDS micelles to encapsulate crystal violet allows researchers to increase the molecule size to such a degree that the size of pores may be used as a speed-controlling function, as demonstrated in this study. The results were enhanced when the membrane-containing capsule was carefully

placed into a research device and moved around in a water-filled beaker with the help of a tipping bridge to avoid diffusion problems within the capsule.
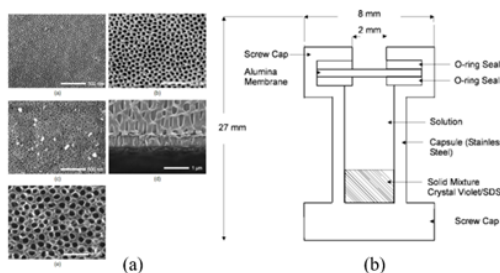
Fig. 1. 11 Nanoporous AAO based diffusion-controlled device: nanoporous AAO membrane with different pore sizes including 20 nm, 50 nm, ANO20 (a); a sketch of the device (b) [122]

Aqueous SDS concentrations were below the threshold micelle concentration for crystal violet after the diffusion device (Fig. 1.11) had been used. (CMC). UV-visible and fluorescence spectroscopies are used to demonstrate the formation of micelles and the encapsulation of crystal violet [122]. Nanoporous alumina membranes can be utilized to speed up the diffusion of crystal violet-containing micelles. These micellar composites are delivered into an aqueous environment at rates of around 1, 3, 5, and 8lg/day for the 20 nm pores, 50 nm pores, commercially available ANO20, and ANO200, respectively. However, due to the low concentration of SDS in the aqueous solution, the micelles are destroyed, and free crystal violet is liberated, which may be measured quantitatively by UV-visible spectroscopy. When the capsule was placed vertically in a beaker that was filled with water and held with a tipping bridge, the best results were obtained.

Gorokh *et al*. [123] used tartaric and malonic acids to create two different aluminum oxide coatings. It was first necessary to make anodic films, and then tungsten oxide was used to implant metal oxide sensors. Sensors based on tartaric acid were shown to be more sensitive as the membrane's porosity was enhanced. In the absence of carbon monoxide, neither of the test sensors responded; nevertheless, they responded significantly better to ammonia.

In microfluidic devices, Tushar Kumeria *et al*. [124] used AAO substrates coated with an ultrathin layer of gold. Reflective interferometric spectroscopy was utilised in two separate ways in this study to investigate the sensing qualities. Thiol-binding AAO that was gold-modified was investigated, as were AAOs that had been antibody-modified to target circulating tumor cells. Biosensing devices capable of detecting a wide range of analytes might be developed on the grounds of the research results.

Mohamed Shaban *et al*. [125] developed a nanoporous CdS/AOA bilayer film by spin coating the CdS film while using AAO as a template. As a result of the

favorable testing results, the bilayer film was considered an accurate, cheap, and comparatively simple glucose biosensor.

Filtration of nanoparticles, impurities, and contaminants from a biological environment is one of the emerging applications of nanoporous AAO membranes in this developing field of biomedical science. The pore diameter of a membrane plays an important role in pressure driven based filtration systems. Narrow pore distribution is a good selectivity factor for nanofiltration. High flux is possible to achieve by decreasing the thickness of a porous membrane up to 10 μm. So far, there have been many industrial and biomedical applications noted for size-based separation. Membranes are categorized based on their average pore diameter 1 μm use for microfiltration and 100 nm for nanofiltration, whereas 10 nm pore diameter is necessary for reverse osmosis systems.

Biofiltration works based on the size of molecules and the chemical affiliation of the filtration membrane. Size-based molecule filtration results in the molecules of a size of more than the pore diameter being not allowed to pass through the nanopores; hence, such molecules are blocked. On the other hand, chemical affinity is associated to the filtering methodology, and selected molecules can be segregated based on lesser or larger chemical affinity for the membranes, as in the interaction of molecules with the permeable layer of a membrane. Any optimization of the filtration method completely depends on those two factors. The simplest example of the porous membrane-based filtration system is that a fluid should be filtered by pouring on the membrane, which results in the filtered fluid being obtained [126-128]. Major applications of nanoporous AAO membranes for filtration are presented in Table 1.6.

Table 1. 6. Application of nanoporous AAO membranes for filtration based on the type of membrane and their pore structure

Diameter of pore, (nm)	Type of membrane	Application	References
3.5	Nanocomposite of silica and surfactant in the AAO membrane	Molecule separation based on size	[129]
20	Tabular AAO membrane	For hemodialysis	[130]
20	AAO filter coated with nafion	Ion separation based on electric field	[131]
25	PDMS microwell with holes and AAO membrane	Filtration of algal solution based on microwell	[132]
30	Sandwich type membrane: two membranes separated with a PDMS layer	Exosomes isolation by using the sandwich type membrane	[133]

31.25	Al supported nanoporous AAO	For better fluid permeability filtration of acetone, water, ethanol, isopropyl alcohol	[134]
38.2	AAO membrane integrated in microfluidic chip	Biomolecule separation based on electrokinetics. Binary separation and detection of molecules	[135]
40	AAO membrane for gas sensing package cover in optical sensor	Filtration interface for air and gas contaminant removal	[136]
50	3D microchannel base on AAO	Molecular separation	[137]
50	Double layered AAO	For hemodialysis devices	[138]
55	AAO with polyrhodanine active carbon deposition	Multi-filtration membrane for heavy metal removal from drugs, water, and food	[139]
60	Tabular AAO film	Filtration of gas and liquid, drug delivery and energy application	[140]
80	Sandwich type AAO membrane	Filtration of nanoparticles based on size.	[133]
100	Fictional nanoparticles embedded in AAO	Enhancing filtration efficiency	[141]
150	Polyrhodanine based AAO	Filtration of heavy metals from wastewater	[142]
200	Fictionalized chitosan AAO membrane	Hemoglobin purification from red blood lysate	[143]
200	Microfluidic channel of AAO with DNA prob sequence	Filtration of DNA probes for electrochemical sensors	[144]
350	Multilayered AAO	Fabrication of wearable hemodialysis devices	[137]

The separation of biomolecules is denoted by applicability in the field of biomedicine. The most important parameters for the application of nanoporous AAO are the high flux rate, the pore diameter, the thickness of the porous membrane, good mechanical and chemical strength with a uniform structure. Porosity and thickness are used to determine the flow rate and mechanical stability of the nanoporous AAO membrane fabricated for biomedical applications. A theoretical study on the AAO membrane for hemodialysis application shows a pressure bearing capacity of up to 0.79 Mpa [145]. For the analysis of deoxyribonucleic acid, an adaptive ultrafiltration layer was produced by utilizing an AAO template in polyprotic acid to offer filtration characteristics [146]. Multi-layered AAO membranes are used for effective dialysis filtration applications and the fabrication of potential biomarkers for an earlier detection of cancer cells [147-148].

Micro/nano porous membranes are denoted by promising potential application in the biomedical field for various purposes including filtration, separation of

biomolecules, drug delivery systems, biosensing, and many more. There are many possibilities to use the nanoporous AAO membrane as a functional element in biomedical engineering with improved characteristics and surface modification separately or by combination with other nano materials. When talking about micro/nanofiltration of particles based on the size, the pore diameter and the thickness of the membrane play an important role in terms of the rate of filtration. Clogging is one of the essential issues arising when the filtration based on particles affects the rate of filtration, but it can be overcome by using acoustic wave modulation while employing the external manipulation actuation method by and using a piezoelectric actuator. An external actuator helps to minimize the clogging problem, but the bulk acoustics helps to manipulate the internal geometry of nanotubes formed along the pores on the surface, which results in an improved filtration rate and a clogging-free micro/nano particle filtration system for biomedical applications.

1.6 Motivation for Research

It has been shown that, so far, numerous inventions have been made in the field of microhydraulics-based microfluidic systems in the biomedical science. There are huge developments ranging from the traditional hydraulics systems to micro/nano hydraulic systems in microfluidics in terms of the capacity of operation, the system size, the operational components, the methods of fabrication, the functioning of different parts, the area of application, the types of application, and the components used for operations.

In the context of microfluidic devices and their application in the field of biomedical engineering, they have a huge impact on the development of micro/nano systems for bioparticle separation, filtration, biosensing, drug delivery, etc. In the recent years, a number of microfluidic devices have been developed based on micro/nano porous membranes fabricated from a variety of polymeric and metal materials by employing different fabrication techniques.

Recently, micro/nano porous anodic aluminum oxide has been gaining a lot of research interest for various applications in biomedical engineering due to its unique characteristics, such as the porous structure, mechanical and chemical stability, the ease of fabrication, and relatively low costs. Yet, there was no application listed for filtration using surface acoustic modulation while employing a micro/nano porous aluminum oxide membrane. It has been previously shown that non-contact type manipulation techniques are more reliable for the manipulation of particles in fluidic devices, especially for red blood cell separation and filtration. It has been established that the combination of a micro/nano porous AAO membrane and the surface acoustic wave modulation technique could be used for the development of a filtration system for a microhydraulic device working as a vibroactive micro/nano filter in the biomedical science.

52

1.7 Chapter Conclusions

This chapter represents a comparison research overview on modern microfluidic devices based on micro/nanoporous membranes, their types, fabrication methods, as well as the literature research on the micro/nano membrane and the AAO membrane application in the biomedical science.

1. The currently available microhydraulic systems offer potential application in biomedical engineering for the separation, filtration, sensing, drug delivery, etc. They are more reliable and are of a relatively more compact design than the traditional system, which makes them more suitable for small scale operation with high efficiency.

2. Membrane-based microfluidic devices have opened a new research area for the development of micro/nano devices in the field of the biomedical science while using various techniques for bioparticle suspension, filtration, separation, and drug delivery systems.

3. The fabrication methods for micro/nano porous membranes exert high influence on the quality of micro/nano porous membranes, including the pore size, the porous structure, the thickness of the membrane, as well as other geometrical parameters.

4. The micro/nano porous membrane application in the field of bioengineering should have specific characteristics for various applications; therefore, it is important to identify these characteristics and structure(s).

5. Micro/nano porous anodic alumina membranes are possible to fabricate at a relatively low cost, without using a high-level technology, and the ease of control on the process for a predefined structure.

6. There has been no previous work done in terms of using nanoporous aluminum oxide membranes for the filtration or separation of bioparticles while using acoustic wave manipulation; therefore, it is important to study this area theoretically and practically for the real application of the AAO membrane in bioengineering.

II. Development of Experimental Setup for the Fabrication of Nanoporous Membrane

Based on the previous findings of the literature review and the formulated research objective, the fabrication process has a huge impact on the characteristics and applicability of the micro/nano porous membrane, as well as on the effect of process parameters (temperature, time of anodization, electrolyte solution, voltage) the quality of the fabricated AAO membrane. Thus, it is important to develop a firm experimental procedure before proceeding further.

This chapter presents a theoretical simulation for the analysis of the efficiency for the designed cooling system for the development of an experimental setup based on the Peltier element. *COMSOL Multiphysics 5.4* software was used for performing temperature analysis during the anodization process, and the obtained results of the temperature of the electrolyte were compared with the temperature measured during the experiment. Based on the findings of the efficiency of the cooling system, an experimental setup was developed for the fabrication of a nanoporous aluminum oxide membrane. The main parameters for the fabrication of a nanoporous AAO membrane are the temperature, the concentration of the electrolyte solution, the anodization time. These parameters were analyzed, and their effect on the membrane characteristics, such as the pore diameter, the interpore distance, and the membrane thickness were explored.

2.1 Theoretical Modeling and Analysis of a Cooling System based on Peltier Element

This section represents the design of a cooling system for the development of the experimental setup based on the Peltier element for maintaining the temperature during the fabrication of nanoporous alumina. The cooling system is an essential part for the experimental setup design for fabrication because the temperature of the electrolyte solution during electrochemical anodization directly affects the porous structure of the fabricated membrane. The theoretical analysis of the cooling system was performed, and the results were compared against the physical experimental setup performance regarding the temperature.

According to the literature analysis, the electro-chemical anodization process is more convenient for AAO membrane fabrication. During the electrochemical anodization process, the temperature of the electrolyte in the anodization jar increases, and, in order to fabricate a high-quality membrane, it is necessary to maintain a constant temperature during anodization. A cooling system has been designed and used for the construction of the experimental setup.

The cooling system for the experimental setup to be used for the fabrication of a membrane consists of a Peltier element (TEC1-12715), with a master cooler system (MLW-D24M) for cooling down the other side of the Peltier element. The schematic of the cooling system is presented in Fig. 2.1; the apparatus consists of a glass jar (1), a Peltier element (2), a master cooler pump (3), a radiator for the

master cooler (4), a power supply unit for the Peltier element, and a master cooler (5), a magnetic stirrer (6), and a stirrer bar (7). Additionally, wires for electric connection and a thermal paste for sticking a Peltier element to the anodization jar were used.
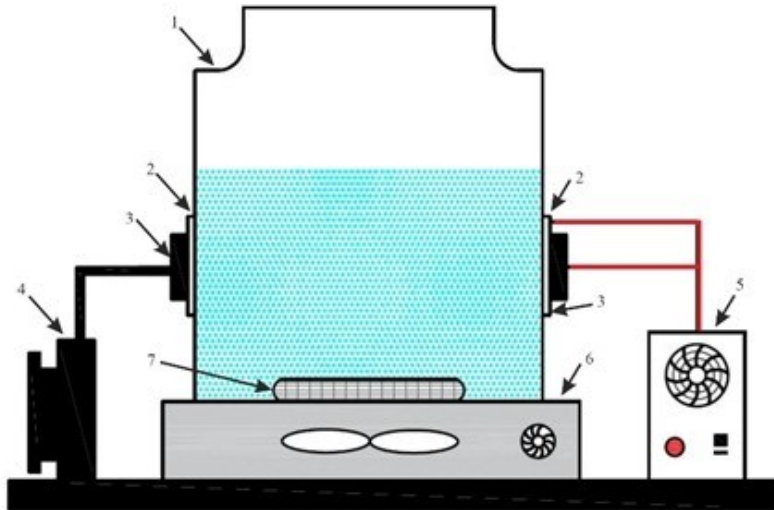
Fig. 2. 1 Schematic diagram of Peltier element-based cooling for the development of the experimental setup: a glass jar (1), a Peltier element (2), a master cooler pump (3), a radiator for the master cooler (4), a power supply unit for the Peltier element and the master cooler (5), a magnetic stirrer (6), and a stirrer bar (7)

The temperature of the electrolyte is maintained by using a Peltier element (a thermoelectric module). The mathematical modeling of the thermoelectric process is of high complexity by itself, although mathematical equations are available to determine the results of this process for the application in mathematical modeling.

In order to calculate the required power for Peltier elements, it is first necessary to determine the passive heating of the system. This requires finding out the contact surface area of the anodization jar with atmospheric air. After designing, the system contact area of the jar with atmospheric air is 42.38 mm^2. The anodization jar is chosen to be made from glass because glass offers good resistance to chemical reactions which occur during the fabrication process of the anodic alumina membrane.

An anodization jar made of glass with a wall thickness of 3 mm was selected for simulation and experimental purposes. The ambient temperature of air and the electrolyte for anodization was selected as 20° C, but the anodization process was done between 0–5 °C temperature in order to fabricate good quality nanoporous anodic alumina. This means that the desired temperature drop in the electrolyte is 15° C. Hence, passive heating can be calculated by using Formula 2.1 [149].

$$Q = \frac{k}{s} A \, dT \qquad\qquad (2.1)$$

Here, Q – passive heating, k – coefficient of thermal conductivity, s – contact wall thickness, A – surface area, and dT – change in temperature.

The coefficient of the thermal conductivity of glass is 0.8 W/(mK), the contact wall thickness is 0.003 m, the surface area is 30386×10^{-6} m, and the required change of temperature is 15 °C.

During the process of anodization, active heating had to take place due to the electrolysis process when, due to the electric potential applied to the membrane, it started to heat up and contributed to active heating during the anodization process. It was assumed that the membrane fabrication process would take place at 60V and at 1 ampere current density during the anodization process. The electric power of those values was calculated with Formula 2.2 with regard to the heating process [150].

$$P = V . I \qquad\qquad (2.2)$$

Here, V – voltage of anodization, and I – current density.

The amount of heat that must be removed from the electrolyte initially also contributes to both active and passive heating. It depends on the change in the specific heat of the electrolyte, the mass, and the temperature of the electrolyte. The main purpose of the theoretical simulation was to remove the heat from 600 ml of the electrolyte solution. The specific heat of the electrolyte solution is 4152 J/kgK [150]. The temperature of the electrolyte solution is assumed to be the same as the ambient temperature, i.e., 20 °C. The calculation of the work done for removing the heat from the electrolyte solution was done by using Formula 2.3:

$$Q = c \times m \times \Delta T \qquad\qquad (2.3)$$

Here, c – specific heat of the electrolyte solution, m – mass, and ΔT – change in temperature.

The cooling system was designed based on the Peltier element; hence, it was necessary to calculate how many Peltier elements are required to achieve the work efficiency of cooling. To achieve faster and more efficient cooling, it is necessary to install a powerful Peltier element. The main purpose of the simulation is to achieve the desired cooling in 600 seconds. The calculation of the desired power can be done by dividing the amount of heat required by the desired cooling duration, while taking into account active and passive heating. Therefore, the calculation of the required Peltier element's power is as follows:

$$P = \frac{Q}{t} + Q_{act} + Q_{pas} \qquad\qquad (2.4)$$

Here, Q – the amount of heat at the initial moment, t – time duration, Q_{act} – active heating, and Q_{pas} – passive heating.

Theoretical calculation of power is applied in the simulation model based on the finite element method. A similar model of the electrolyte solution in a glass jar is used for the simulation using *COMSOL Multiphysics 5.4* software.

The simulation was done under two conditions, including the analysis of temperature without using a Peltier element, and with a Peltier element. The model of the simulation was developed with the software *Solid Works* and imported in *COMSOL Multiphysics* software for further simulation; it is presented in Fig. 2.2. The analysis consists of four basic materials: glass for the jar, electrolyte solution, bismuth telluride for the Peltier element, and aluminum for the membrane.

Because of the complexity of the simulation, Multiphysics simulation was used. It combines three different areas of physics: heat transfer in solid, electric current in the aluminum membrane, and electric current in a Peltier element. As the Peltier element produces heat and frost at the same time, thermoelectric effect physics was used in the consideration of electromagnetic heating for the aluminum membrane.

| A | b |
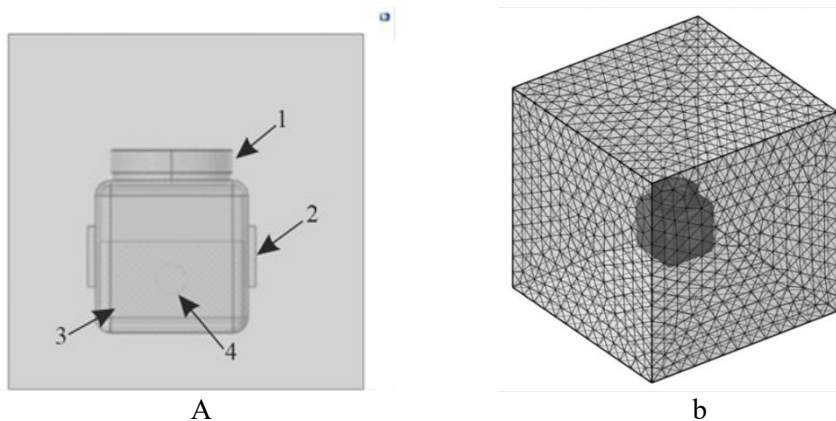
Fig. 2. 2 Simulation model for the cooling system (a), and the finite element mesh model (b)

The simulation of the cooling system for temperature analysis during the anodization process was done by using *COMSOL Multiphysics*; it is shown in Fig. 2.2. It consists of a glass jar (1), a Peltier element (2), electrolyte solution (3), and a membrane (4).

All the elements are set at a temperature of 20 °C for the initial analysis. A special rotating matrix is developed because, under realistic conditions, there would be a magnetic stirrer that would maintain the flow during the anodization process. The hot side of the Peltier element would be cooled by a cooler set at 6000 W / $(m^2 * K)$. In the case of cooling based on a Peltier element, the electrical potential of 60 V was set for the aluminum membrane, and 12 V was selected for the Peltier element. Electrical current was set to 1 amp for the aluminum membrane and 6 amp

for the Peltier element. In the case without a Peltier element, the electric potential was only applied to the alumina membrane, and the Peltier element was disabled.

The finite element decomposition of the model is shown in Fig. 2.2a. The reactor components, broken down into finite elements, are combined into a multifunctional compound to monitor the overall temperature change in the system. The analysis model was chosen to change over time because it was intended to determine how long the electrolyte solution would take to reach 5–6 ºC temperature. This analysis was run from 0 minutes and lasted up to 60 minutes with a 1-minute step.

The obtained results from the simulation for the temperature analysis are presented in Fig. 2.3. The obtained results show the temperature distribution in the vessel and in the environment. The temperature of the Peltier cells cools to 2 °C. The alumina membrane itself heats up slightly, but the temperature of the liquid is not affected, so the temperature of the liquid is constant at 2–3 °C. Since the analysis model is time-varying, the temperature change over time is plotted and shown in Fig. 2.4.
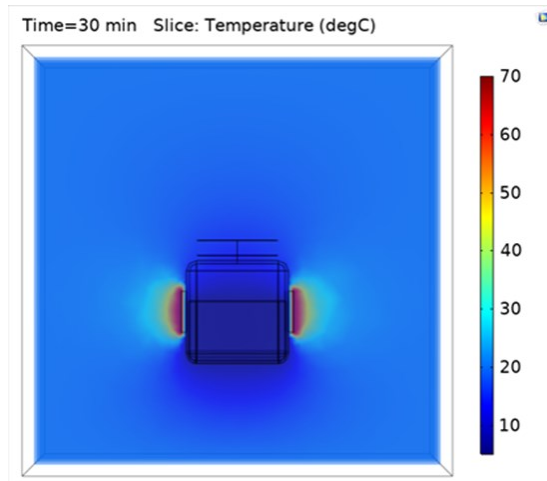
Fig. 2. 3 Simulation results of a cooling system using two Peltier elements

The temperature analysis graph using two Peltier elements is shown in Fig. 2.4 with respect to time. It clearly shows that the temperature inside the jar starts to decrease exponentially in a few minutes, and it becomes constant at 3 °C after 15 minutes.
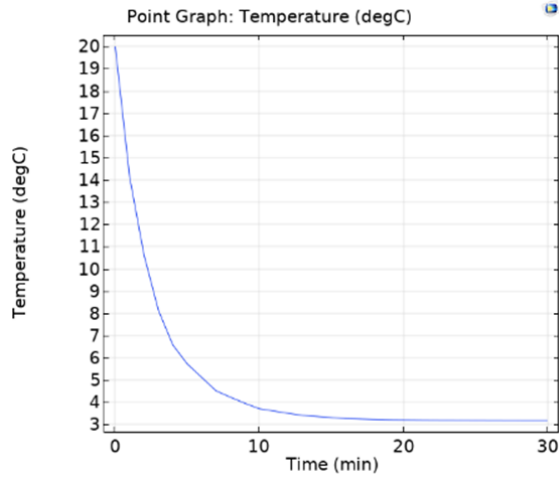
Fig. 2. 4 Temperature change of electrolyte inside the anodization jar when using a cooling system

The simulation analysis of the temperature distribution of the electrolyte without using a Peltier element was performed, and the results of the temperature distribution inside the anodization jar over time are presented in Fig. 2.5.
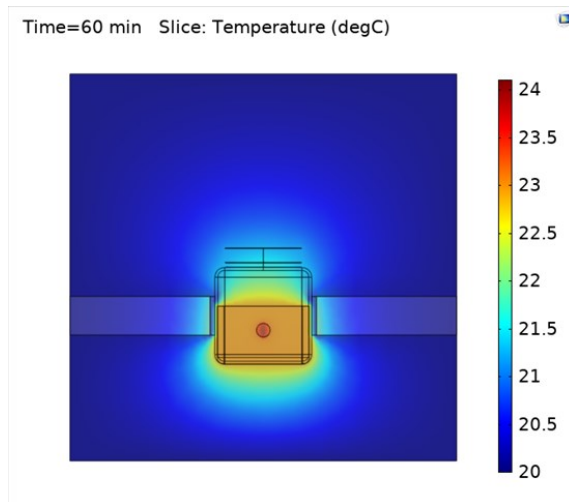
Fig. 2. 5 Simulation results of the temperature distribution of electrolyte without using a Peltier element
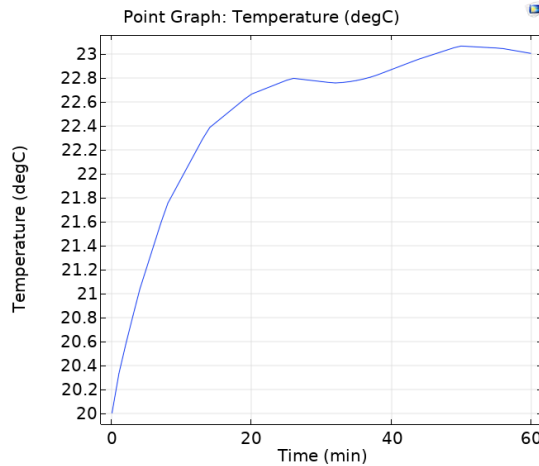
Fig. 2. 6 Temperature change of electrolyte without a cooling system

A simulation of a similar model to analyze the temperature during the anodization process without using a cooling system (a Peltier element) was performed. The result of the simulation without a cooling system is presented in Fig. 2.5, and the temperature plot as a function of time is shown in Fig. 2.6. The function clearly shows that the temperature distribution inside the jar is high, and it is not possible to control the course of reaching the desired temperature during the anodization process. Initially, it starts from 20 °C, and, within one hour, it reaches 23 °C. That means that it will affect the process of the fabrication, and it will result in an irregular porous structure and an unstable reaction.

The simulation results of the temperature analysis with and without a Peltier element cooling system show that the temperature of the electrolyte gradually decreases and reaches 2–3 °C in 15 min, yet, when the temperature analysis was performed without a cooling system, it was determined that the temperature increases and reaches 23 °C in 30 minutes. According to literature, a high temperature disturbs the anodization process and results in a low quality nanoporous structure with uneven pore distribution. The results achieved from the simulation show that the cooling system effectively maintains the temperature inside the jar during anodization, hence, there are two Peltier elements (TEC112715) in use for cooling. The experimental analysis of the cooling system was performed during the actual anodization process, and it will be presented in a further section.

2.2 Design of Experimental Setup for Fabrication of Nanoporous Aluminum Oxide Membrane

The experimental setup for the fabrication of a nanoporous aluminum oxide membrane consisted of a cooling system based on a Peltier element and some additional equipment required for the two-step anodization method including a custom-made aluminum specimen holder, DC power supply, and a thermometer for

60

temperature measurement. The entire setup of the experiment was assembled on a wooden board, and all the equipment was arranged in such a way that the ease of access would be ensured. The experimental setup is shown in Fig. 2.7, and its schematic representation is depicted in Fig. 2.8.
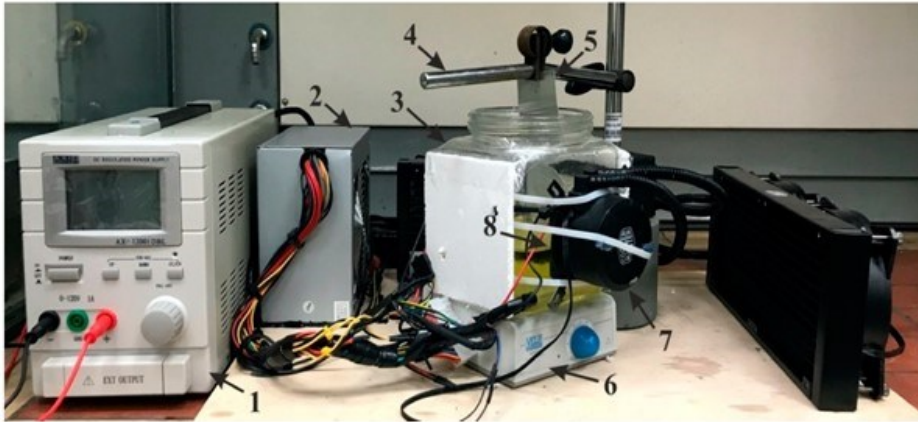
Fig. 2. 7 Designed experimental setup for the fabrication of a nanoporous aluminum oxide membrane: DC power supply (1), a power supply unit for the Peltier element and the master cooler (2), an anodization jar (3), a stand for the specimen holder (4), a specimen (5), a magnetic stirrer (6), a master cooler (7), and a Peltier element (8)
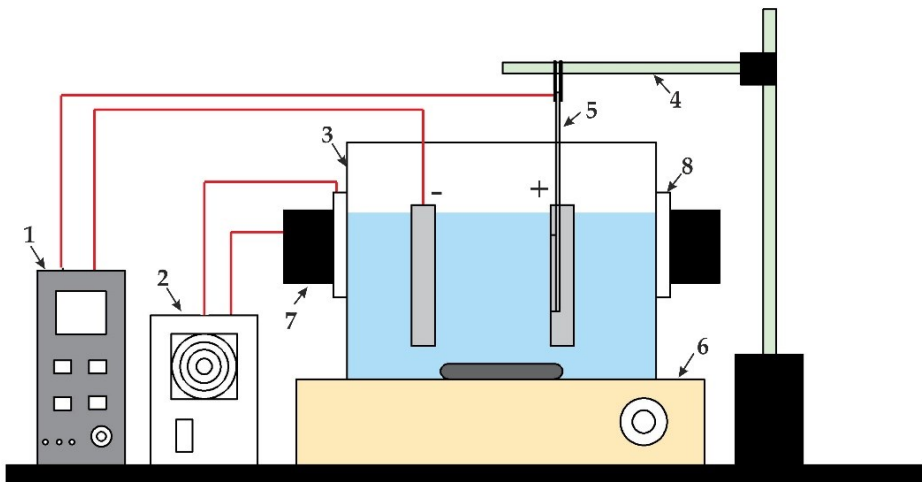
Fig. 2. 8 Schematic of experimental setup for the fabrication of a nanoporous AAO membrane: DC power supply (1), a power supply unit for the Peltier element and the master cooler (2), an anodization jar (3), a stand for the specimen holder (4), a specimen (5), a magnetic stirrer (6), a master cooler (7), and a Peltier element (8)

The experimental setup for the fabrication of a nanoporous membrane (Fig. 2.7) consists of a DC power supply unit (1), for constant current and voltage application to the aluminum plate during the anodization process. A power supply unit (2) is required for providing electricity to the Peltier element and the master cooler attached on the other side (the hot side) of the Peltier element. The anodization jar (3) contains anodizing electrolyte solution, positive and negative electrodes, and a magnetic stirrer bar for constant fluid flow inside the anodization jar. A stand for the specimen holder is shown as (4); a laboratory stand was used for holding the specimen inside the anodization jar during the anodization process. The specimen (5) was an aluminum sheet (1050A) intended for the fabrication of nanoporous alumina. A magnetic stirrer (6) served for continuous fluid mixing during the anodization process so that to reduce the heat concentration at one place. A master cooler (7) was used to cool down the other (i.e., heated) side of the Peltier element in order to overcome a heating failure of the Peltier element. The Peltier element (8) was used to maintain the temperature of the electrolyte solution for a more efficient anodization process. As shown in Figs. 2.7 and 2.8, all the equipment was arranged in the manner of easy accessibility and smooth operation.

2.2.1 Equipment and Instruments Used for the Development of the Experimental Setup

The design of the experimental setup suitable for the fabrication of a nanoporous aluminum oxide (AAO) membrane consisted of several pieces of equipment and instruments serving to control the entire process of electrochemical anodization.

- **Peltier element ITEC112715)**

The Peltier element (Fig. 2.9) is used for the application in the creation of the thermoelectric effect. It creates the temperature difference on either side of the element. For the development of the experimental setup, a Peltier element (TEC112715) from *Hebei I.T.* (Shanghai) Co., Ltd., Shanghai, China was used.

a   b
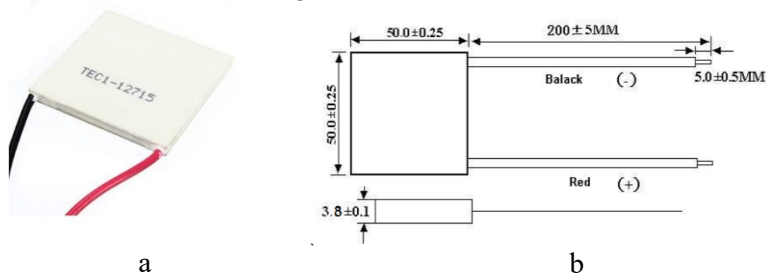
Fig. 2. 9 Photo (a), and dimensions (b) of the Peltier element (TEC112715) [151]

The technical specifications of the Peltier element (TEC112715) are presented in Table 2.1.

Table 2. 1. Technical specifications of the Peltier element (TEC112715) [151]

Max. operating temperature, (T)	≤90 °C
Max. cooling power, (Q_{max})	136
Temperature difference, (ΔT_{max})	70
Max. input voltage, (V_{max})	15.4
Max. current, (I_{max})	15
Resistance, (R)	0.75±0.05
Connection lines	20AWG

This Peltier element works quite well if the hot side of the element is kept cool. After powering on the device, the hot side will swiftly heat up, and the cold side will soon cool down. If the heat generated on the hot side is not removed (through a heat sink or another mechanism), the Peltier element rapidly reaches stasis and stops working. Therefore, in order to cool down the hot side of the Peltier element, a master cooler is attached.

- **Master cooler (MLW-D24M)**

The master cooler (Fig. 2.10) was used for cooling the hot side of the Peltier element. The master cooler model *MLW-D24M* (*Cooler Master Technology Inc.*, Taipei, Taiwan) comes with mini hydraulic pumps which maintain the flow of the fluid and cool down the flowing fluid by using the installed two fans with aluminum fins [152].

Fig. 2. 10 Master cooler [152]

The master liquid cooler works with the help of a dual chamber pump serving to ensure continuous fluid flow. It is attached on the hot side of the Peltier element and ensures work efficiency by maintaining the hot side's temperature. During the anodization process, the master cooler provides a cooling effect for cooling down the hotter side of the Peltier element so that to improve the efficiency of the cooling operation and to maintain the temperature of the electrolyte solution inside the jar at around 0–5 ºC. The technical specifications of the master cooler are presented in Table 2.2.

Table 2. 2. Technical specifications of the master cooler (MLW-D24M) [152]

Fan	Speed, (RPM)	650-2000
	Airflow, (CFM)	66.7

	Air pressure, (mmH$_2$O)	2.34±10%
	Noise level, (dBA)	6-30
	Connector type	4-pin
	No. of fans	2
	Voltage, (DC)	12
Pump	Noise level, (dBA)	15
	Voltage, (DC)	12

- **Magnetic stirrer**

A magnetic stirrer (Fig. 2.11a) from *VELP Scientifica Srl* is used for continuous fluid flow in order to maintain the temperature of the electrolyte solution during the anodization process for the fabrication of a membrane. This device produces a rotating magnetic field by using a rotating magnet or a stationary electromagnet. A stir bar (Fig. 2.11b) is used for immersing it in a liquid and immediately spinning it [153].

A	b

Fig. 2. 11 Magnetic stirrer (a), and magnetic stirrer bar for mixing the electrolyte (b) [153]

The magnetic stirrer helps to reduce the risk of heat concentration during the anodization process for the better formation of the micro/nano porous structure; it also maintains the temperature during the entire process. The technical specifications of the magnetic stirrer are presented in Table 2.3.

Table 2. 3. Technical specifications of the magnetic stirrer [153]

Construction material	Technopolymer
Power, (W)	0.6
Electronic speed regulation, (rpm)	Up to 1100
Stirring volume, (L)	Up to 5
Speed control	High power magnetic type PCM
Dimension, (mm)	120 x 50 x 145

- **DC power supply**

The DC power supply unit (Fig. 2.12) was used for the constant current and voltage application for the fabrication of a nanoporous alumina membrane during the anodization process. It features a simultaneous voltage and current readout,

smart cooling control, and stepless voltage and current adjustment with 0–120 DC voltage and 0–1 Amp current supply [154].

Fig. 2. 12 DC power supply for the fabrication of a nanoporous membrane [154]

The technical specifications of the DC power supply (AX-12001DBL) are presented in Table 2.4.

Table 2. 4. Technical specifications of the DC power supply (AX-12001DBL) [154]

Model	AX-12001DBL
No. of channels	1
Output current, (Amp)	0-1
Output voltage, (VDC)	0-120
Current stability, (mA)	≤0.02%+6mA
Voltage stability, (mV)	≤0.01%+3mV
Supply voltage, (V)	230V AC

By combining together all the equipment, the experimental setup was developed for the quality membrane fabrication by using a cooling system based on a Peltier element. Additionally, a mercury thermometer, a laboratory stand, connecting cables, and a thermal paste for sticking Peltier elements were used.

2.3 Materials and Methods for the Fabrication of a Nanoporous Aluminum Oxide Membrane for Microhydraulic Systems

The fabrication process of a nanoporous AAO membrane requires several chemicals for the process of electrochemical anodization. The basic requirement is the availability of aluminum foil of a certain thickness denoted by high purity. The experiment was performed with a 99.3% pure aluminum sheet (1050A-H24) having a thickness of 0.5 mm. The mechanical properties and the chemical compositions of the aluminum sheet (1050A-H24) are presented in Table 2.5.

Table 2. 5. Mechanical properties and chemical composition of aluminum alloy (1050A) [155]

Mechanical Properties, (Units)	Value	Chemical composition	Values, (%)
Density, (g/cm³)	2.71	Aluminum, (Al)	99.3
Tensile Strength, (Mpa)	100	Iron, (Fe)	0.4
Shear Strength, (Mpa)	60	Silicon, (Si)	0.25
Hardness Vickers, (HV)	36	Zinc, (Zn)	0.07
Elongation, (%)	12	Manganese, (Mn)	0.05
Melting Point, (°C)	650	Titanium, (Ti)	0.05
Modulus of Elasticity, (Gpa)	71	Copper, (Cu)	0.05
Thermal Conductivity, (W/m.k)	147	Magnesium, (MG)	0.05
Electrical Resistivity, (W/m.k)	222		

Aluminum alloy (A1050) is a metal alloy which is very well-known for excellent corrosion resistance, high ductility, high reflective finish, and the anodization process for the fabrication of nanoporous alumina.

Along with metal aluminum, there are various chemicals (Table 2.6) which are used for the anodization process, the etching process and the cleaning process of the aluminum sheet before and after the experiment.

Table 2. 6. Chemicals used for the fabrication of a nanoporous aluminum oxide membrane and their use

Chemical	Composition	Use
Acetone	C_3H_6O	For cleaning
Phosphoric acid	H_3PO_4	For etching solution
Sulfuric acid	H_2SO_4	For etching solution
0.3 M oxalic acid	$C_2H_2O_4$	For anodization
Chromium anhydride	CrO_3	For etching solution
Hydrochloric acid	HCl	For etching solution
Copper chloride dihydrate	$CuCl_2$	For etching solution
Distilled water	H_2O	For dilution and cleaning

The chemicals used for the fabrication of a nanoporous aluminum oxide membrane had various levels of influence on the process. Acetone (C_3H_6O) was used for the cleaning of the aluminum sheet before starting anodization, after mild anodization, after etching, after hard anodization, and, finally, after opening the other side of the membrane for cleaning. Phosphoric acid (H_3PO_4) and sulfuric acid (H_2SO_4) were used for performing the electro-chemical polishing of the aluminum plate before anodization. 0.3 M oxalic acid ($C_2H_2O_4$) was used for the electrochemical anodization solution for hard and mild anodization. Chromium anhydride (CrO_3) was used to prepare an aqueous solution for the alumina layer etching. Hydrochloric acid (HCl) and copper chloride dihydrate ($CuCl_2$) were used for preparing the aqueous solution for the back side aluminum layer etching.

Prior to the anodization process, the aluminum plate is subjected to annealing at 400 °C for 4 hours in nitrogen environment. The annealing of the aluminum plate was done by using a muffle furnace (*Nabertherm LHT 08/16/P310*) shown in Fig. 2.13a, and the arrangement of the aluminum plate sandwich between two glass plates is shown in Fig. 2.13b.

a   b
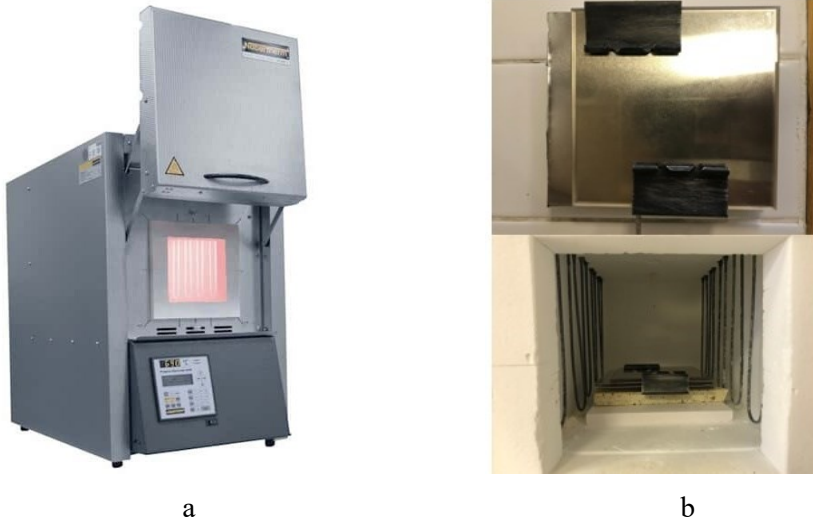
Fig. 2. 13 Photo of a muffle furnace (a), and an aluminum plate sandwich placed inside a furnace (b)

Aluminum plates are cut in a square section sized 15×15 cm. The aluminum plates are positioned between two glass plates and then placed inside the muffle furnace for annealing in nitrogen atmosphere to reduce the internal stress and remove the hardening strain from the aluminum plate for better anodization effect so that to enhance the quality of the fabricated aluminum oxide membrane.

The Vickers hardness test for aluminum sheets was performed to understand the change in hardness of the aluminum sheet after the annealing process performed at 400 ºC for 4 hours in the muffle furnace inert nitrogen environment for a better-controlled anodization process of the fabrication of a nanoporous aluminum oxide membrane. The hardness test conducted on the aluminum plate (0.5 mm thick and 99.3% pure) was performed by using a *Wilson Tukon 2500 Knoop/Vickers Automated Hardness Tester* (t-2500). A testing force of 0.2 kg was applied for the indentation time of 10 s on aluminum plates with and without annealing. Similar loading conditions were used for both specimens, and indentation was repeated eight times while maintaining a distance of 10 mm. A comparison graph of the obtained results is shown in Fig. 2.14.
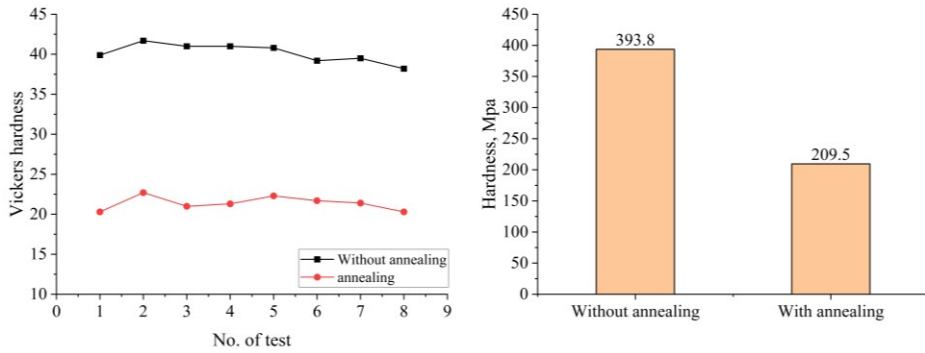
Fig. 2. 14 Results of the hardness test for an aluminum plate with and without annealing

The results of the hardness test of an aluminum plate with and without annealing was determined to be 209.5 Mpa (21.4 HV) and 393.8 Mpa (40.2 HV), respectively. From this result, it can be observed that the annealing of an aluminum plate has a significant difference on the hardness of the plate. From the graph, it is possible to state that the annealing process helps to reduce the hardness of an aluminum plate by almost a half compared to a non-annealed aluminum plate. It is obvious that the fabrication of an AAO membrane while using annealed aluminum plates will provide membranes of excellent quality.

The fabrication of nanoporous AAO was done by using the two-step anodization method (mild anodization and hard anodization). The overall process of fabrication is divided in two steps, in which, the first step (mild anodization) develops non-structured pores which are removed by the etching process, whereas the second step (hard anodization) develops the ordered porous structure of alumina.
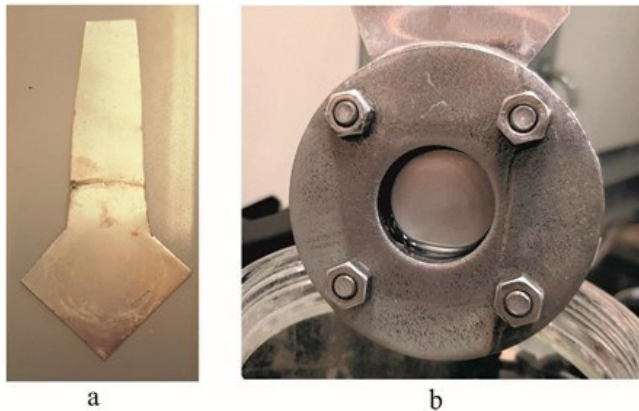
Fig. 2. 15 Coupon-shape specimen (a), custom-made specimen holder (b)

First, an annealed aluminum sheet was cut into specimens of the coupon shape (Fig. 2.15a) for fixing inside the custom-designed specimen holder (Fig. 2.15b). The

specimen holder defines the specific area of anodization in the specimen (diameter: 15–30 mm) and keeps the remaining area of the specimen isolated from anodization. The main body part is made from stainless steel, and the top and the bottom are connected with M16 bolts and nuts. Between two stainless steel plates, acrylonitrile butadiene styrene (ABS) and a silicon gasket are used for insulating the aluminum specimen from the applied DC voltage. A detailed drawing of the designed custom-made specimen holder is shown in Fig. 2.16.
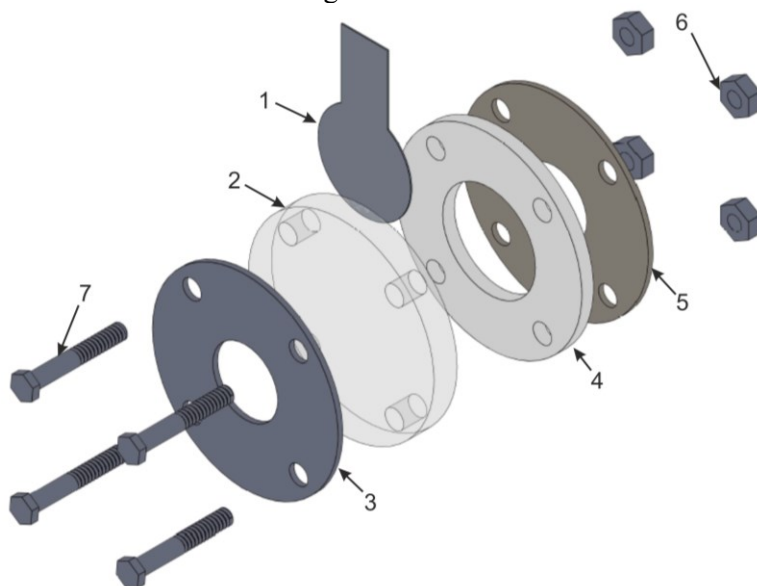
Fig. 2. 16 Detailed assembly drawing of the specimen holder for fabrication of nanoporous AAO membrane: aluminum specimen cut out (1), acrylonitrile butadiene styrene (2), bottom stainless-steel plate (3), silicon gasket (4), top stainless cover (5), M16 nuts (6), and M16 bolts (7)

The custom-made specimen holder (Fig. 2.16) for the fabrication of a nano porous AAO membrane consists of the aluminum specimen cut out (1), acrylonitrile butadiene styrene (2), the bottom stainless-steel plate (3), a silicon gasket (4), the top stainless cover (5), M16 nuts (6), and M16 bolts (7).

After cutting the specimen in the coupon shape, it is subjected to ultra-sonic cleaning in acetone (C_3H_6O) for 5 minutes. Then, the specimens were mechanically cleaned using a buffing disc to remove the stains and scratches from the surface of the specimen. The mechanically cleaned specimen was fixed in the custom-made specimen holder and immersed in concentrated phosphoric acid (H_3PO_4) for 10 minutes to preparing the hydrophilic surface of the specimen; during this process, the surface of aluminum gets covered with dense hydrogen bubbles. Electro-chemical polishing was performed at 20 V for 1 minute in a solution of phosphoric acid (H_3PO_4), sulfuric acid (H_2SO_4), and water with a volumetric proportion of 2:2:1

to achieve low surface roughness. The schematic diagram of the two-step anodization method is presented in Fig. 2.17.
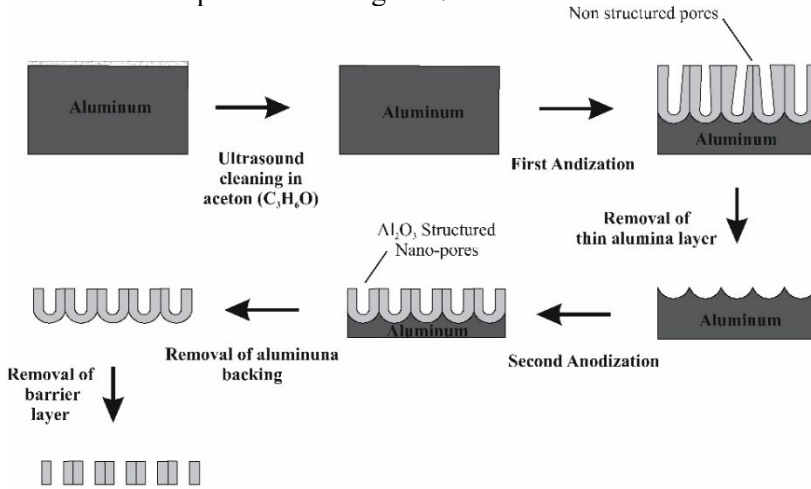
Fig. 2. 17 Schematic diagram of fabrication procedure of the two-step anodization method for the fabrication of AAO membrane

After finishing the pre-anodization procedure, a specimen is placed inside the anodization jar for the two-step anodization (mild and hard anodization). The description of the process of fabrication is presented in Table 2.9.

Table 2. 7. Two-step anodization procedure for the fabrication of nanoporous AAO membrane

Step	Description
1	First, the anodization (mild anodization) process is performed (50/60 V DC) in 0.3M oxalic acid ($C_2H_2O_4$) solution for predefined time.
2	Etching of non-ordered porous structure by using a solution of 3.5% concentrated phosphoric acid (H_3PO_4) and 2% chromium anhydride (CrO_3) acid solution (by volume) in distilled water at predefined time and at predefined temperature of the solution
3	Cleaning of the specimen and the holder with distilled water
4	The second anodization (hard anodization) process is performed (50/60 V DC) in 0.3M oxalic acid ($C_2H_2O_4$) solution for predefined time.
5	After finishing the two-step of anodization, the prepared sample is flipped and again placed in the specimen holder to etch the bottom aluminum layer in a solution of hydrochloric acid (HCL), copper chloride dihydrate ($CuCl_2$), and distilled water (1:0.3:1) at room temperature
6	Cleaning of the specimen with distilled water
7	The cleaned specimen is immersed in 5%wt phosphoric solution to open the other side of the pores (to remove the barrier layer) at room temperature for 15 minutes
8	Finally, the prepared samples are cleaned with distilled water and acetone (C_3H_6O) and dried

In the course of electrochemical anodization, the temperature of the electrolyte solution is maintained at 0–5 °C by using the designed cooling system and continuously mixing the electrolyte solution with a magnetic stirrer. There are six different samples which were prepared by using the two-step anodization procedure. The experimental matrix is presented in Table 2.8.

Table 2. 8. Experiment matrix of fabricated nanoporous AAO membrane

Sample no	Voltage, VDC	Anodization time, (h)		Etching temperature	Etching time	Electrolyte solution	Anodization temperature
		MA	HA				
1A	50	1.5	15				
1B	50	1.5	16			0.3 M Oxalic acid $(C_2H_2O_4)$	
1C	50	1.5	17	60 °C	30 minutes		0-3 °C
2A	60	1.5	15				
2B	60	1.5	16				
2C	60	1.5	17				

Nanoporous AAO membranes were fabricated by using two different anodization voltage conditions and three different hard anodization time intervals. The temperature and time duration of etching is similar: 60 °C and 30 minutes, respectively, for all six nanoporous AAO membranes. The anodic and cathodic reactions during the anodization process are shown in Fig. 2.18.
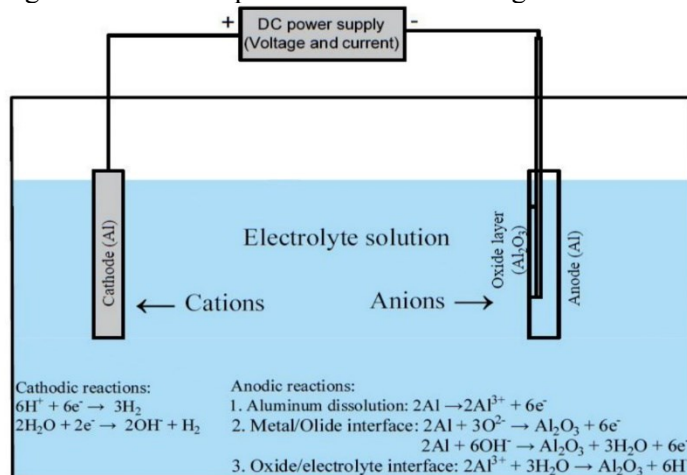
Fig. 2. 18 Anodization mechanism for the fabrication of nanoporous alumina membrane

Photos of the nanoporous AAO membranes fabricated by using two-step anodization methods with different process parameters (Table 2.8) are shown in Figs. 2.19 and 2.20.
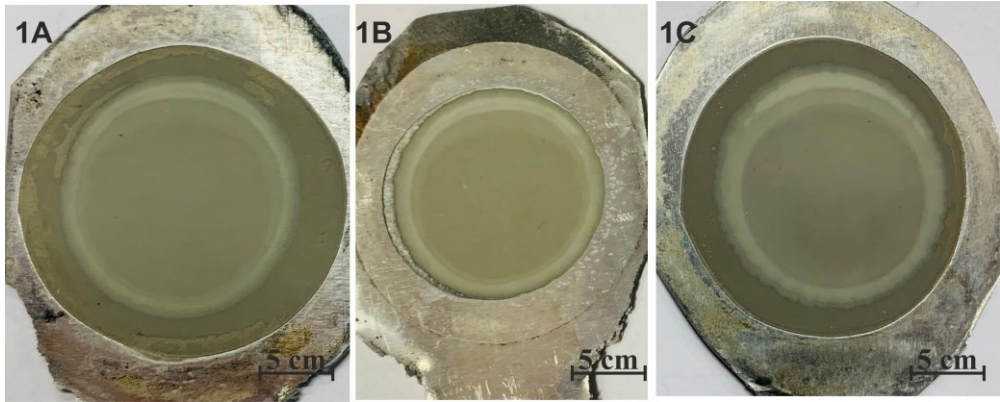
Fig. 2. 19 Nanoporous aluminum oxide membrane fabricated at 50V DC
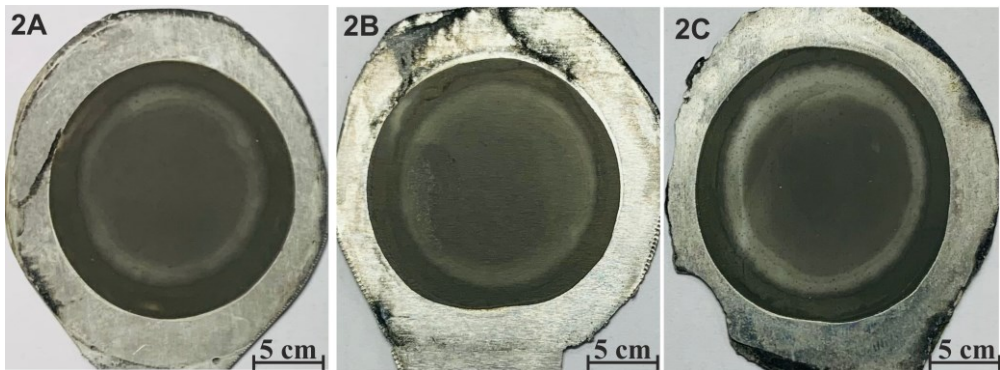
Fig. 2. 20 Nanoporous aluminum oxide membrane fabricated at 60V DC

As shown in Fig. 2.19, three AAO membranes (1A, 1B, and 1C) were fabricated at 50V DC with the anodization times of 15h, 16h, and 17h respectively. Similarly, AAO membranes at 60V DC (Fig. 2.20; membranes 2A, 2B, and 2C) were fabricated with the anodization times of 15h, 16h, and 17h, respectively.

The temperature analysis of the cooling system was done during the anodization process for the fabrication of nanoporous AAO membranes. The simulated and experimental comparison of the drop in temperature is graphically presented in Fig. 2.19.

During the two-step anodization, the analysis of the temperature of fabrication of nanoporous AAO membranes manipulated by the designed cooling system based on a Peltier element shows similar results for the drop in temperature. During the simulation, it was observed that, after 5 min, the drop in temperature from 20 ºC to 5 ºC was recorded. During the 5–10 min timeframe, the temperature of the electrolyte solution became steady at 3 ºC. On the other side, the experimental analysis of the cooling system shows a decrement in the temperature from 20 ºC to 7 ºC after 5 min. During the 5–10 min timeframe, the drop in temperature of the electrolyte solution

was recorded around 5 ºC. However, the temperature rise and fall between 5 ºC and 4 ºC was recorded during the 10–25 min timeframe due to the heat release from the electro-chemical reaction. Finally, a constant temperature of 4 ºC was recorded at 26 min after the beginning of the experiment.
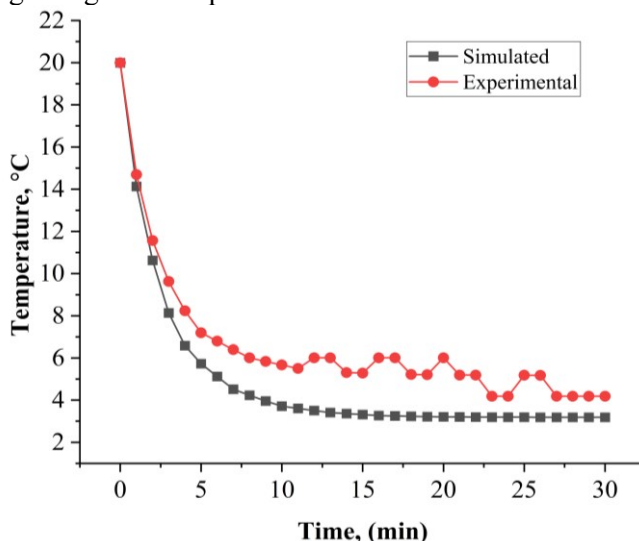
Fig. 2. 21 Comparison of theoretical and experimental results of temperature analysis for the cooling system

The experimental and simulation results of the designed cooling system for the fabrication of nanoporous AAO membranes are 4 ºC and 3 ºC after 30 min, respectively. There was no major difference observed in the results. It is possible to state that the designed cooling system is reliable for maintaining temperature during the electrochemical anodization in the course of fabrication of nanoporous AAO membranes.

2.4 Chapter Conclusions

The following conclusions were made from the simulation and experimental analysis of a cooling system based on a Peltier element. The influence of annealing of an aluminum plate before the anodization process for the fabrication of a nanoporous AAO membrane is as follows.

1. An effective and relevant cooling system based on a Peltier element was developed for maintaining a constant temperature of the electrolyte solution during the anodization process from 5 ºC to 3 ºC. It helps to develop a predefined porous structure while using various process parameters.
2. The fabrication of a nanoporous AAO membrane was done by applying the two-step anodization method while using the developed experimental setup at different process parameters (anodization voltage, time of anodization).

3. Effective tools and equipment were developed for successful experimentation which are bound to be useful for the fabrication of a nanoporous AAO membrane with various process parameters.
4. The annealing of an aluminum plate before anodization reduces the hardness of the aluminum plate, which helps to make the fabrication process more efficient.

III. Characterization of the Fabricated Nanoporous Aluminum Oxide Membrane

The fabricated nanoporous AAO membrane shall be used for the functional element in a microhydraulic device as a vibro-active micro/nano filter. It is important to analyze the geometrical structure, the chemical composition, and the hydrophobic properties for the application area. Recent applications of nanoporous AAO membranes show that the excellent quality of the formed nanoporous structure increases the area of application of the fabricated nanoporous AAO membrane.

This chapter covers the characterization methodology of fabricated nanoporous AAO membranes with various process parameters (anodization time and voltage). The geometrical structure (the pore diameter, the interpore distance, and the thickness of the membrane) analysis using scanning electron microscopy (SEM) and image processing software *ImageJ*, chemical composition analysis using energy-dispersive X-ray spectroscopy (EDS), and hydrophobicity measurement were performed by using the designed experimental setup by measuring the water contact angle on the surface of AAO membranes.

3.1 Characterization Methodology and Tools for the Fabricated Nanoporous AAO Membrane

The characteristics of the fabricated nanoporous aluminum oxide membrane were analyzed by using several tools and techniques. Those tools and techniques shall be explained in this section.

3.1.1 Scanning electron microscopy (SEM)

To analyze the fabricated nanoporous aluminum oxide membrane, a *HITACHI S-3400N* PC based variable pressure scanning electron microscope was used (Fig. 3.1).
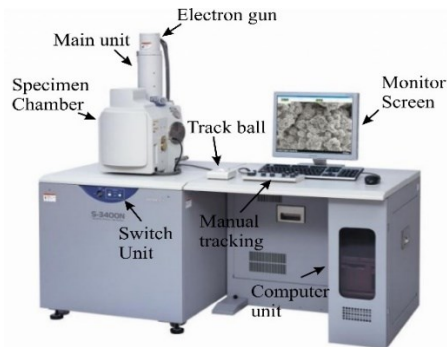
Fig. 3. 1 Scanning electron microscope (*HITACHI S-3400N*)

The *HITACHI* (S-3400N) scanning electron microscope has two modes of operation: a high vacuum mode at 30kV, and a variable pressure mode at 30kV. The scattered electron detector (SED) image resolution is 3.0 nm in the high vacuum mode and 4.0 nm in the variable pressure mode. The microscope chamber can

accommodate specimens up to 200 mm in diameter. Table 3.1 shows the specifications of the scanning electron microscope.

Table 3. 1. Technical specification of *HITACHI* (S-3400N) [156]

Electron source	Pre-centered tungsten hairpin type
Accelerating voltage	300V – 30kV
Magnification range	5X to 300000X
Resolution	3 nm at SED high vacuum mode at 30Kv and 4nm BSED variable pressure mode at 30kV
Imaging detectors	SE detector mode Everhart-Thornley secondary electron detector and BSE detector mode.
Mode of Imaging	High, low vacuum and variable pressure
Analytical capabilities	Continuous variable bias at 3kV, 5kV and 15kv.
Scan mode	Fast, slow, photo scan, single monitor, line scan (SE, BSE, and X-ray)

The BSE and SE procedures are clearly distinct. An element's atomic number has a direct correlation to the prevalence of a back-scattered electron (BSE). Backscattering occurs more frequently with the increase of the atomic number of a chemical element. As a result, BSE may be used to identify numerous phases in the structure involving a combination of various materials. However, scattered electrons (SE) interact with the substance just a few nanometers below the surface. During the primary-secondary electron collision, energy is transferred to the latter. If this energy is not enough to overcome the energy around it, the electron cannot escape through the material's surface. To detect an emitting electron across the surface area, the energy must be strong enough. SE has an energy level below 50 eV [157].

3.1.2 Energy Dispersive X-ray Spectroscopy (EDS Analysis)

EDS is a sample characterization and analysis method based on energy dispersive X-ray spectroscopy (EDS). It is via the interaction of an excitation X-ray and a sample that the electromagnetic emission spectrum of a particular element emits. It is possible to distinguish each chemical element by its atomic number and structure since each element has a unique collection of peaks. EDS can detect concentrations as low as 0.001 percent [158].

Fig. 3. 2 Energy dispersive X-ray spectrometer [159]

SEM with an integrated dispersive X-ray spectrometer detector was employed for the analysis. SEM using this detector Fig. 3.2 shows the entire unit as it features a photo of *X-Flash 4030*, an energy dispersive X-ray spectrum analyzer detector. It was necessary to cool down the 30 mm^2 solid state drift detector during the testing by using a Peltier element. The detector had 133-eV energy resolution at a rate of 100000 cps (MnK). The *X-Flash 4030* detector's technical features are shown in Table 3.2.

Table 3. 2. Technical specifications of *X-flash 4030* detector [159]

Energy resolution	133 eV (Mn Kα) at 100000 cps
Max. pulse load	1000000 cps
Active area	30 mm^2
Detection range	From Boron (5) to Americium (95)
Cooling system	Peltier element-based cooling system
Weight	Approx. 2.5 kg

3.1.3 Fourier Transform Infrared Spectroscopy (FTIR analysis)

FTIR is a method of the analysis of infrared spectra which allows for spectral registration. The infrared light travels through the interferometer, and then through the sample. A changing mirror inside the interferometer also changes the amount of light passing through it. For example, an interferogram shows the light output as a function of the mirror position. By using the Fourier transform, the obtained data is transformed into the desired spectra.

The FTIR method can be used for the analysis of organic and inorganic materials. The major advantage of the method is that a sample can be in any phase of material: solid, liquid, or gas. It is used for identifying the concentration of various compounds for any industrial application. A FTIR made by *Bruker*, USA model No. FTIR vertex 70 is presented in Fig. 3.3.
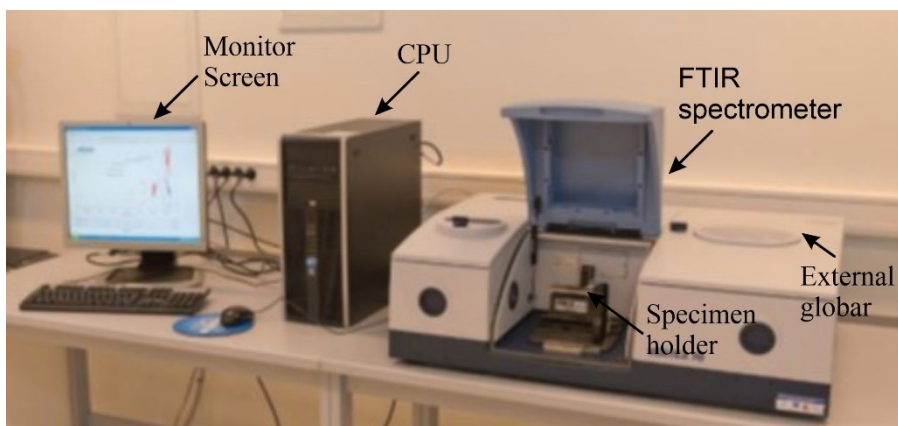
Fig. 3. 3 Fourier transform infrared spectrometer (vertex 70, *Bruker*, USA) [160]

These ranges are 12800^{-10} cm^{-1} for the near infrared, 4000–200 cm^{-1} for the midrange, and 1000^{-50} cm^{-1} for the far infrared (the far infrared region). Various spectrometers operate in the infrared wavelength ranges. The technical specifications of FTIR vertex 70 are shown in Table 3.3.

Table 3. 3. Technical specifications of FTIR (vertex 70, *Bruker*, USA) [160]

Spectra resolution	Mid - IR, NIR, Far – IR / THz, Visible / UV 10 cm^{-1} to 28000 cm^{-1} (360 nm)
Spectra range	0.4 cm^{-1}
Input port	2
Output port	5
Rapid scan	>70 spectra/s at 16 cm^{-1} spectral resolution
Slow and step scan	100 Hz (0.0063 cm/sec), Phase modulation and internal demodulation

3.2 Investigation of Hydrophobicity

The Wettability and surface free energy evaluation were done by using contact angle measurement. It is important to study the wetting behavior of the solvent on the surface of fabricated nanoporous aluminum oxide membrane applicability in biomedical microhydraulic systems for the filtration or separation of biological cells. It also helps to understand the intermolecular communication between the nanoporous membrane and the wetting behavior of the solvent/analytes to enhance the surface properties or the hydrophobic/hydrophilic behavior of the fabricated membrane. The balance force between adhesion and cohesion is identified by the intensity of wetting. It is a fundamentally important term in the field of the biomedical science and microhydraulic device development.
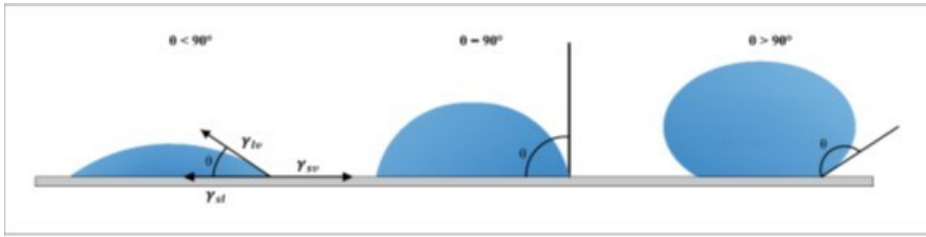
Fig. 3. 4 Contact angle formed on solid surface by liquid drop
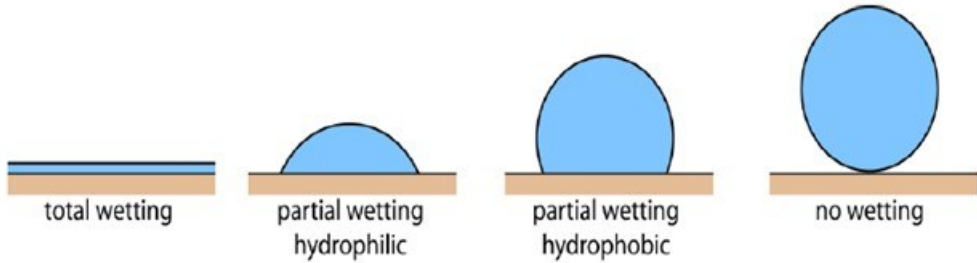
Fig. 3. 5 Wetting phenomenon and surface properties

A schematic illustration of the contact angle formed by a fluid on a solid surface is shown in Fig. 3.4. Contact angle measurements are used to determine the extent to which a liquid is wetted when it comes into contact with a solid surface. There are three probable outcomes if a contact angle of less than (90°) is observed: When the angle is greater than (>>90°), it implies a hydrophobic surface rather than a hydrophilic one. The wetting phenomenon on a solid surface is presented in Fig. 3.5.

There are two possibilities. When a drop of a liquid appears parabolic on the solid surface, it indicates that the surface tension of the liquid is greater than the surface energy of the solid surface; and when a drop of a liquid appears flatter on a solid surface, it indicates that the liquid's surface tension is less than the solid surface's surface energy. This phenomenon is known as wetting; less wetting indicates a larger difference, whereas more wetness indicates a smaller difference.

It is the angle between the tangent of a liquid drop at the three-phase contact point and the solid surface that is known as the contact angle (θ). Thus, the critical surface free energy of the constructed nanoporous aluminum oxide membrane was measured by examining the droplet's interaction with the analyte and the porous surface of the AAO membrane. Cohesion forces act within a substance to keep its molecules together. Work must be done (W_{SL}) to separate a homogenous liquid from the rest of the mixture. To put it simply, cohesion (σ) equals the following:

$$W_{SL} = 2\sigma \tag{3.1}$$

The adhesion force acts between two dissimilar material surfaces. For the separation of two different liquids, extra force is required:

$$\gamma_{SL} = \sigma_S + \sigma_L - W_{SL} \qquad (3.2)$$

Here, γ_{SL} – surface tension between a liquid and a solid, σ_S – the cohesion force of a solid, and σ_L - the cohesion force of a liquid.

Cohesion forces within the material determine the surface tension (γ). Force (F) exerted on a liquid film of length (L) determines the length of the stretched film:

$$F = \gamma L \qquad (3.3)$$

In order to determine the surface free energy (SFE), the critical surface tension of a liquid is used in the Zisman method [161]. At a zero-degree contact angle, the SFE difference between a solid and a liquid is equal to the interfacial tension (γ_{SL}).

$$\gamma_{SL} = \gamma_{SV} - \gamma_{LV} \qquad (3.4)$$

Here, γ_{SV} – surface tension between the solid and the gas and γ_{LV} – surface tension between the liquid and the gas.

In order to calculate the critical surface tension for wettability, Zisman showed that the connection between $\cos \theta$ and σ_1 is frequently linear. This approach does not take into consideration the polar or dispersion fractions of the materials' surface tensions; therefore, interfacial tension may only be calculated by subtracting separate surface tensions from each other.

The experimental setup was designed to perform the measurement of the contact angle (θ). The experimental setup and the testing protocol were designed for the contact angle measurement, as shown in Fig. 3.6. The contact angle measurement was performed for the fabricated nanoporous membrane samples 1A, 1B, 1C, 2A, 2B, and 2C fabricated at different anodization times.
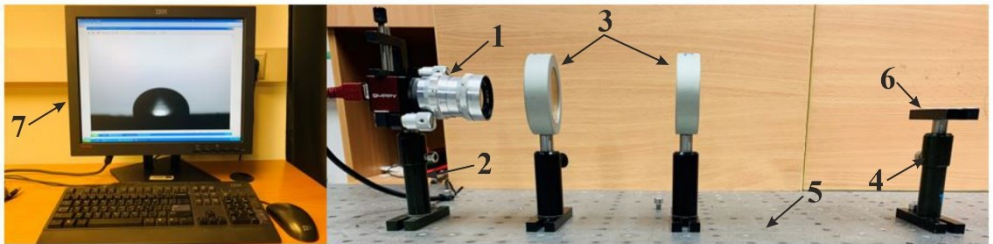
Fig. 3. 6 Experimental setup for the contact angle measurement: a high speed camera (1), an adjustable camera holder (2), a double convex (3), an adjustable stand for a specimen (4), an anti-vibrational table (5), a fabricated nanoporous aluminum oxide membrane (6), and a computer system with the software for capturing high resolution images (7).

The experimental setup (Fig. 3.6) for the contact angle measurement consists of: a high speed camera (*Guppy F-503*, *B&W CMOS* camera, with a resolution of 1595 X 1944, 1394A connection type, frame rate 60 fps, and a ½ inch sensor) (1), an adjustable camera holder (2), double convex lenses (the diameter of the lens 50 mm

80

and the focal length 500 mm) (3), an adjustable stand for the specimen (4), an anti-vibrational table (5), a fabricated nanoporous aluminum oxide membrane (6), and a computer system with software for capturing high resolution images (7). The dispensing of a droplet was done manually by using a glass pipet as shown in Fig. 3.7.

Fig. 3. 7 Drop dispensing glass pipet (Class AS)

The capacity of the pipet for holding liquid is 5 ml. The scale on the pipet is divided into 0.1 ml with the blue marking scale having a drawing error of ± 0.03 ml.

The measurements of the contact angle were carried out with three distinct high purity probe solutions, including distilled water, glycerin, and spirit. The hydrophobicity of a solid surface is determined by the water contact angle formed between a drop of water and a nanoporous aluminum oxide membrane that has been manufactured. However, in order to understand the surface behavior towards liquids with varying properties, two more liquids, specifically, glycerin and spirit, were used, and the contact angle for a drop of each of those two liquids was measured with nanoporous aluminum oxide membranes that had been fabricated (1A, 1B, 1C, 2A, 2B, and 2C). The characteristics of distilled water, glycerin, and spirit are presented in Table 3.4.

Table 3. 4. Properties of distilled water, glycerin, and spirit [162]

Liquid	Surface tension, dyne/cm	Density, Kg/m^3
Distilled water	72.8	997
Glycerin	64.2	1260
Spirit	26.02	793

The experiment was performed under dark lightning conditions in a laboratory room for a drop of liquid which appeared dark black and clear in the image for the sake of accurate measurement. The precautions were taken to prevent the drop of liquid from any external light source and air impurities, such as dust particles.

All the equipment of the experiments was arranged as shown in Fig. 3.6 on a stable antivibration table so that to avoid any external destructive impact of the dispensed drop on the surface of the aluminum oxide membrane. The height of the camera was adjusted according to the sample's height to ensure clear visibility of the image of the dispensed drop of liquid on the membrane's surface. Two convex lenses were placed and adjusted for clear visibility of the drop and maintained the focus on the drop for the sake of excellent image quality for further image processing. The critical distance between the camera, the lenses, and the specimen is very important for capturing high quality focused images. The critical distance between the important optical parts and the specimen is shown in Fig. 3.7.
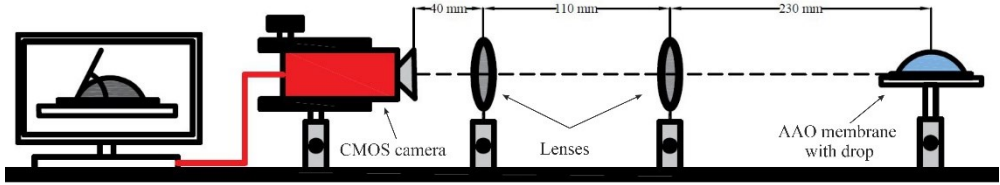
Fig. 3. 8 Critical distance between the optical equipment and a drop of liquid

Before starting the experiment, a glass pipet was cleaned with water and checked for the diffusion of a drop with distilled water. Then, adjustment of the height of the specimen to ensure its parallel position to the camera vision was performed, and we started to place a drop for measurement on the fabricated AAO membrane. For all the measurements, the dispensing height and the quantity of dispensed liquid were kept constant at 15 mm and 0.2 μl respectively. The experiment was repeated in the same manner for all liquids and the fabricated samples. The image of the droplet was captured immediately, a few seconds after dispensing a drop for all the fabricated membranes and liquids. The captured images were analyzed by using freely available image analysis software *ImageJ* (*Dropsnake* plugins) for the contact angle formed by a liquid drop on the fabricated nanoporous AAO membrane samples (1A, 1B, 1C, 2A, 2B, and 2C). The software interface and the contact angle measuring technique is shown in Fig. 3.9.
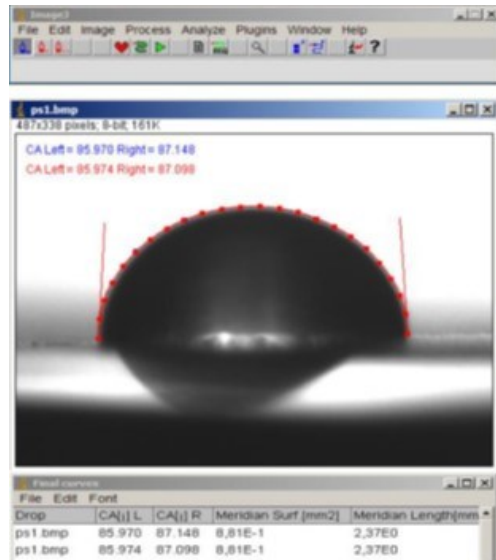
Fig. 3. 9 *ImageJ* software interface for contact angle measurement

Before starting the analysis, the image of a drop should be converted into 8-bit using *ImageJ*, and then, by using dropsnake analysis, we started to put 7–8 notes

from the left lower part and towards the right lower end while covering the drop profile, and, lastly, by double-clicking on the left lower end, we obtain the estimated contact angle and profile as shown in Fig. 3.9 (the red profile of the drop and the values of the contact angle in the left top corner in red (exact values) and in blue (the approximate value of the contact angle).

A similar procedure was used to examine the contact angle measurements of all the collected photos with the fabricated AAO membrane samples (1A, 1B, 1C, 2A, 2B, and 2C) with three different liquids (distilled water, glycerin, and spirit). Eq. 3.5 was used to compute the confidence level interval (CI) for the measurement inaccuracy.

$$CI = \bar{x} \pm z \frac{s}{\sqrt{n}} \tag{3.5}$$

Here, $\bar{x}$ – the average of measurements, Z=1.960 for accuracy level 95%, s – standard deviation, and n – No. of measurement.

Due to the fact that measurements are within the range of the standard deviation of the mean value, the value of Z was derived from the normal distribution (Z=1.960).
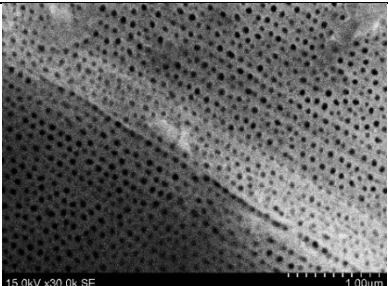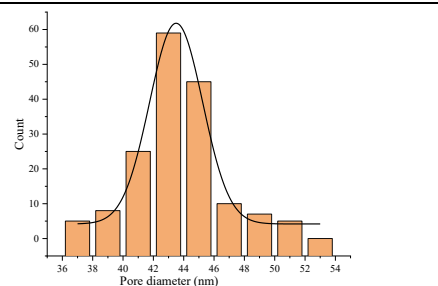
3.3 Results of Analysis

3.3.1 Scanning Electron Microscopy Analysis of AAO Membrane

The scanning electron microscopy (SEM) analysis was done to analyze the pore diameter, the interpore distance, and the thickness of the fabricated nanoporous AAO samples (1A, 1B, 1C, 2A, 2B, and 2C). The effect of annealing on the formation of the nanoporous structure was analyzed.

The SEM images of the fabricated nanoporous AAO membranes 1A, 1B, and 1C at a constant anodizing voltage of 50 VDC and membranes 2A, 2B, and 2C at an anodizing voltage of 60 VDC at anodizing times of 15 h, 16 h, and 17 h, respectively, are presented in Table 3.5.

Table 3. 5. SEM images of the fabricated nanoporous AAO membrane; pore distribution histogram

Sample no	SEM photo	Pore distribution histogram
1A		

1B		
1C		
2A		
2B		

| 2C | | |
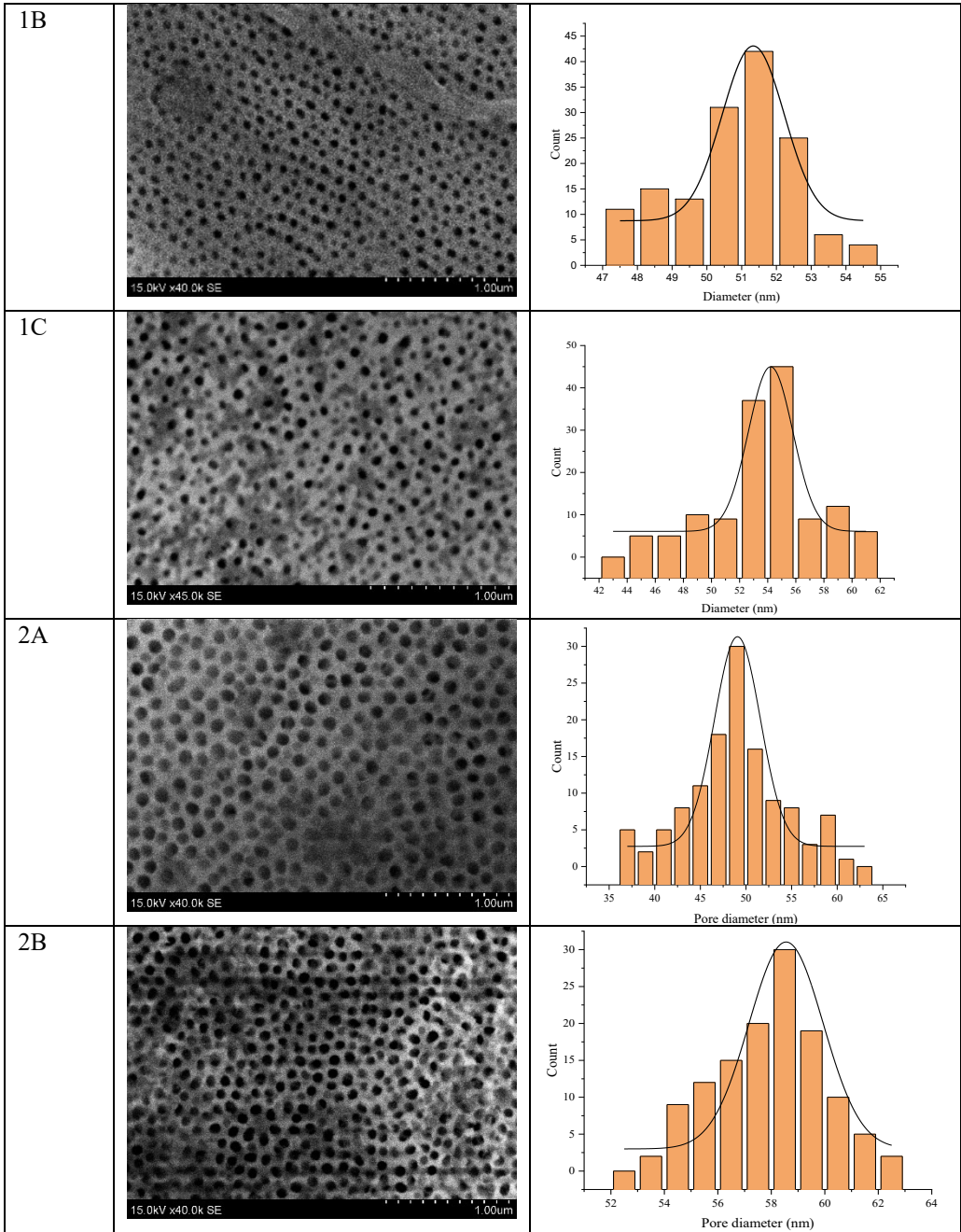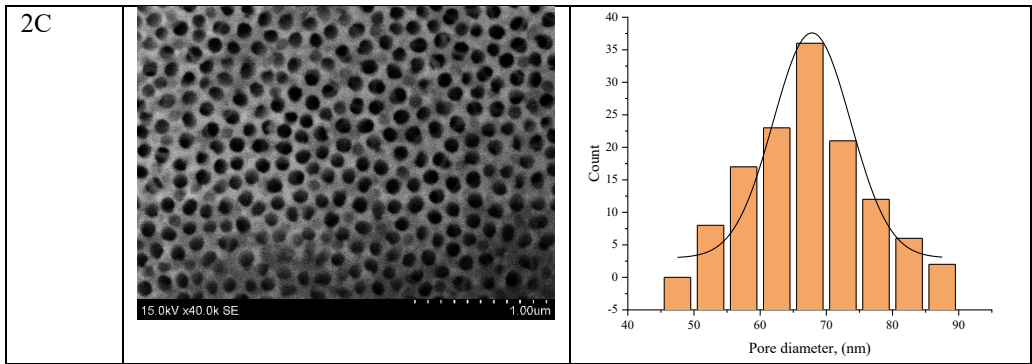
SEM images (Table 3.5) of the fabricated membrane confirm that the porous structure (honeycomb) formed on the AAO membrane and the histogram reveal the pore diameter distribution on the surface of the fabricated AAO membrane.

The pore diameter (D_p), the interpore distance (D_c), the porosity, and the pore occupancy of the sample fabricated by using 50 V (1A, 1B. and 1C) and 60 V (2A, 2B, and 2C) at different anodization times are summarized in Table 3.6.

Table 3. 6. Characteristic parameters of the fabricated nanoporous AAO membranes at 50V and 60V

Sample No.	Anodization time, (h)	Pore diameter, (nm)	Interpore distance, (nm)	Porosity, (%)	Pore occupancy, (cm^{-1}*10^9)
1A	15	43.5 ± 10	111 ± 10	14.25	4.68
1B	16	51.33 ± 8	113 ± 10	19.20	4.14
1C	17	55.62 ± 10	110 ± 10	23.50	3.87
2A	15	49.38 ± 6	115 ± 10	17.14	4.29
2B	16	58.55 ± 5	113 ± 10	22.67	3.87
2C	17	65.81 ± 15	112 ± 10	32.64	3.81

From the results (Tables 3.5 and 3.6), it is possible to conclude that the pore diameter (D_p) depends on the anodization time and the applied voltage. Thus, an increase in the anodization time results in the enhancement of the pore diameter (D_P), yet, on the other hand, the interpore distance was found to be stable in both cases. The biggest pore diameter was achieved in sample 2C (65.81 ± 15 nm) which was fabricated at 17 h by using 60 V. However, the porosity of the membrane depends on the formed porous structure; if the pore diameter is high with respect to the interpore distance, eventually, the porosity of the membrane will be higher as well. By applying 50V during anodization, a porous structure with pore diameters ranging from 43 nm to 55 nm at a time duration of 15–17 hours was obtained. For the applicability of the AAO membrane for a micro hydraulic filtration system, it needs to have relatively high porous structure, which is possible to achieve by using a high anodization voltage and a longer anodization time.

Fig. 3.10. shows the pore diameter, the interpore distance, and the porosity of the fabricated AAO membrane samples at 50V (1A, 1B, and 1C) and 60V (2A, 2B, and 2C) at anodization times of 15 h, 16h, and 17 h. It is evident in the graph that the pore diameter is bigger in both cases: 50 V (1C, 17 h) and 60 V (2C, 17 h) than if the anodization is done for a low anodization time (15h and 16h).
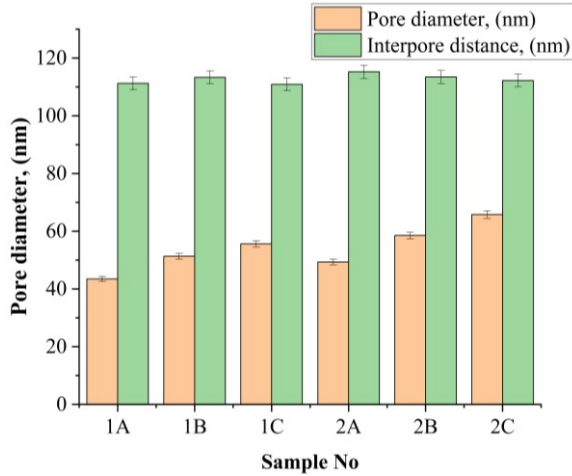
Fig. 3. 10 Pore diameter and interpore distance of the fabricated nanoporous AAO membrane
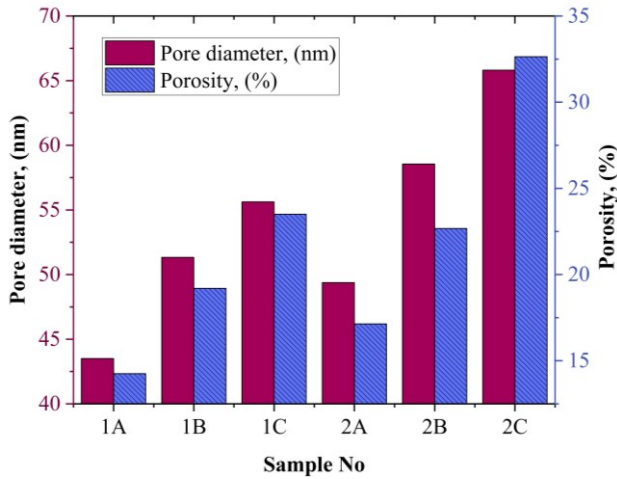
Fig. 3. 11 Pore diameter and porosity of the fabricated nanoporous AAO membrane

Fig. 3.11 shows the calculated porosity of the fabricated nanoporous AAO membrane on the basis of the pore diameter. The porosity of the fabricated AAO membrane is also increasing with an increase in the pore diameter. The porosity of the membranes fabricated at 50V and 60V ranges between 14–24% and 17–33%, respectively.

86

The SEM photo of cross-section of the fabricated nanoporous aluminum oxide membrane is shown in Fig. 3.12. The cross-section images of the fabricated nanoporous membrane at 50V (Fig. 3.12a) and 60 V (Fig. 3.12b) reveals that the formation of nanotubes perpendicular to the nanoporous structure was achieved on the surface of membrane. These nanotubes are connected throughout the upper surface of the membrane to the bottom side of the membranes.

a   b
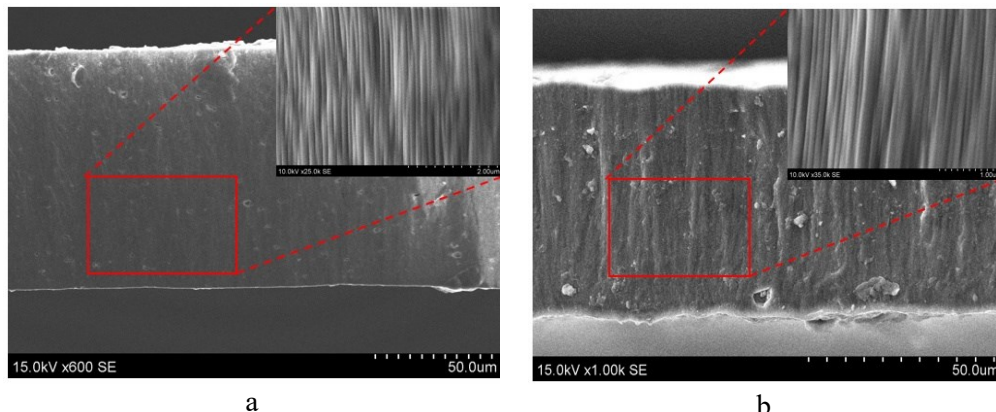
Fig. 3. 12 SEM image of AAO membrane cross-section fabricated at 50V (a), and 60 V (b)

The thickness of the fabricated nanoporous AAO membrane is analyzed from the SEM images of the cross section, and the obtained results are presented in Table 3.7.

Table 3. 7. Thickness of the fabricated nanoporous AAO membrane

Sample No.	Anodization voltage, VDC	Time of anodization, (h)	Thickness of membrane, (μm)
1A	50	15	74.50
1B	50	16	80.4
1C	50	17	83.01
2A	60	15	86.72
2B	60	16	88.6
2C	60	17	95.60

The SEM images of the cross-section of the fabricated nanoporous AAO membrane show that an increase in the voltage and time of anodization affects the formation of the porous layer. An increment in the anodization time increases the thickness of the porous alumina layer.

The effect which the annealing process on a bare aluminum plate has influence on the development of a porous structure during the anodization process is shown in Fig. 3.13. The formation of the porous structure of a membrane fabricated by using a non-annealed aluminum sheet (Fig. 3.13a) yielded a less regular arrangement of pores and a non-ordered structure of the membrane in comparison to the annealed

aluminum sheet. On the other hand, with the AAO membrane fabricated by using an annealed aluminum sheet (Fig. 3.13b), same process parameters yield a regular porous arrangement and a well-defined honeycomb structure with a pore diameter of 65 ± 10 nm, an interpore distance of 110 ± 10 nm, and 23.50% porosity.

A   b
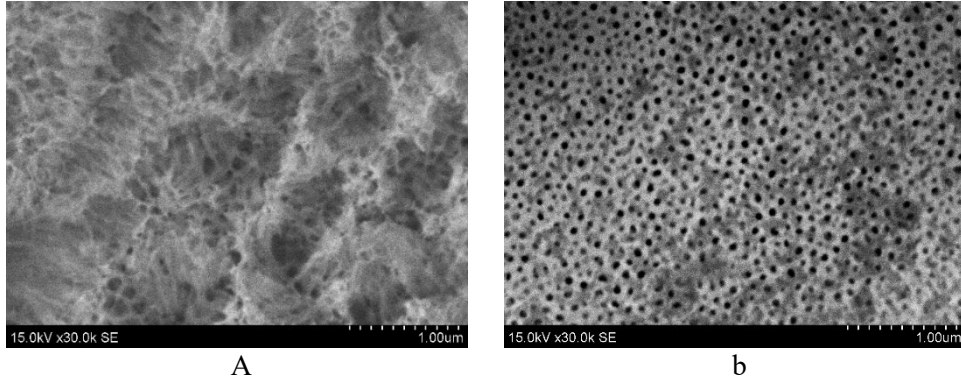
Fig. 3. 13 SEM photo of a membrane fabricated by using a non-annealed (a), and annealed (b) aluminum sheet

For the applicability of the AAO membrane for a micro hydraulic filtration system, it needs to have a relatively high porous structure, which is possible to achieve by using high anodization voltage and a longer anodization time. Also, the annealing of the aluminum plate before the anodization process helps to improve the quality of the nanoporous structure and results in an efficient anodization process.

3.3.2 Chemical Composition Analysis

Energy-dispersive X-ray spectroscopy (EDS) was done by using pulse height analysis, and the chemical composition of two AAO membranes fabricated by using different anodization voltages (50V and 60V) and an anodization time of 17 h for both nanoporous aluminum oxide membranes (1C and 2C) was investigated. The EDS spectrum and the inset elemental mapping of the nanoporous AAO membrane sample 1C fabricated at 50V for 17 h is presented in Fig. 3.14.
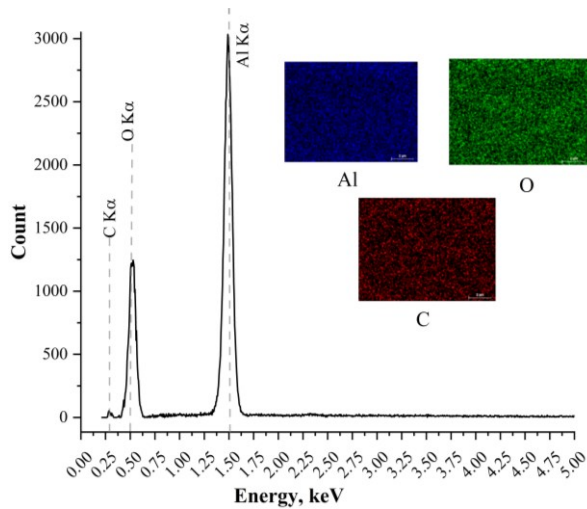
Fig. 3. 14 EDS spectra and inset elemental mapping of nanoporous AAO sample 1C

The Carbon Kα peak was registered at about 0.27 keV for sample 1C. The energy resolution of the Oxygen (O) Kα peak appeared approximately at 0.5 keV. The highest peak of Aluminum (Al) Kα was specified at an energy resolution of 1.50 keV. The elemental mapping of the distribution and the relative proportion of the chemical elements over the scanned area is presented in Table 3.8.
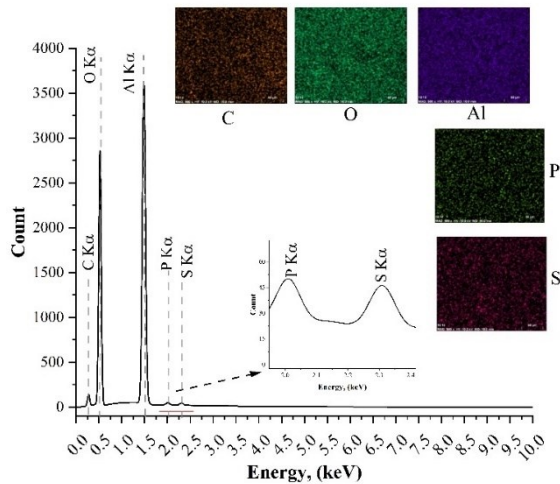
Fig. 3. 15 EDS spectra and inset elemental mapping of nanoporous AAO sample 2C

Table 3. 8. Chemical characterization of nanoporous AAO membrane sample 1C

Element	Normalized concentration (norm. wt.%)	Atomic weight percent (norm. at.%)	Error in the weight percent concentration (%)
Carbon, (C)	0.32	0.20	0.0
Oxygen, (O)	48.84	63.58	6.2
Aluminum, (Al)	50.84	36.22	2.4

Following the energy dispersive spectra with the inset elemental mapping of the fabricated nanoporous AAO membrane sample 2C in Fig. 3.15, Carbon (C) Kα registered a smaller peak at 0.27 keV. The energy resolution of the Oxygen (O) Kα peak was registered at 0.5 keV. The highest peak was registered for Aluminum (Al) at 1.5 keV, equivalent to sample 1C. Two other small peaks of energy resolution were registered in this sample for Phosphorus (P) and Sulfur (S) at 2.013 keV and 2.307 keV, respectively. A map of the distribution and relative proportion of chemical elements over the scanned area is presented in Table 3.9.

Table 3. 9. Chemical characterization of nanoporous AAO membrane sample 2C

Element	Normalized concentration (norm. wt.%)	Atomic weight percent (norm. at.%)	Error in the weight percent concentration (%)
Carbon, (C)	4.64	6.25	0.77
Oxygen, (O)	66.52	67.20	7.64
Aluminum, (Al)	43.31	25.94	1.97
Sulphur, (S)	0.55	0.27	0.054
Phosphorus, (P)	0.59	0.31	0.057

For each element in the tables, their designated position in the tables corresponds to a characteristic peak in the sample that corresponded to the transition in its electron shell. Carbon (C), oxygen (O), and aluminum (Al) were the three primary elements identified in both samples. The EDS analysis of both samples shows the dominance of aluminum oxide (Al_2O_3). The registered intensity value was strongly reliant on the excited X-Ray intensity, as well as on the efficiency of the X-Ray detector across the energy spectrum and on the geometry of the studied sample itself, among other factors.

3.3.3 Fourier-Transform Infrared Spectroscopy Analysis (FTIR)

The FTIR analysis of the fabricated nanoporous AAO membrane samples 1C and 2C was done and is presented in this chapter. The results are shown in Figs. 3.16 and 3.17 for nanoporous AAO membrane samples 1C and 2C respectively. The FTIR transmittance spectra were selected as 4000–500 cm^{-1}, as this is the typical spectrum range for this kind of analysis.
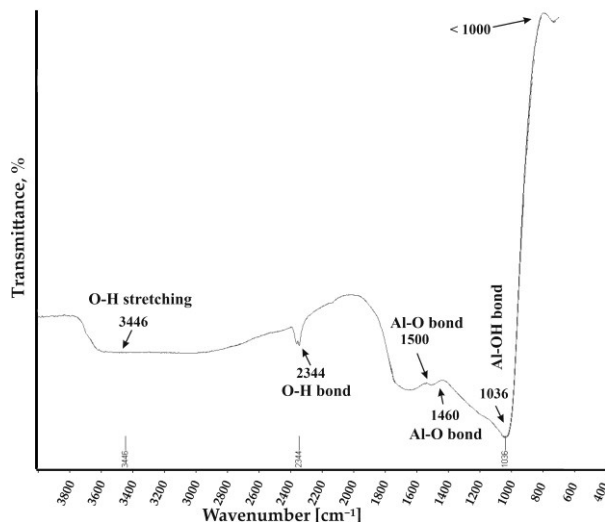
Fig. 3. 16 FTIR spectra of the fabricated nanoporous AAO membrane 1C

The FTIR spectra of sample 1C fabricated at 50V for 17 h (Fig. 3.16) strong and weak peaks were observed across the whole spectrum. Peaks at 3446 cm^{-1} show the O-H stretching due to the presence of water molecules in the structure. A small vibrational peak is visible at 2344 cm^{-1} due to the link of C-O bonding. Two small peaks were observed at 1500 cm^{-1} and 1460 cm^{-1} due to carboxyl anions and the bonding of Al-O. A major peak was observed between 1100 cm^{-1} to 800 cm^{-1} which is characteristic of the vibration of Al-OH bonding. The entire cluster of FTIR spectra is corresponds to the FTIR spectra of Al$_2$O$_3$ [163].

Similarly, the FTIR spectra of sample 2C fabricated at 60V for 17 h (Fig. 3.17) registered strong and weak peaks across the whole spectrum. The O-H stretching peak was registered at 3445 cm^{-1} due to the presence of water molecules. Other peaks were registered at 2344 cm^{-1}, 1570 cm^{-1}, 1477 cm^{-1}, 1036 cm^{-1}, and 868 cm^{-1}; they were registered for O-H bonding, Al-O bonding, and Al-OH bonding, respectively. All the observed spectra have a characteristic similar to sample 1C, and the spectra have peaks similar to those of the spectrum of AL$_2$O$_3$.
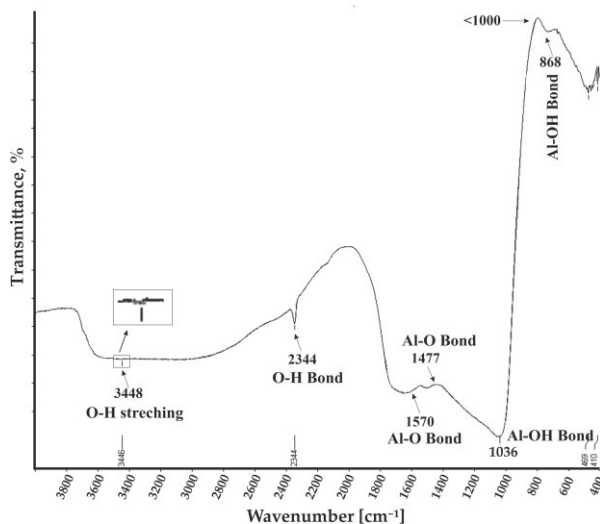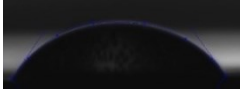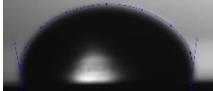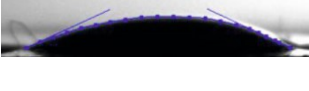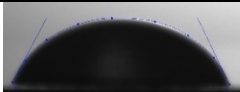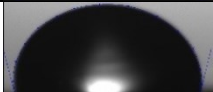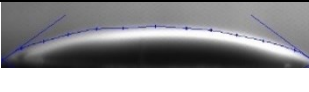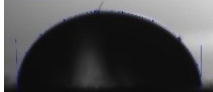
Fig. 3. 17 FTIR spectra of the fabricated nanoporous AAO membrane sample 2C

The FTIR absorption spectra of sample 2C fabricated at a constant voltage 60 VDC correspond to the FTIR spectra of aluminum oxide (Al_2O_3) [164]. From the results of the FTIR spectra of each sample (1C and 2C), it corresponds to the spectra of aluminum oxide, which confirms that the successful fabrication of the aluminum oxide membrane by using the two-step anodization method at 50V and 60V was achieved.

3.3.4 Hydrophobicity Analysis (Contact Angle Measurement)

Hydrophobicity analysis was done by using water contact angle measurement on the surface of the fabricated nanoporous AAO membrane samples (1A, 1B, 1C, 2A, 2B, and 2C). Contact angle measurement was done by using three different fluids: distilled water, glycerin, and spirit. All the measurements were done with similar measurement techniques and process parameters. The analyzed captured images with three different fluids on all the six samples are presented in Table 3.10. The images of drops of all liquids on the surface of the fabricated nanoporous AAO membrane were done by using image analysis software *ImageJ* as explained in Section 3.2. Due to the different surface properties (the pore diameter and the interpore distance), the formation of a liquid drop on the samples proceeded appeared differently, as shown in Table 3.10.

Table 3. 10. Illustration of the contact angle formed by drops of different liquids on the surface of the fabricated samples of nanoporous AAO membrane

Sample	Different fluids		
	Distilled water	Glycerin	Spirit
1A			
1B			
1C			
2A			
2B			
2C			

The measured contact angle on the surface of the fabricated nanoporous AAO membrane samples 1A, 1B, 1C, 2A, 2B, and 2C with distilled water, glycerin, and spirit are presented in Table 3.11.

Table 3. 11. Measured values of the contact angle for three different fluids

Sample No.	Distilled water, θ, deg.	Glycerin, θ, deg.	Spirit, θ, deg.
1A	$55.87 \pm 0.69º$	$98.67 \pm 0.32º$	$22.73 \pm 0.48º$
1B	$54.38 \pm 0.30º$	$64.16 \pm 0.69º$	$21.13 \pm 0.62º$
1C	$45.16 \pm 0.60º$	$63.78 \pm 0.24º$	$19.32 \pm 0.72º$
2A	$67.44 \pm 0.56º$	$104.27 \pm 0.21º$	$15.02 \pm 0.76º$
2B	$66.58 \pm 0.50º$	$97.4 \pm 0.36º$	$14.97 \pm 0.62º$
2C	$64.07 \pm 0.90º$	$86.5 \pm 0.33º$	$14.89 \pm 0.40º$

The water contact angle (θ) was tested on all the six nanoporous AAO membrane samples 1A, 1B, 1C, 2A, 2B, and 2C. Each sample of a drop was analyzed several times, and the mean values of the measured contact angle for samples 1A, 1B, 1C, 2A, 2B, and 2C are $55.87 \pm 0.69º$, 54.38 ± 0.30 º, $45.16 \pm 0.60º$, $67.44 \pm 0.56º$, $66.58 \pm 0.50º$, and $64.07 \pm 0.90º$, respectively. The graphical representation of the measured contact angle of distilled water on the fabricated nanoporous AAO surfaces is shown in Fig. 3.18.
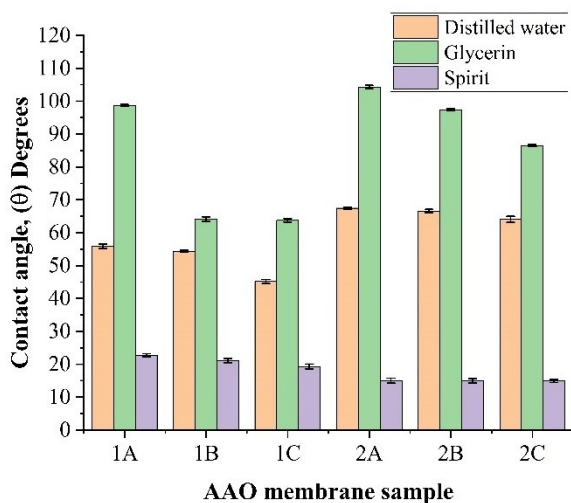
Fig. 3. 18 Measured contact angle for three different fluids on the surface of AAO membranes

From the results of the contact angle measurement, it can be observed that the fabricated nanoporous AAO membranes were found to possess hydrophilic behavior with all the samples. Samples 1A, 1B, and 1C fabricated at 15 h, 16 h, and 17 h by using 50V featured water contact angles between 45–56º. It is clear from the results that the surface of the fabricated nanoporous AAO membrane has hydrophilic behavior towards water. On the other hand, samples 2A, 2B, and 2C fabricated at 15 h, 16 h, and 17 h by using 60V had water contact angles between 64–68º. The obtained results also fell under 90º, which means that those samples also had hydrophilic behavior towards water. In both cases, it was observed that an increase in the anodization time results decreases the contact angle (i.e., an increase in the pore diameter results in a decrease in the contact angle).

The contact angle measurement for glycerin and spirit shows totally different behaviors for the two liquids. The measured contact angle of a drop of glycerin on samples 1A, 1B, and 1C are $96.67 \pm 0.32º$, $64.16 \pm 0.69º$, and $63.78 \pm 0.24º$. The surface of sample 1A had a contact angle of more than 90º, which means that it has hydrophobic behavior with glycerin, but, on the other hand, samples 1B and 1C have a contact angle of less than 90º, which means those two samples fall in the range of the hydrophilic surface. Moreover, samples 2A and 2B have contact angles $104.27 \pm 0.21º$ and $97.4 \pm 0.36º$, which is higher than 90º and which denotes hydrophobic behavior and lower wetting than sample 2C. Among the three samples, 2C had the lowest contact angle with glycerin $86.5 \pm 0.33º$, which falls in the range of hydrophilic behavior with glycerin.

The contact angle of a spirit drop on the surface of fabricated nanoporous AAO membrane samples 1A, 1B, 1C, 2A, 2B, and 2C are $22.73 \pm 0.48º$, 21.13 ± 0.62 º, $19.32 \pm 0.70º$, $15.02 \pm 0.76º$, $14.97 \pm 0.62º$, and $14.89 \pm 0.40º$, respectively.

94

All the samples had hydrophilic behavior with a drop of spirit. This is due to the fact that the density of spirit is lower than that of distilled water and glycerin.

In order to understand the wetting phenomenon of the fabricated nanoporous AAO membrane, a study of the water contact angle was performed based on time dependence. The images of a water droplet on the surface of nanoporous AAO membrane samples (1A, 1B, 1C, 2A, 2B, and 2C) surfaces were captured at different time intervals. Then, the images were analyzed by using the same method and image analysis software for the reduction in the contact angle with respect to time. The evaluated water contact angle for different time intervals on the surface of the AAO membrane sample is plotted in Fig. 3.19.
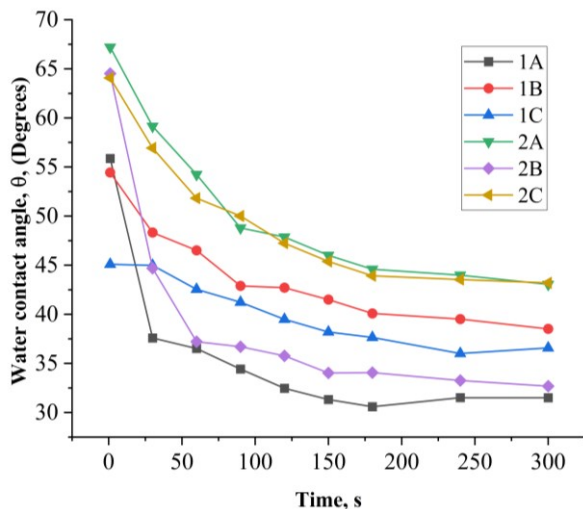
Fig. 3. 19 Time dependence study of the water contact angle on the surface of the fabricated samples of nanoporous AAO membrane

Analysis of the water contact angle based on time dependency was done from 1 s to 300 s with the time interval of 30 s for each measurement for all the samples of the fabricated nanoporous AAO membrane. For all the samples, a similar effect in the reduction of the contact angle was observed, as shown in Fig. 3.19. Initially, after 30 s from dispensing the drop onto the surface of the AAO membrane, for all the samples, a significant decrement in the contact angle was observed for samples 1A, 1B, 1C, 2A, 2B, and 2C, specifically, 18.29º, 6.12º, 0.11º, 8.05º, 19.83º, and 7.14º, respectively. Moreover, a similar contact angle decrement of about 2–4º was observed for all the samples after 30 s during the interval segment till 150 s. During the time interval segment of 150–300 sec, the water contact angles for all the samples were found to be relatively more stable than within the interval segment of 1–150 s. There was only a change of 1º in the contact angle observed for all the samples as shown in Fig. 3.19.

From the result of the time dependence study, it is possible to conclude that a drop of water is shipped in the nanoporous AAO membrane with respect to time.

Due to the shipping of the water droplet into nanopores, a decrement in the water contact angle is observed.

Similarly, a time-dependent study of the contact angle was performed for glycerin with all the nanoporous AAO membrane samples (1A, 1B, 1C, 2A, 2B, and 2C). The decrement in the contact angle was observed similarly to that of the water contact angle during the initial time interval, while, afterwards, it was found to be stable.

The studies of Zisman show a relationship between the contact angle's cosine and the surface tension of a specific liquid. It is known as the critical surface tension (σ_{cri}) if the surface tension can be extrapolated to $\cos(\theta) = 1$ (i.e., the contact angle is 0°). In order to determine the critical surface tension of the fabricated nanoporous AAO membrane, a Zisman plot was devised, as shown in Fig. 3.20.
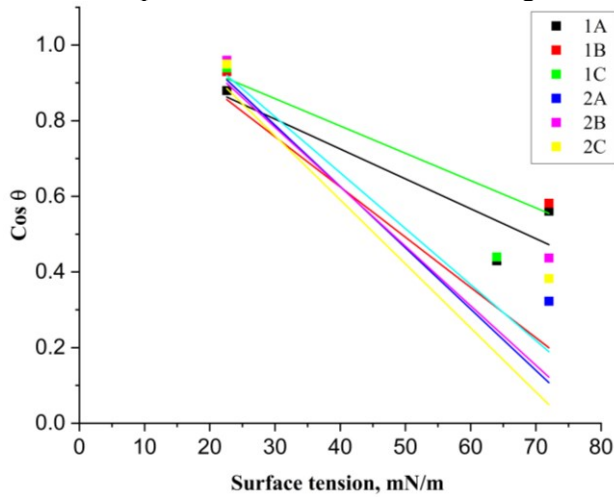
Fig. 3. 20 Determination of the critical surface tension of the fabricated nanoporous AAO membrane samples by using the Zisman method

The results sourced from the determination of the Zisman plot (Fig. 3.20) imply that the critical surface tension for sample 1A is σ_{cri} = 12.03 mN/m, for 1B σ_{cri} = 5.9 mN/m, for 1C σ_{cri} = 11.5 mN/m, for 2A σ_{cri} = 16.03 mN/m, for 2B σ_{cri} = 16.50 mN/m, and for 2C σ_{cri} = 17.30 mN/m. The obtained results are commonly referred to as the surface free energy of a solid substrate. This means that these results represent the surface free energy of the fabricated nanoporous AAO membrane. The critical surface tension of the fabricated nanoporous AAO membranes is presented in Table 3.12.

Table 3. 12. Critical surface tension of fabricated nanoporous AAO membranes

Sample No.	1A	1B	1C	2A	2B	2C
Critical surface tension, σ_{cri}, mN/m	12.03	5.9	11.5	16.03	16.50	17.30

The contact angle of any liquid always depends on the materials and its chemical nature. There is a clear correlation between the quantity and the kind of interphase sites, the surface texture, and the surface roughness of the fabricated nanoporous AAO membranes. From the results of wetting and the time dependency, it could be possible to conclude that these types of nanoporous AAO membranes are viable candidates for application in microhydraulic devices for filtration and separation purposes.

3.4 Chapter Conclusions

The following conclusions were made from the employed methods for the characterization of the researched samples: SEM analysis, EDS analysis, and FTIR analysis of the fabricated nanoporous AAO membranes. Analysis of the effect of the anodization time and voltage on the formation of the structure of nanopores was performed. The influence of the annealing of an aluminum plate before the anodization process for the fabrication of a nanoporous AAO membrane was investigated. The hydrophobicity and wetting analysis of the fabricated nanoporous AAO membranes by using contact angle measurement was conducted.

1. For the geometrical analysis of the fabricated nanoporous AAO membranes, scanning electron microscopy (SEM) revealed a honeycomb structure formed with a pore diameter from 43 nm to 85 nm by using 50V and 60V DC supply and 15h, 16h, and 17h of anodization time.

2. The effect of the anodization parameters was analyzed based on the SEM analysis. The SEM results of the fabricated nanoporous AAO membrane show that the increment in the anodization time and the applied voltage results in an increment in the pore diameter and the thickness of the AAO membrane. However, the interpore distance is not affected by these process parameters. It makes the fabrication process feasible, and it is possible to obtain a membrane suitable for application in microhydraulic devices for the filtration of micro-nano particles.

3. The chemical composition analysis of the fabricated nanoporous alumina membranes by using EDS analysis showed the dominance of aluminum oxide (Al_2O_3). The fabricated nanoporous AAO membranes were composed of two major chemical components: Aluminum (Al) and Oxygen (O). However, small quantities of Phosphorus (P) and Sulphur (S) were also observed in the samples fabricated by using 60V anodization voltage.

4. The FTIR analysis of the fabricated nanoporous AAO membrane showed strong and weak transmittance spectra from 4000–500 cm^{-1}. The cluster of the entire FTIR spectra corresponds to Al_2O_3.

5. Hydrophobicity measurement of the fabricated nanoporous AAO membranes obtained the water contact angles (θ) ranging from 55º to 67º. This means that the surface of the fabricated nanoporous AAO membranes is hydrophilic. The time dependence study showed a decrement in the contact angle (which means that a drop of water is shipped into the nanopores of AAO membranes). These

properties of the fabricated nanoporous membranes make them suitable for application in microhydraulic devices for filtration and separation.

IV. Mechanical Characteristics and Resonance Frequency Analysis

Mechanical characterization of the fabricated nanoporous aluminum oxide membranes is most important for their application in microhydraulic systems for the filtration and separation of nanoparticles. The fabricated nanoporous AAO membranes shall be used for filtration and separation for microhydraulic devices by employing acoustophoresis manipulation of particles while employing a piezoelectric (PZT) actuator. Thus, resonance frequencies shall be analyzed within a different frequency range while using a PZT ring type actuator with a fabricated nanoporous AAO membrane.

This chapter contains analysis of the hardness and elastic modulus of the fabricated nanoporous AAO membranes by using the micro indentation test at different loading conditions. Later, resonance frequencies shall be evaluated for a ring type piezoelectric actuator attached to a fabricated nanoporous AAO membrane. A different mode of vibrations was achieved by using COMSOL Multiphysics and experimentally verified by adopting non-destructive testing methods, a 3D scanning vibrometer, and a holographic PRISM system.

4.1 Micro Indentation Test of Fabricated Nanoporous AAO Membranes

Micro indentation is a measurement technique for the mechanical characterization of the properties of any thin-layered materials, including hardness and the elastic modulus. The micro indentation test works on the depth sensing indentation, in which, the indenter is continuously penetrated into the surface of the sample, and the indenter's load and the displacement into the sample are measured. During the loading and displacement into the solid surface, continuous recording of the entire measurement was done by using a micro-indentation software program from CSM Micro-indentation. This measurement provides the load-vs.-displacement curve, and, from the curve, hardness and the elastic modulus for the AAO samples was calculated.

The micro indentation test for the samples of the fabricated nanoporous AAO membranes (1A, 1B, 1C, 2A, 2B, and 2C) was performed by using *Micro-Combi*, *CSM Instruments*, Peseaux, Switzerland. The experimental setup of micro indentation is presented in Fig. 4.1. The measured results are recorded and presented by micro indentation software in the form of a graph.

The experimental setup for the micro indentation test of the fabricated nanoporous AAO membrane samples consists of: a nanoporous AAO membrane (1), a sample holding table (2), a movable platform for up-and-down movement of the sample (3), an indentation tip (4), a microscope probe (5) for capturing the indentation mark, a motor guide for moving the platform to the left or right (6), a motor guide for moving the platform forward or backwards (7), and a computer system with indentation software (8) for continuous collection of the measured data.
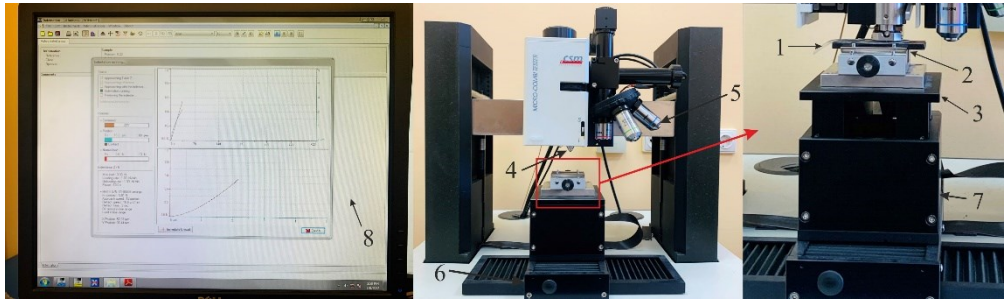
Fig. 4. 1 Experimental setup for the micro indentation test of the fabricated nanoporous AAO membranes: nanoporous AAO membrane (1), sample holding table (2), platform for up-and-down movement of the sample (3), indentation tip (4), microscope probe (5), motor for moving the platform to the left or right (6), motor guide for moving the platform forward or backwards (7), a computer system with indentation software (8)

The technical specifications of the Micro indentation CSM micro combi testing machine are presented in Table 4.1.

Table 4. 1. Technical specifications of the Micro-combi micro hardness testing machine

Max. load range	0.03 to 10 N
Load resolution	0.3 mN
Max. load	30 N
Min. load	10 mN
Loading rate	Up to 300 N/min
Contact force hold time	Unlimited
Max. indentation depth	200 µm
Depth resolution	0.3 nm
Max. indented range	1 mm
Max. sample size (X, Y, Z)	230 × 580 × 120 mm
Usable area of analysis (X and Y)	70 × 20 mm

A graphical representation of the indentation parameters and a schematic representation of the contact between the indenter and the sample are shown in Fig. 4.2 and Fig. 4.3.
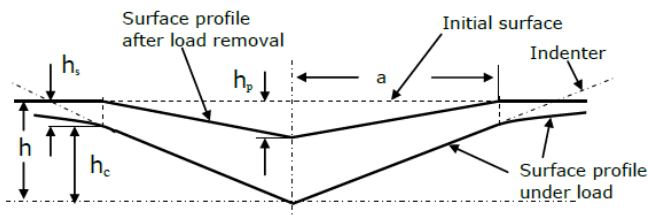
Fig. 4. 2 Schematic representation of the contact between the indenter and the sample

100
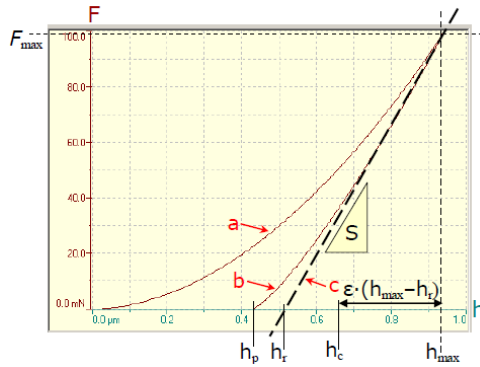
Fig. 4. 3 Indentation parameters for the micro indentation test

The indentation parameters shown in Fig. 4.3 are as follows: a represents the applied force, b – curve during unloading, c – tangent to the unloading curve at F_{max}, F – applied force, F_{max} – max. test force, h_p – permanent depth of indentation, h_r – tangent indentation depth, h_c – contact depth of the indenter with the sample at F_{max}, h_{max} – maximum indentation depth, S – contact stiffness, and ε – geometric constant.

By using the approach of Olive and Pharr, a nanoporous AAO membrane was subjected to the micro-indentation test for mechanical characterization. The power law method acknowledges that the initial portion of the unloading curve may not be linear and can be represented by a simple power law relationship:

$$F = k \, (h - h_p)^m \tag{4.1}$$

If the indenter is made of diamond, the value of *m* is 2.0, which means that *k* is constant and *m* is an exponent that depends on the geometry of the indenter.

The power law function to describe the upper part of the unloading data can be described by using Formula 4.2 [165]:

$$F = F_{max} \left(\frac{h - h_p}{h_{max} - h_p} \right)^m \tag{4.2}$$

Here, *m* is constant 2.0, and h_p is described by determining the least squares fitting procedure.

S(=1/C) material stiffness is given by the derivative at the peak load by using Formulas 4.3–4.5 [165].

$$S = \left(\frac{dF}{dh} \right)_{max} \tag{4.3}$$

$$= m \, F_{max} \left[\frac{(h - h_p)^{m-1}}{(h_{max} - h_p)^m} \right] \tag{4.4}$$

$$= m \, F_{max} \, (h_{max} - h_p)^{-1} \tag{4.5}$$

Calculation for S can be done by using h_r – tangent indentation depth, h_c – contact depth of the indenter with the sample at F_{max} by using Formulas 4.6 and 4.7 [165].

$$h_r = h_{max} - {^{F_{max}}}/_S \qquad (4.6)$$

$$h_c = h_{max} - \varepsilon\,(h_{max} - h_r) \qquad (4.7)$$

Here, h_r – tangent indentation depth, h_c – contact depth of the indenter with the sample at F_{max}, F_{max} – maximum force, h_{max} – maximum indentation depth, S – contact stiffness, and ε – geometric constant (0.7268) for the cone type indenter shape.

The determination of hardness and Young's modulus, Vickers hardness HV can be determined by the maximum applied force F_{max} by the indenter on the AAO membrane sample; it can be estimated by using Formulas 4.8 and 4.9. Both faces of the square based pyramid type meet at an angle of 68° [166].

$$HV = \frac{F}{A_d} = \frac{F}{A_p}\,sin68° = \frac{2F}{D^2}\,sin68° \qquad (4.8)$$

$$HV = 1.8544 \cdot \frac{F}{D^2} \qquad (4.9)$$

Here, A_d is the developed contact area of the indenter, A_p is the projected contact area, F is the applied force, and D is the diagonal corresponding area under the applied force.

Since hardness is determined in terms of the anticipated contact area under load, it may not be identical to the 'conventional' hardness. The elastic recovery is significant during unloading. Formula 4.10 establishes a relationship between the elastic modulus and the contact area; it measures unloading stiffness [166].

$$E_r = \frac{\sqrt{\pi}\,S}{2\,\beta\sqrt{A_p\,(h_c)}} \qquad (4.10)$$

Here, β – Geometric factor for the diamond shape indenter (1.012), E_r – reduced elastic modulus, A_p is the projected contact area, and h_c – contact depth of the indenter with the sample at $F_{max.}$

The fact that elastic displacements occurs in both the sample and the indenter is taken into consideration when calculating the reduced elastic modulus. Hence, the plane strain modulus can be determined by using Formula 4.11 [165].

$$E^* = \frac{1}{\frac{1}{E_r} - \frac{1-v_i^2}{E_i}} \qquad (4.11)$$

Here, E_r – reduced elastic modulus, v_i – Poisson's ratio of the indenter tip (0.07) and E_i – elastic modulus of the indenter (1141 GPa).

By using the plain strain modulus and Poisson's ration of a nanoporous AAO sample (0.22), the calculation for the elastic modulus is possible by using Formula 4.12 [166].

$$E_{IT} = E^* (1 - v_s{}^2)$$ (4.12)

Here, v_s – Poisson's ratio of the nanoporous AAO membrane (0.22) [166].

The analysis of the hardness and elastic modulus of the samples of the fabricated nanoporous AAO membranes (1A, 1B, 1C, 2A, 2B, and 2C) was done at three different loading conditions until the values became stable. The samples for measurement are shown in Fig. 4.4.

1A   1B   1C

2A   2B   2C
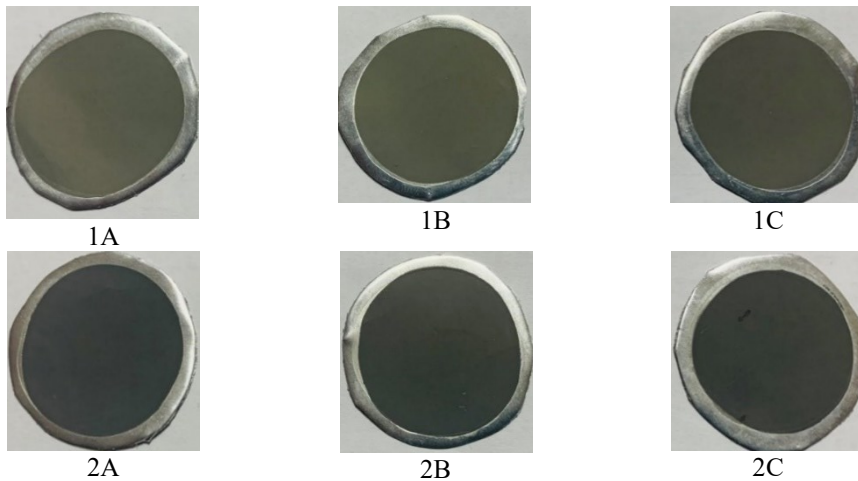
Fig. 4. 4 Nanoporous AAO membranes for hardness and elastic modulus measurement using the micro indentation test

The samples of nanoporous AAO membranes used for micro hardness testing were prepared by using the two-step anodization method described in Chapter 3. The characteristics of the samples of the fabricated nanoporous AAO membranes (the pore diameter, porosity, and thickness) 1A, 1B, 1C, 2A, 2B, and 2C are shown in Table 4.2.

Table 4. 2. Characteristics of the fabricated nanoporous AAO membranes for micro indentation

Sample no	Pore diameter, D_p, (nm)	Porosity, (%)	Thickness of membrane, (μm)
1A	43.5 ± 10	14.25	74.50
1B	51.33 ± 8	19.20	80.4
1C	55.62 ± 10	23.50	83.01
2A	49.38 ± 6	17.40	86.72
2B	58.55 ± 5	22.67	88.60
2C	65.81 ± 15	32.64	95.60

Vickers indentations diamond tips were employed under the following conditions: at an angle of 136°, and 68° angle between the diamond pyramid's axis and its three sides, an area of (A_d) 26.43 mm of contact, and an area of (A_p) 24.54 mm of the projected contact perpendicular to the surface of nanoporous alumina. Five indentations with a distance of 1 mm between the neighboring indentation sites were performed under various loading conditions. For the tests, three distinct loading conditions (0.25 N, 0.5 N, and 1N) were used, as well as a continuous loading and unloading rate of 1 N/min and a 10-second rest period. They were subjected to a steady escalation and a constant loading rate until a predetermined load was reached, which was then maintained for 10 seconds before gradually discharging at a constant rate. Loading and unloading hysteresis data was collected, while the applied load and penetration depth were being monitored. According to this method, the hardness of a material can be determined.

The hysteresis loop of the applied load and the penetration depth increases proportionally with an increase in the applied load. The mechanical properties of nanoporous alumina membranes highly depend on the geometry of the pores, the loading condition, and the thickness of the membrane [167].

4.2 Results of the Micro Indentation Test of Fabricated Nanoporous AAO Membranes

The mechanical characteristics 'hardness' and 'elastic modulus' of the fabricated samples of nanoporous AAO membranes 1A, 1B, 1C, 2A, 2B, and 2C were analyzed by using a micro indentation diamond tip indenter. Samples 1A, 1B, and 1C were fabricated at 50 V DC anodization voltage, and the time of anodization was 15h, 16h, and 17h, respectively. On the other hand, samples 2A, 2B, and 2C were fabricated at 60 V DC anodization voltage, whereas the time of anodization was 15h, 16h, and 17h, respectively. The hysteresis loop curve of the applied load and the penetration depth for all the samples were recorded for three different loading conditions 0.25 N, 0.5 N, and 1N, as shown in Fig. 4.5.

The data from the micro indentation test was recorded and then plotted as applied vs. the penetration depth curves for samples 1A, 1B, and 1C. The typical load-penetration depth hysteresis loop consists of the loading, holding, and unloading sections. During loading, nanoporous AAO membranes (all the three samples) experience elastic and inelastic deformation, whereas, during unloading, this material only experiences elastic behaviors. From the hysteresis loop of samples 1A, 1B, and 1C, relevant observations were made.
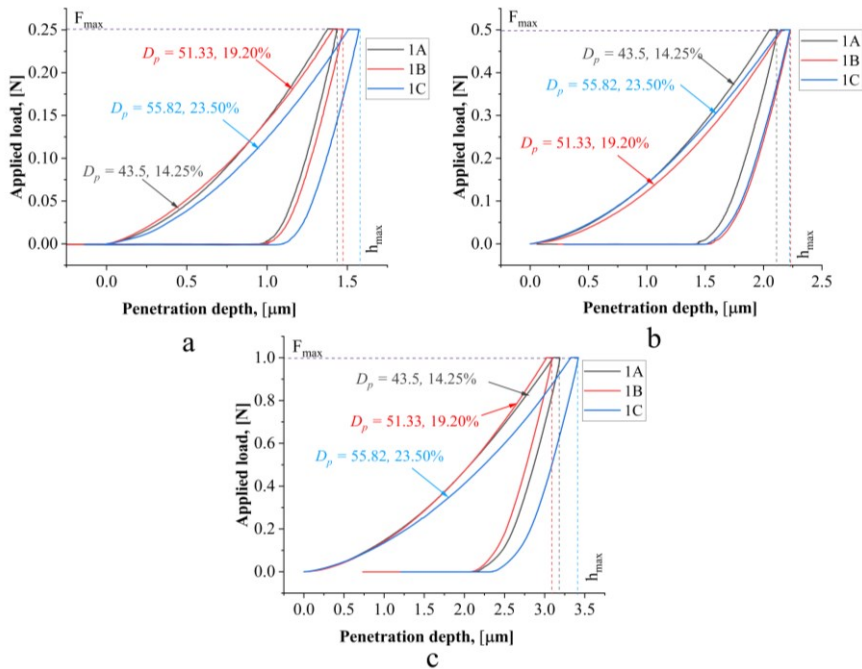
Fig. 4. 5 Load-displacement plots of AAO membranes 1A, 1B, 1C fabricated at 50V DC at loads 0.25 N (a), 0.5 N (b), and 1 N (C)

Firstly, as clearly shown in Figs. 4.5a, 4.5b, and 4.5c, the hysteresis loops for all the three samples (1A, 1B, and 1C) are different due to the different porosity of the AAO membranes. The membrane denoted by high porosity experienced more penetration depth than the membrane with a lower porosity under a similar loading condition (0.25N). This trend indicates that an increase in porosity decreases the hardness of the AAO membrane. Similar effects were observed for the loading and unloading hysteresis loop for the researched loading conditions (0.5 N and 1N). Moreover, an increase in the penetration depth affects the hardness of the AAO membrane, which results in a decrease in hardness.

Secondly, a minor difference was observed in the penetration depth when using the same loading conditions for all the three samples (i.e., the indenter did not penetrate the nanoporous AAO sample 1A as much as samples 1B and 1C). These results suggest that the nanoporous AAO membrane of sample 1A appears to withstand the state of deformation; this behavior is ascribed to the difference in the pore diameter which was achieved by using different fabrication parameters during the anodization process.
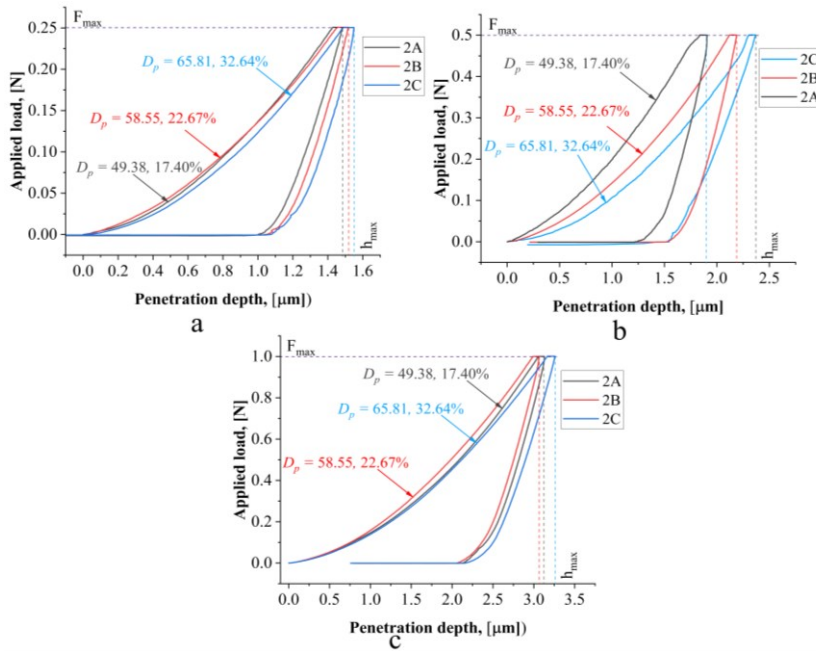
Fig. 4. 6 Load-displacement plots of AAO membranes 2A, 2B, 2C fabricated at 60V DC at loads 0.25 N (a), 0.5 N (b), and 1 N (C)

The data of the penetration depth achieved during micro indentation for samples 1A, 1B, and 1C at three different loads 0.25 N, 0.5 N, and 1 N is presented in Table 4.3.

The micro indentation data recorded for samples 2A, 2B, and 2C in the form of a hysteresis loop of 0.25 N, 0.5 N, and 1 N applied loads – the penetration depth is shown in Fig. 4.6. The hysteresis loop of the applied load vs. the penetration depth of the samples fabricated at 60 V DC is different during the loading and unloading behavior with a porosity of 17.40% (2A), 22.37% (2B), and 32.64% (2C). Each curve consists of the loading, holding, and unloading processes.

Table 4. 3. Penetration depth for nanoporous AAO samples at 0.25 N, 0.5 N, and 1 N

Sample No.	Maximum penetration depth [μm] at load		
	0.25 N	0.5 N	1 N
1A	1.36	2.10	3.18
1B	1.48	2.20	3.12
1C	1.57	2.24	3.43
2A	1.47	1.90	3.10
2B	1.52	2.20	3.07
2C	1.56	2.38	3.27

106

First, as clearly shown in Fig. 4.6, the indentation depth for the samples (2A, 2B, and 2C) is higher than for samples (1A, 1B, and 1C) at similar loading because of the high porosity of the nanoporous AAO membranes in comparison to the membranes fabricated at 50V DC. There is a slight disturbance observed in the hysteresis loop because of a micro crack or a collapse of nanopores during the load application. Moreover, these defects in the hysteresis loop may have originated due to the presence of moisture in porous structures; a similar effect was observed in another study [167]. This observation was made for each loading condition during the indentation, and the values of the penetration depth are presented in Table 4.3.
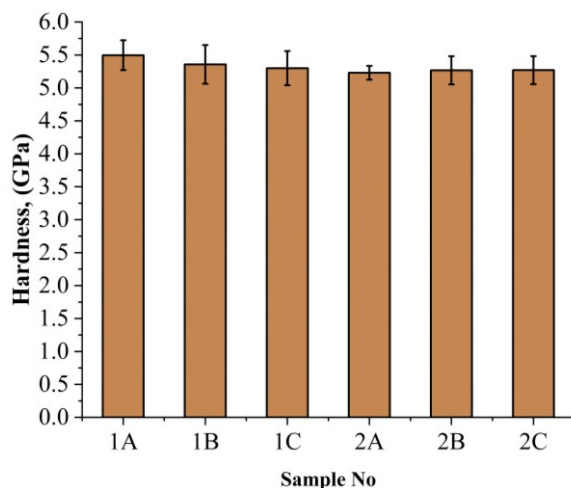
Fig. 4. 7 Hardness of the fabricated samples of nanoporous AAO membranes

The measured values of the hardness of the fabricated samples of nanoporous AAO membranes (1A, 1B, 1C, 2A, 2B, and 2C) are plotted in Fig. 4.7. There are two regions that can be highlighted in terms of the hardness dependence over the load and the depth of the indenter. Firstly, at a lower load of 0.25 N, the penetration depth of the indenter was up to 1.57 μm, and there was no significant difference observed in the hardness of all the six AAO membranes. The hardness values of AAO membranes 1A, 1B, 1C, 2A, 2B, and 2C are 5.49 GPa, 5.35 GPa, 5.30 GPa, 5.23 GPa, 5.26 GPa, and 5.27 GPa, respectively. The slow decrement in the hardness of AAO membranes 1A, 1B, and 1C was observed by the increase in the pore diameter and the increase in the indentation depth. Similarly, for AAO membrane samples 2A, 2B, and 2C, an insignificant decrement was observed in terms of hardness.

The hardness of samples (2A, 2B, and 2C) was observed to be lower than that of samples (1A, 1B, and 1C); this is due to an increase in the pore diameter and the porosity of the fabricated nanoporous AAO membranes. The average results of the hardness and the elastic modulus calculated from the indentation data for nanoporous AAO samples are presented in Table 4.4. Also, from Fig. 4.7, it can be

observe that the highest hardness was achieved with a lower pore diameter (as calculated from the indentation data).

Table 4. 4. Hardness and elastic modulus for nanoporous AAO samples

Sample No.	Hardness, H, (GPa)	Elastic modulus, E, (GPa)
1A	5.49 ± 0.22	128.91 ± 4.67
1B	5.35 ± 0.29	126.58 ± 5.32
1C	5.30 ± 0.29	124.26 ± 4.39
2A	5.23 ± 0.10	126.16 ±2.97
2B	5.26 ± 0.43	126.26 ± 5.84
2C	5.27 ± 0.47	127.87 ± 6.40

It was determined that the hardness of the tested AAO membranes decreased significantly when the load was increased by about two times until reaching the threshold of 0.25 N. This means that the indentation depth is increasing, and, as a result, a larger area of the contact between the indenter and the AAO membrane test material is forming, and the AAO membrane hardness is decreasing as a result. Oxide material is denoted by a highly porous and fragile structure, which may explain this behavior. When the indenter tip penetrates into the material, it causes cracks to form in the lower layers.

In contrast, when the penetration depth and the load increase, the hardness of the AAO membrane samples 1A, 1C, and 2A begins to remain constant, which partially reflects the mechanical properties of a crushed oxide material. The porous structure of the AAO membrane is expected to result in a deformation mechanism through the crushed pores, while a bigger barrier may partially relieve the crushed pores under the indenter's tip.

Moreover, an increase in the penetration depths gives nearly stable values of the hardness of the samples of AAO membranes, but, in the cases of samples with a high pore diameter, these samples experience a slightly higher decrement in hardness at high loadings. This phenomenon stems from the fact that the indenter's tip is approaching the backing aluminum layer, and it results in a lower hardness of the AAO membrane.
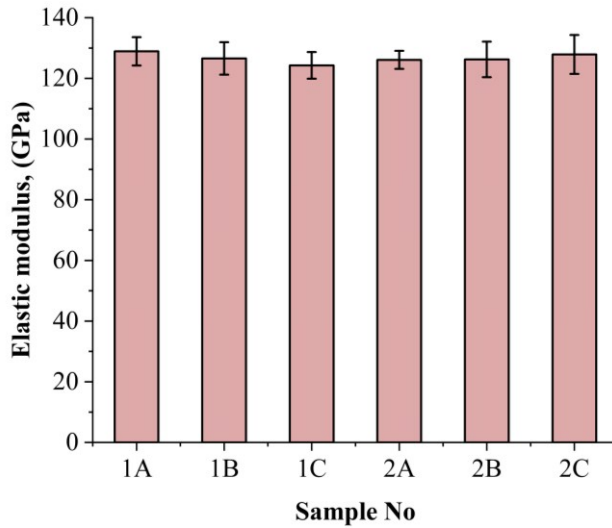
Fig. 4. 8 Elastic modulus of the fabricated samples of nanoporous AAO membranes

The elastic modulus of the fabricated samples of nanoporous AAO membranes 1A, 1B, 1C, 2A, 2B, and 2C are calculated from the indentation data and presented in Fig. 4.8 and Table 4.4. The elastic modulus of all the samples is calculated until reaching the maximum penetration depth until achieving constant values of measurement. The obtained values of the elastic modulus for AAO membrane samples 1A, 1B, 1C, 2A, 2B, and 2C are 128.91 ± 4.67 GPa, 126.58 ± 5.32 GPa, 124.26 ± 4.39 GPa, 126.10 ± 2.97 GPa, 126.26 ± 5.84 GPa, and 127.87 ± 6.40 GPa, respectively. Moreover, the values of elastic modulus are slightly lower (by about 12%) than those found in literature [168] because the average pore diameter of the fabricated AAO membrane in this study is higher. Additionally, the measured values of elastic modulus and hardness are also related with either the absorbed moisture and residual water from electrochemical anodization, or with air exposure.

4.3 Numerical and Experimental Analysis for the Mode of Vibration Forms on the Surface of the Fabricated Nanoporous AAO Membranes

Based on the findings of the literature review and the formulated objectives, the possible application of the fabricated nanoporous aluminum oxide membranes for the filtration of micro/nano particles in micro hydraulic systems for micro fluidics have to be investigated before proceeding to the subsequent steps.

Therefore, numerical modeling was conducted by using bulk acoustic wave modulation in the form of standing acoustic waves in order to identify the various mode vibrations for acoustophoresis particle separation and manipulation at the micro/nano scale dimensions. The properties of the nanoporous membranes are used according to the findings of the characteristics and the mechanical properties

evaluated in the previous chapters (porosity, thickness, hardness, and elastic modulus).

4.3.1 Numerical Simulation of the Mode of Vibrations and the Working Principle of Piezoelectric Actuator

Numerical modeling was performed to find the operating resonance frequencies and the different mode of vibrations on the surface of AAO membranes by using a cylindrical piezoelectric (PZT) actuator by using *COMSOL Multiphysics 5.4*. The model for actuation is shown in Fig. 4.9; it was designed by using *Solid Works 2019* and *COMSOL Multiphysics 5.4* to run the simulation.
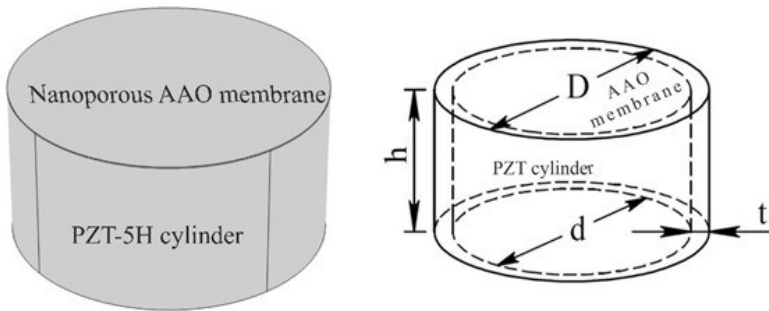
Fig. 4. 9 3D model for actuation and its parameters

The model for simulation consists of a fabricated nanoporous AAO membrane attached on the top of the ring type piezoelectric actuator (PZT-5H). The cylindrical actuator having inner diameter d = 26 mm, thickness t = 2 mm, and height h = 15mm, and an AAO membrane having diameter D = 30 mm and thickness 0.13 mm is attached on the top of the piezoelectric actuator (Fig. 4.9).

The finite element model was developed to analyze the modal frequency and the harmonic response of the PZT actuator on the surface of the AAO membrane for acoustic wave formation. The 3D model of the piezoelectric actuator is divided into 484 triangular finite elements (minimum element quality = 0.74) with a maximum of 5.74 mm^2 and a minimum of 0.0194 mm^2 as shown in Fig. 4.10a. The boundary conditions applied to the model during numerical simulation are presented in Fig. 4.10b.
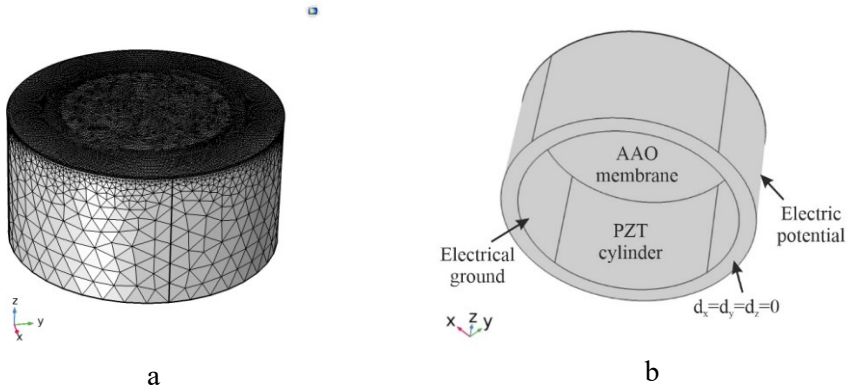
Fig. 4. 10 Finite element mesh model (a) and boundary condition (b)

The boundary condition of the analyzed model is as follows: the bottom side of the PZT-5H cylinder actuator is fixed and electrically ground. Electric potentials were applied to the wall of the cylinder which generates the piezoelectric effect and transfers it to the AAO membrane. For the numerical simulation, a solid mechanics module, an electrostatic module, and piezoelectric material multiphysics were used. The deformation of the actuator in the *X*, *Y*, and *Z* axes allows finding the resonance frequencies and the 3D model vibration modes for the model applicability for the filtration of micro/nano particles in the microhydraulic system.

The displacement field $\{u\}$ and the electrical potential $\{\varphi\}$ can be written in terms of the nodal displacement $\{u_i\}$ and the electrical potential $\{\varphi_i\}$ by using the shape function $[N_u]$ and $[N_\varphi]$ as Formulas 4.13 and 4.14 [169]:

$$\{u\} = [N_u]\{u_i\} \tag{4.13}$$

$$\{\varphi\} = [N_\varphi]\{\varphi_i\} \tag{4.14}$$

The strain vector $\{\varepsilon\}$ and the electric field $\{E\}$ are related to the displacement field $\{u\}$ and the electric potential $\{\varphi\}$ by using Formulas 4.15 and 4.16 [169].

$$\{\varepsilon\} = [D]\{u\}$$

(4.15)

$$\{E\} = [B_\varphi] - \nabla \varphi$$

(4.16)

Here, $[D]$ is the derivation operator defined as

$$\begin{bmatrix} \dfrac{\partial}{\partial x} & 0 & 0 & 0 & \dfrac{\partial}{\partial z} & \dfrac{\partial}{\partial y} \\[2mm] 0 & \dfrac{\partial}{\partial y} & 0 & \dfrac{\partial}{\partial z} & 0 & \dfrac{\partial}{\partial x} \\[2mm] 0 & 0 & \dfrac{\partial}{\partial z} & \dfrac{\partial}{\partial y} & \dfrac{\partial}{\partial x} & 0 \end{bmatrix}^{T}$$

∇ is the gradient operator. When substituting the values of $\{u\}$ and φ in the above equations, the strain and the electrical field can be expressed in relation to the displacement nodal values $\{u_i\}$ and the electrical potential $\{\varphi_i\}$:

$$\{\varepsilon\} = \ [B_u] - \{u_i\} \tag{4.17}$$

$$\{E\} = \ [B_\varphi] - \{\varphi_i\} \tag{4.18}$$

Here, $[B_u] = [D][N_u]$ and $[B_\varphi] = -\nabla [N_\varphi]$

The mechanical and piezoelectric properties of all the materials used in the model are presented in Table 4.5.

Table 4. 5. Material properties of PZT-5H and AAO membrane

Material property, (Symbol)	PZT-5H [169]	AAO membrane
Density	7500 kg/m^3	3950 kg/m^3
Young's modulus	5.5×10^{10} N/m^2	127 GPa
Poisson's ratio	0.33	0.22
Coupling coefficient, (k_{33})	0.75	
Displacement coefficient, (d_{33})	650×10^{-12} m/V	
Voltage coefficient, (g_{33})	19×10^{-3} V m/N	
Mechanical Q factor	32	

112
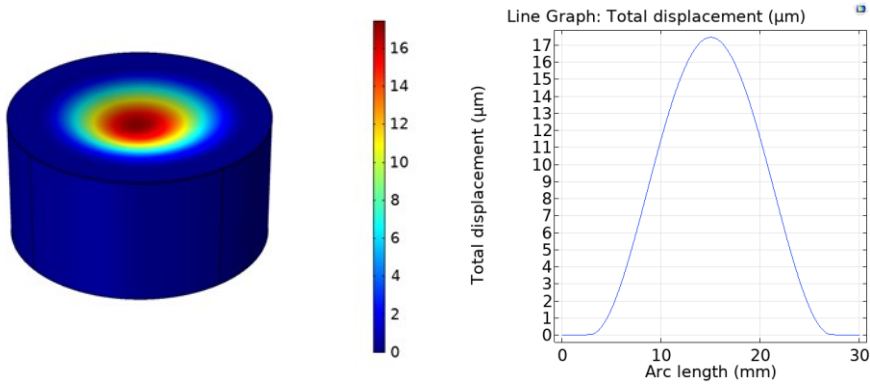
Fig. 4. 11 First mode of the vibration of AAO membrane at 3.50 kHz frequency

Fig. 4.11 displays the findings of the membrane dynamic response when actuated by a cylinder-type PZT-5H actuator at a frequency of 3.5 kHz with the application of 0.43 V of electrical potential excitation. The membrane was deformed, and the first mode of vibration was obtained. It can be seen in Fig. 4.11 that the membrane oscillates in half mode, and that its geometry is displaced, with most of the deformation occurring in the core of the AAO membrane with the total displacement of 17 µm.

The second mode of the system is achieved at a frequency of 4.94 kHz at an electrocortical potential of 1 V, as shown in Fig. 4.12. There are two halves of the AAO membrane on the surface with 180 shifts in the phase. Also, the axial displacement of the AAO membrane surface is lower than the first mode. The total displacement in the surface of the AAO membrane was achieved at 8.2 µm. The displacement of the AAO membrane surface can be seen in the graph presented in Fig. 4.12.
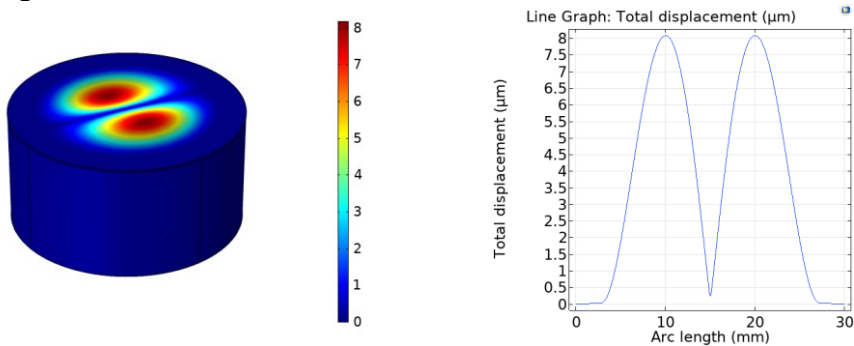
Fig. 4. 12 Second mode of the vibration of AAO membrane at 4.94 kHz frequency

In the third mode (Fig. 4.13), the surface of the AAO membrane is divided in four quadrants at a frequency of 7.89 kHz. Also, the displacement of the AAO membrane is lower than first and second mode 4.5 μm.
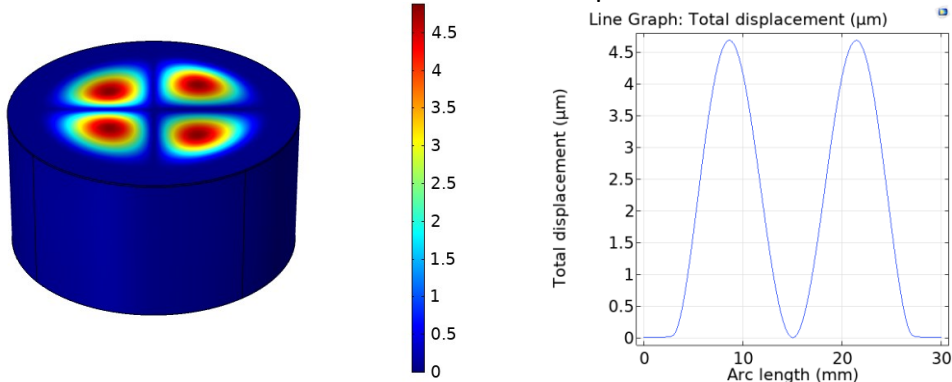
Fig. 4. 13 Third mode of the vibration of AAO membrane at 7.89 kHz frequency

Based on the simulation results, it is evident how the oscillation of the AAO membrane changes with an increase in the driving frequency. The values of the surface displacement decrease with the increase in the driving frequency. The level of the displacement of the surface of the AAO membrane decreases from first mode; specifically, the values for the first mode, the second mode, and the third mode are 17 μm, 8 μm, and 4.5 μm, respectively.

4.3.2 Experimental Analysis of the Mode of Vibrations and the Working Principle of a Piezoelectric Actuator

In order to study the proposed theory, the validation of the operating principle of the piezo actuator (PZT-5H) was required; with the objective to verify the vibration modes and the operating resonance frequencies, an experiment was performed by using nondestructive testing equipment: holographic interferometry (PRISM system) and a 3D scanning vibrometer (*Polytec*). The piezo transducer was actuated within the range from 3.8 kHz to 10 kHz for the validation of the simulation results. The experimental setup of the non-destructive holographic interferometry PRISM system is shown in Fig. 4.14.

a

b
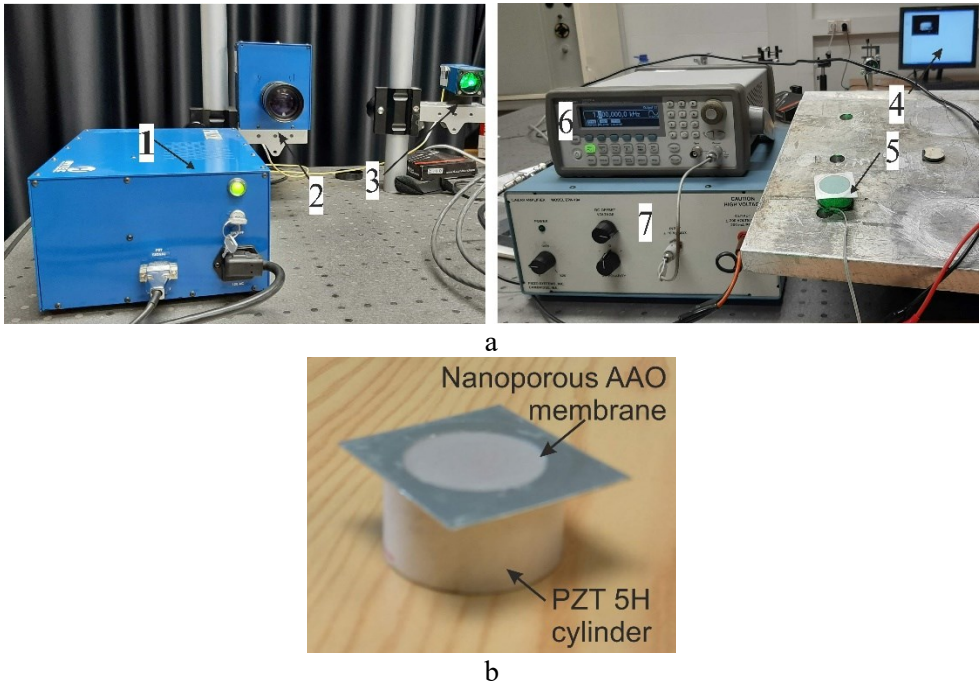
Fig. 4. 14 Experimental setup of the holographic PRISM system (a) and the prototype model (b)

The experimental setup of the holographic interferometry PRISM system consists of a control block (1), a video head (2), an illumination beam head (3), a computer system (4), a nanoporous AAO membrane mount on the PZT actuator (5), a signal generator (*Agilent Technologies, Inc*, Loveland, Colorado, USA) (6), and a linear voltage amplifier (*FLC P200*, from *FLC Electronics AB*, Sweden), and a prototype model of a nanoporous AAO membrane attached onto a PZT-5H cylinder. The prototype model consisted of a piezoelectric 5H cylinder (outer diameter 30 mm, wall thickness 2 mm, and height 15 mm) with an attached fabricated nanoporous AAO membrane (diameter of the membrane 30 mm, membrane thickness 0.13 mm) on top of the PZT-5H cylinder. A schematic illustration of the working scheme and the principle of operation is shown in Fig. 4.15. The main characteristics of the PRISM system are outlined in Table 4.6.

Table 4. 6. Technical specification of holographic PRISM system

Measurement sensitivity	< 20 nm
Dynamic measurement boundary	100 μm
Measurement boundary	> 100 μm
Measurement area	Max. 1 m diameter
Distance to object	>1/4 m
Data registration frequency	30 Hz
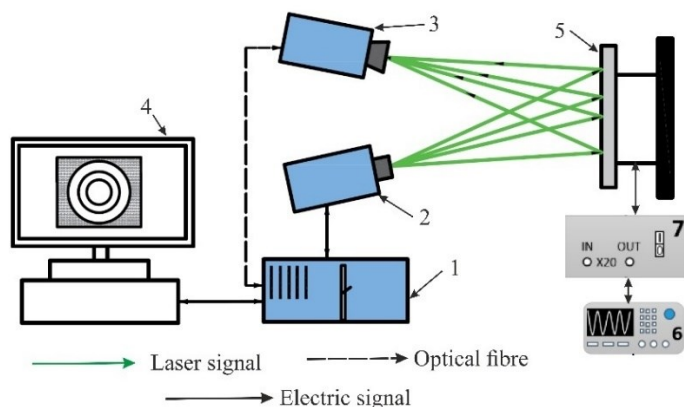
Fig. 4. 15 Schematic illustration of the PRISM system: control block (1), video head (2), illumination beam head (3), computer system (4), nanoporous AAO membrane mount on PZT actuator (5), signal generator *UNI-T UTG2025A* (6), voltage amplifier *FLC A400*

Fig. 4.15 depicts the experimental setup for actuating the AAO membrane by using the holographic interferometry PRISM system. A two-beam speckle pattern interferometer using a green laser (532 nm wavelength, 20 mV power) was employed. The actuating membrane is illuminated by two beams: an object beam and a reference beam, both of which are recorded with a camera. The object scatters laser light, which the camera lens collects and uses to generate an image of the object on the CCD camera sensors. To analyze the image of the object, a programme called *PRISM DAQ* (*Hy-Tech Forming Systems* (USA), Phoenix, AZ, USA) is used to send the image from the camera to the computer system. On the computer screen, the AAO membrane's dynamic response is shown at different frequencies.

The obtained results from the holographic interferometry for the determination of the working and resonant frequency of the system with the nanoporous AAO membrane actuated by using a piezoelectric transducer are shown in Fig. 4.16.

The results of the deformation of the membrane at different frequencies are presented in Fig. 4.16. The first mode (Fig. 4.16a) was obtained at 3.80 kHz frequency at a voltage of 0.43 V. It has similar deformation to that achieved during the simulation at a frequency of 3.50 kHz. There is an error of 8.2% between the simulation and the experimental results for the first mode.

The second mode (Fig. 4.16b) was obtained at a frequency of 5.18 kHz at a voltage of 0.44 V and 4.94 kHz at a voltage of 1 V, respectively, with an error of 4.7% between the simulation and the experimental results. Meanwhile, the third mode (Fig. 4.16c) for the fabricated nanoporous AAO membrane was achieved at a frequency of 8.06 kHz at 2.12 V, and, during the simulation, a similar mode of vibration was achieved at a frequency of 7.89 kHz at 2 V with 2.1% error between the experimental and the simulation results.

a   b

c
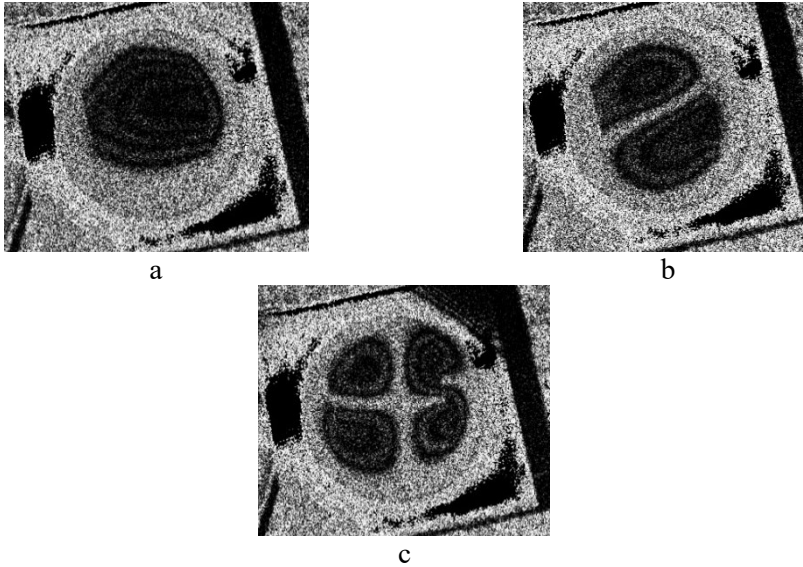
Fig. 4. 16 Vibration forms obtained by using the PRISM system: 3.80 kHz (a), 5.18 kHz (b), and 8.06 kHz (c)

In the next step, the study of vibration modes and the displacement of the fabricated nanoporous AAO membrane by using the cylinder type PZT 5H actuator were analyzed by adopting a non-destructive testing method, and a 3D scanning vibrometer (*PSV-500-3D-HV*, *Polytech*, Germany). The displacement of the surface of the AAO membrane was analyzed for signal inputs at different frequencies. Each of the forms of deformation was determined from the peak values of deformation and compared with the displacement achieved during the numerical simulation.

Fig. 4. 17 Experimental setup of the 3D scanning vibrometer for the actuation of the fabricated nanoporous membrane: cylindrical *PZT-5H* actuator (1), linear voltage amplifier (*FLC P200*) (2), 3D vibrometer *PSV-500-3D-HV* (3), a computer interface with analysis software (4), anti-vibrating table (5)

117

The experimental setup (Fig. 4.17) consisted of a cylindrical *PZT-5H* actuator, a linear voltage amplifier (*FLC P200*), a 3D vibrometer *PSV-500-3D-HV*, a computer interface with analysis software, and an anti-vibrating table. A prototype model of the piezoelectric actuator (inset of Fig. 4.17) served as a vibro-active-nano filter.

The experiment was carried out under steady settings, which means that there were no external vibrations acting on the membrane. The PZT actuator was adhesive-taped to the steel plate and positioned on the anti-vibration table. An electrode linked the *PZT 5H* cylinder type actuator to the linear voltage amplifier for voltage amplification. Points were established with the *Polytech* laser at the periphery of the AAO membrane covering the measuring geometry by using a computer system with integrated software (Fig. 4.17, computer screen). An electrical signal of 5 V caused vibrations in the actuator. Fig. 4.18 depicts a scheme of the experimental setup using the 3D scanning vibrometer.
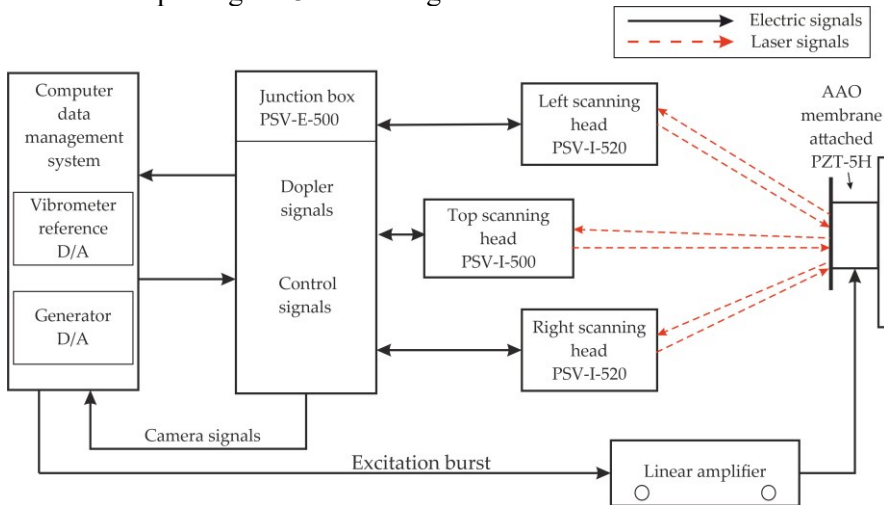
Fig. 4. 18 Schematic illustration of experimental scheme 3D vibrometer

This laser vibrometer has three laser sensor heads (*Polytec GmbH*, Waldbronn, Germany). In addition to the full HD camera (20x zoom) for perception, arrangements, and video triangulation, the top head (*PSV-I-500*) has a geometry filter unit (*PSVG-500, Polytec GmbH*, Waldbronn, Germany). The left and right scanning heads (*PSV-I-520, Polytec GmbH*, Waldbronn, Germany) are separate from the camcorder and the geometry scan unit. A sign generator and three computerized broadband decoders are used. The input from the filtering head to the decoder yields high frequency Doppler data. *PSV-E-530* (*Polytec GmbH*, Waldbronn) connects the scanning heads to the front end unit. The computer receives the estimation data via an ethernet port. The three laser heads must be aligned before measuring the AAO membrane's predefined geometry.

Each of the subsequent types of deformation has a unique zonal distribution. The higher is the shape mode, the smaller is the deformation zone of each peak of a point, but the greater is the number of points. Fig. 4.19 depicts the displacement of the nanoporous AAO membrane employing a cylinder-type *PZT-5H* transducer for different modes at resonance frequencies.

a

b

c
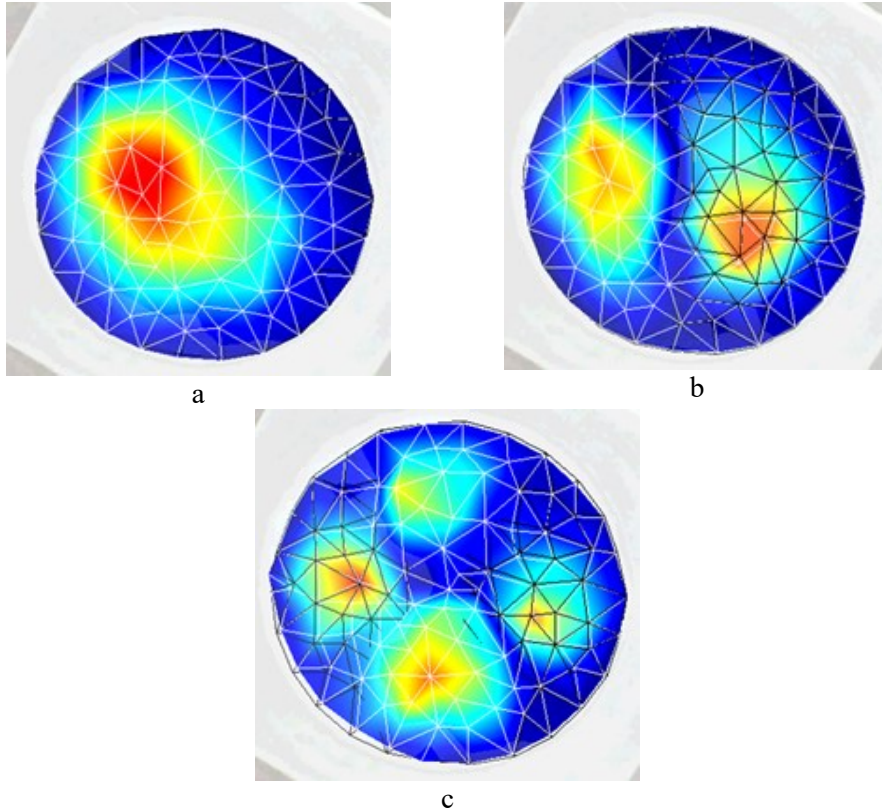
Fig. 4. 19 Experimental results of a 3D scanning vibrometer's response of the actuator on the surface of the AAO membrane at resonance frequencies: 3.62 kHz (a), 5.17 kHz (b), and 7.89 kHz (c)

The result of the response of the *PZT-5H* actuator on the surface of the AAO membrane is shown in Fig. 4.19. The deformation of the nanoporous AAO membrane was electrically generated at a frequency of vibrations of 3.62 kHz where the first mode was generated (Fig. 4.19a) with an axial displacement of 12.25 µm as shown in Fig. 4.20a. The second mode (Fig. 4.19b) of the vibration was achieved at a frequency of 5.17 kHz with two poles on the surface of the nanoporous AAO membrane surface with the peak point displacement of 6.41 µm (Fig. 4.20b). Finally, the third mode of vibration (Fig. 4.19c) received at a frequency of 7.89 kHz

had four poles on the surface of the AAO membrane with the peak point displacement of the surface of the nanoporous membrane at 5.34 μm (Fig. 4.20c).
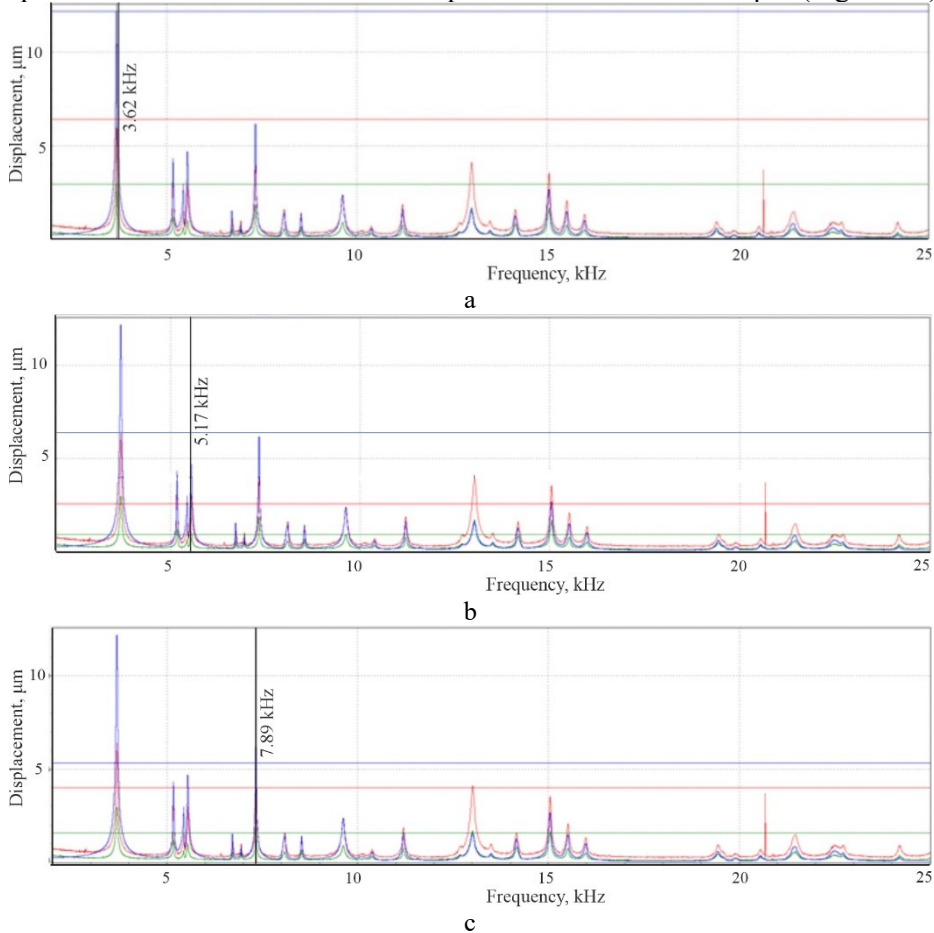
Fig. 4. 20 Displacement of the surface of the nanoporous membrane at resonance mode from 3D scanning vibrometer frequency response at resonance frequencies: 3.62 kHz (a), 5.17 kHz (b), and 7.89 kHz (c); colors x – green, y – red, and z – blue

In the course of the analysis of the vibration model, three different modes of deformation were achieved by using a 3D scanning vibrometer. The resonance mode of the actuator at a different magnitude of frequency was analyzed, and the obtained magnitude is presented in Fig. 4.20 in terms of the displacement magnitude in the y-z plane of the nanoporous AAO membrane.

From the experimental results of the 3D scanning vibrometer, the greatest axial displacement values were obtained during the first mode of vibration, at 12.25 μm. Meanwhile, an increase in the mode of vibration decreases the axial displacement on the surface of the nanoporous AAO membrane. When comparing

the results from the simulation, the PRISM system, and the Polytech vibrometer, the oscillation of the resonance frequencies 3.62 kHz, 5.17 kHz, and 7.89 kHz are the most suitable for the development of the vibroactive nanofiltration device for a microhydraulic system. The amplitude of the oscillation shape in the tangent direction offers the maximum displacement, which helps to reduce the risk of clogging and ensures efficient operation of filtration.

4.4 Chapter Conclusions

The following conclusions were made from the employed method for the mechanical characterization (micro indentation) and theoretical (COMSOL Multiphysics 5.4) and experimental analysis (non-destructive testing methods, PRISM system and Polytec 3D vibrometer) results of the AAO membrane actuation when using a piezoelectric actuator.

1. The method of effective tools and techniques was used to analyze the mechanical characteristics of hardness and the elastic modulus of the fabricated nanoporous AAO membrane.
2. The hardness of the fabricated nanoporous AAO membrane was evaluated for the samples 1A, 1B, 1C, 2A, 2B, and 2C, and the obtained values were 5.49 GPa, 5.35 GPa, 5.30 GPa, 5.23 GPa, 5.26 GPa, and 5.27 GPa, respectively. Also, the elastic modulus for the samples 1A, 1B, 1C, 2A, 2B, and 2C were 128.91 ± 4.67 GPa, 126.58 ± 5.32 GPa, 124.26 ± 4.39 GPa, 126.10 ± 2.97 GPa, 126.26 ± 5.84 GPa, and 127.87 ± 6.40 GPa, respectively.
3. The mechanical characteristics of the fabricated nanoporous AAO membranes were found to be relatively similar for all the fabricated membranes. There was no significant difference to be observed. Yet, it is possible to conclude that the porosity and the pore diameter have some influence on the hardness and the elastic modulus of the AAO membrane.
4. The simulation results of the optimal geometrical forms at oscillations of the AAO membrane at different frequencies change with an increase in the driving frequency. Three different modes were obtained on the surface of the nanoporous AAO membrane at a frequency of 3.50 kHz, 4.94 kHz, and 7.89 kHz. Displacement of the surface of the AAO membrane was observed for the first mode, the second mode, and the third mode to the extent of 17 μm, 8.2 μm, and 4.5 μm, respectively.
5. Experimental analysis of the tangential oscillation of the nanoporous AAO membrane when using a PZT actuator shows that similar forms of vibrations were achieved at frequencies 3.62 kHz, 5.71 kHz, and 7.89 kHz; a difference of only 4.7%, 8.2%, and 2.1% in the three different modes between the simulation and the experimental results was achieved. The resonance mode of the prototype was achieved at a frequency of 3.14 kHz because of the maximum tangential displacement of 17 μm from the surface of the nanoporous AAO membrane when using a PZT actuator.

6. The evaluated mechanical characteristics, the optimal geometrical forms, and the oscillation modes of the AAO membrane make it suitable for the development of a vibroactive nano-filtration device for microhydraulic systems in biomedicine.

V. Investigation of Acoustic Pressure and Fluid Flow in Nanotubes and Surface Acoustics for Nanofiltration

The fabricated nanoporous AAO membrane was proposed to be used for micro/nano filtration from the fluid in micro-hydraulic systems in biomedicine. Therefore, it is important to analyze the flow characteristics, the acoustic pressure distribution, and the particle motion inside the nanotubes formed in the nanoporous AAO membrane. *COMSOL Multiphysics* was used for the analysis of the flow of the fluid, the acoustic pressure distribution, and the particle motion.

5.1 Numerical Analysis of the Flow Characteristic in Nanotubes Formed inside Nanoporous Aluminum Oxide Membranes

For the calculation of the laminar flow in nanotubes formed in the nanoporous AAO membrane, the highest achieved diameter for nanotubes was that of 200 nm. The flow was determined by the dimensionless criteria, specifically, the Reynolds number. What concerns the fluid flow in the circular cavity, the Reynolds number can be calculated from Formula 5.1.

$$R_e = u \; \frac{d}{v}$$

(5.1)

Here, u – average speed, d – diameter of nanotube, and v – kinematic viscosity coefficient of the fluid.

According to [170], laminar flow occurs when the Reynolds number is less than or equal to 2320. When the number surpasses 2320 but does not yet reach 4000, the flow is said to be indeterminate. When the number exceeds 4000, the flow is said to be determinate. For the calculation of the flow rate of the nanoporous AAO membrane, it is necessary to find the flow rate for the single nanotube of the laminar flow at a difference of 1 pa. This can be calculated from Poisson's formula [172].

$$Q = \frac{\pi R^2}{8\eta} \frac{\Delta p}{l}$$

(5.2)

Here, R – the radius of the nanotube, η – the dynamic viscosity coefficient of the liquid, Δp – the pressure difference between the two sides of the tube, and l – the length of the tube (2 μm).

The numerical analysis of the laminar flow was calculated for water, and the dynamic coefficient of the water at 20 °C is 1.0019×10^{-3} Pa [173]. The diameter of the nanotube varies, but, in this calculation, the diameter of the tube is assumed to equal 200 nm, whereas the length of the tube is 2 μm. The calculated flow rate for a single nanotube is 1.95877×10^{-20} m³/s, as obtained from Formula 5.2. The average velocity of the fluid for a single nanotube, as calculated from Formula 5.3 is 6.238×10^{-7} m/s.

$$V = \frac{Q}{S}$$

(5.3)

Here, V – the velocity of the fluid, Q – the flow rate, and S – the cross section of the nanotube.

For the membrane having a pore density per square meter of 10^{13}, the total flow rate is 0.117 l/min through the AAO membrane surface area.

Furthermore, a numerical simulation was performed in order to compare the results of calculation by using *COMSOL Multiphysics 5.4*. For the simulation, an axisymmetric model of a single tube was created (Fig. 5.1). The simulation model involved four different wall boundary conditions.
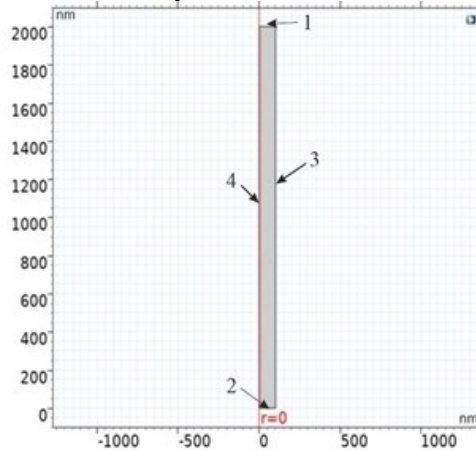
Fig. 5. 1 Simulation model for flow and velocity inside a nanotube consist of the inlet (1), the outlet (2), the external wall of the nanotube (3), and the axisymmetric line of the model (4)

During the calculation, the inlet flow of the fluid was defined as 1 Pa pressure, and the pressure at the outflow was 0 Pa. The temperature of the liquid, as applied in the simulation, was 20 ºC. This model of simulation is shown in Fig. 5.1, and calculations were run by using a study of a steady-state system. The simulation results were obtained for the laminar flow velocity distribution inside the nanotube; they are presented in Fig. 5.2.
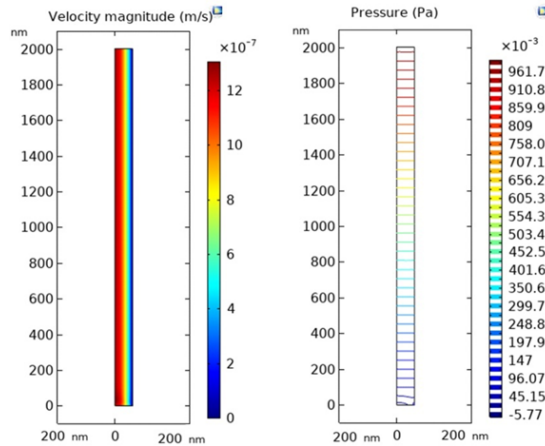
Fig. 5. 2 Results of the simulation for the laminar flow in a nanotube

The laminar flow distribution inside the nanotube was obtained from these results which were typical for this flow type. From the velocity distribution, the average flow rate can be easily calculated. The results of this simulation (Fig. 5.2) revealed that the average velocity of the liquid in the nanotubes is 6.22×10^{-7} m/s. The simulation results are close to the results obtained during calculation. A difference of as little as 0.16% was found between the calculated and the simulated velocity for a fluid inside the nanotube.

5.2 Numerical Analysis of Acoustic Pressure formed inside Nanoporous Aluminum Oxide Membranes

The micro/nano particle control in a microhydraulic system is widely used based on the acoustic pressure technique. By using this method, it is possible to create a pressure difference in the center of a nanotube in order to reduce the friction and the mechanical damage to the bioparticles. The wavelength must be less than or equal to 200 nm because the wavelength must fit within the nanotube diameter. The wave propagation speed in water is 1480 m/s. Also, it helps to monitor the movement of the micro/nano particles due to the generated acoustic pressure. For this purpose, a numerical simulation was performed to determine the acoustic pressure distribution, the particle motion, and the operating frequencies for the nanotubes distributed in nanoporous AAO membranes. For the simulation, a 2D rectangular model was created by using *COMSOL Multiphysics 5.4* for the analysis of the acoustic pressure model and the particle flow model. Similarly, another study was created to analyze the time to align the micro/nano particle in the center of nanotube.

The first study aimed to find the values of the pressure distribution, from which, acoustic pressure was generated. This pressure distribution must focus the particles in the center to protect them from possible deformation. This can occur by increasing the pressure differences in the pores. This would lead to an increased

flow rate, and then, to a higher force and a faster deformation of the particles. This can change the structure of the cell and cause irreversible processes.
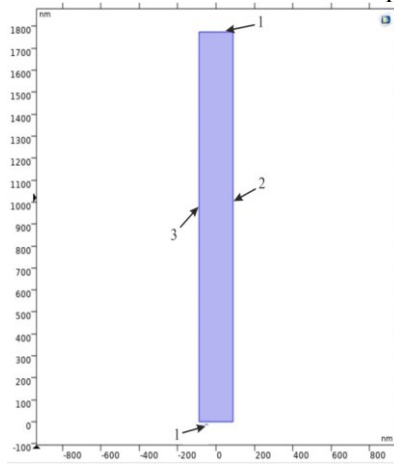
Fig. 5. 3 Simulation 2D model of nanocavity: 1 – plane wave radiation; 2 – normal acceleration; 3 – sound hard boundary

For this purpose, a mathematical model with the selected geometric parameters is defined. The entire domain is defined as the area in which the acoustic pressure analysis will take place. The simulation model is decomposed by finite element methods. The defined and decomposed model is presented in Fig. 5.3. The analysis range from 1 GHz to 7.4 GHz as selected for the study.

Table 5. 1. 2D model simulation parameter

Parameter	Values
Driving frequency, Hz	7.4×10^8
Speed of sound, m/s	1480
Wavelength, m	2×10^{-7}
Transducer diameter, m	2×10^{-7}
Reflector diameter, m	2×10^{-7}
Height, m	2×10^{-6}
Viscous boundary layer thickness, m	2.5×10^{-8}
Particle diameter, m	8.8×10^{-8}
Particle density, Kg/m^3	500
Normal acceleration of transducer, m/s^2	1.5×10^{-8}

The simulation analysis showed that, at 7.4 GHz (Fig. 5.4), two zones with zero pressures are formed in the nanotube formed in the AAO membrane. This can be explained by the acoustic wave distribution graph. When the full wave period oscillates, the wave curve intersects the major axis twice, which results in the formation of two zero zones. The zero zone must be one to keep the particles in the center.

126
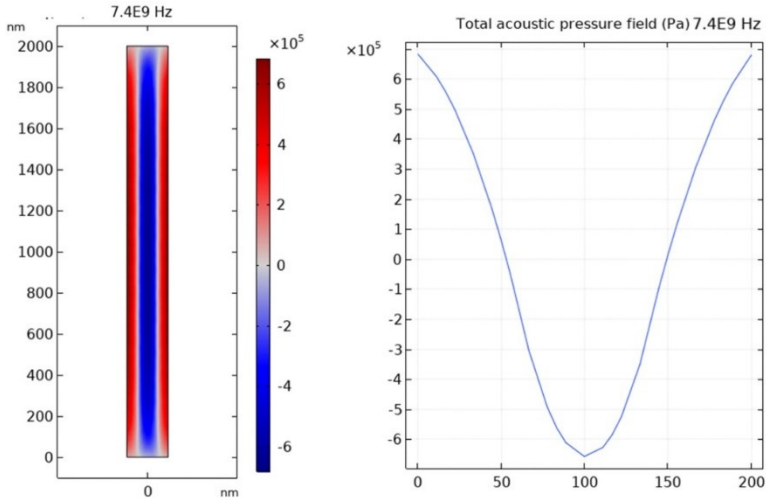
Fig. 5. 4 Acoustic pressure distribution inside a nanotube at 7.4 GHz

After the numerical simulation, the desired results were obtained at 3.7 GHz frequency as a theoretically predictable one. In these results, the maximum acoustic pressure is 5.57×10^6 Pa. The results of the acoustic pressure analysis are shown in Fig. 5.5.
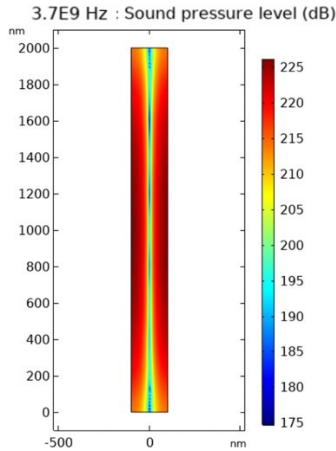
Fig. 5. 5 Sound pressure level inside a nanotube at 3.7 GHz frequency

An image of the sound pressure is presented in Fig. 5.5, in which, the pressure drop in the zero zone is clearly visible, which results in an intense movement of the particles towards the center. The difference between the maximum and the minimum sound pressure limits is 50 (dB).
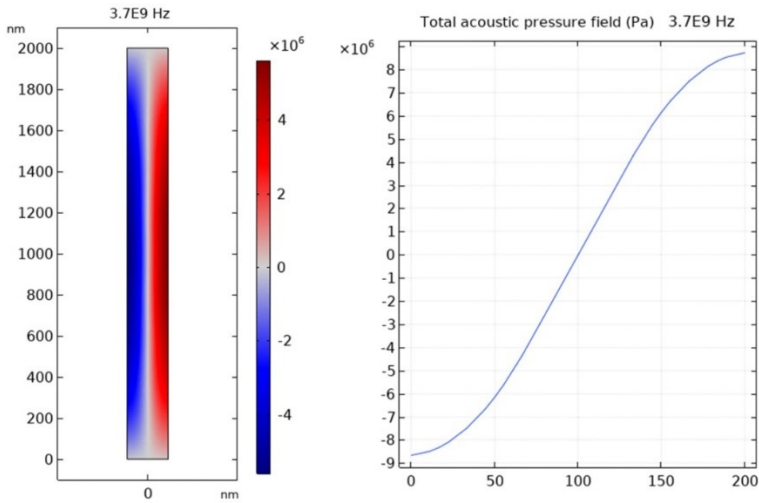
Fig. 5. 6 Acoustic pressure distribution inside a nanotube at 3.7 GHz

From the simulation results, two different graphs were plotted for the acoustic pressure distribution inside a nanotube at frequencies of 3.7 GHz and 7.4 GHz, which shows the pressure change in the cross-section of the nanotube. From the figure, it is clearly seen that the uniform change in pressure and the curves is very close to harmonic oscillation. During the separation of the filtration of nano/micro particles in the field of the acoustic pressure wave, they propagate precisely to a low acoustic pressure level zone which is seen in the center of the nanotube (Fig. 5.6). This physical phenomenon can be applied to separate/filter nanoparticles while using mechanical vibrations.

The obtained result of the simulation of the pressure distribution inside a nanotube was further used for the analysis of the nanoparticle motion inside a nanotube and the time for the center the nanoparticle. From the simulation analysis of acoustic pressure, it is clear that an increase in the driving frequency results in disorder of the acoustic pressure, and it causes friction between nanoparticles and the nanotube wall. Eventually, it will damage the nanoparticle or the bio particle while passing through the nanotubes. In order to understand how much time it takes to center the nanoparticle inside a nanotube, a second study is performed to determine the dependence on time.

The following analysis uses some of the results obtained at 3.7 GHz and 7.4 GHz. A simulation model of the same dimensions and fragmentation as in the first simulation model was used to develop the second analytical study. A model describing and resolving the motion of particles in a liquid is included in this study. In this analysis, the size of the particles is ten times smaller than the nanotube under analysis. The particle density was chosen to be 5000 kg/m³. A constant temperature of 20 °C was maintained during the simulation analysis. The gravity effect was also added to this simulation model, and it can affect the particle motion and the obtained

128

results. As the analysis of this model was performed over time, the analysis range is specified from 0 to 0.3 seconds with an increment of 0.0001 s. After the analysis, the obtained results of the particle motion are presented in Fig. 5.7 and Fig. 5.8.
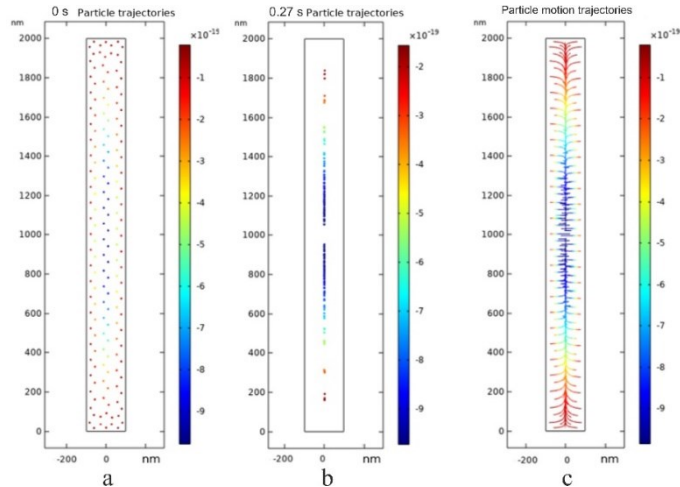
Fig. 5. 7 Results of nanoparticle motion and positioning inside a nanotube at 3.7 GHz frequency

The obtained results of particle positioning over time at a frequency of 3.7 GHz are presented in Fig. 5.7. The obtained results show that the initial positions of the nanoparticles at 0 s (Fig. 5.7a) are evenly distributed in the acoustic field. After 0.27 s, the nanoparticles moved and were aligned in the nanotube due to a lower acoustic pressure (Fig. 5.7b) and a lower sound pressure level observed in the center of the nanotube and perpendicular to the flow. Moreover, when analyzing the effect of the acoustic pressure on the movement of the nanoparticles starts to settle down in a certain area of the acoustic wave nodes and anti-nodes (in the center of the nanotube) in Fig. 5.7b, it shows the intense movement of the nanoparticle in the lower acoustic pressure field. Therefore, there is a net force pushing the nanoparticles towards the anti-node (in the center of the nanotube). When acoustic waves were applied to each other, a resonating liquid led to the disturbance of the nanoparticles in the nanotube. A travelling acoustic wave generates the streaming the flow with micro/nano particles.

The simulation results for the particle positioning and the motion of nanoparticles at a frequency of 7.4 GHz are presented in Fig. 5.8. The result of the simulation shows the nanoparticle positioning at 0 s (Fig. 5.8a) and 0.27 s (Fig. 5.8b). It clearly shows two concentration zones of nanoparticles, as determined for this acoustic pressure distribution. The concentration zone of the nanoparticles is near the nanotube wall. This means that it is likely to damage the micro/nano particle due to the friction between the nanotube wall and the particle periphery.

From Fig. 5.8c, it is clear that the motion of the nanoparticle is less intense than observed at a frequency of 3.7 GHz.
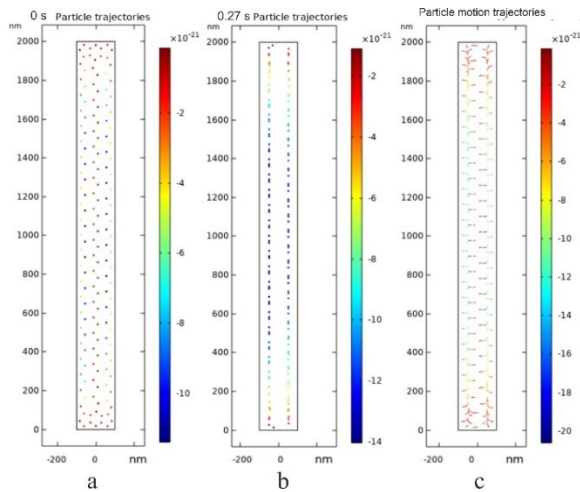
Fig. 5. 8 Results of nanoparticle motion and positioning inside a nanotube at 7.4 GHz frequency

From the obtained results of particle motion and positioning at a frequency of 3.7 GHz and 7.4 GHz, it is clearly seen that, after 0.27 s, nano particles are concentrated in the center of nanotubes at a frequency of 3.7 GHz; this can help to perform the filtration or the separation process of micro/nano particles in a micro hydraulic system without any damage of the particle, thus ensuring smooth operations in filtration devices in biomedicine.

Similarly, at a frequency of 7.4 GHz, the movement and the nanoparticle concentration were observed in two lower acoustic pressure zones inside the nanotube. The motion of the nanoparticle after 0.27 s was found to involve intense movement towards the lower sound pressure zone, which is due to the acceleration of the driving frequency.

After performing analyzes of laminar flow and particle motion under acoustic pressure, the obtained results are combined into one joint model. This model shall visualize the motion of particles in a membrane nanotube by using a simultaneous flow and acoustic pressure. The parameters and the model itself remain analogous to the study performed under acoustic pressure, but the fluid flow from the first analysis (which was 6.22×10^7 m/s) is additionally included in this analysis. Similar results were obtained from the analysis results (i.e., there was no change observed in the particle positioning). Due to the stronger force generated by acoustic pressure, the laminar flux failed to overcome the force; thus, this simulation model could be used for periodic focusing of micro/nano particles in the center of a nanotube during the filtration and separation process in microhydraulic devices.

5.3 Nanoporous AAO Membrane Application for Filtration and Separation

The fabricated nanoporous AAO membrane used for the development of prototype could be used for vibroactive nanofiltration devices in microhydraulic devices for biomedicine. The prototype of a vibroactive device consists of a piezoelectric actuator (PZT-5H), the fabricated nanoporous AAO membrane, and a fluid container. The surface of the fabricated nanoporous AAO membrane is actuated by using bulk acoustic waves by applying the electric potential at a different frequency range which helps to manipulate the geometrical nanopores. The particles and impurities presented in the fluid having a size bigger than the pores will be denied the passage through the nano tubes to the other side. The physics testing prototype for fluid permeation through the nanoporous AAO membrane is shown in Fig. 5.9.
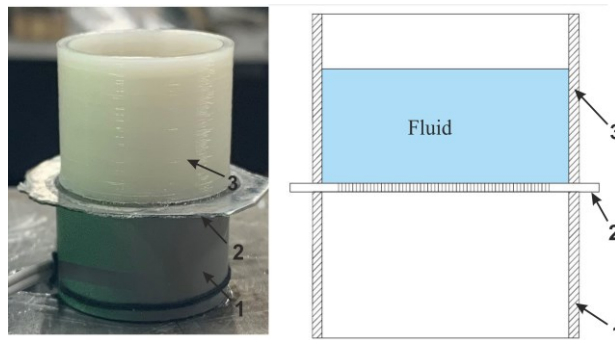
Fig. 5. 9 Prototype of fluid permeation consists of a piezoelectric actuator (1), the fabricated nanoporous AAO membrane (2), and a fluid container (3)

In order to check the fluid permeation through the fabricated nanoporous AAO membrane at some resonance frequency mode, a simple prototype was prepared, as shown in Fig. 5.9. The prototype of fluid permeation and acoustic wave modulation contains a piezoelectric cylinder type actuator featuring an outer diameter of 30 mm, wall thickness 2 mm, and height 15 mm; the fabricated nanoporous AAO membrane was attached on the top of the actuator, and a plastic container for storing fluid was also attached. The evaluation of the formation of the bulk acoustic wave on the surface of the nanoporous AAO membrane by actuating a piezoelectric actuator was done by using a PRISM system at a different frequency. The experimental setup for different forms of vibration while using the PRISM system is shown in Fig. 5.10.
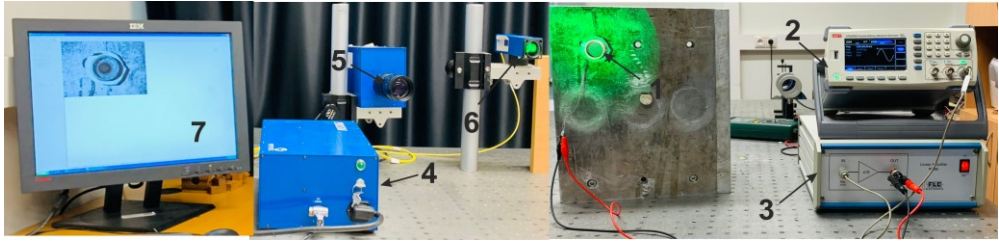
Fig. 5. 10 Experimental setup for the vibration analysis of the prototype for fluid permeation

The experimental setup for the analysis of various forms of vibration of the system consists of the prototype (1) attached onto the fixed surface, a frequency generator (2) connected to a linear voltage amplifier (3) for voltage amplification, a PRISM system control block (4), a camera (5), a green laser (6), and a monitor (7).

The prototype (1) is attached to a stable base with the help of glue at the periphery of the piezoelectric actuator, which allows isolating the vibrations of the AAO membrane from the external source so that to evaluate only the dynamic properties of the AAO membrane. This is essential in order to accurately determine the vibration patterns, the nature, and the excitation frequency of the AAO membrane. The AAO membrane (the inner side of the fluid container), illuminated by the PRISM system laser, begins to vibrate when the piezoceramic actuator is excited by an AC electrical signal, and the vibration shapes on the surface of the AAO membrane are monitored in real time on the PRISM system monitor. The recorded main resonant forms are presented in Fig. 5.11.

3.56 kHz

4.5 kHz

6.15 kHz

7.16 kHz

| 15.60 kHz | 41.82 kHz |
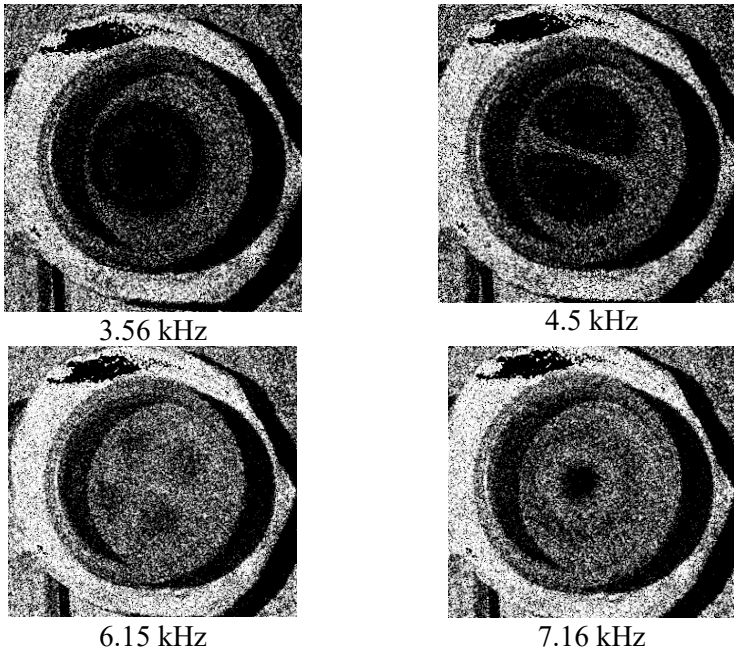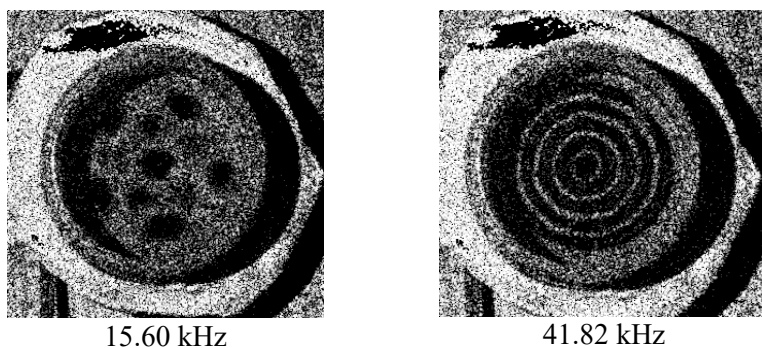
Fig. 5. 11 Vibration forms and frequency of the nanoporous AAO membrane

Based on the obtained images (Fig. 5.11), according to the arrangement of the peaks of the oscillation forms, the locations of the formation of the maximum displacement forms were selected for the filtration prototype. In the PRISM system, the performed measurements suffer from one drawback as it only captures the amplitude of the oscillations in the normal direction of the sample surface, which does not allow the nature and the amplitude of the tangential oscillations to be assessed. Based on the previous findings from the *Polytec* 3D vibrometer experiment, it can be stated that the frequencies 3.56 kHz, 4.5 kHz, and 41.82 kHz may be suitable for the filtration procedure because the peaks and nodes of the oscillation forms of acoustic waves observed in these interferograms are arranged correctly, and the tangential oscillations will be maximal in the respective zones. In Chapter 4, the maximum displacement was observed at a frequency of 3.6 kHz in the experimental practice when using a 3D scanning vibrometer.

The nanoporous AAO membrane at a frequency 3.56 kHz oscillates at half wavelength, i.e., $\lambda/2$. The operating principle of the prototype for the standing acoustic wave modulation for filtration is presented in Fig. 5.12.
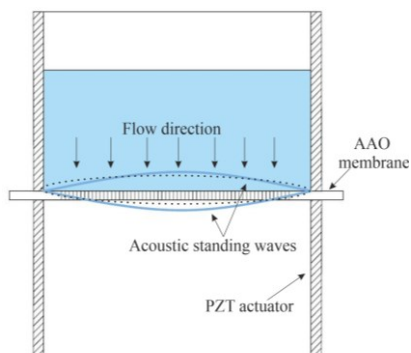
Fig. 5. 12 Working principle of the prototype for filtration

The experimental investigation of the filtration system (Fig. 5.13) based on bulk acoustic waves consists of the filtration prototype (1), a frequency signal generator (2), a linear amplifier (3), an optical microscope (*Nikon ECLIPSE LV150*) (4), and a monitor (5).
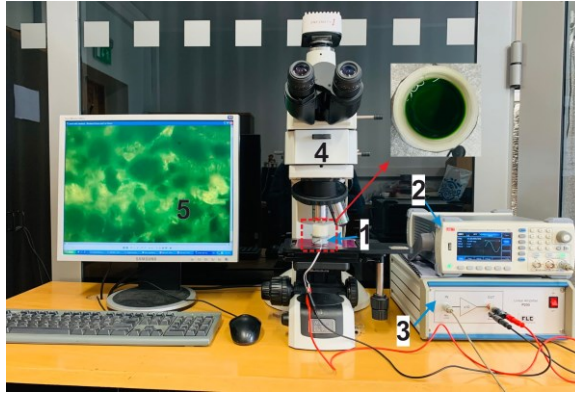
Fig. 5. 13 Experimental setup for fluid permeation: filtration prototype (1), frequency signal generator (2), linear amplifier (3), optical microscope (*Nikon ECLIPSE LV150*) (4), monitor (5)

The container contains green-colored distilled water (10 ml) in order to check the fluid permeation on the other side of the nanoporous AAO membrane surface. Firstly, the analysis of the prototype was performed without any frequency, and, after 2 hours, there were just a few green spots which appeared on the other side of the nanoporous AAO membrane without any external pressure. The microscopic image of the membrane from the other side for fluid permeation without any frequency is shown in Fig. 5.14a.

a   b
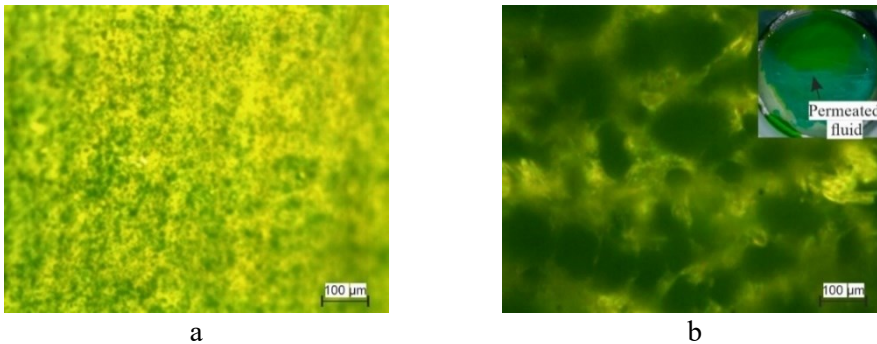
Fig. 5. 14 Fluid permeation through AAO membrane without any frequency (a) and at 3.56 kHz frequency (b)

On the other hand, fluid permeation through the nanoporous AAO membrane was observed in the identical quantity when the membrane was excited by using a piezoelectric actuator at a frequency of 3.56 kHz. The microscopic image and the
134

photo of the fluid permeated through the AAO membrane is shown in Fig. 5.14b. From the experimental results of the fluid permeation through the nanoporous AAO membrane, it is clear that the fabricated nanoporous AAO membrane can be used for the filtration of the particles in a microhydraulic system for biomedicine. Moreover, acoustic waves forming on the surface of the nanoporous AAO membrane help to develop a vibroactive nano filtration device which helps to reduce the risk of clogging and to short the particles of a size bigger than nanopores (i.e., particles having a size bigger than the developed nanopores/nanotubes in the AAO membrane will be ejected/collected or shorted).

In water and gas separation, the membrane technology has gained a lot of attention due to its low energy costs and environmental concerns, thereby making it a highly competitive alternative. Among numerous membrane technologies, nanoporous aluminum oxide membrane-based technologies have attracted attention due to the excellent properties, such as a regular porous structure, pore density, and availability across a wide range of thickness. Recently, the removal of toxic acids and CO_2 from natural gases has been carried out on a large scale by using a membrane-based separation process. There is a wide range of materials and methods which are available for the fabrication of a membrane with micro/nano scale pores.

In order to check the applicability of the fabricated nanoporous AAO membrane, an experiment was performed on the fabricated AAO membrane having a pore diameter of 70 nm, 32.64% porosity, and 96 μm thickness. The fabrication process of the nanoporous AAO membrane is described in Chapter 3. There were three different gases in use: carbon dioxide (CO_2), nitrogen (N_2), and Methane (CH_4). The experimental setup for the gas permeation test is shown in Fig. 5.15.
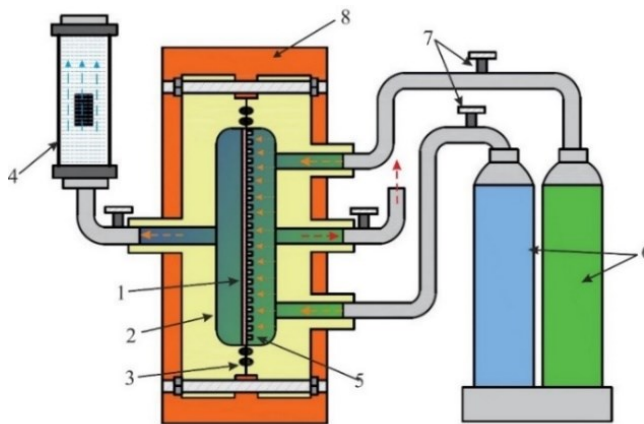
Fig. 5. 15 Experimental setup of the gas permeation test

The experimental setup for the gas permeation test consists of the fabricated nanoporous AAO membrane (1), a module for testing (2), rubber O-rings for leakage preventions (3), a soap bubble flow meter (4), a porous metal disc for

supporting the tested sample (5), gas tanks (6), control valves for gas supply (7), and a heating chamber (8).

To determine the separation and selectivity of the three different gases in use (CO_2/CH_4 and CO_2/N_2), the permeability test was used at three different temperatures, specifically, 20 ºC, 40 ºC, 60 ºC, with the pressure ranging between 0–0.5 bar. The experiment was performed in a gas permeation system while using a circular AAO membrane with the effective diameter of 20 mm. The tested sample of the AAO membrane is shown in Fig. 5.16.
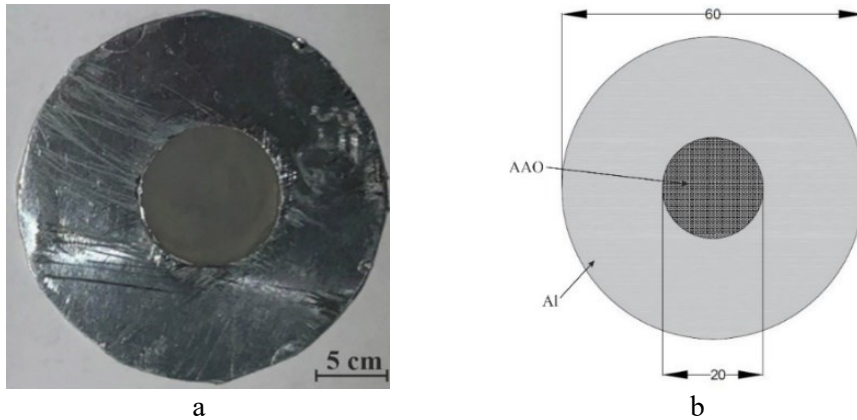
Fig. 5. 16 A photo (a) and the dimensions of the nanoporous AAO membrane for the gas permeation test

The fabricated nanoporous sample was sandwiched between two aluminum sheets having a diameter of 60 mm with an open area in the center for the nanoporous AAO diameter of 20 mm. The AAO membrane has a support of an aluminum sheet and is placed in the testing module. Then, the testing module was gently tightened with fasteners and deflated by using a vacuum pump to remove all the remaining gases from the testing module and the cells. Before the measurement of each gas, the same procedure was performed. The feed flow of each gas was passing through the nanoporous AAO membrane by adjusting the pressure from 0 to 0.5 bar at different temperatures in the range of 20–60 ºC. The measurement of the gas permeability and selectivity has been performed three times, and the average values were recorded. The gas permeability was calculated by using Formula 5.4.

$$P = \frac{Ql}{\Delta pA} \qquad (5.4)$$

Here, Q – the flow rate of the gas (cm^3/s), A – open area of the AAO membrane (cm^2), l – the thickness of the AAO membrane (cm), and Δp – the transmembrane pressure difference (bar).

The properties of used gases for gas permeation test are shown in Table 5.2.

Table 5. 2. Properties of gases used for the gas permeation test [174]

Properties	Carbon dioxide, CO_2	Nitrogen, N_2	Methene, CH_4
Molecular weight	44.009	28.01	16.042
Normal boiling point, ºC	-78.46	-135.8	-162
Specific gravity	1.521	0.9737	0.554
Specific heat, kJ/kg ºC	3.713	1.04	1.709
Density, kg/m^3	1.977	1.2506	0.657
Critical temp, ºC	30.978	-146.9	-82.59
Critical pressure, bar	73.8	33.95	45.95

The permeability test of all the three gases CO_2, N_2, and CH_4 on the fabricated nanoporous AAO membrane at a temperature 20 ºC was done as shown in Fig. 5.17.

The evaluation of the gas permeability of the pure gases permeation experiment was carried out by using three different pure gases CO_2, N_2, and CH_4 at a pressure range from 0 to 0.5 bar with the objective to investigate the efficiency of the fabricated nanoporous AAO membrane gas separation. Initially, in order to understand the permeability of gases without deteriorating the AAO membrane properties, a lower pressure and a lower temperature were used.

From the obtained results, it is evident that, by increasing the feed pressure from 0 to 0.5 bar, the permeability of CO_2, N_2, and CH_4 is increased. The permeability of CO_2 gas increases from 377717 to 699266 Barrer by increasing the feed pressure ranges from 0 to 0.5 bar. Similarly, the permeability of N_2 increased gradually from 294471 to 642328 Barrer. Moreover, the permeability of CH_4 was increased with an increase in the feed pressure (0 to 0.5 bar) 395102 – 907597 Barrer. This behavior attributes the increase in the driving force for the transport of gas via the fabricated nanoporous AAO membrane. The macromolecular segments are moved closer together as the pressure increases. As a result, the intersegmental empty space shrinks, while the selected layer area expands, thereby increasing the permeability of gases.
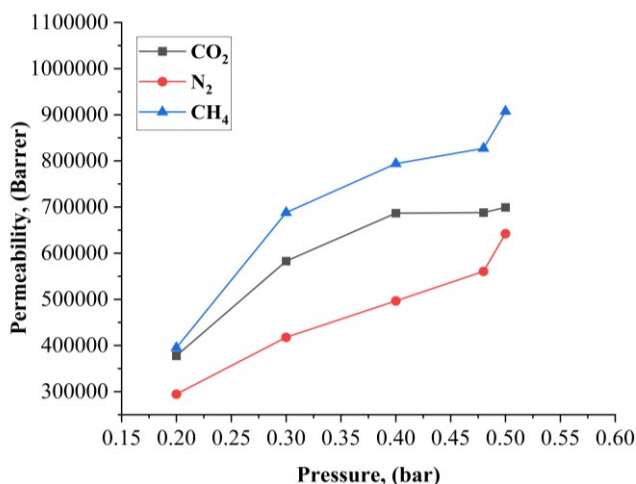
Fig. 5. 17 Effect of feed pressure 0–0.5 bar on three different gases CO_2, N_2, and CH_4 permeability values of the fabricated nanoporous AAO membrane at 20 ºC

Moreover, CH_4 demonstrates the maximum permeability; its value is higher than that of CO_2 and N_2. This is because CH_4 molecules are denoted by a higher affinity and diffusivity for the manufactured nanoporous AAO membrane than CO_2 and N_2 molecules. The effect of different temperatures (from 20 to 40 ºC) on the permeability of different gases CO_2, N_2, and CH_4 for the fabricated nanoporous AAO membrane at a pressure ranging from 0 to 0.5 bar was determined. The results of gas permeability at three different temperatures are shown in Fig. 5.18.

The effect on the permeability of different gases CO_2, N_2, and CH_4 at different temperatures ranging from 20 to 40 ºC for various levels of pressure ranging from 0 to 0.5 bar is shown in Fig. 5.18. The results suggest that, with an increase in the temperature from 20 to 40 ºC, the permeability of gases CO_2, N_2, and CH_4 increased through the fabricated nanoporous AAO membrane. For CO_2 (Fig. 5.18a), the permeability increased at 0.5 bar from 679266.3 to 774830.3 Barrer at temperatures from 20 to 40 ºC, respectively. Similarly, the permeability of N_2 (Fig. 5.18b) increased from 642328.3 to 650603.2 Barrer at temperatures from 20 to 40 ºC, respectively. Moreover, the permeability of CH_4 (Fig. 5.18c) through the fabricated nanoporous AAO membrane increased from 307598 to 996210.6 Barrer when the temperature rose from 20 to 40 ºC. This implies that the permeability of CO_2, N_2, and CH_4 for the fabricated nanoporous AAO membrane increased by about 13.14, 1.3, and 105.63%, respectively, when the temperature was raised from 20 to 40 ºC.
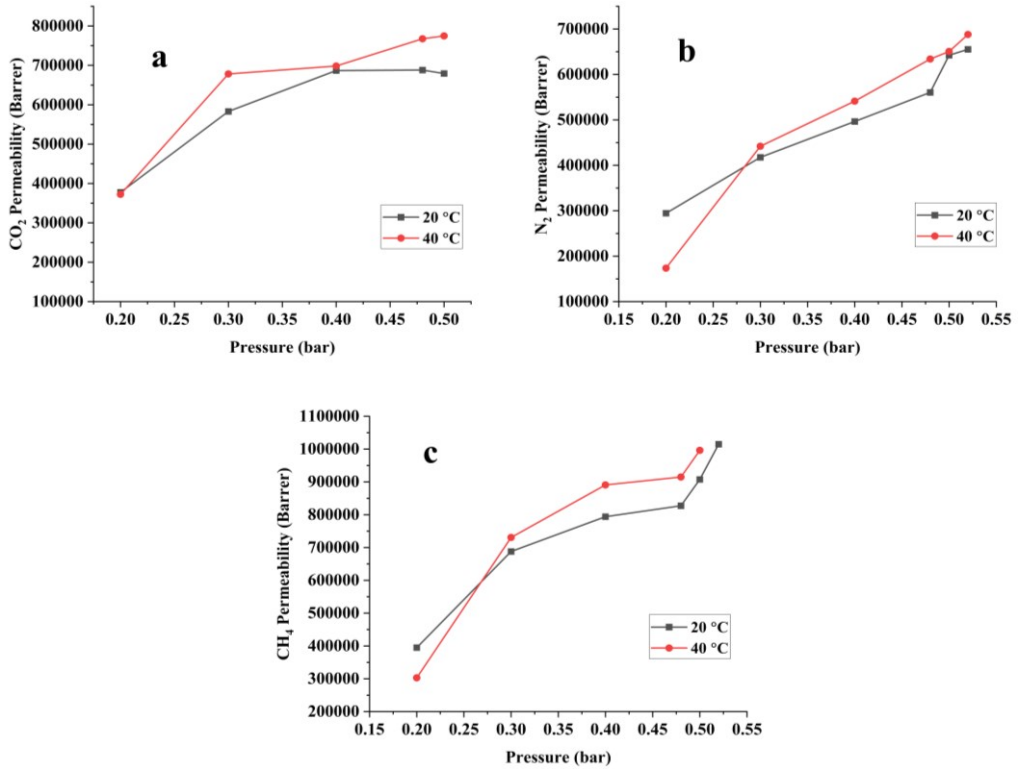
Fig. 5. 18 Effect of different temperatures on the permeability values of three gases CO_2 (a), N_2 (b), and CH_4 (c) for the fabricated nanoporous AAO membrane

The evaluation of gas selectivity was performed for CO_2/N_2 and CO_2/CH_4 at pressures ranging from 0 to 0.5 bar at a temperature of 20 ºC. Selectivity is a measure of how well a nanoporous AAO membrane can separate two gases, and it is expressed as the permeability ratio of pure gas components. The results of selectivity for CO_2/N_2 (Fig. 5.19a) and CO_2/CH_4 (Fig. 5.19b) at pressures ranging from 0 to 0.5 bar at a temperature of 20 ºC is presented in Fig. 5.19.
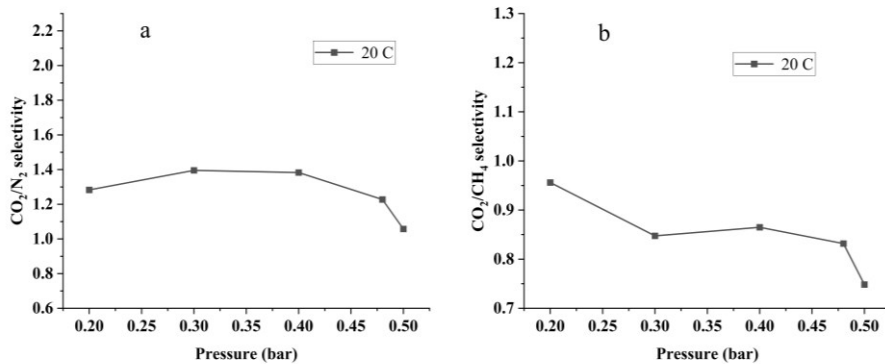
Fig. 5. 19 CO_2/N_2 and CO_2/CH_4 selectivity behavior at pressures from 0 to 0.5 bar at 20 ºC temperature

The result shows that, by an increase in pressure (0 to 0.5 bar), the selectivity is decreasing. The CO_2/N_2 (Fig. 5.19a) and CO_2/CH_4 (Fig. 5.19b) selectivity decreased from 1.26 to 1.05 and from 0.96 to 0.74, respectively, with a decrease rate of 18.18% and 25.88%. In comparison with CO_2/N_2 and CO_2/CH_4 gases, it is observed that CO_2/N_2 exhibits the highest gas selectivity. This behavior of selectivity stems from the gas diffusion and solubility mechanism. The maximum selectivity obtained for CO_2/N_2 for the fabricated nanoporous AAO membrane is 1.39 without any decrease in the permeability. Several aspects can influence the effectiveness of the fabricated nanoporous AAO membrane separation parameter of CO_2 from various gases including the process of separation, the pore orientation, and the processing technique. From the experimental results, it may be concluded that the fabricated nanoporous AAO membrane can be used for gas filtration and separation.

5.4 Chapter Conclusions

The following conclusions were made from the theoretical analysis of the fluid flow, acoustic pressure, and particle motion inside the nanotubes. Also, the experimental analysis of fluid permeation through the nanoporous AAO membrane and gas separation was conducted.
1. The fabricated membrane was used for a microhydraulic device for the filtration of micro/nano particles. The flow simulation inside the nanotube was done. The influence of the acoustic pressure on the microparticle distribution and its dynamics were investigated. The results of the laminar flow modeling show that the membrane flow per square meter at one Pascal pressure difference between the different sides of the membrane is 0.01175 l/min.
2. This diaphragm flow is optimum, thereby allowing the nanoporous AAO membrane to be employed in microhydraulic systems. At a frequency of 3.7 GHz, microparticles were discovered to concentrate in the middle of the

nanotube, which allowed them to pass through the nanotube without any contact with the inner walls. At the double level of frequency, i.e., 7.4 GHz, two centering zones were found which may increase the risk of friction between the micro/nanoparticles and the inner wall of the nanotube and thus disorient the particle trajectory in the AAO membrane.

3. The simulation result of the nanoparticle motion inside the nanotube formed in a nanoporous AAO membrane shows that the micro/nano particles having a density of 500 kg/m^3 take 0.27 s to align in the center of the nanotube (i.e., in the lower acoustic field).

4. The numerical simulation results for the particle motion inside the nanotube and the flow inside the nanotube was developed for the application in a microhydraulic device for the filtration and separation of nanoparticles show that the developed numerical model can be used for the filtration and separation of nanoparticles and that the phenomenon of the acoustic waves helps to reduce the risk of clogging stemming from the particle size exceeding the size of the pores in the structure.

5. Considering the application of the fabricated nanoporous AAO membrane based on bulk acoustics, the prototype model for fluid permeation was developed. The results show that, at a frequency of 3.56 kHz, the fluid permeates through the membrane better than without any frequency. This means that the acoustic waves modulation and the improved porous structure (i.e., a high pore diameter and a lower thickness) of the membrane help to improve the filtration process.

6. The results of the gas separation experiment involving the fabricated membrane at a pressure range from 0 to 0.5 bar was done by using three gases, specifically, CO_2, N_2, and CH_4. It was observed that the highest gas separation selectivity through the membrane was achieved for CO_2/N_2 for the fabricated nanoporous AAO membrane; the highest reached value is 1.39 without any decrease in the permeability. From the experimental results, it is possible to conclude that the fabricated nanoporous AAO membrane can be used for gas filtration and separation.

Conclusions

The following conclusions were made according to the formulated research objectives on the thematic area of the research topic.

1. A review of the research work on micro hydraulics pertaining to the dissertation thematic area was carried out; the aim and the objectives were formulated. The currently used membranes in microfluidics are mostly based on the polymeric materials and used methods for fabrication are expensive and require complex methods for fabrication. Membrane-based microfluidics have been gaining substantial attention for particle separation and filtration by using contact and non-contact type particle manipulation in the micro fluidic work bench. Among all the methods and the membranes used for micro hydraulics, the developed nanoporous alumina membrane has gained substantial attention during past few decades due to the ease of fabrication and its unique characteristics. The use of the surface acoustic method for particle manipulation in microfluidics while using an AAO membrane enhances the filtration process in micro hydraulics systems for bioparticle separation and filtration in biomedical devices.

2. Based on the analysis of the relevant scientific literature, an experimental setup for the fabrication of an aluminum oxide membrane was developed with a cooling system based on a Peltier element. The designed cooling system for the experiment maintains the temperature at around 5–3 ºC during the anodization process, which helps for the ease of the anodization process. There is no significant difference to be found between the results of the simulation and the experimental analysis of the cooling system for the temperature analysis. Also, the fabrication of six AAO membranes was done at different process parameters while using the developed experimental setup, and the temperature of the electrolyte was found to be stable (5–3 ºC) during the anodization process when using the designed cooling system based on a Peltier element.

3. The geometry of the fabricated nanoporous AAO membrane was analyzed by employing SEM analysis. The research revealed that the fabricated nanoporous AAO membrane has a pore diameter from 43 nm to 85 nm with a stable interpore distance from 110 to 115 nm at an anodization voltage of 50 and 60 VDC. The thickness of the membrane between 74 and 95 nm was achieved for the anodization time ranging from 15 to 17 h. Moreover, it was found that an increase in the anodization time and voltage also increases the pore diameter and the thickness of the AAO membrane. EDS analysis shows the dominance of aluminum oxide (Al_2O_3). The fabricated nanoporous AAO membranes were composed of two major chemical components – Aluminum (Al) and Oxygen (O). However, small quantities of Phosphorus (P) and Sulphur (S) were detected for the sample fabricated at 60 VDC. The spectra of the FTIR analysis of the fabricated AAO membrane correspond to aluminum oxide (Al_2O_3). The hydrophobicity measurement of the fabricated nanoporous AAO membranes indicated the following water contact angle (θ) values for samples 1A, 1B, 1C,

2A, 2B, and 2C: 55.87 ± 0.69º, 54.38 ± 0.30 º, 45.16 ± 0.60º, 67.44 ± 0.56º, 66.58 ± 0.50º, and 64.07 ± 0.90º. This means that the surface of the fabricated nanoporous AAO membranes is hydrophilic. The time dependence study showed that a decrement in the contact angle, which means that a drop of water is shipped in the nanopores of the AAO membrane. Those properties of the fabricated nanoporous membrane make it suitable for the application in microhydraulic devices for filtration and separation.

4. The mechanical properties of hardness and elastic modulus of the fabricated nanoporous AAO membrane were evaluated; the hardness for samples 1A, 1B, 1C, 2A, 2B, and 2C was determined to be equal to 5.49 GPa, 5.35 GPa, 5.30 GPa, 5.23 GPa, 5.26 GPa, and 5.27 GPa, respectively. The elastic modulus for samples 1A, 1B, 1C, 2A, 2B, and 2C was determined to be 128.91 ± 4.67 GPa, 126.58 ± 5.32 GPa, 124.26 ± 4.39 GPa, 126.10 ± 2.97 GPa, 126.26 ± 5.84 GPa, and 127.87 ± 6.40 GPa, respectively. No significant difference was observed, yet it was determined that the porosity and the pore diameter exert influence on the hardness and the elastic modulus of the AAO membrane. By using piezoelectric actuator bulk acoustic wave modulation, three different forms were observed on the surface of the AAO membrane at the following frequencies: 3.50 kHz, 4.94 kHz, and 7.89 kHz. The difference of 4.7%, 8.2%, and 2.1% was determined in the three different modes between the simulation and the experimental results. The resonance mode of the prototype was achieved at a frequency of 3.14 kHz because of the maximum tangential displacement of 17 μm on the surface of the nanoporous AAO membrane when using a PZT actuator.

5. When taking into account the applicability of the AAO membrane in micro hydraulic devices, theoretical modeling was developed for particle manipulation and controlling the trajectory of the micro/nano particles inside the nanotube of the AAO membrane based on the acoustophoresis method. The physical prototype of fluid permeation was tested experimentally by using the bulk acoustic wave at a frequency of 3.56 kHz permeating the fluid through the AAO membrane. This simple prototype can be used for the filtration of impurities from the fluid of a size higher than the pore diameter of the membrane. However, the system can be improved by customizing the porous structure of the AAO membrane during the anodization process. The developed method for particle separation based on acoustophoresis increases the applicability of the fabricated nanoporous AAO membrane in the development of a microhydraulic system for increasing the filtration efficiency in micro devices in biomedicine. The fabricated AAO membrane may also be used for the removal of toxic gases, and the results of gas separation show that the highest gas separation selectivity level through the membrane (specifically, 1.39) was achieved for CO_2/N_2 for the fabricated nanoporous AAO membrane without any decrease in permeability. The use of the fabricated nanoporous AAO membrane for gas filtration and separation was determined to be a feasible solution.

SANTRAUKA

ĮVADAS

Dvidešimt pirmajame amžiuje sparčiai tobulėjant nanotechnologijoms, buvo pasiūlyta daugybė sprendimų, norint sukurti ypatingomis savybėmis pasižyminčias medžiagas. Tokios medžiagos gali būti naudojamos įprastose sistemose, siekiant padidinti jų veikimo efektyvumą, arba pritaikytos sąveikai su mikroorganizmais, sudarant sąlygas proveržiui sveikatos priežiūros srityje. Nanosistemos paprastai plėtojamos remiantis tais pačiais mechaninės inžinerijos principais kaip ir įprastų sistemų atveju, tačiau kartu tai reikalauja gilesnio supratimo apie medžiagų prigimtį ir chemijos inžinerijos principus. Įprastose sistemose veikiančių elementų, pvz., skysčio siurblio, sumažinimas pritaikymui nanosistemose taip pat yra sudėtingas techninis iššūkis. Dėl nanotechnologijų galima ženkliai sumažinti laboratorinės įrangos dydį, todėl pasireiškia nemažai naudingų savybių: kompaktiškumas, mažesnės reagentų sąnaudos, didesnis reakcijos greitis ir tiksliau nustatomi analizuojamieji parametrai. Atsižvelgiant į efektyvesnio ir aplinką tausojančio skysčių filtravimo proceso poreikį, mokslinėje literatūroje didelis dėmesys buvo skiriamas pažangiomis savybėmis pasižyminčių medžiagų, pvz., filtravimo įrangoje naudojamų nanopluošto membranų, tyrimams. Biologinių dalelių atskyrimas ir filtravimas yra svarbus etapas atliekant kokybinės ir kiekybinės analizės eksperimentus biochemijos ir biomedicinos pramonės srityse, projektuojant naujus efektyvesnius gamybos įrenginius, todėl itin aktualus šio metodo našumo didinimo klausimas. Didesnis mikrofluidinių prietaisų, naudojamų filtravimo ir atskyrimo procesuose mikro- ir nanolygmenyje, veiksmingumas gali būti pasiektas jų gamyboje pritaikius membraninę mikrofiltravimo techniką. Todėl akivaizdu, jog itin svarbu sukurti efektyvią ir komerciškai prieinamą membraninę technologiją, kur dėl paviršiaus akustikos reiškinio būtų atliekamas mikro- / nano- dalelių atskyrimas / filtravimas. Kadangi aliuminio oksido nanomembranų tyrimai vis dar yra ankstyvojoje stadijoje, svarbu išvystyti metodus, kurie leistų išplėsti jų pritaikymo galimybes bei gilinti žinias apie jų gamybos metu vykstančius procesus. Šiame darbe pristatomi filtravimo / atskyrimo procesuose pritaikomų nanoporėtų aliuminio oksido membranų tyrimai ir plėtra, įskaitant gamybos procesą, charakterizavimą, savybių aprašymą ir paviršinių akustinių bangų moduliavimą nanoporėtos AAO membranos paviršiuje naudojant PZT keitiklį. Be to, apžvelgiamos nanoporėtos AAO membranos panaudojimo dujų atskyrimui galimybės.

Tyrimo tikslas ir uždaviniai

Pagrindinis tyrimo tikslas – sukurti nanoporėtos aliuminio oksido membranos pagrindu veikiančius funkcinius mikro- / nano- elementus, kurie galėtų būti naudojami mikrohidraulinėje sistemoje biomedicinos tikslais. Šiam tikslui pasiekti buvo iškelti tokie uždaviniai:

1. Atlikti lyginamąją tradicinės hidraulikos ir mikrofluidikoje taikomos mikrohidraulikos procesų analizę, apžvelgti membraninės mikrofluidikos ir nanoporėto anodinio aliuminio oksido pritaikymo galimybes biomedicinos srityje, siekiant apsibrėžti inovatyvią tyrimo kryptį.
2. Suprojektuoti ir išvystyti eksperimentinį stendą, leidžiantį gaminti tolygios porėtos struktūros nanomembranas, pritaikant dviejų etapų elektrocheminio anodavimo procedūrą ir aušinimo sistemą su Peltje elementu.
3. Įvertinti pagamintų nanoporėtų aliuminio oksido membranų geometrinę struktūrą, cheminę sudėtį ir hidrofobines savybes.
4. Ištirti mechanines funkcinių elementų charakteristikas, įvertinti optimalias geometrines formas bei nustatyti pagamintų nanoporėtų aliuminio oksido membranų rezonanso dažnius, siekiant jas pritaikyti fizikinio prototipo, kuris būtų veiksmingas atliekant mikro- / nano- filtravimą mikro- / nano- hidraulinėse sistemose, sukūrimui.
5. Sukurti skaitmeninį fizikinio prototipo modelį, skirtą akustinio slėgio pasiskirstymo nanovamzdelyje nustatymui, ir, remiantis paviršiaus akustinio reiškinio ypatybėmis bei naudojant pagamintą nanoporėtą aliuminio oksido membraną, sukurti nanofiltravimui skirtą mikro- / nano- hidraulinę sistemą, kuri galėtų būti pritaikyta biomedicinos srityje. Taip pat atlikti potencialaus pagamintos nanoporėtos AAO membranos pritaikymo dujų atskyrimui analizę.

Tyrimo metodai ir įranga

Nanoporėtų AAO membranų gamyba buvo atlikta naudojant suprojektuotą eksperimentinį stendą ir dviejų etapų elektrocheminio anodavimo metodą.

Pagamintų nanoporėtų AAO membranų cheminė sudėtis ir geometrinė struktūra, įskaitant porų skersmenį, atstumą tarp porų ir storį, buvo nustatyta naudojant skenuojantį elektroninį mikroskopą (SEM) „HITACHI S-3400N". Pagamintų AAO membranų hidrofobinių savybių įvertinimas buvo atliktas naudojant suprojektuotą eksperimentinį stendą, o vaizdai analizuoti naudojant vaizdo apdorojimo programinę įrangą „ImageJ".

Pagamintų nanoporėtų aliuminio oksido dangų mechaninės savybės buvo analizuojamos atliekant mikrokietumo matavimus („CSM Instruments", mikrokietmatis „Micro combi tester") Olive ir Pharr metodu, naudojant deimantinį keitiklio antgalį.

Siekiant pritaikyti nanoporėtas membranas akustinių bangų pasiskirstymo analizei, virpesių ir paviršinių akustinių bangų fizikos teorijos buvo tiriamos naudojant pjezoelektrinį keitiklį. Rezonanso dažniai buvo nustatyti naudojant programą „COMSOL Multiphysics 5.4". Skaičiavimo rezultatai buvo patvirtinti atliekant neardomuosius testavimo eksperimentus naudojant 3D skenuojantį vibrometrą („POLYTECH") ir holografinės interferometrijos metodą („PRISM"

sistema), analizuojant įvairias geometrines formas ir tiriant sistemos rezonansinį dažnį.

Siekiant įvertinti dujų perdavimo ir atskyrimo efektyvumą, eksperimentas buvo atliekamas naudojant trijų skirtingų rūšių dujas: CO_2, N_2 ir CH_4.

Moksliniai tyrimai buvo atliekami Kauno technologijos universiteto Mechanikos inžinerijos ir dizaino fakultete, Mechatronikos institute, Medžiagų mokslo institute. Taip pat membranų analizė buvo vykdoma Lietuvos energetikos institute (Kaunas) ir Vytauto Didžiojo universiteto Žemės ūkio akademijoje (Kaunas).

Mokslinis darbo naujumas

1. Remiantis Peltje elemento aušinimo sistemos principais, buvo sukurtas efektyvaus elektrocheminio anodavimo eksperimentinis stendas, skirtas vykdyti pageidaujamomis funkcinėmis savybėmis pasižyminčių nanoporėtų aliuminio oksido membranų gamybą, kad vėliau jas būtų galima pritaikyti mikrofluidiniams prietaisams gaminti.

2. Sukurtas efektyvus ir nebrangus eksperimentinis tyrimo metodas ir stendas, skirtas nanoporėtų aliuminio oksido membranų ir kitų mikro- / nano-inžinerijoje naudojamų paviršių hidrofobinių savybių įvertinimui.

3. Sukurtas skaitmeninis paviršinių akustinių bangų moduliavimui nanoporėtos membranos paviršiuje skirtas modelis, siekiant pritaikyti pagamintą membraną nanofiltravimo procesuose naudojant pjezoelektrinį keitiklį.

4. Sukurtas skaitmeninis modelis, skirtas akustinio slėgio pasiskirstymo nanovamzdelyje matavimui ir laiko, per kurį dalelės tolygiai pasiskirsto nanovamzdelio centre, įvertinimui, siekiant sumažinti trintį tarp dalelių ir vamzdelio sienelės nanofiltracijos metu biomedicininės paskirties mikroelektromechaninėse (MEMS) sistemose.

Praktinė vertė

1. Eksperimentinis gamybos proceso tyrimas leidžia tinkamai parinkti parametrus ir nebrangiai pagaminti nanoporėtas membranas, kurias sudaro pageidaujamos geometrinės struktūros poros ir vamzdeliai. Taip taip jis padeda kontroliuoti geometriją formavimo proceso metu.

2. Eksperimentiniai membranų hidrofobinių savybių tyrimai leidžia suprasti struktūrinių savybių ypatybes bei numatyti membranos paviršiaus elgseną esant sąveikai su skirtingos prigimties skysčiais.

3. Akustinio sužadinimo filtravimo modeliui sukurti panaudotas paviršinių akustinių bangų skaitmeninis modeliavimas. Jo pritaikymas skirtinguose eksperimentuose galimas keičiant modelio parametrus naudojant tą patį akustinio veikimo principą.

146

4. Skaitmeninis akustinio slėgio paskirstymo modeliavimas leidžia suprasti slėgio pasiskirstymo nanovamzdelio viduje reiškinį veikiant paviršiaus akustikai ir gali būti panaudotas kuriant mikrohidraulinį filtravimo įrenginį pritaikant PZT valdymą.

Ginamieji teiginiai

1. Peltje elemento pagrindu sukurta aušinimo sistema leidžia kontroliuoti arba palaikyti pastovią temperatūrą elektrocheminio anodavimo proceso metu, o tai tiesiogiai veikia membranos nanoporėtos struktūros kokybę, kuri savo ruožtu įtakoja pritaikymą mikro- / nano- biodalelių filtravimo / atskyrimo procesuose.
2. Sukurta eksperimentinio tyrimo metodika, leidžianti įvertinti mikro- / nano- elemento funkcionalumą ir panaudojimą mikrohidraulinėms arba mikrofluidinėms sistemoms biomedicinos srityje.
3. Veikiančio dažnio padidinimas sukelia įvairias membranos formos deformacijas ir leidžia koreguoti nanoporėtoje membranoje susidariusių nanovamzdelių formą, kad būtų pašalinama užsikimšimo tikimybė ir padidinamas mikrohidraulinėse sistemose vykstančio filtravimo proceso efektyvumas biomedicininės paskirties prietaisuose.

Tyrimo rezultatų publikavimas ir aprobavimas

Disertacijoje pateikti tyrimo rezultatai publikuoti septyniuose moksliniuose straipsniuose. Du iš jų skelbti Q1 ir Q4 žurnaluose „Web of Science" duomenų bazėje su citavimo indeksu, trys iš jų – „Web of Science" duomenų bazėje be citavimo indekso, o dar du įtraukti į konferencijos pranešimų medžiagą. Tyrimo rezultatai buvo pristatyti devyniose tarptautinėse konferencijose: „Materials today" pranešimų medžiaga: „3rd International Conference on Aspects of Materials Science and Engineering" (ICAMSE 2021, Indija), „Materials today" pranešimų medžiaga: „2nd International Conference on Aspects of Materials Science and Engineering" (ICAMSE 2022, Indija), „IEEE XVIth International Conference on the Perspective Technologies and Methods in MEMS Design" (MEMSTECH, Ukraina 2020), „SPIE: Frontiers in Ultrafast Optics: Biomedical, Scientific, and Industrial Applications" (JAV 2020), NATO seminaras apie pažangias nanomedžiagas ChBRB aptikimui (Ukraina, 2019), 65-oji tarptautinė fizinių bei gamtos mokslų studentų ir jaunųjų mokslininkų konferencija („Open readings" 2022, Lietuva), 2-asis tarptautinis tyrėjų seminaras Biomechaninės mikrosistemos (IRWBM 2021, Lietuva), 63-ioji tarptautinė fizinių bei gamtos mokslų studentų ir jaunųjų mokslininkų konferencija („Open readings" 2020, Lietuva) ir tarptautinis tyrėjų Biomechaninės mikrosistemų seminaras (IRWBM 2019, Lietuva).

Disertacijos apimtis ir struktūra

Daktaro disertaciją sudaro įvadas, 5 pagrindiniai skyriai, išvados, literatūros sąrašas, disertacijos santrauka ir autoriaus publikacijų sąrašas bei gyvenimo aprašymas (CV). Disertacijos apimtis – 176 puslapiai. Pagrindinėje disertacijos dalyje, apimančioje 118 puslapių, yra 93 paveikslai, 36 lentelės ir 191 mokslinės literatūros šaltinis.

1. Funkcinėmis savybėmis pasižyminčių mikro- / nano- porėtų membranų, naudojamų biomedicininės paskirties mikrohidrauliniuose prietaisuose, gamybos ir pritaikymo apžvalga

Norint sukurti naujos kartos mikro- / nano- komponentus mikrohidrauliniuose įrenginiuose, reikalingas tinkamas eksperimentinių veiksmų planas ir funkcinio elemento, skirto mikro- / nano- dalelėms skystyje filtruoti ir atskirti, gamybos būdas. Atsižvelgiant į šiuos aspektus, svarbu suprojektuoti efektyvią eksperimentinę schemą ir kontroliuojamos porėtos struktūros mikro- / nano- membranų gamybos metodą, kad gautos membranos galėtų būti naudojamos įvairiems tikslams biomedicinos srityje.

Biologinių dalelių atskyrimas ir filtravimas yra svarbus etapas atliekant kokybinės ir kiekybinės analizės eksperimentus biochemijos ir biomedicinos pramonės srityse, projektuojant naujus efektyvesnius gamybos įrenginius, todėl itin aktualus tampa šio metodo našumo didinimo klausimas. Naujausi tyrimų rezultatai rodo, jog mikrofluidinių prietaisų, skirtų filtravimo ir atskyrimo procesams mikro- / nano- lygmenyje, veikimas gali būti patobulintas pritaikius membraninio mikrofiltravimo techniką [37–38]. Mikro- / nano- membraninis filtravimas yra gana naujas metodas, pasižymintis tam tikrais privalumais, pvz., gebėjimas plūduriuoti, mažas energijos suvartojimas, skysčių valymas nenaudojant cheminių medžiagų arba žema darbinė temperatūra. Anksčiau skysčių valymui buvo naudojamos įvairios technologijos, įskaitant distiliavimą ir apdorojimą cheminėmis dezinfekavimo priemonėmis. Pastaruoju metu nanoporėtos anoduotos aliuminio oksido membranos (AAO) sulaukia didelio tyrėjų dėmesio dėl universalaus pritaikymo mikroelektromechaninių sistemų (MEMS) srityje [41]. Naujos kartos mikrofluidiniai prietaisai, kuriuose naudojamos nanoporėtos membranos, turi pasižymėti išskirtinėmis savybėmis, kad galėtų efektyviai vykdyti dalelių filtravimo ir atskyrimo procesus biologinėje aplinkoje [43].

Manipuliacijos dalelėmis pageidaujamos daugelyje pritaikymo sričių, pvz., biomedicininės paskirties prietaisuose, klinikinėje diagnostikoje, vaistų pristatymo procesuose ir savaime išsivalančių paviršių technologijoje. Sparti mikro- ir nanoinžinerijos pažanga paskatino sukurti daugybę manipuliavimo dalelėmis būdų, įskaitant jau įprastus mikrofluidinius metodus [75]. Atskira dalelė turi unikalų dydį, tankį ir manipuliacijos dažnius. Todėl įvairūs metodai, naudojami dalelių valdymui mikro- / nano- erdvėje, apima hidrodinaminius metodus, akustinį metodą, elektrinį metodą, optinį pincetą ir magnetinį metodą [78–80]. Bekontaktis akustoforezės

metadas, leidžiantis manipuliuoti skystyje esančiomis dalelėmis: akustinė jėga, kuri išsklaido daleles į erdvės pakraščius, arba akustinė jėga, sukurianti srautą, leidžiantį daleles tempti kartu su skysčiu. Dalelių tvarkymas ir valdymas šiuo metodu vadinamas akustoforeze [86]. Tokiu būdu galima valdyti pavienes daleles ar didelius jų kiekius bekontakčiu būdu, sukuriant akustinį srautą. Remiantis akustoforezės reiškiniu, akustinio slėgio naudojimas dalelių manipuliavimui mikro- / nano- vamzdelyje gali būti generuojamas pjezoelektrinio sužadinimo būdu. Tai padeda mikro- / nano- dalelėms susitelkti nanovamzdelių centre ir tokiu būdu sumažinti trintį tarp dalelių ir nanovamzdelio sienelės. Naudojant šį metodą, sumažėja biomedicinos prietaisuose vykstančiuose filtravimo ir atskyrimo procesuose dalyvaujančių biodalelių pažeidimo rizika. Todėl svarbu sukurti pagamintų nanoporėtų aliuminio oksido membranų, naudojamų vibroaktyvaus nanofiltravimo procesuose, paviršinių akustinių bangų, akustinio slėgio nanovamzdelio viduje ir rezonansinio režimo skaitmeninį modelį ir atlikti eksperimentinę analizę.

Anksčiau publikuotų tyrimų rezultatai rodo, jog nanoporėtos aliuminio oksido membranos gali būti sėkmingai pritaikytos skirtingose biologinėse sistemose mikro- / nano- filtravimo, vaistų pristatymo, dalelių rūšiavimo, nanomodeliavimo ir biodalelių ultrafiltravimo procesuose [108–110]. Biomolekulių atskyrimas taikomas biomedicinos srityje. Svarbiausios nanoporėto AAO savybės yra didelis srauto greitis, porų skersmuo, porėtos membranos storis, geras mechaninis ir cheminis atsparumas ir tolygi struktūra. Poringumo ir storio parametrai naudojami nustatant biomedicininiams tikslams naudojamos nanoporėtos AAO membranos srauto greitį ir mechaninį stabilumą [163]. Nanoporėtos AAO membranos hidrofobinių savybių nustatymas yra svarbus norint suprasti skysčio ir pagamintos membranos sąveiką ir pagerinti skysčio prasiskverbimą. Tam reikia parinkti tinkamą išskirtinėmis charakteristikomis pasižyminčių nanoporėto aliuminio oksido membranų gamybos būdą ir įrangą bei ištirti susidariusio nanoporėto sluoksnio struktūrą, storį, hidrofobines bei mechanines savybes.

Todėl akivaizdu, kad itin aktualus tampa veiksmingos ir nebrangios membranų gamybos technologijos, panaudojant paviršinių bangų akustiką mikro- / nano- dalelių atskyrimui / filtravimui, vystymo klausimas. Šiame darbe pristatomi filtravimo / atskyrimo procesuose pritaikomų nanoporėtų aliuminio oksido membranų tyrimai ir plėtra, įskaitant gamybos procesą, charakterizavimą, savybių ištyrimą ir paviršiaus akustinių bangų moduliavimą nanoporėtos AAO membranos paviršiuje naudojant PZT keitiklį. Be to, apžvelgiamos nanoporėtos AAO membranos panaudojimo dujų atskyrimui galimybės.

2. Aušinimo sistemos su Peltje elementu sukūrimas ir pritaikymas nanoporėtų aliuminio oksido membranų gamybai skirtame eksperimentiniame stende

Disertacijos tikslas – suprojektuoti Peltje elemento pagrindu veikiančią aušinimo sistemą ir pritaikyti ją eksperimentiniame stende, skirtame nanoporėtų tolygios struktūros aliuminio oksido membranų gamybai, naudojant dviejų etapų

elektrocheminį anodavimo procesą, kad jos būtų sėkmingai pritaikytos mikrohidraulinio filtravimo įrenginiuose ir nanodalelių atskyrimui biomedicinos sistemose. Remiantis mokslinės literatūros analizės duomenimis, tolygi porėta struktūra suformuojama, kai elektrolito temperatūra elektrocheminio anodavimo proceso metu svyruoja nuo 0 iki 5 ºC [126]. Aušinimo sistema buvo suprojektuota ir naudojama konstruojant eksperimentinį stendą, skirtą efektyviam elektrocheminio anodavimo procesui, kurio metu gaminamos nanoporėtos AAO membranos. Aušinimo sistemą, skirtą eksperimentiniam membranos gamybos stendui sukurti, sudaro Peltje elementas („TEC1-12715") su pagrindine aušintuvo sistema („MLW-D24M"), skirta vėsinti kitą Peltje elemento pusę. 1 pav. pavaizduota aušinimo sistemos schema, kuri susideda iš stiklinio indo (1), Peltje elemento (2), pagrindinio aušintuvo siurblio (3), pagrindinio aušintuvo radiatoriaus (4), maitinimo bloko Peltje elementui ir pagrindinio aušintuvo (5), magnetinės maišyklės (6) ir maišyklės magnetuko (7). Papildomai buvo naudojami elektros laidai ir termopasta, skirta Peltje elementui pritvirtinti prie stiklinio indo.
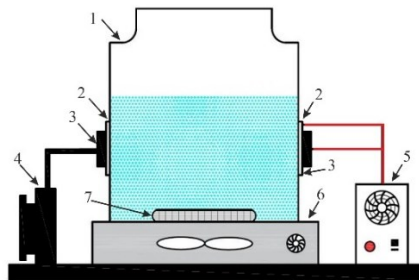
1 pav. Eksperimentiniame stende naudojama aušinimo sistemos su Peltje elementu schema

Teorinė anodavimo proceso metu vykstančių temperatūros pokyčių simuliacija atlikta naudojant programą „COMSOL Multiphysics 5.4". Temperatūros analizės simuliacijos modelis pavaizduotas 2 pav.


a   b
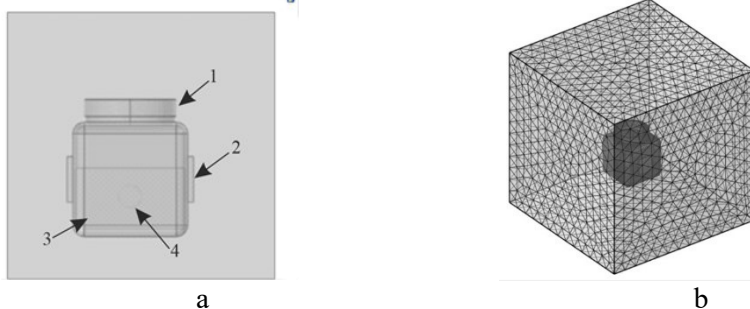
**2 pav.** Simuliacijos modelis aušinimo sistemai (a) ir į baigtinius elementus suskaidyto tinklo modelis (b)

Aušinimo sistemos simuliacijos modelis, skirtas temperatūros analizei anodavimo proceso metu (2 pav.), susideda iš stiklinio indo (1), Peltje elemento (2), 150

elektrolito tirpalo (3) ir membranos (4). Iš pradžių visų elementų temperatūra buvo nustatyta ties 20 ºC. Elektrinis potencialas aliuminio membranai buvo nustatytas ties 60 V, o Peltje elementui ties 12 V. Elektros srovė aliuminio membranai buvo nustatyta ties 1 A aliuminio membranai ir ties 6 A Peltje elementui. Laikui bėgant analizės modelis buvo keičiamas, nes jis skirtas įvertinti, per kiek laiko elektrolito tirpalas pasieks 5–6 ºC temperatūrą. Ši analizė truko nuo 0 iki 60 minučių esant 1 minutės intervalui.

3 pav. pavaizduoti temperatūros analizės simuliacijos rezultatai, kuriais remiantis galima įvertinti temperatūros pasiskirstymą inde ir aplinkoje. Peltje elementų temperatūra nukrenta iki 2 °C. Pati aliuminio oksido membrana šiek tiek įkaista, tačiau skysčio temperatūrai tai įtakos neturi, todėl skysčio temperatūra išlieka pastovi, t. y. maždaug 2–3 °C.
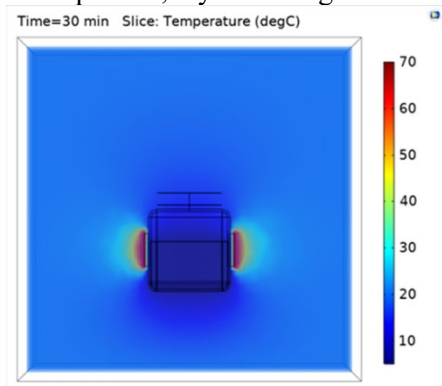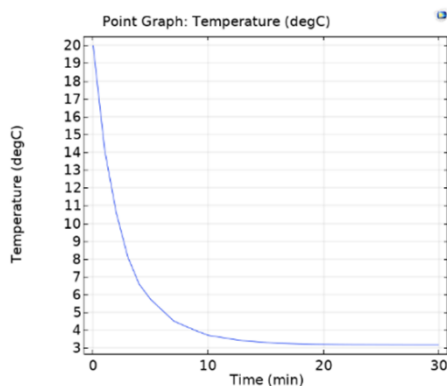
3 pav. Aušinimo sistemos simuliacijos rezultatai naudojant du Peltje elementus (a) ir elektrolito temperatūros priklausomybės nuo laiko grafikas (b)

Temperatūros analizės su Peltje elemento aušinimo sistema ir be jos simuliacijos rezultatai rodo, kad elektrolito temperatūra palaipsniui mažėja ir per 15 min. pasiekia 2–3 °C. Simuliacijos rezultatai rodo, kad aušinimo sistema efektyviai palaiko temperatūrą stiklinio indo viduje anodavimo metu, todėl aušinimui naudojami du Peltje elementai („TEC112715").
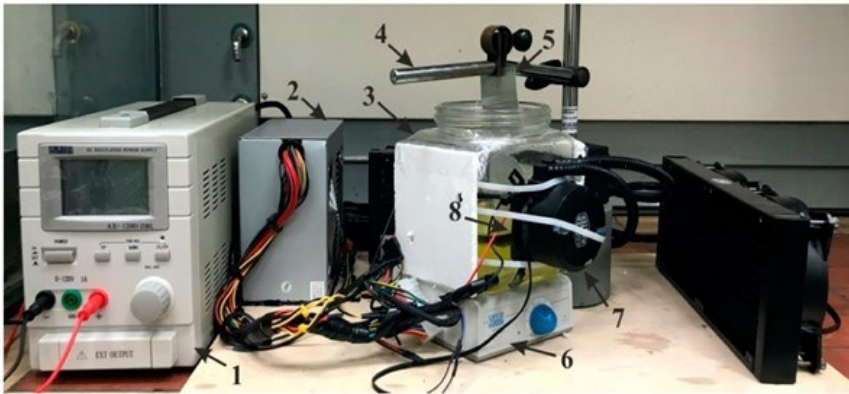
4 pav. Sukurtas eksperimentinis nanoporėtų aliuminio oksido membranų gamybos stendas

Remiantis gautais duomenimis, buvo sukurtas nanoporėtų AAO membranų gamybai skirtas eksperimentinis stendas (4 pav.) Eksperimentinį stendą sudaro nuolatinės srovės maitinimo šaltinis (1), skirtas nuolatinei srovei ir įtampai tiekti į aliuminio plokštelę anodavimo proceso metu. Maitinimo blokas (2) skirtas elektrai tiekti į Peltje elementą ir pagrindinį aušintuvą, pritvirtintą kitoje Peltje elemento pusėje (karštojoje pusėje). Stiklinio indo (3) viduje yra anodavimui naudojamas elektrolito tirpalas, teigiamas ir neigiamas elektrodai bei magnetinė maišyklė, skirta užtikrinti pastovų skysčio judėjimą stiklinio indo viduje. Stovas mėginių laikikliui (4) buvo naudojamas bandinio tvirtinimui stikliniame inde anodavimo proceso metu. Bandinys (5) – aliuminio lakštas (1050A) – buvo naudojamas nanoporėtos struktūros aliuminio oksidui gaminti. Magnetinė maišyklė (6) skirta nuolatiniam skysčio maišymui anodavimo proceso metu, siekiant sumažinti šilumos koncentraciją vienoje vietoje. Pagrindinis aušintuvas (7) naudojamas kitai kaistančiai Peltje elemento pusei atvėsinti, siekiant išvengti Peltje elemento perkaitimo. Peltje elementas (8) naudojamas palaikyti elektrolito tirpalo temperatūrą, siekiant užtikrinti efektyvesnį anodavimo procesą.

Aliuminio oksido membranos gamybai buvo pasirinktas 400 ºC temperatūroje 4 valandas azoto aplinkoje atkaitinto aliuminio lakštas (99,3 % gryno aliuminio, 0,5 mm storio), siekiant sumažinti aliuminio plokštelės kietumą ir užtikrinti efektyvų anodavimo procesą. Nanoporėtos AAO membranos buvo gaminamos naudojant dviejų etapų anodavimo metodą (švelnusis anodavimas ir kietasis anodavimas). Visas gamybos procesas yra suskirstytas į du etapus. Pirmajame etape (švelnusis anodavimas) sukuriamos nestruktūrizuotos poros, kurios pašalinamos ėsdinimo metu, o antrasis etapas (kietasis anodavimas) sukuria tvarkingą porėtą aliuminio oksido struktūrą.

Pirmiausia atkaitintas aliuminio lakštas buvo supjaustytas į atskirus numatytos formos bandinius, kad būtų galima juos pritvirtinti sukurto mėginio laikiklio viduje (5a pav.). Detalus suprojektuoto bandinio laikiklio brėžinys pavaizduotas 5b pav. Mėginio laikiklis leidžia pasirinkti konkrečią pageidaujamą bandinio anodavimo

sritį (skersmuo, 15–30 mm), o likusį bandinio plotą izoliuoja nuo anodavimo proceso.

a

b
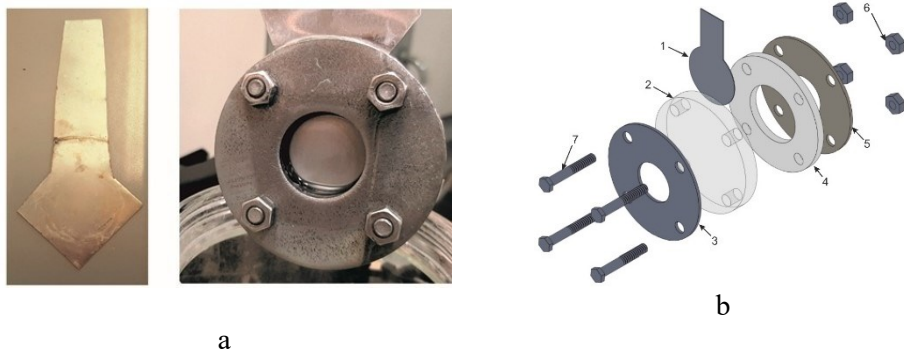
5 pav. Naudotos formos bandinys ir pagal užsakymą pagamintas mėginių laikiklis (a) bei detalus mėginio laikiklio brėžinys (b)

Pagal užsakymą pagamintą bandinių laikiklį (5b pav.), skirtą nanoporėtų AAO membranų gamybai, sudaro išpjautas aliuminio lakšto mėginys (1), akrilnitrilo butadieno stirenas (2), apatinė nerūdijančio plieno plokštelė (3), silikoninė tarpinė (4), viršutinis nerūdijančio plieno dangtelis (5), M16 veržlės (6) ir M16 varžtai (7).

1 lentelė. Dviejų etapų anodavimo procedūra, skirta nanoporėtų AAO membranų gamybai

| Žingsnis	Aprašymas
1	Pirmasis anodavimo (švelniojo anodavimo) procesas vykdomas numatytą laiką (50/60 V DC) 0,3 M oksalo rūgšties ($C_2H_2O_4$) tirpale.
2	Netvarkingos porėtos struktūros ėsdinimas numatytą laiką naudojant tam tikros temperatūros 3,5 % fosforo rūgšties (H_3PO_4) ir 2 % chromo anhidrido (CrO_3) rūgšties tirpalą (pagal tūrį) distiliuotame vandenyje.
3	Mėginio ir laikiklio valymas distiliuotu vandeniu.
4	Antrasis anodavimo (kietojo anodavimo) procesas vykdomas numatytą laiką (50/60 V DC) 0,3 M oksalo rūgšties ($C_2H_2O_4$) tirpale.
5	Pabaigus du anodavimo etapus, paruoštas mėginys apverčiamas ir vėl dedamas į mėginio laikiklį, kad apatinis aliuminio sluoksnis būtų nuėsdintas druskos rūgšties (HCl), vario chlorido dihidrato ($CuCl_2$) ir distiliuoto vandens (1 : 0,3 : 1) tirpale esant kambario temperatūrai.
6	Mėginio valymas distiliuotu vandeniu.
7	Nuvalytas mėginys panardinamas į 5 % fosforo tirpalą 15-ai minučių esant kambario temperatūrai, kad būtų atidaryta kita porų pusė (pašalinamas barjerinis sluoksnis).
8	Galiausiai paruošti mėginiai nuplaunami distiliuotu vandeniu ir acetonu (C_3H_6O) bei išdžiovinami.

Prieš pradedant dviejų etapų anodavimo procesą (žr. 1 lentelę), bandinys buvo supjaustytas į numatytosios formos atskirus mėginius, kurie buvo nuvalyti acetone

153

(C$_3$H$_6$O) naudojant ultragarsą 5 minutes. Siekiant pašalinti aliuminio bandinio paviršiuje esančius įbrėžimus, buvo atliktas mechaninis valymas naudojant poliravimo diską. Po to buvo atliktas elektrocheminis poliravimas 1 minutę esant 20 V įtampai fosforo rūgšties (H$_3$PO$_4$), sieros rūgšties (H$_2$SO$_4$) ir vandens tirpale santykiu 2 : 2 : 1, kad būtų sumažintas paviršiaus šiurkštumas. Atlikus išankstinio anodavimo procedūrą, mėginys buvo pritvirtintas laikiklyje ir įdėtas į elektrolitu pripildytą stiklinį indą, kuriame vykdoma dviejų etapų anodavimo procedūra. Naudojant dviejų etapų anodavimo procedūrą, buvo paruošti šeši skirtingi mėginiai. Eksperimentinė matrica pateikta 2 lentelėje.

2 lentelė. Pagamintų nanoporėtų AAO membranų eksperimentinė matrica

Mėginio Nr.	Įtampa, VDC	Anodavimo laikas, (h)		Ėsdinimo temperatūra	Ėsdinimo laikas	Elektrolito sudėtis	Anodavimo temperatūra
		I etapas	II etapas				
1A	50	1,5	15				
1B	50	1,5	16			0,3 M Oksalo rūgštis (C$_2$H$_2$O$_4$)	
1C	50	1,5	17	60 °C	30 minučių		0–3 °C
2A	60	1,5	15				
2B	60	1,5	16				
2C	60	1,5	17				

Nanoporėtų AAO membranų, pagamintų naudojant dviejų etapų anodavimo metodą, esant skirtingiems proceso parametrams (2 lentelė), nuotraukos pateiktos 6 ir 7 pav.
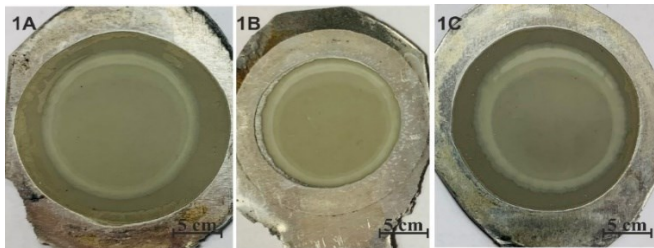

6 pav. Nanoporėta aliuminio oksido membrana, pagaminta esant 50 V nuolatinei įtampai
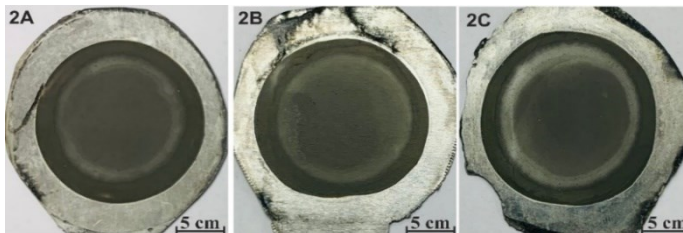
7 pav. Nanoporėta aliuminio oksido membrana, pagaminta esant 60 V nuolatinei įtampai

Kaip parodyta 6 pav., trys AAO membranos (1A, 1B ir 1C) buvo pagamintos esant 50 V nuolatinei įtampai, kai anodavimo laikas atitinkamai yra 15 val., 16 val. ir 17 val. Analogiškai, trys AAO membranos (2A, 2B ir 2C) buvo pagamintos esant 60 V nuolatinei įtampai, kai anodavimo laikas atitinkamai yra 15 val., 16 val. ir 17 val. (7 pav.). Anodavimo proceso metu, gaminant nanoporėtas AAO membranas, buvo atlikta eksperimentinė aušinimo sistemos temperatūros analizė (8 pav.).
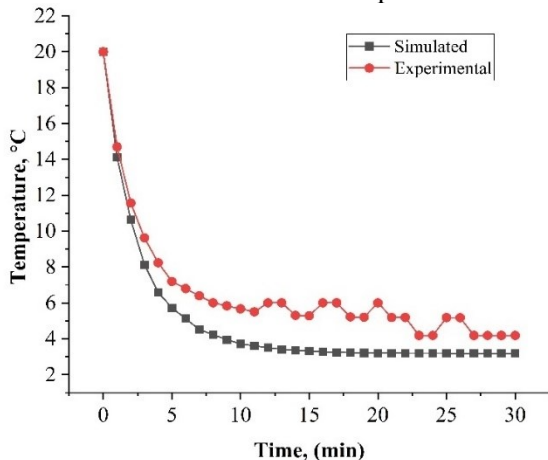
8 pav. Aušinimo sistemos temperatūros analizės teorinių ir eksperimentinių rezultatų palyginimas

Nanoporėtų AAO membranų gamyboje naudojamos aušinimo sistemos eksperimentiniai ir simuliacijos rezultatai yra atitinkamai 4 ºC ir 3 ºC po 30 min. Ženklaus rezultatų skirtumo nepastebėta. Galima teigti, kad suprojektuota aušinimo sistema yra patikima palaikant pastovią temperatūrą nanoporėtų AAO membranų gamybos metu taikant elektrocheminio anodavimo procedūrą.
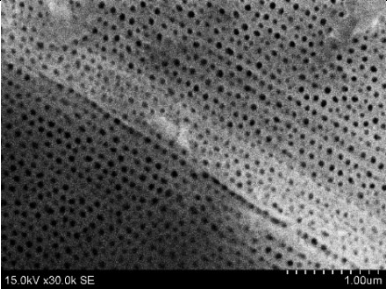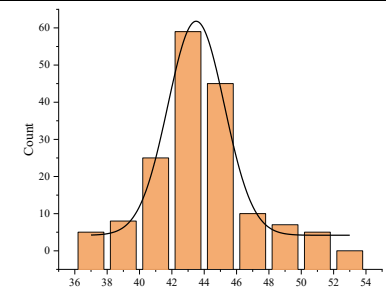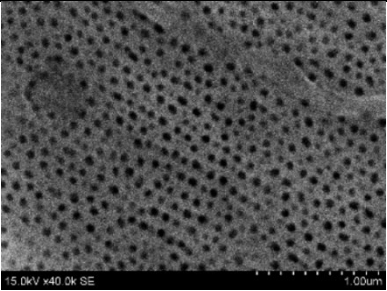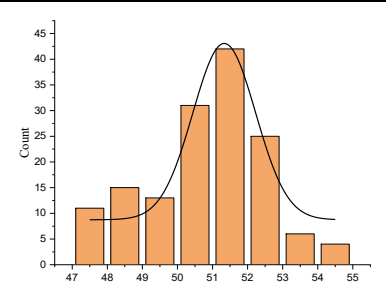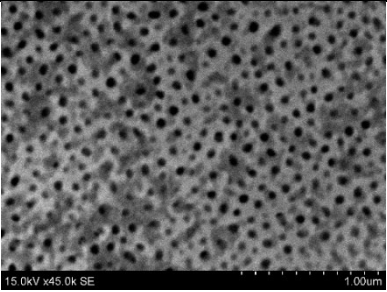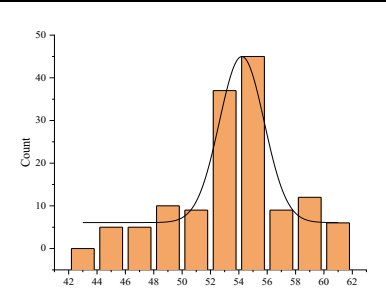
3. Pagamintų nanoporėtų aliuminio oksido membranų geometrinės struktūros, sintezės ir hidrofobinių savybių tyrimas

Pagamintos nanoporėtos AAO membranos bus naudojamos kaip vibroaktyvus mikro- / nano- filtras mikrohidrauliniame įrenginyje. Taigi, atsižvelgiant į pritaikymo sritį, svarbu atlikti geometrinės struktūros, cheminės sudėties ir hidrofobinių savybių analizę.

Skenuojančios elektroninės mikroskopijos (SEM) analizė buvo atlikta siekiant įvertinti pagamintų nanoporėtų AAO mėginių (1A, 1B, 1C, 2A, 2B ir 2C) porų skersmenį, atstumą tarp porų ir sluoksnio storį. Pagamintų nanoporėtų AAO membranų 1A, 1B ir 1C (esant pastoviai 50 VDC anodavimo įtampai) ir 2A, 2B ir 2C (pagamintų esant anodavimo įtampai 60 VDC) SEM vaizdai, kai anodavimo laikas yra 15 val., 16 val. ir 17 val., pateikiami 3 lentelėje.

Pagamintų membranų SEM vaizdai patvirtina, kad AAO membranas sudaro porėta struktūra (korio tipo), o histograma parodo porų skersmens pasiskirstymą pagamintos AAO membranos paviršiuje.

3 lentelė. Pagamintų nanoporėtų AAO membranų SEM nuotraukos ir porų pasiskirstymo histograma

Mėginio Nr.	SEM nuotrauka	Porų pasiskirstymo histograma
1A		
1B		
1C		

Informacija apie mėginių, pagamintų naudojant 50 V (1A, 1B ir 1C) ir 60 V (2A, 2B ir 2C) įtampą ir esant skirtingiems anodavimo laikams, porų skersmenį (D_p), atstumą tarp porų (D_c), poringumą ir porų užpildymą apibendrinta 4 lentelėje.

4 lentelė. Pagamintoms nanoporėtoms AAO membranoms būdingi parametrai, kai anodavimui naudojama 50 V ir 60 V įtampa

Mėginio Nr.	Anodavimo laikas, (val.)	Porų skersmuo, (nm)	Atstumas tarp porų, (nm)	Poringumas, (%)	Porų užpildymas, (cm⁻¹*10⁹)	Membranos storis, (µm)
1A	15	43,5 ± 10	111 ± 10	14,25	4,68	74,50
1B	16	51,33 ± 8	113 ± 10	19,20	4,14	80,40
1C	17	55,62 ± 10	110 ± 10	23,50	3,87	83,01
2A	15	49,38 ± 6	115 ± 10	17,14	4,29	86,72
2B	16	58,55 ± 5	113 ± 10	22,67	3,87	88,60
2C	17	65,81 ± 15	112 ± 10	32,64	3,81	95,60

157

Atsižvelgiant į gautus rezultatus, galima matyti, kad porų skersmuo (D_P) priklauso nuo anodavimo laiko ir pasirinktos įtampos. Kitaip tariant, ilgėjant anodavimo laikui porų skersmuo (D_P) padidėja, tuo tarpu atstumas tarp porų išlieka nepakitęs nepriklausomai nuo pasirinktos įtampos. Didžiausias porų skersmuo nustatytas analizuojant 2C mėginį (65,81 ± 15 nm), kuris buvo anoduojamas 17 val. naudojant 60 V įtampą. Tiesa, membranos poringumas priklauso nuo susiformavusios struktūros. Kitaip tariant, jei lyginant su atstumu tarp porų, porų skersmuo yra didelis, membranos poringumas taip pat bus didesnis. Siekiant pritaikyti AAO membraną mikrohidraulinėse filtravimo sistemose, ji turi pasižymėti gana didelio poringumo struktūra, kurią, remiantis gautis rezultatais, būtų galima išgauti naudojant aukštesnę anodavimo įtampą ir ilgesnį anodavimo laiką.
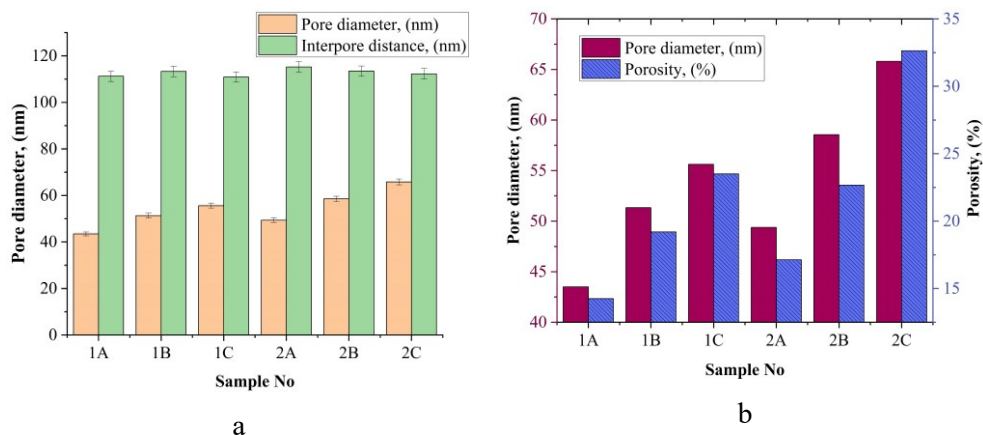
9 pav. Pagamintų nanoporėtų AAO membranų porų skersmuo ir atstumas tarp porų (a) bei porų skersmuo ir poringumas (b)

Pagamintų nanoporėtų AAO membranų porų skersmens ir atstumo tarp porų (9a pav.) bei porų skersmens ir poringumo (9b pav.) rezultatai priklauso nuo dviejų etapų anodavimo procedūros parametrų. Buvo apskaičiuotas pagamintos nanoporėtos AAO membranos poringumas atsižvelgiant į porų skersmenį. Pagamintų AAO membranų poringumas taip pat didėja didėjant porų skersmeniui. Membranų, pagamintų esant 50 V ir 60 V įtampai, poringumas svyruoja atitinkamai intervaluose nuo 14 iki 24 % ir nuo 17 iki 33 %. Pagamintų nanoporėtų AAO membranų storis taip pat priklauso nuo anodavimo laiko ir naudojamos įtampos. Pagamintos nanoporėtos AAO membranos skerspjūvio nuotrauka (10 pav.) patvirtina, kad nanovamzdeliai susiformuoja tarsi poringo paviršiaus liestinės.
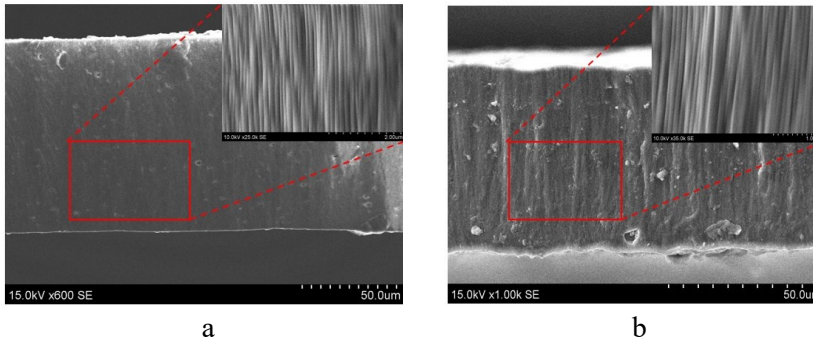
10 pav. AAO membranos, pagamintas esant 50 V (a) ir 60 V (b) įtampai, skerspjūvio SEM nuotrauka

Tokiu būdu buvo ištirta dviejų AAO membranų (1C ir 2C), pagamintų naudojant skirtingą anodavimo įtampą (50 V ir 60 V), tačiau vienodą anodavimo laiką (17 val.), elementinė sudėtis, o rezultatai yra pateikiami 11 pav.
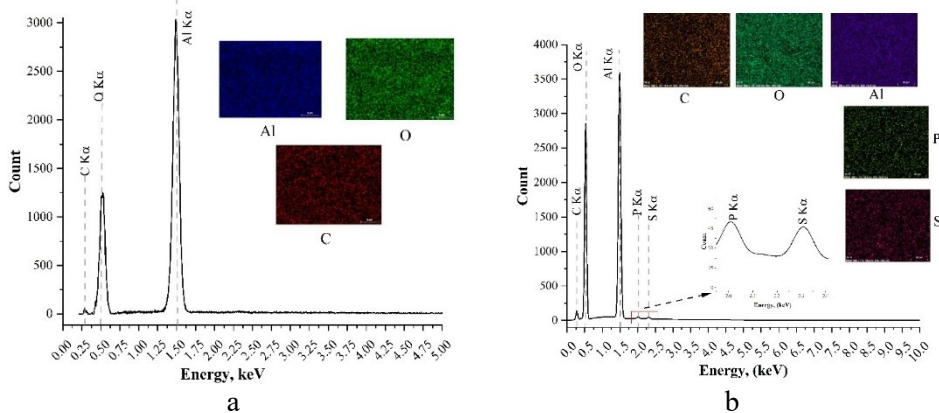
11 pav. Pagamintų nanoporėtų AAO membranų mėginių 1C (a) ir 2C (b) EDS analizė

1C pavyzdyje, pagamintame esant 50 V nuolatinei įtampai ir 17 val. anodavimo trukmei (11a pav.), anglies (C) Kα smailė buvo užfiksuota ties maždaug 0,27 keV. Deguonies (O) Kα smailės išryškėjo esant maždaug 0,5 keV. Aukščiausia aliuminio (Al) Kα smailė užfiksuota esant 1,50 keV. Panašiai kaip ir 2C mėginio atveju (11b pav.), anglies (C) Kα smailė buvo mažesnė, esant 0,27 keV. Deguonies (O) Kα smailės atsiskyrimas buvo užregistruotas esant 0,5 keV. Kaip ir 1C mėginio analizės atveju, aukščiausia smailė buvo užfiksuota aliuminiui (Al) esant 1,5 keV. Šiame pavyzdyje buvo užfiksuotos dar dvi nedidelės smailės, atitinkančios fosforą (P) ir sierą (S), atitinkamai esant 2,013 keV ir 2,307 keV.

Specialiose lentelėse nurodyta kiekvieno elemento padėtis atitinka būdingą mėginio smailę, nurodančią perėjimą jo elektroniniame apvalkale. Anglis (C), deguonis (O) ir aliuminis (Al) yra trys pagrindiniai elementai, nustatyti abiejuose

159

měginiuose. Abiejų měginių EDS analizė rodo aliuminio oksido (Al_2O_3) dominavimą.
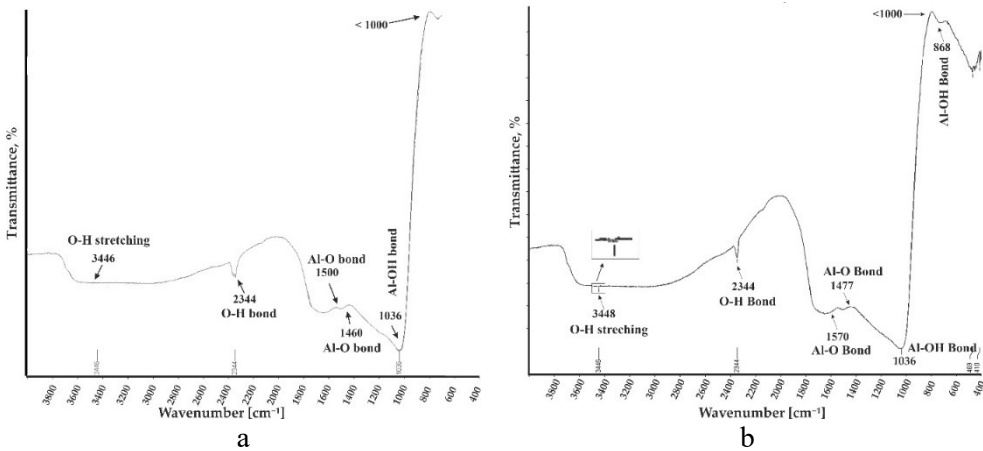
12 pav. Pagamintų nanoporėtų AAO membranų měginių 1C (a) ir 2C (b) FTIR spektrai

Toliau aprašoma pagamintų nanoporėtų AAO membranų měginių 1C ir 2C FTIR analizė. Nanoporėtų AAO membranų měginių 1C ir 2C rezultatai pateikiami atitinkamai 12a ir 12b pav. FTIR pralaidumo spektrams buvo pasirinktas intervalas 4000–500 cm^{-1}, nes tai yra tipiškas tokio tipo analizės spektro intervalas.

Abiejų měginių (1C ir 2C) FTIR spektrai atitinka aliuminio oksido spektrus, o tai patvirtina sėkmingą aliuminio oksido membranos gamybą naudojant dviejų etapų anodavimo metodą esant 50 V ir 60 V įtampai [180–181].

Kadangi pagaminta nanoporėta AAO membrana bus naudojama vibroaktyviam nanofiltravimui mikrohidrauliniame įrenginyje, svarbu įvertinti AAO membranos paviršiaus hidrofobines savybes. Pagamintų nanoporėtų AAO membranų hidrofobinės savybės buvo analizuojamos išmatuojant distiliuoto vandens lašo kontaktinį kampą ant pagamintos nanoporėtos AAO membranos paviršiaus naudojant sukurtą stendą (13 pav.).
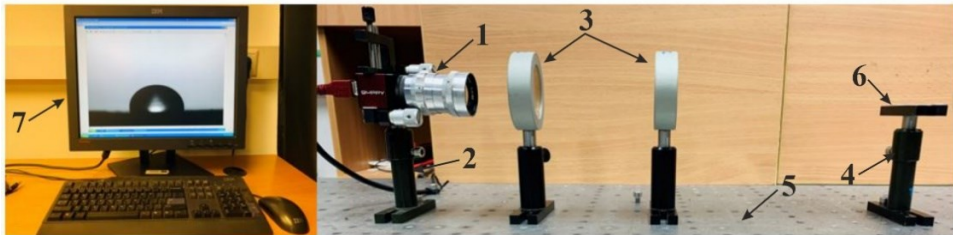
13 pav. Eksperimentinis stendas, skirtas kontaktiniam kampui matuoti

Eksperimentinis stendas (13 pav.), skirtas kontaktiniam kampui matuoti, susideda iš: didelės spartos kameros („Guppy F-503, B&W CMOS" kamera, 1595 x 1944 raiška, 1394A ryšio tipas, kadrų dažnis 60 kadrų per sekundę ir ½ colio

jutiklis) (1), reguliuojamo fotoaparato laikiklio (2), dvigubai išgaubtų lęšių (objektyvo skersmuo 50 mm ir židinio nuotolis 500 mm) (3), reguliuojamo mėginio stovo (4), antivibracinio stalo (5), pagamintos nanoporėtos aliuminio oksido membranos (6) ir kompiuterinės sistemos su programine įranga, kuri yra skirta didelės raiškos vaizdams užfiksuoti (7).
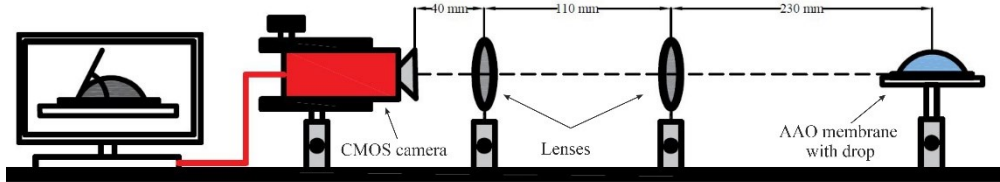
14 pav. Kritinis atstumas tarp optinės įrangos ir skysčio lašo

Kritinis atstumas tarp fotoaparato, objektyvo ir mėginio labai svarbus norint užfiksuoti itin aukštos kokybės vaizdus. Kritinis atstumas tarp svarbių optinių dalių ir bandinio yra pavaizduotas 14 pav.
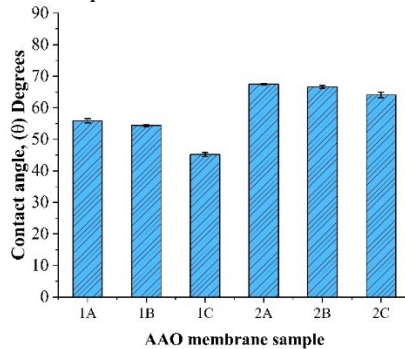
15 pav. Pagamintų nanoporėtų AAO membranų hidrofobinių savybių palyginimas

Remiantis kontaktinio kampo matavimo rezultatais (15 pav.), buvo pastebėta, kad visi pagamintų nanoporėtų AAO membranų pavyzdžiai pasižymi hidrofilinėmis savybėmis. Tyrimo metu buvo išmatuotas vandens lašo kontaktinis kampas (θ) ant visų šešių nanoporėtų AAO membranų bandinių 1A, 1B, 1C, 2A, 2B ir 2C paviršių. Naudojant kiekvieną bandinį, t. y. 1A, 1B, 1C, 2A, 2B ir 2C, buvo atlikti keli matavimai, o išmatuoto kontaktinio kampo vidutinė vertė kiekvienam bandiniui atitinkamai yra $55,87 \pm 0,69°$, $54,38 \pm 0,30°$, $45,16 \pm 0,60°$, $67,44 \pm 0,56°$, $66,58 \pm 0,50°$ ir $64,07 \pm 0,90°$. Taip pat buvo gautas grafinis išmatuoto distiliuoto vandens lašo kontaktinio ant skirtingų pagamintų nanoporėtų AAO paviršių vaizdas. Gautos kontaktinio kampo vertės yra mažesnės nei 90°, vadinasi, tiriamieji mėginiai taip pat pasižymi hidrofilinėmis savybėmis vandens atžvilgiu. Abiem atvejais buvo pastebėta, kad pailgėjus anodavimo laikui kontaktinio kampo vertė sumažėja. Kitaip tariant, padidėjus porų skersmeniui, kontaktinio kampo vertė sumažėja.

Zismano diagramos analizės rezultatai rodo, kad 1A pavyzdžio kritinė paviršiaus įtampa yra σ_{cri} = 12,03 mN/m, 1B pavyzdžio σ_{cri} = 5,9 mN/m, 1C – σ_{cri} = 11,5 mN/m, 2A – σ_{cri} = 16,03 mN/m, 2B – σ_{cri} = 16,50 mN/m, o 2C – σ_{cri} = 17,30 mN/m. Didžiausias kritinis paviršiaus įtempis buvo nustatytas pagamintam nanoporėtos AAO membranos mėginiui 2C, t. y. 17,30 mN/m.

Bet kokio skysčio kontaktinis kampas visada priklauso nuo medžiagų ir jo cheminės prigimties. Yra nustatyta aiški koreliacija tarp tarpfazių vietų kiekio ir rūšies, paviršiaus tekstūros ir pagamintos nanoporėtos AAO membranos paviršiaus šiurkštumo. Iš drėkinimo ir laiko priklausomybės rezultatų galima daryti išvadą, kad tokio tipo nanoporėta AAO membrana gali būti naudojama mikrohidrauliniuose įrenginiuose filtravimo ir atskyrimo tikslais.

4. Mechaninių savybių, geometrinių formų ir rezonansinio dažnio tyrimas

Siekiant pagamintas nanoporėtas aliuminio oksido membranas pritaikyti mikrohidraulinėje nanodalelių filtravimo ir atskyrimo sistemoje, svarbiausias rodiklis yra jų mechaninės savybės. Pagamintos nanoporėtos AAO membranos bus naudojamos filtravimo ir atskyrimo procesuose mikrohidrauliniuose įrenginiuose, pritaikant dalelių akustoforezės reiškinį dalelių manipuliavimui naudojant pjezoelektrinį (PZT) keitiklį. Atsižvelgiant į tai, rezonansiniai dažniai buvo analizuojami skirtinguose dažnių diapazonuose, naudojant PZT žiedo tipo keitiklio ir pagamintos nanoporėtos AAO membranos konstrukciją.

Pagamintų nanoporėtų AAO membranų mėginių (1A, 1B, 1C, 2A, 2B ir 2C) mikrokietumo testai buvo atlikti naudojant prietaisą „Micro-Comb", gamintojas „CSM Instruments", Peseaux, Šveicarija. Eksperimentinis mikrokietumo matavimams skirtas stendas parodytas 16 pav. Išmatuoti rezultatai registruojami ir apdorojami mikrokietumo matavimams skirta programine įranga bei pateikiami grafiko pavidalu.
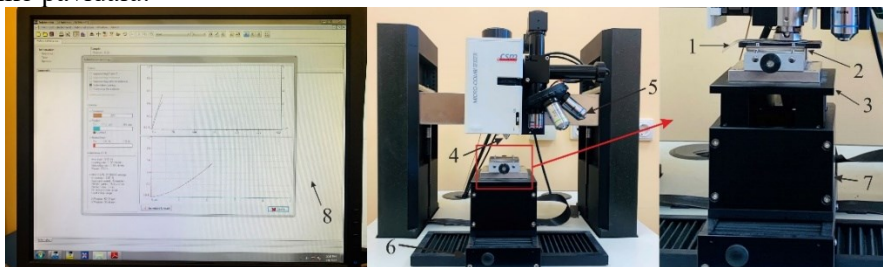
16 pav. Eksperimentinis pagamintų nanoporėtų AAO membranų mikrokietumo matavimams skirtas stendas

Pagamintų nanoporėtų AAO membranų mėginių mikrokietumo matavimams skirtą eksperimentinį stendą sudaro: nanoporėta AAO membrana (1), mėginio laikiklis (2), mobili platformą mėginio judinimui aukštyn ir žemyn (3), keitiklio antgalis (4), mikroskopo zondas (5), skirtas užfiksuoti įbrėžimo žymę, variklio kreiptuvai platformai judinti į kairę ir į dešinę (6), variklio kreiptuvai platformai

judinti pirmyn ir atgal (7) ir kompiuterinė sistema su mikrokietumo matavimų rezultatų apdorojimui skirta programine įranga (8), kad būtų saugomi istoriniai duomenys.
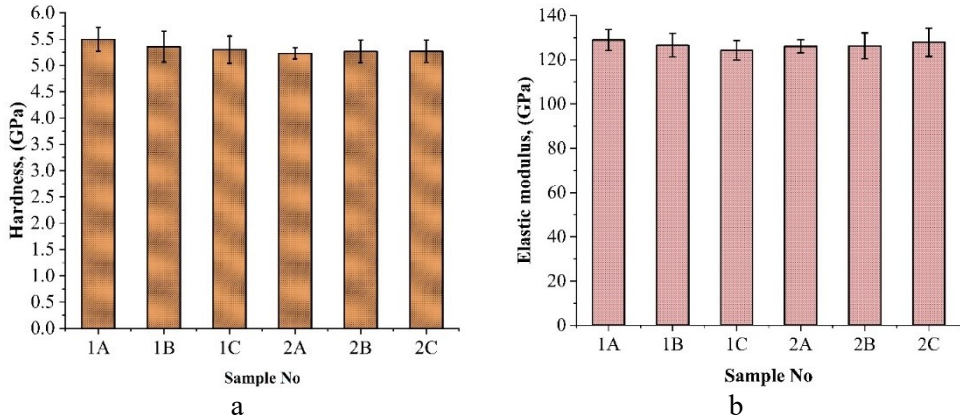
17 pav. Pagamintų nanoporėtų AAO membranų mikro kietumo (a) ir tamprumo modulio (b) rezultatai

17 pav. yra grafiškai pateikiamos išmatuotos pagamintų nanoporėtų AAO membranų mėginių (1A, 1B, 1C, 2A, 2B ir 2C) kietumo ir tamprumo modulio vertės. 1A, 1B, 1C, 2A, 2B, ir 2C AAO membranų kietumas (17a pav.) yra atitinkamai 5,49 GPa, 5,35 GPa, 5,30 GPa, 5,23 GPa, 5,26 GPa ir 5,27 GPa. Lėtas 1A, 1B ir 1C AAO membranų kietumo sumažėjimas buvo pastebėtas didėjant porų skersmeniui ir poringumui. Analogiškai pastebėtas nežymus 2A, 2B ir 2C AAO membranos mėginių kietumo sumažėjimas. Pastebėta, jog 2A, 2B ir 2C mėginių kietumas yra mažesnis nei 1A, 1B ir 1C mėginių. Tai yra susiję su padidėjusiu porų skersmeniu ir didesniu pagamintų nanoporėtų AAO membranų poringumu.

17b paveiksle yra grafiškai pavaizduotos pagamintų nanoporėtų AAO membranų 1A, 1B, 1C, 2A, 2B ir 2C mėginių tamprumo modulio vertės. Nustatytos 1A, 1B, 1C, 2A, 2B, ir 2C AAO membranų mėginių tamprumo modulio reikšmės atitinkamai yra 128,91 ± 4,67 GPa, 126,58 ± 5,32 GPa, 124,26 ± 5,32 GPa, 124,26 ± 5,32 GPa ir 124,26 ± 4,39 GPa, 124,26 ± 4,39 GPa, 126,1 ± 6,40 GPa. Be to, tamprumo modulio reikšmės yra šiek tiek mažesnės (apie 12 %) nei pateiktos mokslinėje literatūroje [186], nes šiame darbe pagamintoms AAO membranoms yra būdingas didesnis vidutinis porų skersmuo. Be to, išmatuotos tamprumo modulio ir kietumo vertės taip pat priklauso nuo absorbuotos drėgmės ir po elektrocheminio anodavimo likusio vandens kiekio.

Remiantis mokslinės literatūros šaltiniuose pateiktomis išvadomis ir išsikeltais tikslais, prieš pereinant prie tolesnių žingsnių, pirmiausia reikėjo įvertinti potencialų pagamintos nanoporėtos aliuminio oksido membranos pritaikymo galimybes mikro-/ nano- dalelių filtravimo procese mikrohidraulinėje sistemoje. Todėl skaitmeninis modeliavimas buvo atliktas naudojant paviršinių akustinių bangų moduliaciją

stovinčių akustinių bangų pavidalu, siekiant nustatyti įvairių režimų virpesius, skirtus dalelių atskyrimui ir manipuliavimui mikro- / nano- lygmenyje pritaikant akustoforezės reiškinį.

Skaitinis modeliavimas atliktas siekiant įvertinti veikimo rezonanso dažnius ir skirtingus virpesių režimus AAO membranos paviršiuje, naudojant cilindrinį pjezoelektrinį (PZT) keitiklį ir programą „COMSOL Multiphysics 5.4". Simuliacinį modelį sudaro pagaminta nanoporėta AAO membrana, pritvirtinta prie žiedinio tipo pjezoelektrinio keitiklio („PZT-5H") viršaus. Cilindrinis keitiklis, kurio vidinis skersmuo d = 26 mm, storis t = 2 mm, o aukštis h = 15 mm, ir AAO membrana, kurios skersmuo d = 30 mm ir storis t = 0,13 mm, pritvirtinta pjezoelektrinio keitiklio viršuje (18 pav.).
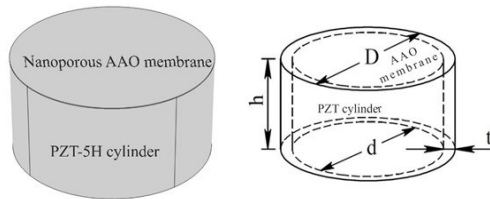
18 pav. 3D sužadinimo modelis ir jo parametrai
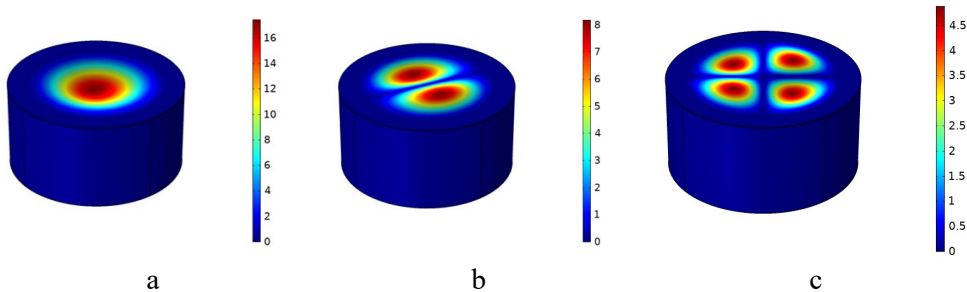
19 pav. AAO membranos virpesių forma esant skirtingiems režimams: pirmasis režimas 3,50 kHz (a), antrasis režimas 4,94 kHz (b) ir trečiasis režimas 7,89 kHz (c)

Analizuojant dinaminį membranos atsaką, kai sužadinimui naudojamas cilindrinis PZT keitiklis, nustatyta, jog pirmasis vibracijos režimas pasiekiamas esant 3,50 kHz dažniui, antrasis režimas – 4,94 kHz dažniui, o trečiasis režimas pasiekiamas esant 7,89 kHz dažniui. Remiantis simuliacijos rezultatais, galima aiškiai matyti, kaip AAO membranos virpesiai keičiasi didėjant valdymo dažniui. Paviršiaus poslinkio reikšmės mažėja didėjant valdymo dažniui. AAO membranos paviršiaus poslinkio sumažėjimas nuo pirmojo režimo, antrojo režimo ir trečiojo režimo atitinkamai yra 17 μm, 8 μm ir 4,5 μm.

Siekiant ištirti pasiūlytą teoriją, patvirtinti pjezo keitiklio („PZT-5H") veikimo principus bei patikrinti vibracijos režimus ir veikimo rezonanso dažnius, analizė

buvo atlikta naudojant neardomąjį holografinės interferometrijos („PRISM" sistema) metodą ir 3D skenuojantį vibrometrą („Polytec").
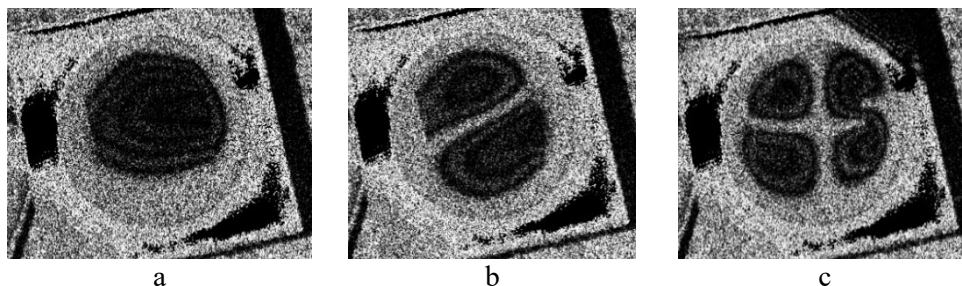
20 pav. Virpesių formos vizualizavimas naudojant „PRISM" sistemą: 3,81 kHz (a), 4,94 kHz (b) ir 7,89 kHz (c)

Siekiant nustatyti nanoporėtos AAO membranos sistemos, aktyvuojamos naudojant pjezoelektrinį keitiklį, darbinio ir rezonansinio dažnio vertes, buvo atlikta holografinės interferometrijos rezultatų, pateiktų 20 pav., analizė. Pirmasis režimas (20a pav.) nustatytas esant 3,80 kHz dažniui ir 0,43 V įtampai. Jam būdinga panaši deformacija, kuri buvo pasiekta atliekant simuliaciją esant 3,50 kHz dažniui. Paklaida, nustatyta lyginant simuliacijos rezultatus ir eksperimentinius rezultatus, yra 8,2 %. Antrasis režimas (20b pav.) nustatytas atitinkamai esant 5,18 kHz dažniui ir 0,44 V įtampai bei esant 4,94 kHz dažniui ir 1 V įtampai. Šiuo atveju paklaida tarp simuliacijos metu gautų rezultatų ir eksperimentiškai nustatytų rezultatų yra 4,7 %. Tuo tarpu trečiasis režimas (20c pav.) pagamintai nanoporėtai AAO membranai buvo nustatytas esant 8,06 kHz dažniui ir 2,12 V įtampai. Simuliacijos metu panašus vibracijos režimas buvo nustatytas esant 7,89 kHz dažniui ir 2 V įtampai, kai paklaida tarp eksperimentinių ir simuliacijos rezultatų yra 2,1 %.
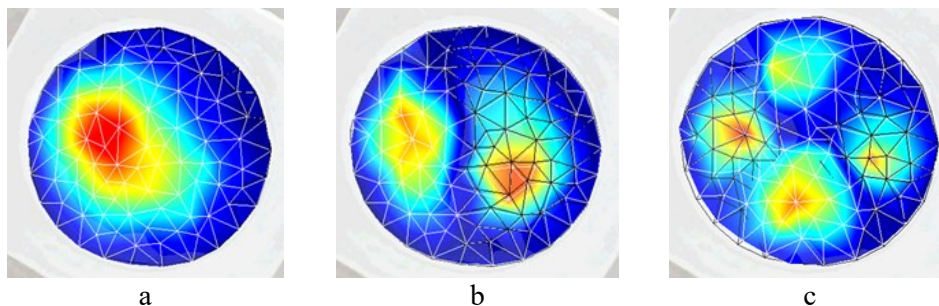
21 pav. Eksperimentiškai gautas 3D skenuojančio vibrometro atsakas AAO membranos paviršiuje esant rezonansiniams dažniams: 3,62 kHz (a), 5,17 kHz (b) ir 7,89 kHz (c)
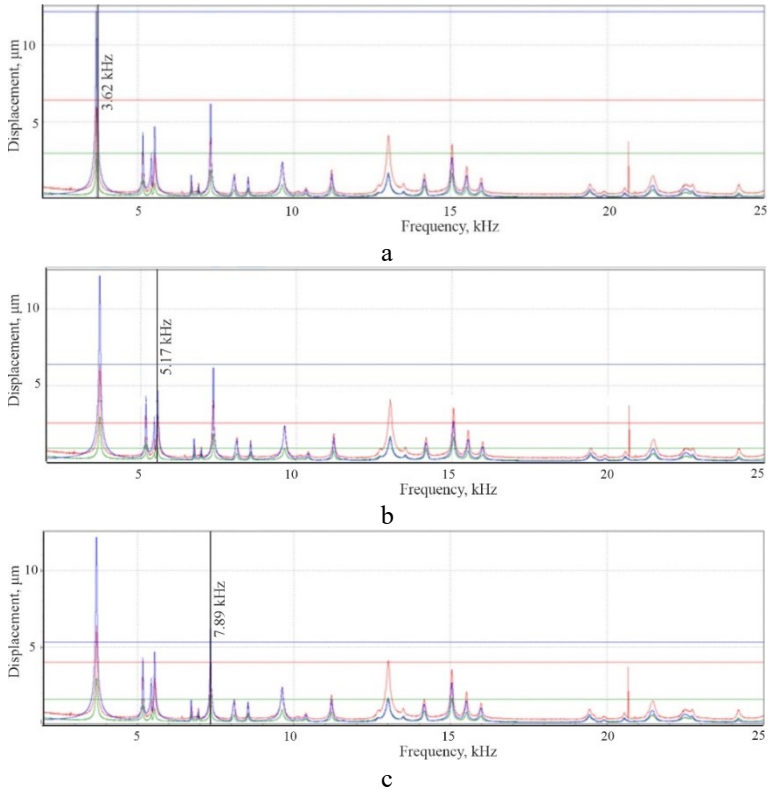
22 pav. Nanoporėtos membranos paviršiaus poslinkis esant rezonansiniam režimui nuo 3D skenuojančiu vibrometru gauto dažnio atsako esant 3,62 kHz dažniui (a), 5,17 kHz dažniui (b) ir 7,89 kHz dažniui (c), kai x – žalia spalva, y – raudona spalva ir z – mėlyna spalva

„PZT-5H" keitiklio atsako į AAO membranos paviršių rezultatai pavaizduoti 21 pav. Nanoporėtos AAO membranos deformacija buvo generuojama elektra. 3,62 kHz dažnis generuoja pirmąjį virpesių režimą (21a pav.), kai ašinis poslinkis yra 12,25 μm (22a pav.). Antrasis vibracijos režimas (21b pav.), kuriam būdingi du poliai nanoporėtos AAO membranos paviršiuje, buvo pasiektas esant 5,17 kHz dažniui, kai didžiausias poslinkis yra 6,41 μm (22b pav.). Galiausiai, trečiasis vibracijos režimas (21c pav.), kuriam būdingi keturi poliai nanoporėtos AAO membranos paviršiuje, nustatytas esant 7,89 kHz dažniui, kai didžiausias nanoporėtos membranos paviršiaus poslinkis yra 5,34 μm (22c pav.).

Remiantis eksperimentiniais 3D skenuojančio vibrometro rezultatais, didžiausios ašinio poslinkio reikšmės, t. y. 12,25 μm, buvo gautos pirmojo virpesių režimo atveju. Tuo tarpu aukštesnio virpesių režimo atveju sumažėja ašinis poslinkis nanoporėtos AAO membranos paviršiuje. Lyginant simuliacijos, „PRISM" sistemos ir „Polytech" vibrometro rezultatus, 3,62 kHz, 5,17 kHz ir 7,89 kHz rezonanso

dažnio virpesiai yra tinkamiausi mikrohidraulinės sistemos vibroaktyvaus nanofiltravimo įrenginio kūrimui. Virpesių formos amplitudė liestinės kryptimi turi didžiausią poslinkį, kuris padeda sumažinti užsikimšimo riziką ir efektyvų filtravimo procesą.

5. Nanofiltravimo sistemos sukūrimas ir akustinio slėgio bei dalelių judėjimo AAO membranos nanovamzdeliuose tyrimas

Pagaminta nanoporėta AAO membrana galėtų būti pritaikyta naudoti skysčio mikro- / nano- filtravimo procesuose biomedicinos reikmėms sukurtose mikrohidraulinėse sistemose. Todėl svarbu išanalizuoti srauto charakteristikas, akustinio slėgio pasiskirstymą ir dalelių judėjimą nanoporėtoje AAO membranoje susidariusių nanovamzdelių viduje. „COMSOL Multiphysics 5.4" programa buvo naudojama skysčio srauto, akustinio slėgio pasiskirstymo ir dalelių judėjimo analizei.

Skaitinė laminarinio srauto analizė atlikta vandens atžvilgiu, todėl vandens dinaminis koeficientas 20 °C temperatūroje yra $1,0019 \times 10^{-3}$ Pa [190]. Pagal 5.3 formulę apskaičiuotas srautas vienam nanovamzdeliui yra $1,95877 \times 10^{-20}$ m^3/s. Apskaičiuotas vidutinis greitis viename nanovamzdelyje yra $6,238 \times 10^{-7}$ m/s.

Nanovamzdelių skersmuo skiriasi, tačiau atliekant minėtus skaičiavimus yra laikoma, kad nanovamzdelio skersmuo yra 200 nm, o jo ilgis – 2 μm. Siekiant palyginti skaičiavimo rezultatus, skaitmeninė simuliacija atlikta naudojant programą „COMSOL Multiphysics 5.4". Šioje programoje skaičiavimams naudojamas ašiai simetrinis modelis (23 pav.). Simuliacinį modelį sudaro keturių skirtingų sienų ribinės sąlygos.
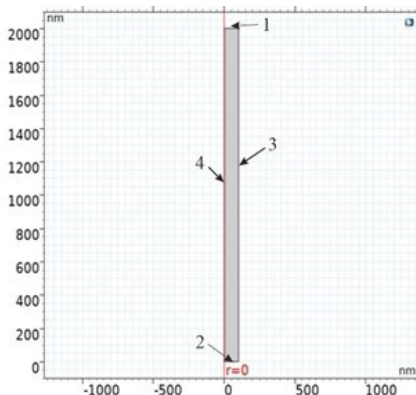
23 pav. Srauto ir greičio nanovamzdelio viduje simuliacinis modelis susideda iš įėjimo (1), išėjimo angos (2), išorinės nanovamzdelio sienelės (3) ir modelio ašių simetrijos linijos (4)

Analogiškai, kaip ir atliekant skaičiavimus, simuliacijos metu tekančio srauto siena fiksuojama turinti 1 Pa slėgį, o ištekančioje vietoje nurodomas 0 Pa slėgis. Taikant simuliacinį modelį, pasirinkta skysčio temperatūra yra 20 ºC. Šis simuliacinis modelis yra pavaizduotas 23 pav. Matematinis modelis skaičiuojamas

167

naudojant nusistovinčios sistemos tyrimą. Laminarinio srauto greičio pasiskirstymo nanovamzdelio viduje modeliavimo rezultatai pateikti 24 pav.
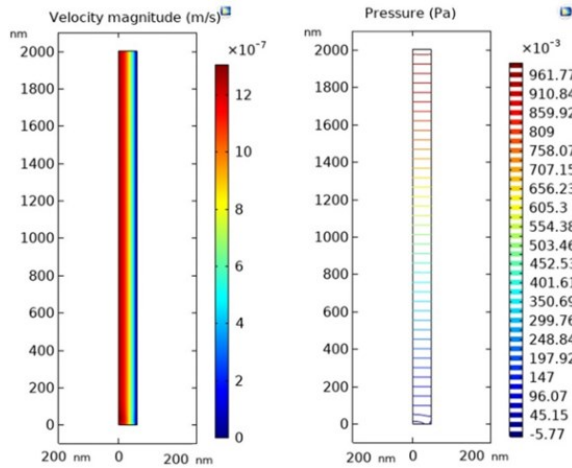
24 pav. Laminarinio srauto nanovamzdelyje simuliacijos rezultatai

Remiantis šiais rezultatais, gaunamas laminarinis srauto pasiskirstymas nanovamzdelyje, būdingas būtent šiam srauto tipui. Iš gauto grafiko nesunkiai galima apskaičiuoti vidutinį srauto greitį. Šio simuliacinio modelio rezultatai (24 pav.) parodė, kad vidutinis skysčio greitis nanovamzdeliuose yra $6,22×10^{-7}$ m/s. Atlikus skaičiavimus nustatyta, kad gauti rezultatai yra artimi teoriniams skaičiavimams. Pastebėtas vienintelis 0,16 % skirtumas tarp apskaičiuoto ir imituoto skysčio greičio nanovamzdelyje.

Dažniausiai mikro- / nano- dalelių valdymas mikrohidraulinėje sistemoje atliekamas taikant akustinio slėgio techniką. Taikant šį metodą, nanovamzdelio centre galima sukurti slėgio skirtumą ir tokiu būdu sumažinti trintį bei mechaninius biodalelių pažeidimus. Taigi, siekiant nustatyti akustinio slėgio pasiskirstymą, dalelių judėjimą ir valdymo dažnius nanoporėtoje AAO membranoje suformuotuose nanovamzdeliuose, buvo atliktas skaitmeninis modeliavimas. Modeliavimui buvo sukurtas 2D stačiakampis modelis naudojant programą „COMSOL Multiphysics 5.4". Jis yra skirtas akustinio slėgio modelio ir dalelių srauto modelio analizei. Analogiškai buvo sukurtas kitas modelis, skirtas išmatuoti laiką, per kurį mikro- / nano- dalelės susikaupia nanovamzdelio centre.

Šiam tikslui buvo pasirinktas matematinis modelis su konkrečiais geometriniais parametrais. Visa sritis apibrėžiama kaip sritis, kurioje bus atliekama akustinio slėgio analizė. Simuliacinis modelis išskaidomas baigtinių elementų metodu. Apibrėžtas ir išskaidytas modelis pateiktas 25 pav.

168
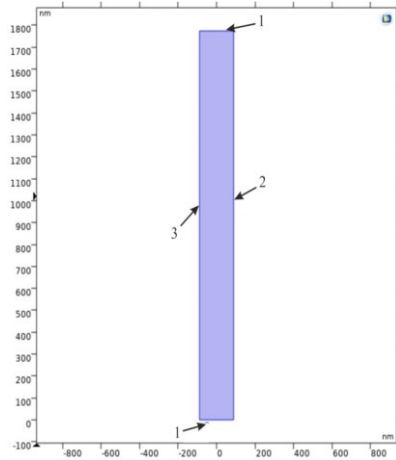
25 pav. Nanoertmės 2D simuliacinis modelis: 1 – plokščiosios bangos spinduliavimas; 2 – vibruojantis paviršius; ir 3 – kietas paviršius

a   b
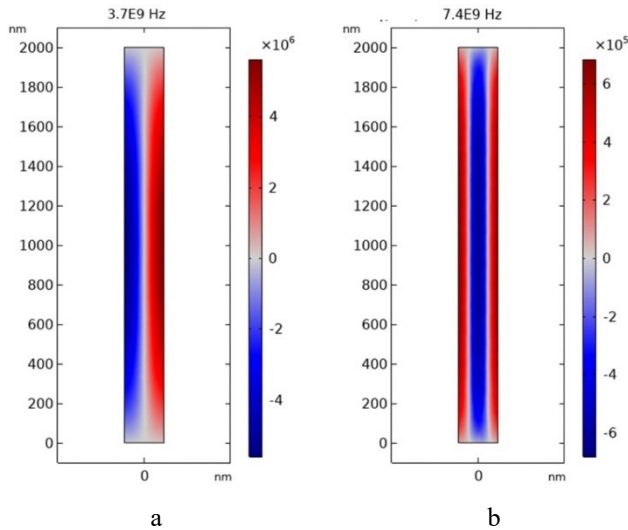
26 pav. Akustinio slėgio pasiskirstymas nanovamzdelio viduje esant 3,7 GHz (a) ir 7,4 GHz (b)

Atlikus kompiuterinius skaičiavimus (26 pav.), pageidaujami rezultatai, kaip ir buvo teoriškai numatyta, buvo gauti esant 3,7 GHz dažniui (26a pav.). Remiantis šiais rezultatais nustatyta, jog didžiausias akustinis slėgis yra $5,57 \times 10^6$ Pa. Simuliacinė analizė parodė, kad esant 7,4 GHz dažniui (26b pav.), AAO membranoje suformuotame nanovamzdelyje susidaro dvi zonos su nuliniu slėgiu. Nulinė zona turi būti viena, kad dalelės būtų išlaikytos centre ir sumažėtų jų pažeidimų rizika bei trintis tarp ląstelių arba mikro- / nano- dalelių.

169

Slėgio pasiskirstymo nanovamzdelyje modeliavimo rezultatai toliau buvo naudojami analizuojant nanodalelių judėjimą nanovamzdelyje ir apskaičiuojant laiką, reikalingą nanodalelėms sutelkti jo centre. Remiantis akustinio slėgio modeliavimo analizės rezultatais, galima aiškiai matyti, kad valdymo dažnio padidėjimas sukelia akustinio slėgio sutrikimą ir sukelia trintį tarp nanodalelių ir nanovamzdelio sienelės. Galų gale tai lemia per nanovamzdelį judančių nanodalelių arba biologinių dalelių pažeidimus. Norint suprasti, kiek laiko reikia nanodalelėms sucentruoti nanovamzdelyje, buvo atliktas kitas tyrimas.

Šioje analizėje dalelių dydis yra dešimt kartų mažesnis už analizuojamąją porą. Pasirinktas dalelių tankis – 5000 kg/m³. Modeliavimo analizės metu buvo palaikoma pastovi 20 °C temperatūra. Šiame simuliacijos modelyje taip pat įvertinamas gravitacijos efektas, kuris gali turėti įtakos dalelių judėjimui ir skaičiavimo rezultatams. Kadangi šio modelio analizė atliekama besikeičiant laikui, matavimo intervalas nurodomas nuo 0 iki 0,3 sekundės, esant 0,0001 s žingsniui. Analizės metu gauti dalelių judėjimo duomenys yra pateikiami 27 ir 28 pav.
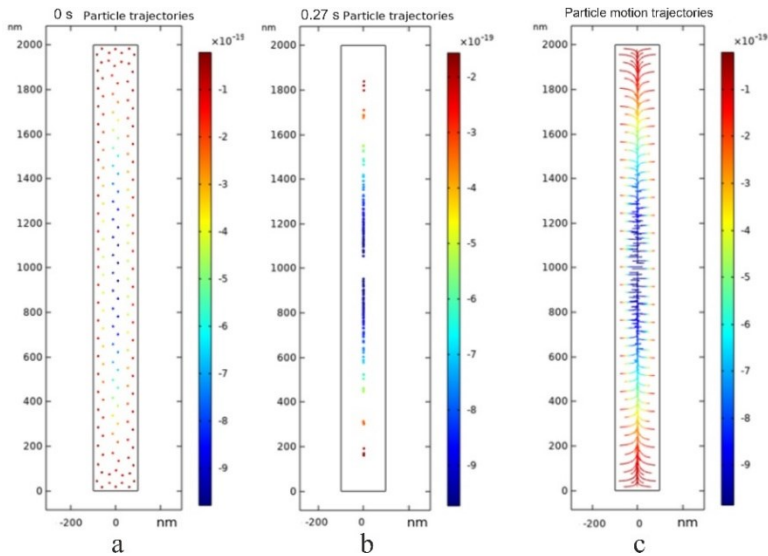
17 pav. Nanodalelių judėjimo ir padėties nustatymo nanovamzdelyje rezultatai esant 3,7 GHz dažniui

Gauti rezultatai rodo, kad pradinė nanodalelių padėtis yra ties 0 s (27a pav.). Po 0,27 s nanodalelės juda ir išsilygina nanovamzdelyje dėl mažesnio akustinio slėgio (27b pav.). Be to, 27c pav. parodytas intensyvus nanodalelių judėjimas dėl mažesnio akustinio slėgio lauko. Modeliavimo rezultatai rodo nanodalelių padėtį ties 0 s (28a pav.) ir po 0,27 s (28b pav.). Tai aiškiai parodo, kad pasiskirstant akustiniam slėgiui, susidaro dvi nanodalelių koncentracijos zonos. Nanodalelių koncentracijos zona yra netoli nanovamzdelio sienelės. Tai reiškia, kad yra tikimybė pažeisti mikro- / nano- daleles dėl trinties tarp nanovamzdelio sienelės ir

nanovamzdelio kraštuose esančių dalelių. Atsižvelgiant į 28c pav., galima matyti, kad nanodalelės judėjimas yra mažiau intensyvus, nei nustatyta esant 3,7 GHz dažniui.
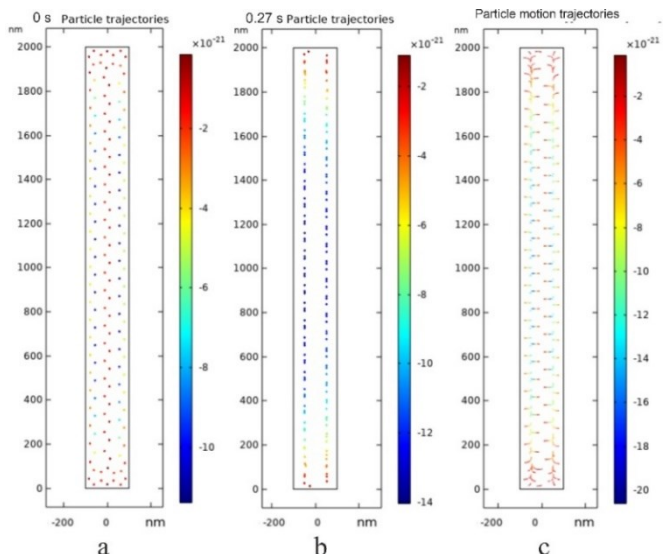
28 pav. Nanodalelių judėjimo ir padėties nustatymo nanovamzdelyje rezultatai esant 7,4 GHz dažniui

Naudojant pagamintą nanoporėta AAO membraną buvo sukurtas prototipas, kuris galėtų būti pritaikytas vibroaktyvaus nanofiltravimo įrenginio konstrukcijoje mikrohidrauliniuose biomedicinos prietaisuose. Vibroaktyvaus įrenginio prototipą sudaro pjezoelektrinis keitiklis („PZT-5H"), pagaminta nanoporėta AAO membrana ir skysčio talpykla. Pagamintos nanoporėtos AAO membranos paviršius suaktyvinamas naudojant paviršines akustines bangas, taikant elektrinį potencialą esant skirtingam dažnių diapazonui, kuris padeda keisti geometrinę nanoporų formą.

Skysčio prasiskverbimo pro nanoporėtą membraną, naudojant paviršines akustines bangas, bandymo prototipas parodytas 29 pav.
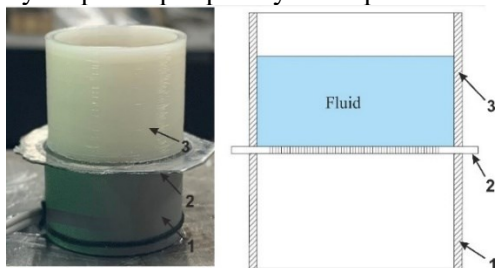
29 pav. Skysčio prasiskverbimo prototipas: pjezoelektrinis keitiklis (1), pagaminta nanoporėta AAO membrana (2) ir skysčio talpykla (3)

Skysčio prasiskverbimo ir akustinių bangų moduliacijos prototipą sudaro pjezoelektrinis cilindro tipo keitiklis, kurio išorinis skersmuo yra 30 mm, sienelės storis 2 mm, o aukštis 15 mm, pagaminta nanoporėta AAO membrana, pritvirtinta keitiklio viršuje, ir skysčiu pripildytas plastikinis indas. Paviršinių akustinių bangų susidarymo įjungus pjezoelektrinį keitiklį nanoporėtos AAO membranos paviršiuje įvertinimas atliktas naudojant „PRISM" sistemą (30 pav.) esant skirtingiems dažniams.
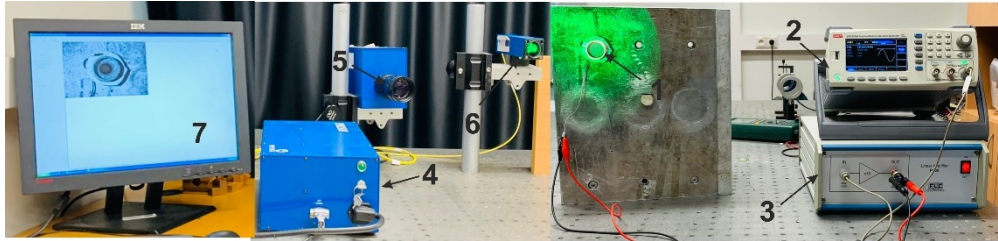
30 pav. Eksperimentinis stendas su „PRISM" sistema skirtingoms virpesių formoms

Įvairių sistemos virpesių formų analizės eksperimentinį stendą sudaro ant nejudančio paviršiaus pritvirtintas prototipas (1), dažnio generatorius (2), prijungtas prie tiesinės įtampos stiprintuvo (3), skirto įtampai sustiprinti, „PRISM" sistemos valdymo blokas (4), kamera (5), žalias lazeris (6) ir monitorius (7). Didžiausias poslinkis AAO membranos paviršiuje pasiektas esant rezonanso režimui (31 pav.) ties 3,56 kHz dažniu atitinka 3D skenuojančiu vibrometru „Polytech" gautus rezultatus ir gali būti panaudojamas filtravimo procesuose, nes šiose interferogramose stebimų akustinių bangų virpesių formų smailės ir mazgai yra išdėstyti teisingai, o tangentiniai virpesiai atitinkamose zonose bus didžiausi.

Paviršinių akustinių bangų veikimu pagrįstos filtravimo sistemos eksperimentinis tyrimas (31 pav.) susideda iš filtravimo prototipo (1), dažnių signalų generatoriaus (2), linijinio stiprintuvo (3), optinio mikroskopo („Nikon ECLIPSE LV150") (4) ir monitoriaus (5).
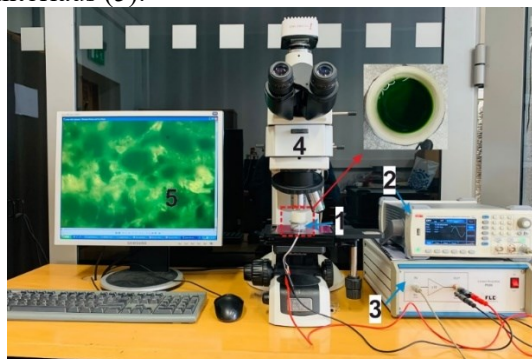
31 pav. Eksperimentinis stendas skysčių prasiskverbimui įvertinti

Talpykloje yra žalios spalvos distiliuoto vandens (10 ml), kad būtų galima patikrinti skysčio prasiskverbimą kitoje nanoporėtos AAO membranos paviršiaus pusėje.

a   b
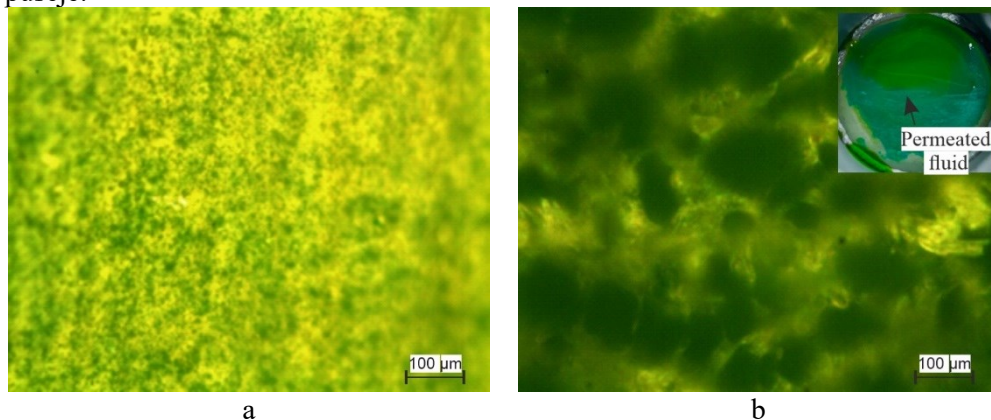
32 pav. Skysčio prasiskverbimas per AAO membraną neaktyvavus dažnio (a) ir esant 3,56 kHz dažniui (b)

Pirmiausia prototipo analizė buvo atlikta neaktyvavus dažnio, po 2 valandų kitoje nanoporėtos AAO membranos pusėje atsirado vos kelios žalios dėmės be jokio išorinio spaudimo (32a pav.). Kita vertus, skysčio prasiskverbimas per nanoporėtą AAO membraną buvo labai panašus, kai membrana buvo sužadinta naudojant pjezoelektrinį keitiklį esant 3,56 kHz dažniui (32b pav.). Skysčių prasiskverbimo analizė parodė, kad pagaminta nanoporėta AAO membrana gali būti naudojama dalelių filtravimui biomedicininės paskirties mikrohidraulinėse sistemose. Be to, nanoporėtos AAO membranos paviršiuje susidariusios akustinės bangos padeda sukurti vibroaktyvų nanofiltravimo įrenginį, kuris leidžia sumažinti užsikimšimo riziką ir sumažinti daleles, didesnes už nanoporų skersmenį (t. y. dalelės, kurių dydis didesnis nei AAO membraną sudarančių nanoporų / nanovamzdelių skersmuo, bus išstumtos / surinktos arba sumažintos).

Pastaruoju metu dideliu mastu atliekamas nuodingų rūgščių ir CO_2 pašalinimas iš gamtinių dujų naudojant membraninį atskyrimo procesą. Yra daug įvairių medžiagų ir metodų, skirtų membranoms su mikro- / nano- dydžio poromis gaminti. Siekiant patikrinti pagamintos nanoporėtos AAO membranos pritaikymo galimybes, buvo atliktas eksperimentas naudojant pagamintą AAO membraną, kurios porų skersmuo 70 nm, poringumas 32,64 %, o storis 96 µm. Buvo naudojamos trijų skirtingų rūšių dujos: anglies dioksidas (CO_2), azotas (N_2) ir metanas (CH_4). Norint nustatyti naudojamų trijų skirtingų rūšių dujų CO_2/CH_4 ir CO_2/N_2 atskyrimą ir selektyvumą, buvo atliktas pralaidumo testas esant trims skirtingoms temperatūroms: 20 ºC, 40 ºC, 60 ºC ir keičiant slėgį nuo 0 iki 0,5 baro. Eksperimentas buvo atliktas dujų pralaidumo sistemoje, naudojant apskritą AAO membraną, kurios efektyvusis skersmuo 20 mm. Tiriamasis AAO membranos mėginys pavaizduotas 33 pav.

a   b
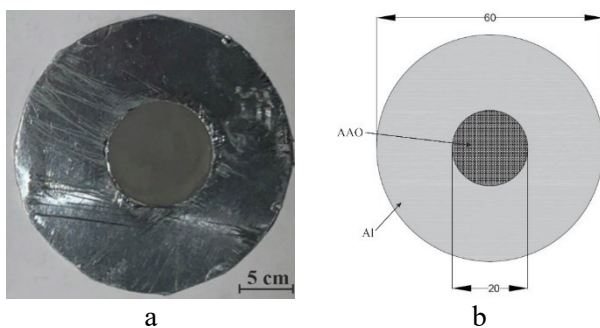
33 pav. Nanoporėtos AAO membranos nuotrauka (a) ir matmenys dujų pralaidumo tyrimui (b)

Atliktų visų trijų CO_2, N_2 ir CH_4 dujų pralaidumo tyrimų, naudojant pagamintą nanoporėtą AAO membraną 20 ºC temperatūroje, rezultatai pateikiami 34 pav.
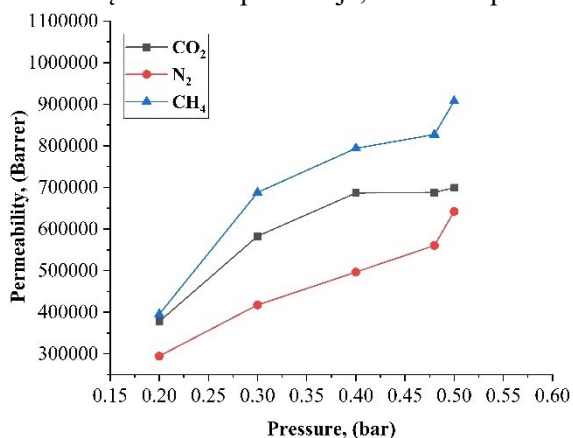
34 pav. Tiekimo slėgio 0–0,5 bar įtaka trijų skirtingų dujų CO_2, N_2 ir CH_4 pralaidumo per pagamintą nanoporėtą AAO membraną vertėms esant 20 ºC

Iš gautų rezultatų galima matyti, kad padidinus tiekimo slėgį nuo 0 iki 0,5 bar, padidėja CO_2, N_2 ir CH_4 pralaidumas. CO_2 dujų pralaidumas padidėja nuo 377717 iki 699266 Barrer padidinus tiekimo slėgį nuo 0 iki 0,5 bar. Panašiai N_2 pralaidumas palaipsniui padidėjo nuo 294471 iki 642328 Barrer. Be to, CH_4 pralaidumas padidėjo nuo 395102 iki 907597 Barrer padidėjus tiekimo slėgiui (nuo 0 iki 0,5 bar). CH_4 dujos yra būdingas didesnis pralaidumas nei CO_2 ir N_2 dujų atveju. Taip yra todėl, kad CH_4 molekulės pasižymi didesniu afiniškumu ir greitesne difuzija vykstant judėjimui per pagamintą nanoporėtą AAO membraną nei CO_2 ir N_2 molekulės.

Taip pat atliktas CO_2/N_2 ir CO_2/CH_4 dujų selektyvumo vertinimas esant 0–0,5 bar slėgiui ir 20 ºC temperatūrai. Selektyvumas yra matas, nurodantis, kaip gerai nanoporėta AAO membrana gali atskirti dviejų rūšių dujas, ir yra išreiškiamas kaip grynų dujų komponentų pralaidumo santykis. CO_2/N_2 (35a pav.) ir CO_2/CH_4 (35b

pav.) selektyvumo rezultatai esant 0–0,5 bar slėgiui ir 20 ºC temperatūrai pateikti 35 pav.
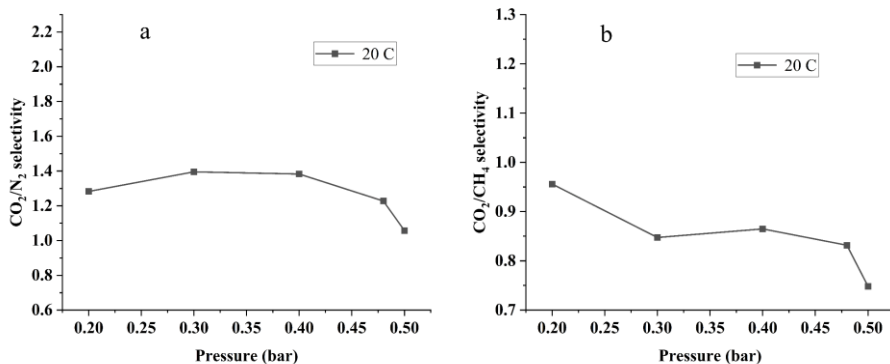
35 pav. CO_2/N_2 ir CO_2/CH_4 selektyvumas esant 0–0,5 baro slėgiui ir 20 ºC temperatūrai

Rezultatai rodo, kad didėjant slėgiui (nuo 0 iki 0,5 bar) selektyvumas sumažėja. CO_2/N_2 (35a pav.) ir CO_2/CH_4 (35b pav.) selektyvumas sumažėjo atitinkamai nuo 1,26 iki 1,05 ir 0,96 iki 0,74, kai sumažėjimas siekia 18,18 ir 25,88 %. Lyginant CO_2/N_2 ir CO_2/CH_4 dujų sistemas pastebėta, kad CO_2/N_2 pasižymi didžiausiu dujų selektyvumu. Toks selektyvumo elgesys būdingas dėl dujų difuzijos ir tirpumo mechanizmo. Didžiausias pagamintos nanoporėtos AAO membranos CO_2/N_2 selektyvumas yra 1,39, nesumažėjus pralaidumui. Net keletas aspektų gali turėti įtakos pagamintos nanoporėtos AAO membranos CO_2 dujų atskyrimo nuo kitų dujų efektyvumui, įskaitant atskyrimo procesą, porų orientaciją, apdorojimo techniką.

Išvados

Remiantis tiriamojo darbo tema išsikeltais uždaviniais, buvo suformuluotos šios išvados.

1. Darbo metu buvo atlikta tradicinės hidraulinės sistemos ir mikrohidraulikos mokslinių tyrimų apžvalga disertacijos tema, suformuluotas tikslas ir išsikelti uždaviniai. Šiuo metu mikrofluidikoje naudojamos membranos dažniausiai yra pagamintos iš polimerinių medžiagų, o jų gamyboje naudojami metodai paprastai yra brangūs ir reikalauja sudėtingų technologinių sprendimų. Membraninių komponentų pritaikymas dalelių atskyrimo ir filtravimo procesuose mikrofluidinėse sistemose taikant kontaktinio ir nekontaktinio tipo manipuliacijas dalelėmis sulaukia didelio mokslininkų dėmesio. Iš visų žinomų mikrohidraulinių sistemų kūrimui naudojamų metodų ir membranų nanoporėta aliuminio oksido membrana per pastaruosius kelis dešimtmečius sulaukė didelio susidomėjimo dėl gamybos paprastumo ir unikalių savybių. Paviršiaus akustinio metodo taikymas manipuliavimui dalelėmis mikrofluidikoje naudojant AAO

membraną padidina mikrohidraulinėje sistemoje vykstančių biodalelių atskyrimo ir filtravimo procesų efektyvumą biomedicinos prietaisuose.

2. Remiantis mokslinės literatūros analize, buvo sukurtas eksperimentinis aliuminio oksido membranos gamybos stendas, kuriame naudojama aušinimo sistema su Peltje elementu. Eksperimentui suprojektuota aušinimo sistema anodavimo proceso metu palaiko apie 5–3 ºC temperatūrą, o tai palengvina anodavimo procesą. Temperatūros analizės metu reikšmingo skirtumo tarp aušinimo sistemos simuliacijos rezultatų ir eksperimentiškai gautų rezultatų nepastebėta. Taip pat sėkmingai atlikta šešių atskirų AAO membranų gamyba, esant skirtingiems proceso parametrams, ir, naudojant sukurtą eksperimentinį stendą, nustatyta, kad elektrolito temperatūra išlieka stabili (5–3 ºC) anodavimo proceso metu, kai naudojama suprojektuota aušinimo sistema su Peltje elementu.

3. Pagamintų nanoporėtų AAO membranų geometrija buvo ištirta naudojant SEM analizę, kurios metu paaiškėjo, kad pagamintų nanoporėtų AAO membranų porų skersmuo yra nuo 43 nm iki 85 nm, o atstumas tarp porų išlieka pastovus (110–115 nm), esant 50 ir 60 V nuolatinės srovės anodavimo įtampai. Nustatyta, jog ilgėjant anodavimo laikui nuo 15 iki 17 valandų membranos storis padidėja nuo 74 iki 95 nm. Be to, buvo nustatyta, kad anodavimo laiko ir įtampos padidėjimas sąlygoja didesnį AAO membranos porų skersmenį ir storį. EDS analizė rodo, kad dominuoja aliuminio oksido (Al_2O_3) fazė. Pagamintos nanoporėtos AAO membranos susideda iš dviejų pagrindinių cheminių komponentų: aliuminio (Al) ir deguonies (O). Tačiau mėginyje, pagamintame esant 60 V nuolatinės srovės įtampai, buvo pastebėtas nedidelis fosforo (P) ir sieros (S) kiekis. Pagamintos AAO membranos FTIR analizės spektrai patvirtina aliuminio oksido (Al_2O_3) susidarymą. Pagamintos nanoporėtos AAO membranos hidrofobinių savybių tyrimas parodė, kad vandens lašo kontaktinis kampas (θ) ant pagamintų nanoporėtų AAO membranų mėginių 1A, 1B, 1C, 2A, 2B ir 2C paviršiaus atitinkamai yra 55,87 ± 0,69º, 54,38 ± 0,30º, 45,16 ± 0,60º, 67,44 ± 0,56º, 66,58 ± 0,50º ir 64,07 ± 0,90º. Tai reiškia, kad pagamintų nanoporėtų AAO membranų paviršius pasižymi hidrofilinėmis savybėmis. Priklausomybės nuo laiko tyrimas rodo kontaktinio kampo sumažėjimą, o tai reiškia, kad vandens lašas patenka į AAO membranos nanoporas. Dėl šių pagamintų nanoporėtų membranų savybių ji gali būti pritaikyta naudoti mikrohidrauliniuose filtravimo ir atskyrimo įrenginiuose.

4. Tyrimo metu buvo įvertintos pagamintų nanoporėtų AAO membranų mechaninės savybės, t. y. kietumas ir tamprumo modulis. Nustatyta, kad 1A, 1B, 1C, 2A, 2B ir 2C mėginių kietumas yra atitinkamai 5,49 GPa, 5,35 GPa, 5,30 GPa, 5,23 GPa, 5,26 GPa ir 5,27 GPa. 1A, 1B, 1C, 2A, 2B ir 2C mėginių tamprumo modulis yra atitinkamai 128,91 ± 4,67 GPa, 126,58 ± 5,32 GPa, 124,26 ± 4,39 GPa, 126,10 ± 2,97 GPa, 126,26 ± 5,84 GPa ir 127,87 ± 6,40 GPa. Reikšmingo skirtumo nepastebėta, tačiau nustatyta, kad poringumas ir porų skersmuo turi įtakos AAO membranos kietumui ir tamprumo moduliui.

Naudojant pjezoelektrinio keitiklio paviršiaus akustinės bangos simuliaciją, AAO membranos paviršiuje buvo stebimos trys skirtingos formos ties 3,50 kHz, 4,94 kHz ir 7,89 kHz dažniais. Trijų skirtingų režimų atveju nustatytas vienintelis 4,7 %, 8,2 % ir 2,1 % skirtumas tarp simuliacinio modelio ir eksperimentinių rezultatų. Prototipo rezonansinis režimas buvo pasiektas esant 3,14 kHz dažniui dėl maksimalaus 17 μm tangentinio poslinkio nanoporėtos AAO membranos paviršiuje naudojant PZT keitiklį.

5. Atsižvelgiant į potencialų AAO membranos pritaikymą mikrohidrauliniame įrenginyje, buvo sukurtas teorinis simuliacinis modelis, skirtas manipuliuoti dalelėmis ir valdyti mikro- / nano- dalelių trajektoriją AAO membranos nanovamzdelio viduje pasitelkus akustoforezės metodą. Buvo sukurtas prototipas, skirtas eksperimentiškai įvertinti skysčių prasiskverbimą per AAO membraną naudojant paviršinę akustinę bangą, kurios dažnis 3,56 kHz. Šis paprastas prototipas gali būti naudojamas skysčiuose esančioms priemaišoms, didesnėms nei membranos porų skersmuo, filtruoti. Tačiau sistemą galima patobulinti pritaikant porėtą AAO membranos struktūrą, kurią nesunkiai galima keisti anodavimo proceso metu. Sukurtas dalelių atskyrimo metodas, pagrįstas akustoforezės principu, padidina pagamintų nanoporėtų AAO membranų pritaikymo galimybes mikrohidraulinių sistemų kūrimo pramonėje, nes jų naudojimas leidžia padidinti filtravimo proceso efektyvumą biomedicininės paskirties mikroprietaisuose. Pagaminta AAO membrana taip pat gali būti naudojama nuodingosioms dujoms šalinti. Dujų atskyrimo rezultatai rodo, jog didžiausias dujų atskyrimo selektyvumas pro pagamintą nanoporėtą AAO membraną buvo nustatytas CO_2/N_2 sistemai (1,39), kai tuo tarpu pralaidumas nesumažėja. Taigi, galima daryti išvadą, kad pagamintas nanoporėtas AAO membranas galima pritaikyti dujų filtravimo ir atskyrimo procesuose.

REFERENCES

1. Prakash, S., & Yeom, J. (2014). Energy and Environmental Applications. Nanofluidics and Microfluidics, 241–269.

2. Aksimentiev, A., Brunner, R. K., Cruz-Chú, E., Comer, J., & Schulten, K. (2009). Modeling Transport Through Synthetic Nanopores: Simulating biomolecules in synthetic nanopores presents various challenges. IEEE Nanotechnology Magazine, 3(1), 20–28.

3. Kwon, S. K., Kou, S., Kim, H. N., Chen, X., Hwang, H., Nam, S. W., Kim, S. H., Swamy, K. M. K., Park, S., & Yoon, J. (2008). Sensing cyanide ion via fluorescent change and its application to the microfluidic system. Tetrahedron Letters, 49(26), 4102–4105.

4. Duan, C., Karnik, R., Lu, M. C., & Majumdar, A. (2012). Evaporation-induced cavitation in nanofluidic channels. Proceedings of the National Academy of Sciences of the United States of America, 109(10), 3688–3693.

5. Shen, F., Ai, M., Ma, J., Li, Z., & Xue, S. (2020). An easy method for pressure measurement in microchannels using trapped air compression in a one-end-sealed capillary. Micromachines, 11(10).

6. Cubas, J. M. C., Stel, H., Ofuchi, E. M., Marcelino Neto, M. A., & Morales, R. E. M. (2020). Visualization of two-phase gas-liquid flow in a radial centrifugal pump with a vaned diffuser. Journal of Petroleum Science and Engineering, 187, 106848.

7. Chen, M. C., Lake, J. R., Heyde, K. C., & Ruder, W. C. (2018). Three-dimensional printing of thermoplastic materials to create automated syringe pumps with feedback control for microfluidic applications. Journal of Visualized Experiments, 2018(138).

8. Qian, B., Fan, H., Liu, G., Zhang, J., & Li, P. (2021). Self-Supporting Microchannel Liquid-Cooled Plate for T/R Modules Based on Additive Manufacturing: Study on Its Pass Design, Formation Process and Boiling Heat Transfer Performance. Metals 2021, Vol. 11, Page 1731, 11(11), 1731.

9. Kirby, B. (2010). Micro- and Nanoscale Fluid Mechanics. Micro- and Nanoscale Fluid Mechanics.

10. Gao, Y., Wu, M., Lin, Y., Zhao, W., & Xu, J. (2020). Acoustic bubble-based bidirectional micropump. Microfluidics and Nanofluidics, 24(4).

11. Tang, S. Q., Li, K. H. H., Lee, S. J., Zeng, J. J., & Ng, S. H. (2019). Novel multi-way microvalve with ease of fabrication and integration for microfluidics application. Sensors and Actuators, B: Chemical, 286, 289–300.

12. Ayoib, A., Hashim, U., Gopinath, S. C. B., Md Arshad, M. K., Karim, N. A. A. A., Thivina, V., Nordin, N.K.S., & Yopop, R. (2017). Low cost design and fabrication of PDMS microfluidics micromixers for DNA extraction. Proceedings of the 2017 IEEE Regional Symposium on Micro and Nanoelectronics, RSM 2017, 227–230.

13. Majeed, B., Zhang, L., Tezcan, D. S., Soussan, P., & Fiorini, P. (2011). Silicon microfilter device fabrication and characterization for diverse microfluidics applications. Proceedings - Electronic Components and Technology Conference, 1834–1838.

14. Olanrewaju, A., Beaugrand, M., Yafia, M., & Juncker, D. (2018). Capillary microfluidics in microchannels: From microfluidic networks to capillaric circuits. Lab on a Chip, 18(16), 2323–2347.

15. Ou, J. (2015). Microfluidic Chip-Based Electrochromatography. Encyclopedia of Microfluidics and Nanofluidics, 1891–1901.

16. Wang, H., & Zou, Z. Q. (2006). Self-organized growth of Mn nanocluster arrays on Si(111)-(7×7) surfaces. Applied Physics Letters, 88(10), 103115.

17. Godavarthi, S., Porcayo-Calderon, J., Vazquez-Velez, E., Casales-Diaz, M., Ortega-Toledo, D. M., & Martinez-Gomez, L. (2015). Influence of the chemical composition in the electrochemical response of permanent magnets. Journal of Spectroscopy, 2015.

18. Ríos, Á., & Zougagh, M. (2013). Sample preparation for micro total analytical systems (μ-TASs). TrAC - Trends in Analytical Chemistry, 43, 174–188.

19. Yusuf, A., Sodiq, A., Giwa, A., Eke, J., Pikuda, O., De Luca, G., Di Salvo, J, & Chakraborty, S. (2020). A review of emerging trends in membrane science and technology for sustainable water treatment. Journal of Cleaner Production, 266.

20. Kim, J.; Gale, B.K. (2008). Quantitative and qualitative analysis of a microfluidic DNA extraction system using a nanoporous AlOx membrane. Lab Chip, 8, 1516.

21. Thorslund, S., Klett, O., Nikolajeff, F., Markides, K., & Bergquist, J. (2006). A hybrid poly(dimethylsiloxane) microsystem for on-chip whole blood filtration optimized for steroid screening. Biomedical Microdevices, 8(1), 73–79.

22. Sheng, Y., & Bowser, M. T. (2012). Size selective DNA transport through a nanoporous membrane in a PDMS microfluidic device. Analyst, 137(5), 1144–1151.

23. Yuan, Y., Cui, Z., Jia, H., & Wang, J. (2022). High Efficiency Membrane Technology in Microfluidic Systems,1–18.

24. De Jong, J., Lammertink, R. G. H., & Wessling, M. (2006). Membranes and microfluidics: A review. Lab on a Chip, 6(9), 1125–1139.

25. Xiang, F., Lin, Y., Wen, J., Matson, D. W., & Smith, R. D. (1999). An integrated microfabricated device for dual microdialysis and on-line ESI-ion trap mass spectrometry for analysis of complex biological samples. Analytical Chemistry, 71(8), 1485–1490.

26. Schuster, A., Lakshmanan, R., Ponton, J., & Sefiane, K. (2003). Modelling a novel miniaturised reactor/separator system. Journal of Chemical Technology and Biotechnology, 78(2–3), 342–346.

27. Long, Z., Liu, D., Ye, N., Qin, J., & Lin, B. (2006). Integration of nanoporous membranes for sample filtration/preconcentration in microchip electrophoresis. Electrophoresis, 27(24), 4927–4934.

28. Gao, H., Sun, R., He, L., Qian, Z. J., Zhou, C., Hong, P., … Li, C. (2020). In Situ Growth Visualization Nanochannel Membrane for Ultrasensitive Copper Ion Detection under the Electric Field Enrichment. ACS Applied Materials and Interfaces, 12(4), 4849–4858.

29. Gao, H., Sun, R., He, L., Qian, Z. J., Zhou, C., Hong, P., … Li, C. (2020). In Situ Growth Visualization Nanochannel Membrane for Ultrasensitive Copper Ion Detection under the Electric Field Enrichment. ACS Applied Materials and Interfaces, 12(4), 4849–4858.

30. Bolwien, C., Erhardt, C., Sulz, G., Thielecke, H., Johann, R., Pudlas, M., Mertsching, H., & Koch, S. (2010). A system for the rapid detection of bacterial contamination in cell-based therapeutica. Biomedical Vibrational Spectroscopy IV: Advances in Research and Industry, 7560, 756009.

31. Noblitt, S. D., Kraly, J. R., VanBuren, J. M., Hering, S. V., Collett, J. L., & Henry, C. S. (2007). Integrated membrane filters for minimizing hydrodynamic flow and filtering in microfluidic devices. Analytical Chemistry, 79(16), 6249–6254.

32. Nguyen, H. L., Cao, H. H., Nguyen, D. T., & Nguyen, V. A. (2017). Sodium Dodecyl Sulfate Doped Polyaniline for Enhancing the Electrochemical Sensitivity of Mercury Ions. Electroanalysis, 29(2), 595–601.

33. Pham, M. H., & Barz, D. P. J. (2017). Bonding Nafion® with polydimethysiloxane: A versatile approach towards ion-exchange membrane microfluidic devices. Journal of Membrane Science, 537, 310–314.

34. Xu, J., Vaillant, R., & Attinger, D. (2010). Use of a porous membrane for gas bubble removal in microfluidic channels: Physical mechanisms and design criteria. Microfluidics and Nanofluidics, 9(4–5), 765–772.

35. Jensen, K. H., Lee, J., Bohr, T., & Bruus, H. (2009). Osmotically driven flows in microchannels separated by a semipermeable membrane. Lab on a Chip, 9(14), 2093–2099.

36. Zhao, Y., Yi, U. C., & Cho, S. K. (2007). Highly efficient in-droplet particle concentration and separation by twDEP and EWOD for digital microfluidics. Proceedings of the IEEE International Conference on Micro Electro Mechanical Systems (MEMS), 537–540.

37. Mahmoudifard, M., Vossoughi, M., Soudi, S., & Soleimani, M. (2018). Electrospun polyethersolfone nanofibrous membrane as novel platform for protein immobilization in microfluidic systems. Journal of Biomedical Materials Research - Part B Applied Biomaterials, 106(3), 1108–1120.

38. Nama, N., Barnkob, R., Mao, Z., Kähler, C. J., Costanzo, F., & Huang, T. J. (2015). Numerical study of acoustophoretic motion of particles in a PDMS microchannel driven by surface acoustic waves. Lab on a Chip, 15(12), 2700–2709.

39. Gao, H., Sun, R., He, L., Qian, Z. J., Zhou, C., Hong, P., Sun, S., Mo, R., & Li, C. (2020). In Situ Growth Visualization Nanochannel Membrane for Ultrasensitive Copper Ion Detection under the Electric Field Enrichment. ACS Applied Materials and Interfaces, 12(4), 4849–4858.

40. Peng Lee, K., & Mattia, D. (2013). Monolithic nanoporous alumina membranes for ultrafiltration applications: Characterization, selectivity-permeability analysis and fouling studies. Journal of Membrane Science, 435, 52–61.

41. Pramanik, S. K., & Suzuki, H. (2020). Switchable Microvalves Employing a Conducting Polymer and Their Automatic Operation in Conjunction with Micropumps with a Superabsorbent Polymer. ACS Applied Materials and Interfaces, 12(33), 37741–37749.

42. Malinauskas, M., Gilbergs, H., Ukauskas, A., Purlys, V., Paipulas, D., & Gadonas, R. (2010). A femtosecond laser-induced two-photon photopolymerization technique for structuring microlenses. Journal of Optics, 12(3).

43. Kuwahara, M., Nakano, T., Tominaga, J., Lee, M. B., & Atoda, N. (1999). High-speed optical near-field photolithography by super resolution near-field structure. Japanese Journal of Applied Physics, Part 2: Letters, 38(9 A/B).

44. Sun, H. B., & Kawata, S. (2004). Two-photon photopolymerization and 3D lithographic microfabrication. Advances in Polymer Science, 170, 169–273.

45. Li, X., Chen, W., Liu, G., Lu, W., & Fu, J. (2014). Continuous-flow microfluidic blood cell sorting for unprocessed whole blood using surface-micromachined microfiltration membranes. Lab on a Chip, 14(14), 2565–2575.

46. Tabani, H., Dorabadi Zare, F., Alahmad, W., & Varanusupakul, P. (2020). Determination of Cr(III) and Cr(VI) in water by dual-gel electromembrane extraction and a microfluidic paper-based device. Environmental Chemistry Letters, 18(1), 187–196.

47. Sticker, D., Rothbauer, M., Lechner, S., Hehenberger, M. T., & Ertl, P. (2015). Multi-layered, membrane-integrated microfluidics based on replica molding of a thiol-ene epoxy thermoset for organ-on-a-chip applications. Lab on a Chip, 15(24), 4542–4554.

48. Nama, N., Barnkob, R., Mao, Z., Kähler, C. J., Costanzo, F., & Huang, T. J. (2015). Numerical study of acoustophoretic motion of particles in a PDMS microchannel driven by surface acoustic waves. Lab on a Chip, 15(12), 2700–2709.

49. Xiang, F., Lin, Y., Wen, J., Matson, D. W., & Smith, R. D. (1999). An integrated microfabricated device for dual microdialysis and on-line ESI-ion trap mass spectrometry for analysis of complex biological samples. Analytical Chemistry, 71(8), 1485–1490.

50. Palevicius A, Janusas G, Ragulskis M, Palevicius P, Sodah A. (2018). Design, analysis and application of dynamic visual cryptography for visual inspection of biomedical systems. In: Nanostructured materials for the detection of CBRN. Springer, Dordrecht, pp 223–232.

51. Tseng, W. Y., & Van Dam, R. M. (2014). Compact microfluidic device for rapid concentration of PET tracers. Lab on a Chip, 14(13), 2293–2302.

52. Lucas, K., Dehghani, M., Khire, T., Gaborski, T., Flax, J. D., Waugh, R. E., & McGrath, J. L. (2021). A predictive model of nanoparticle capture on ultrathin nanoporous membranes. Journal of Membrane Science, 633.

53. Mohanty, K., & Purkait, M. K. (Eds.). (2011). Membrane Technologies and Applications.

54. Lai, S. M., Ng, C. P., Martin-Aranda, R., & Yeung, K. L. (2003). Knoevenagel condensation reaction in zeolite membrane microreactor. Microporous and Mesoporous Materials, 66(2–3), 239–252.

55. Sridharamurthy, S. S., Dong, L., & Jiang, H. (2007). A microfluidic chemical/biological sensing system based on membrane dissolution and optical absorption. Measurement Science and Technology, 18(1), 201–207.

56. Ostasevicius, V.; Janusas, G.; Palevicius, A.; Gaidys, R.; Jurenas, V. (2017). Biomechanical Microsystems: Design, Processing and Applications; Springer International Publishing: Cham, Switzerland, 24.

57. Palevičius, A.; Janušas, G.; Čekas, E.; Patel, Y.R. (2018). Composite Piezoelectric Material for Biomedical Micro Hydraulic System; Springer: Basel, Switzerland, pp. 49–58. ISSN 0302-9743.

58. Kozuka, T., Yasuia, K., & Hatanaka, S. ichi. (2012). Acoustic micromanipulation in a microchannel. AIP Conference Proceedings, 1474(1), 363–366.

59. Ang, K. M., Yeo, L. Y., Hung, Y. M., & Tan, M. K. (2017). Acoustially-mediated microfluidic nanofiltration through graphene films. Nanoscale, 9(19), 6497–6508.

60. Karimi, A., Yazdi, S., & Ardekani, A. M. (2013). Hydrodynamic mechanisms of cell and particle trapping in microfluidics. Biomicrofluidics, 7(2).

61. Liu, X., & Ma, P. X. (2009). Phase separation, pore structure, and properties of nanofibrous gelatin scaffolds. Biomaterials, 30(25), 4094–4103.

62. Yeo, L. Y., & Friend, J. R. (2014). Surface acoustic wave microfluidics. Annual Review of Fluid Mechanics, 46, 379–406.

63. Jones, T. B., Gunji, M., Washizu, M., & Feldman, M. J. (2001). Dielectrophoretic liquid actuation and nanodroplet formation. Journal of Applied Physics, 89(2), 1441–1448.

64. Lenshof, A., & Laurell, T. (2010). Continuous separation of cells and particles in microfluidic systems. Chemical Society Reviews, 39(3), 1203–1217.

65. Puri, I. K., & Ganguly, R. (2014). Particle transport in therapeutic magnetic fields. Annual Review of Fluid Mechanics, 46, 407–440.

66. Van Reenen, A., De Jong, A. M., Den Toonder, J. M. J., & Prins, M. W. J. (2014). Integrated lab-on-chip biosensing systems based on magnetic particle actuation-a comprehensive review. Lab on a Chip, 14(12), 1966–1986.

67. Reichert, P., Deshmukh, D., Lebovitz, L., & Dual, J. (2018). Thin film piezoelectrics for bulk acoustic wave (BAW) acoustophoresis. Lab on a Chip, 18(23), 3655–3667.

68. Wu, J. (2018). Acoustic streaming and its applications. Fluids, 3(4).

69. Dual, J., & Möller, D. (2012). Acoustofluidics 4: Piezoelectricity and application in the excitation of acoustic fields for ultrasonic particle manipulation. Lab on a Chip, 12(3), 506–514.

70. Choi, Y. M., Lee, Y. L., Lim, E. S., Trimzi, M. A., Hwangbo, S. A., & Ham, Y. B. (2020). Performance improvement of ring-type PZT ceramics for ultrasonic dispersion system. Micromachines, 11(2).

71. Ostasevicius, V., Jurenas, V., Gaidys, R., Golinka, I., Kizauskiene, L., & Mikuckyte, S. (2020). Development of a piezoelectric actuator for separation and purification of biological microparticles. Actuators, 9(3).

72. Wiklund, M. (2012). Acoustofluidics 12: Biocompatibility and cell viability in microfluidic acoustic resonators. Lab on a Chip, 12(11), 2018–2028.

73. Darinskii, A. N., Weihnacht, M., & Schmidt, H. (2017). Acoustomicrofluidic application of quasi-shear surface waves. Ultrasonics, 78, 10–17.

74. Nava, G., Bragheri, F., Yang, T., Minzioni, P., Osellame, R., Cristiani, I., & Berg-Sørensen, K. (2015). All-silica microfluidic optical stretcher with acoustophoretic prefocusing. Microfluidics and Nanofluidics, 19(4), 837–844.

75. Ali, H. O. (2017). Review of porous anodic aluminium oxide (AAO) applications for sensors, MEMS and biomedical devices. Transactions of the Institute of Metal Finishing, 95(6), 290–296.

76. Osmanbeyoglu, H. U., Hur, T. B., & Kim, H. K. (2009). Thin alumina nanoporous membranes for similar size biomolecule separation. Journal of Membrane Science, 343(1–2), 1–6.

77. Yang, Q., Lin, X., & Su, B. (2016). Molecular Filtration by Ultrathin and Highly Porous Silica Nanochannel Membranes: Permeability and Selectivity. Analytical Chemistry, 88(20), 10252–10258.

78. Lin, X., Yang, Q., Ding, L., & Su, B. (2015). Ultrathin Silica Membranes with Highly Ordered and Perpendicular Nanochannels for Precise and Fast Molecular Separation. ACS Nano, 9(11), 11266–11277.

79. Warkiani, M. E., Bhagat, A. A. S., Khoo, B. L., Han, J., Lim, C. T., Gong, H. Q., & Fane, A. G. (2013). Isoporous micro/nanoengineered membranes. ACS Nano, 7(3), 1882–1904.

80. Nasrollahi, S., Banerjee, S., Qayum, B., Banerjee, P., & Pathak, A. (2017). Nanoscale Matrix Topography Influences Microscale Cell Motility through Adhesions, Actin Organization, and Cell Shape. ACS Biomaterials Science and Engineering, 3(11), 2980–2986.

81. Wang, Q., Long, Y., & Sun, B. (2013). Fabrication of highly ordered porous anodic alumina membrane with ultra-large pore intervals in ethylene glycol-modified citric acid solution. Journal of Porous Materials, 20(4), 785–788.

82. Nikam, S. B., & Sk, A. (2020). Enantioselective Separation Using Chiral Amino Acid Functionalized Polyfluorene Coated on Mesoporous Anodic Aluminum Oxide Membranes. Analytical Chemistry, 92(10), 6850–6857.

83. Sun, M., Han, K., Hu, R., Liu, D., Fu, W., & Liu, W. (2021). Advances in Micro/Nanoporous Membranes for Biomedical Engineering. Advanced Healthcare Materials, 10(7), 2001545.

84. Cho, H., Kim, J., Park, H., Won Bang, J., Seop Hyun, M., Bae, Y., … Suh, K. Y. (2014). Replication of flexible polymer membranes with geometry-controllable nano-apertures via a hierarchical mould-based dewetting. Nature Communications, 5.

85. Liang, Z., Tu, Y., & Peng, F. (2021). Polymeric Micro/Nanomotors and Their Biomedical Applications. Advanced Healthcare Materials, 10(18).

86. Stucki, M., Loepfe, M., & Stark, W. J. (2018). Porous Polymer Membranes by Hard Templating – A Review. Advanced Engineering Materials, 20(1).

87. Ciganė, U., Palevičius, A., & Janušas, G. (2021). Review of nanomembranes: materials, fabrications and applications in tissue engineering (bone and skin) and drug delivery systems. Journal of Materials Science, 56:24, 56(24).

88. Adiga, S. P., Jin, C., Curtiss, L. A., Moteiro-Riviere, N. A., & Narayan, R. J. (2009). Nanoporous membranes for medical and biological applications. Wiley Interdisciplinary Reviews. Nanomedicine and Nanobiotechnology, 1(5), 568–581.

89. Adiga, S. P., Curtiss, L. A., Elam, J. W., Pellin, M. J., Shih, C. C., Shih, C. M., & Narayan, R. J. (2008). Nanoporous materials for biomedical devices. JOM, 60(3), 26–32.

90. Kuwahara, M.; Nakano, T.; Tominaga, J.; Lee, M.B.; Atoda, N. (1999). High-Speed Optical Near-Field Photolithography by Super Resolution Near-Field Structure. Jpn. J. Appl. Phys., 38, L1079.

91. Pimpin A, Srituravanich W, (2012). Review on micro- and nanolithography techniques and their applications. Eng J 16:37–56.

92. Wu, Z.; Richter, C.; Menon, L. A. (2007). Study of Anodization Process during Pore Formation in Nanoporous Alumina Templates. J. Electrochem. Soc., 154, E8.

93. Tu, F., Späth, A., Drost, M., Vollnhals, F., Krick Calderon, S., Fink, R.H., & Marbach, H. (2017). Exploring the fabrication of Co and Mn nanostructures with focused soft X-ray beam induced deposition. J. Vac. Sci. Technol. B Nanotechnol. Microelectron. Mater. Process. Meas. Phenom., 35, 031601.

94. Peinado, P., Sangiao, S., & De Teresa, J.M. (2015). Focused Electron and Ion Beam Induced Deposition on Flexible and Transparent Polycarbonate Substrates. ACS Nano, 9, 6139–6146.

95.   Stankevičius E, Gedvilas M, Voisiat B, Malinauskas M, & Račiukaitis G. (2013). Fabrication of periodic micro-structures by holographic lithography. Lith J Phys 53(4):227–237.

96.   Grigorescu AE & Hagen CW. (2009). Resists for sub-20-nm electron beam lithography with a focus on HSQ: state of the art. Nanotechnol. 10, 20-29.

97.   Lin, J., Chen, S., Huang, S.H., Hun, C.W., & Chen, C.C. (2017). Challenges to Fabricate Large Size-Controllable Submicron-Structured Anodic-Aluminum-Oxide Film, Atlas J. Mater. Sci., 2 (2), pp. 65-72.

98.   Wang J, Ren Z, Hou Y, Yan X, Liu P, Zhang H, Zhang HX, & Guo J. (2020). A review of graphene synthesis at low temperatures by CVD methods. New Carbon Mater 35:193–208.

99.   Bae, C., Shin, H., & Nielsch, K. (2011). Surface modification and fabrication of 3D nanostructures by atomic layer deposition. MRS Bull, 36, 887–897.

100.Kelly, D.N., Wakabayashi, R.H., & Stacy, A.M. (2014). A Modified Sol–Gel Technique for Pore Size Control in Porous Aluminum Oxide Nanowire Templates. ACS Appl. Mater. Interfaces, 6, 20122–2012.

101.Aramesh, M. & Cervenka, J. (2014). Surface modification of porous anodic alumina for medical and biological applications A. Seifalian, A. de Mel, Deepak M. Kalaskar (Eds.), Nanomedicine, One Central Press (OCP), Manchester, UK, 439-467.

102.Chia HN, Wu BM, (2015). Recent advances in 3D printing of biomaterials. J Biol Eng 9:4.

103.Masuda H, Yamada H, Satoh M, Asoh H, Nakao M. (1997). Highly ordered nanochannel-array architecture in anodic alumina. Appl Phys Lett, 71(19):2770–2772.

104.Baik, J.M., Schierhorn, M., & Moskovits, M. (2018). Fe nanowires in nanoporous alumina: Geometric effect versus influence of pore walls. J. Phys. Chem. C, 112, 2252–2255.

105. Raspal, V., Awitor, K. O., Massard, C., Feschet-Chassot, E., Bokalawela, R. S. P., & Johnson, M. B. (2012). Nanoporous surface wetting behavior: The line tension influence. Langmuir, 28(30), 11064–11071.

106. Sulka, G. D., & Parkoła, K. G. (2006). Anodising potential influence on well-ordered nanostructures formed by anodisation of aluminium in sulphuric acid. Thin Solid Films, 515(1), 338–345.

107. Santos, A., Kumeria, T., & Losic, D. (2013). Nanoporous anodic aluminum oxide for chemical sensing and biosensors. TrAC - Trends in Analytical Chemistry, 44, 25–38.

108. Kushwaha, M. K. (2014). A comparative Study of Different Electrolytes for Obtaining Thick and Well-ordered nano-porous Anodic Aluminium Oxide (AAO) Films. Procedia Materials Science, 5, 1266–1273.

109. Sulka, G. D., & Hnida, K., (2012). Distributed Bragg reflector based on porous anodic alumina fabricated by pulse anodization. Nanotechnology, 23(7).

110. Schwirn, K., Lee, W., Hillebrand, R., Steinhart, M., Nielsch, K., & Gösele, U. (2008). Self-ordered anodic aluminum oxide formed by H2SO4 hard anodization. ACS Nano, 2(2), 302–310.

111. Furneaux RC, Rigby WR, Davidson AP. (1989). The formation of controlled-porosity membranes from anodically oxidized aluminium. Nature 1989;337:147–9.

112. Chen, W., Wu, J.-S., & Xia, X.-H. (2008). Porous Anodic Alumina with Continuously Manipulated Pore/Cell Size. ACS Nano, 2, 959–965.

184

113. Zaraska, L., Brudzisz, A., Wierzbicka, E., & Sulka, G.D. (2016). The effect of electrolyte change on the morphology and degree of nanopore order of porous alumina formed by two-step anodization. Electrochim. Acta , 198, 259–267.

114. Buijnsters JG, Zhong R, Tsyntsaru N, & Celis J-P. (2013). Surface Wettability of Macroporous Anodized Aluminum Oxide. 31 ACS Appl Mater Interfaces, 5:3224–3.

115. Lee W, Kim J-C, & GÃ sele U. (2010). Spontaneous Current Oscillations during Hard Anodization of Aluminum under Potentiostatic Conditions. Adv Funct Mater, 20:21–7.

116. Ferré-Borrull J, Rahman MM, Pallarès J, & Marsal LF. (2016). Tuning nanoporous anodic alumina distributed-Bragg reflectors with the number of anodization cycles and the anodization temperature. Nanoscale Res Lett, 9, 410.

117. Chung CK, Zhou RX, Liu TY, Chang WT. (2009). Hybrid pulse anodization for the fabrication of porous anodic alumina films from commercial purity (99%) aluminum at room temperature. Nanotechnology, 20:055301.

118. Wang, Q., Long, Y., & Sun, B. (2013). Fabrication of highly ordered porous anodic alumina membrane with ultra-large pore intervals in ethylene glycol-modified citric acid solution. J. Porous Mate, 20, 785–788.

119. O'sullivan J and GW. (1997). The morphology and mechanism of formation of porous anodic films on aluminium. Proc R Soc London A Math Phys Sci, 317, 511–43.

120. Lee W, & Park S-J. (2014). Porous Anodic Aluminum Oxide: Anodization and Templated Synthesis of Functional Nanostructures. Chem Rev, 114, 7487–556.

121. Zhou, Z.; Nonnenmann, S.S. (2019). Progress in nanoporous templates: Beyond anodic aluminum oxide and towards functional complex materials. Materials, 12, 2535.

122. Kipke, S., & Schmid, G., (2004). Nanoporous alumina membranes as diffusion controlling systems. Advanced Functional Materials, 14(12), 1184–1188.

123. Gorokh G, Mozalev A, Solovei D, Khatko V, Llobet E, Correig X. (2006). Anodic formation of low-aspect-ratio porous alumina films for metal-oxide sensor application. Electrochim Acta, 52, 1771–80.

124. Kumeria T, Kurkuri M, Diener K, Zhang C, Parkinson L, Losic D. (2011). Reflectometric interference biosensing using nanopores: Integration into microfluidics. vol. 8204.

125. Shaban M, Mustafa M, & Khan A.A.P. (2020). Hexagonal diameter in cadmium sulfide/anodic alumina nanoporous bi-layer membrane by a sol–gel spin coating and their sensing application. Appl Phys A Mater Sci Process, 126.

126. W. Shi, Y. Shen, D. Ge, M. Xue, H. Cao, S. Huang. (2008). "Functionalized anodic aluminum oxide (AAO) membrane for affinity protein separation", J. Membr. Sci, vol. 325, pp. 801-808.

127. Lee, S. B., Mitchell, D. T., Trofin, L., Nevanen, T. K., Söderlund, H., & Martin, C. R. (2002). Antibody-based bio-nanotube membranes for enantiomeric drug separations. Science, 296(5576), 2198–2200.

128. Lee, W., & Park, S.-J. (2014). Porous Anodic Aluminum Oxide: Anodization and Templated Synthesis of Functional Nanostructures. Chem. Rev., 114, 7487–7556.

129. Yamaguchi, A., Uejo, F., Yoda, T., Uchida, T., Tanamura, Y., Yamashita, T., & Teramae, N. (2004). Self-assembly of a silica-surfactant nanocomposite in a porous alumina membrane. Nature Materials, 3(5), 337–341.

130. Kasi, A. K., Kasi, J. K., Hasan, M., Afzulpurkar, N., Pratontep, S., Porntheeraphat, S., & Pankiew, A. (2012). Fabrication of low cost anodic aluminum oxide (AAO) tubular membrane and their application for hemodialysis. Advanced Materials Research, 550–553, 2040–2045.

131. Park, Y., Kim, S., Jang, I. H., Nam, Y. S., Hong, H., Choi, D., & Lee, W. G. (2016). Role of the electric field in selective ion filtration in nanostructures. Analyst, 141(4), 1294–1300.

132. Wen, F. Y., Chen, P. S., Liao, T. W., & Juang, Y. J. (2018). Microwell-assisted filtration with anodic aluminum oxide membrane for Raman analysis of algal cells. Algal Research, 33, 412–418.

133. Chang, Y. J., Yang, W. T., & Wu, J. C. (2019). Isolation and detection of exosomes via AAO membrane and QCM measurement. Microelectronic Engineering, 216.

134. Aminullah, Kasi, A. K., Kasi, J. K., & Bokhari, M. (2018). Fabrication of mechanically stable AAO membrane with improved fluid permeation properties. Microelectronic Engineering, 187–188, 95–100.

135. Kim, Y., Misun C., Yosep C., Hyunsang Joo and JL. (2013). Electrokinetic separation of biomolecules through multiple nano-pores on membrane. Chem Phys Lett, 561, 63–7.

136. Ma Y, Kaczynski J, Ranacher C, Roshanghias A, Zauner M, Abasahl B. (2018). Nano-porous aluminum oxide membrane as filtration interface for optical gas sensor packaging. Microelectron Eng, 198, 29–34.

137. Kasi, A. K., Kasi, J. K., Afzulpurkar, N., Bohez, E., Tuantranont, A., & Mahaisavariya, B. (2010). Novel anodic aluminum oxide (AAO) nanoporous membrane for wearable hemodialysis device. ICCE 2010 - 3rd International Conference on Communications and Electronics, 98–101.

138. Hasan, M., Kasi, A. K., Kasi, J., Afzulpurkar N. (2012). Anodic Aluminum Oxide (AAO) to AAO Bonding and Their Application for Fabrication of 3D Microchannel. Nanosci Nanotechnol Lett, 4, 569-573(5).

139. Chang, H-C., Y-H. Chen, A-T. Lo, S-S. Hung, S-L. Lin, I-N. Chang and J-CL. (2014). Modified nanoporous membranes on centrifugal microfluidic platforms for detecting heavy metal ions. Mater Res Innov, 18, S2-685.

140. Hun CW, Chiu Y-J, Luo Z, Chen CC, Chen SH. (2018). A new technique for batch production of tubular anodic aluminum oxide films for filtering applications. Appl Sci, 8.

141. Phuong, N. T., Andisetiawan, A., Van Lam, D., Kim, J. H., Choi, D. S., Whang, K. H., Nahm, J., You, Y., & Yoon, J. S. (2016). Nano sand filter with functionalized nanoparticles embedded in anodic aluminum oxide templates. Scientific Reports, 6.

142. Song J, Oh H, Kong H, Jang J. (2011). Polyrhodanine modified anodic aluminum oxide membrane for heavy metal ions removal. J Hazard Mater, 187, 311–71.

143. Kim, Y. J., Jones, J. E., Li, H., Yampara-Iquise, H., Zheng, G., Carson, C. A., Cooperstock, M., Sherman, M., & Yu, Q. (2013). Three-dimensional (3-D) microfluidic-channel-based DNA biosensor for ultra-sensitive electrochemical detection. Journal of Electroanalytical Chemistry, 702, 72–78.

144. Shi, W., Shen, Y., Ge, D., Xue, M., Cao, SH., (2008), Functionalized anodic aluminum oxide (AAO) membranes for affinity protein separation. J Memb Sci, 325, 801–8.

145. Ashraf, M. W., Qureshi, M. Z., Ghaffar, F., Tayyaba, S., & Afzulpurkar, N. (2016). Structural study of AAO membrane during the dialysis process. 2016 International Conference on Intelligent Systems Engineering, ICISE 2016, 226–231.

146. Thormann A, Berthold L, Gšring P, Lelonek M, Heilmann A. (2012). Nanoporous Aluminum Oxide Membranes for Separation and Biofunctionalization. Procedia Eng, 44, pp. 1107–11.

147. Kasi, A. K., Afzulpurkar, N., Kasi, J. K., Tuantranont, A., & Dulyaseree, P. (2011). Utilization of cracks to fabricate anodic aluminum oxide nanoporous tubular and rectangular membrane. Journal of Vacuum Science & Technology B, Nanotechnology and Microelectronics: Materials, Processing, Measurement, and Phenomena, 29(4), 04D107.

148. Chang, Y. J., Yang, W. T., & Wu, J. C. (2019). Isolation and detection of exosomes via AAO membrane and QCM measurement. Microelectronic Engineering, 216.

149. Crump, J. R. , A heat transfer textbook by John H. Lienhard, prentice hall, 1981. AIChE Journal, 27(4), 700–700, 1981.

150. Enescu, D. & Virjoghe, EO. (2014). A review of thermoelectric cooling parameters and performance. Renewable and Sustainable Energy Reviews, 38, 903-916.

151. Hebei IT. (n.d.). TEC1-12715 Datasheet.

152. CPU COOLER S_MULTI / MLW-D24M-A18PCR2 COOLER MASTER | Varle.lt. (n.d.). Retrieved April 12, 2022, from https://www.varle.lt/ausintuvai/cpu-cooler-s_multimlw-d24m-a18pcr2-cooler-master--14205049.html

153. Magnetic Stirrer Bar Singapore. (n.d.). Retrieved May 12, 2022, from https://www.diakonie-annaberg.de/magnetic-stirrer/magnetic-stirrer-bar-singapore.html

154. AX-12001DBL, Laboratory Power Supplies - axiomet.eu. (n.d.). Retrieved April 12, 2022, from https://axiomet.eu/gb/en/product/axiomet/laboratory-power-supplies/ax-12001dbl/100165/

155. 1050A-H24 Aluminum:: MakeItFrom.com. (n.d.). Retrieved April 12, 2022, from https://www.makeitfrom.com/material-properties/1050A-H24-Aluminum

156. Hitachi Model S-3400N Variable-Pressure SEM Specifications Hitachi Model S-3400N PC-Based Variable Pressure Scanning Electron Microscope. (n.d.).

157. Goldsmith, C. S. & Miller, S. E. (2009). Modern uses of electron microscopy for detection of viruses. Clinical Microbiology Reviews, 22(4), 552-563.

158. Goldstein, J., Newbury, D. E., Joy, D. C., Lyman, C. E., Echlin, P., Lifshin, E., Sawyer, L. & Michael, J. R. (2003). Scanning electron microscopy and X-ray microanalysis. Springer, US, ISBN 978-0-306-47292-3.

159. XFlash® 6 | 30 Detector [online]. 2019 [viewed on 13 April 2022]. Available from www.bruker.com/products/x-ray-diffraction-and-elemental-analysis/edswds-ebsd-sem-micro-xrf-and-sem-micro-ct/quantax-eds-for-sem/quantax-hardware/xflashr-6-30-detector.html.

160. Infrared spectroscopy at ColourLex [online]. 2019 [viewed on 13 April 2022] Available from https://colourlex.com/project/infrared-spectroscopy/.

161. Zisman, W.A. (1964). Contact Angle, Wettability and Adhesion: Advances in Chemistry Series. Am. Chem. Soc. 1964, 43, 1.

162. Patel, Y. R. (2018). Investigation of Young's modulus and hydrophobicity of PZT composite materials for biosensor applications (p. 78) [Book]. p. 78. Kaunas: Kauno technologijos universitetas. Prieiga per eLABa – nacionalinė Lietuvos akademinė elektroninė biblioteka.

163. Gangwar, J.; Gupta, B.K.; Tripathi, S.K.; Srivastava, A.K. (2015). Phase dependent thermal and spectroscopic responses of Al2O3 nanostructures with different morphogenesis. Nanoscale, 7, 13313–13344.

164. Prashanth, P.A.; Raveendra, R.S.; Hari Krishna, R.; Ananda, S.; Bhagya, N.P.; Nagabhushana, B.M.; Lingaraju, K.; Raja Naika, H. (2015). Synthesis, characterizations, antibacterial and photoluminescence studies of solution combustion-derived α-Al2O3 nanoparticles. J. Asian Ceram. Soc., 3, 345–351.

165. Oliver, W.C., & Pharr, G.M. (2004). Measurement of Hardness and Elastic Modulus by Instrumented Indentation: Advances in Understanding and Refinements to Methodology, J. Mater. Res. 19 (1), 3-20.

166. USA :: Anton-Paar.com. (n.d.). Retrieved April 20, 2022, from https://www.anton-paar.com/us-en/

167. Bankova, A., Videkov, V., & Tzaneva, B. (2014). Development of topologically structured membranes of aluminum oxide. Journal of Physics: Conference Series, 514(1), 012027.

168. Ng, K., Y. Lin, and Ngan, A., (2009). "Deformation of anodic aluminum oxide nano-honeycombs during nanoindentation," Acta Materialia, 57(9), pp. 2710–2720.

169. Samantilleke, A. P., Carneiro, J. O., Azevedo, S., Thuy, T., & Teixeira, V. (2013). Electrochemical Anodizing, Structural and Mechanical Characterization of Nanoporous Alumina Templates. Journal of Nano Research, 25, 77–89.

170. Chen, F., Kong, L., Song, W., Jiang, C., Tian, S., Yu, F., Qin, L., Wang, C., Zhao, X., (2019). The electromechanical features of LiNbO3 crystal for potential high temperature piezoelectric applications, *Journal of* Materiomics, 5(1), 73-80.

171. Nguyen, V. T., Kumar, P., & Leong, J. Y. C. (2018). Finite Element Modellingand Simulations of Piezoelectric Actuators Responses with Uncertainty Quantification. Computation 2018, Vol. 6, Page 60, 6(4), 60.

172. Reynolds number | Definition & History | Britannica. (n.d.). Retrieved May 10, 2022, from https://www.britannica.com/science/Reynolds-number

173. Sharipov, F., & Benites, V. J., (2020). Transport coefficients of multi-component mixtures of noble gases based on ab initio potentials: Viscosity and thermal conductivity. Physics of Fluids, 32(7), 077104.

174. Universal Industrial Gases, Inc...Nitrogen N2 Properties, Uses, Applications - Gas and Liquid. (n.d.). Retrieved May 3, 2022, from http://www.uigi.com/nitrogen.html

188

Curriculum Vitae

Yatinkumar Patel
y.patel@ktu.lt

Education:

1996 - 2006	Basic and high school education at Sardar Vinay mandir, Vadodara, India
2006 - 2009	Diploma in Mechanical Engineering, Technical education board, Gandhinagar, India
2009 - 2012	Bachelor degree in Mechanical Engineering, Rajiv Gandhi Technical University, Bhopal, India
2016 - 2018	Master degree in Mechanical Engineering, Kaunas University of Technology, Kaunas, Lithuania
2018 - 2022	PhD in Mechanical Engineering, Kaunas University of Technology, Kaunas, Lithuania

Professional Experience:

2012 - 2015	Production Engineer, Danke Electricals. PVT. LTD., India
2015 - 2016	Design Engineer, DEMAT Engineering (KYB Conmat India PVT. LTD), India
2019 - 2022	Project Junior Researcher, Kaunas University of Technology, Kaunas, Lithuania

Research Interests:

Microhydraulic system, Electrochemical Anodization, Micro/nano Fluidics, Piezocomposites, Micro/nano porous membranes, MEMS

Scientific articles on the topic of dissertation:

ARTICLES IN PEER-REVIEWED SCIENTIFIC PUBLICATIONS
Indexed in the Web of Science with Impact Factor

1. Patel, Yatinkumar; Janusas, Giedrius; Palevicius, Arvydas; Vilkauskas, Andrius. Development of nanoporous AAO membrane for nano Ffltration using the acoustophoresis method // Sensors. Basel : MDPI. ISSN 1424-8220. 2020, vol. 20, iss. 14, art. no. 3833, p. 1-24. DOI: 10.3390/s20143833. [Science Citation Index Expanded (Web of Science); Scopus; DOAJ] [IF: 3.576; AIF: 3.906; IF/AIF: 0.915; Q1 (2020. InCites JCR SCIE)] [CiteScore: 5.80; SNIP: 1.555; SJR: 0.636; Q1 (2020, Scopus Sources)]

2. Patel, Yatinkumar; Janusas, Giedrius; Palevicius, Arvydas; Vilkauskas, Andrius; Lepsik, Petr. Investigation of the hydrophobic properties of piezoelectric nanocomposites and applications in biomedical micro-hydraulic devices // Materiali in tehnologije = Materials and technology. Ljubljana : Institute of Metals and Technology. ISSN 1580-2949. eISSN

1580-3414. 2020, vol. 54, iss. 3, p. 407-415. DOI: 10.17222/mit.2019.249. [Science Citation Index Expanded (Web of Science); Scopus] [IF: 0.638; AIF: 4.773; IF/AIF: 0.133; Q4 (2020. InCites JCR SCIE)] [CiteScore: 1.50; SNIP: 0.557; SJR: 0.270; Q3 (2020, Scopus Sources)]

Indexed in the Web of Science or Scopus without Impact Factor or SNIP

1. Patel, Yatinkumar; Janusas, Giedrius; Palevicius, Arvydas. Fabrication of nanoporous free standing anodic alumina using two-step anodization for applicability in microhydraulic system as nano filter using surface acoustics // Materials today: proceedings. Oxford : Elsevier. ISSN 2214-7853. 2021, vol. 45, pt. 6, p. 5059-5064. DOI: 10.1016/j.matpr.2021.01.571. [Conference Proceedings Citation Index - Science (Web of Science); Scopus] [CiteScore: 1.80; SNIP: 0.657; SJR: 0.341; Q3 (2020, Scopus Sources)]

2. Patel, Yatin; Ciganas, Justas; Janusas, Giedrius; Palevicius, Arvydas. Development of nano cavities in aluminum oxide membrane for bioparticle manipulation by acoustophoresis method // 2020 IEEE XVI international conference on the perspective technologies and methods in MEMS design (MEMSTECH), Lviv, April 22-26, 2020: proceedings. Piscataway, NJ : IEEE, 2020. ISBN 9781728171791. eISBN 9781728171807. ISSN 2573-5373. p. 59-63. DOI: 10.1109/MEMSTECH49584.2020.9109515. [Conference Proceedings Citation Index - Science (Web of Science); Scopus; INSPEC]

3. Patel, Yatinkumar; Palevicius, Arvydas; Naginevicius, Vytenis; Liaudanskaite, Judita; Janusas, Giedrius. Aluminum oxide membrane as a functional element for filtering bioparticles in micro hydraulic devices // Proceedings of SPIE: Frontiers in ultrafast optics: biomedical, scientific, and industrial applications XX, 1-6 February 2020, San Francisco, California, United States / editors: Peter R. Herman, Michel Meunier, Roberto Osellame. Bellingham, WA : SPIE, 2020. ISBN 9781510614680. ISSN 0277-786X. eISSN 1996-756X. 2020, vol. 11270, art. no. 1127004, p. 1-7. DOI: 10.1117/12.2541640. [Conference Proceedings Citation Index - Science (Web of Science); Scopus] [CiteScore: 0.80; SNIP: 0.261; SJR: 0.192; Q4 (2020, Scopus Sources)]

Articles in Conference Proceedings

1. Patel, Yatinkumar; Janusas, Giedrius; Palevicius, Arvydas. Fabrication of nanoporous alumina in 0.3 M oxalic acid and study on mechanical properties using micro indentation test // Materials today: proceedings: Third international conference on aspects of materials science and engineering / edited by S. Sehgal, P. Goyal. Amsterdam : Elsevier. ISSN 2214-7853. 2022, vol. 57, pt. 2, p. 630-635. DOI:

190

10.1016/j.matpr.2022.02.044. [CiteScore: 1.80; SNIP: 0.657; SJR: 0.341; Q3 (2020, Scopus Sources)]

2. Patel, Y.; Justas, C.; Naginevičius, V.; Palevicius, A. Replicated computer generated microstructure onto piezoelectric nanocomposite and nanoporous aluminum oxide membranes usage in microfluidics // Advanced nanomaterials for detection of CBRN: proceedings of the NATO advanced research workshop on advanced nanomaterials for detection of CBRN, Odessa, Ukraine, 2–6 October 2019 / edited by: Janez Bonča and Sergei Kruchinin. Dordrecht : Springer, 2020. ISBN 9789402420296. eISBN 9789402420302. p. 235-246. (NATO science for peace and security series A: Chemistry and biology, ISSN 1874-6489, eISSN 1874-6527). DOI: 10.1007/978-94-024-2030-2_16.

Other Conference Abstracts and Non-Peer Reviewed Conference Papers

1. Patel, Yatinkumar; Palevicius, Arvydas; Janusas, Giedrius. Fabrication and characterization of nanoporous anodic alumina membrane for nanofiltration appliation // Open readings 2022: 65th international conference for students of physics and natural sciences, March 15-18: abstract book / editors: Š. Mickus, S. Pūkienė, L. Naimovičius. Vilnius : Vilnius University Press. 2022, O4-1, p. 46.

2. Patel, Yatinkumar; Palevičius, Arvydas. Low-cost Fabrication of nanoporous aluminium oxide membrane and its application in microfluidics // IRWBM 2021: 2nd international research workshop in biomechanical microsystems 2021: October 22, 2021, Kaunas University of Technology, Lithuania: program and abstracts. Kaunas : Kaunas University of Technology. 2021, p. 13.

3. Patel, Yatinkumar; Palevicius, Arvydas; Janusas, Giedrius. Self ordered nanoporous aluminum oxide membrane for nanofiltration using surface acoustic waves for microhydrualic devices in biomedicine // Open Readings 2020: 63rd international conference for students of physics and natural sciences, March 17-20, Vilnius, Lithuania: abstract book. Vilnius : Vilnius University, 2020, O7-2. ISBN 9786090703779. p. 57.

4. Patel, Yatinkumar; Lepsik, Petr. Investigation of mechanical and hydrophobic properties of PZT composite materials and application in biomedical micro hydraulic devices // IRWBM 2019: International research workshop in biomechanical microsystems 2019, October 23, 2019, Kaunas University of Technology, Lithuania: program and abstracts. Kaunas : [KTU]. 2019, p. [14].